Science

AAAS

Cuba reconnects

Thaw brightens prospects for science

CONTENTS

760 & 803
Personalized cancer vaccines

751

766

CONTENTS

ON THE COVER

A young woman in Havana checks her smartphone last month. Warmer ties between Cuba and the United States are expected to better integrate Cuban scientists into the global community and boost joint research on topics as diverse as the island's stunning coral reefs and the mosquito-borne chikungunya disease. See pages 735 and 746. *Photo: REUTERS/Enrique de la Osa*

Published by AAAS

Science serves as a forum for discussion of important issues related to the advancement of science by publishing material on which a consensus has been reached as well as including the presentation of minority of conflicting points of view. Accordingly, all articles published in *Science*—including editorials, news and comment, and books reviews—are signed and reflect the individual views of the authors and not official points of view adopted by AAAS or the institutions with which the authors are affiliated.

INFORMATION FOR AUTHORS See pages 678 and 679 of the 6 February 2015 issue or access www.sciencemag.org/about/authors

Published by AAAS

Science in U.S.-Cuba relations

Last month, after more than half a century of estrangement, the presidents of Cuba and the United States sat together for talks in Panama at the Summit of the Americas. This truly symbolic step in the already agreed-upon path toward restoring diplomatic ties has increased expectations in scientific circles. However, any impact will depend on what policy-makers and researchers make of this long-awaited opportunity.

Indeed, in spite of political differences, the two countries share a history of working well together in science. This relationship extends back to the mid–19th century, when the founders of national research institutions in both capitals (Felipe Poey in Havana and Joseph Henry in Washington) began exchanging letters, literature, and specimens. From that correspondence sprang many seminal scientific interactions, including the groundbreaking work of Cuban researcher Carlos Finlay and U.S. physician Jesse Lazear. Their partnership in 1900 confirmed Finlay's earlier theories about mosquitoes as the vector for yellow fever and turned the tide in controlling that disease. Likewise, just last year, in response to the Ebola epidemic in West Africa, both nations were engaged as the two main providers for a World Health Organization effort to contain the exponential initial spread of the disease. Once again, their partnership demonstrated what Cuba and the United States can achieve by working side by side for the common good.

And yet, most of the past scientific interactions between them have been feeble because of political limitations. After 1959, diplomatic links between Cuba and the United States were severed. In trying to bridge the divide, scientists in both countries restarted links with a 1980 agreement between the U.S. Smithsonian Institution and the Cuban Academy of Sciences to build on past shared resources, challenges, and abilities. Similar scientific agreements followed in the 1990s between the Cuban Academy and the New York Botanical Garden, Social Sciences Research Council, and other centers and universities. Last year, the American Association for the Advancement of Science (AAAS) and the Cuban Academy agreed to jointly focus on biomedical research in cancer, infectious diseases, drug resistance, and neurosciences, and earlier this year, the two countries discussed how to start working together to protect the marine environment between them—a mere 90 miles of ocean, where among other shared scientific challenges, both faced the Deepwater Horizon catastrophe.

We cannot squander scientific opportunities if a new era in U.S-Cuban relations is launched. But to cultivate true scientific relations requires more than just lifting existing embargo limitations. It would be easy for the United States to simply repeat the past and just consider Cuba as another close market of plantations, mining industries, and tourism, as was the case during the early 20th century. Cuban scientists, engineers, and educators, together with U.S. entrepreneurship and resources, must promote scientific collaboration between them and with other nations. For example, there is great global need to identify and handle emerging infectious disease threats. Both nations should be free to share data and knowledge to improve global monitoring and prevention. Climate scientists in Cuba and the United States should share their expertise and technologies in hurricane science and disaster management, as well as in the evaluation of the impact of climate change and the adaptations needed to mitigate its effects.

In both societies, there are uncertainties about this new path to the future, given the long history of confrontation and distrust. Many aspects of the relationship require lengthy negotiations to build consensus. However, science continues to be a means to show how to proceed to success. Cuban and U.S. scientists can achieve important results that have impact beyond their own countries' borders only if policy-makers can ensure conditions in each country that support robust collaboration. That includes removing visa obstacles and allowing unobstructed sharing of data, resources, and knowledge. Such actions would be a first strong step in creating a solid foundation for the diplomacy that has to be built anew between Cuba and the United States.

– **Sergio Jorge Pastrana**

"We cannot squander scientific opportunities if a new era... is launched."

Sergio Jorge Pastrana is the Foreign Secretary of the Cuban Academy of Sciences, Havana, Cuba. E-mail: pastrana@ceniai.inf.cu

PHOTOS: (TOP RIGHT) CUBAN ACADEMY OF SCIENCES; (INSET) PABLO MARTINEZ MONSIVAIS/AP IMAGES

NEWS

IN BRIEF

Liberia cautiously hails Ebola's end

Women in Liberia celebrate the announcement of the end of the Ebola epidemic in their country.

The Ebola epidemic in Liberia is officially over. Cases have been declining there since October, and on 9 May—42 days after the last confirmed Ebola patient was buried—the World Health Organization (WHO) declared the country free of the disease. (The incubation period for Ebola is up to 21 days, and WHO requires a country go twice that period without cases before it declares the official end of an outbreak.) The epidemic claimed more than 4700 lives in Liberia, including nearly 200 health care workers. Replacing lost doctors and nurses is only one of the daunting challenges the country still faces, however. The epidemic continues in neighboring Guinea and Sierra Leone and could cross the border again. Although scientists still don't know where the virus lurks in wildlife, many predict that another outbreak in West Africa is only a matter of time. Liberian President Ellen Johnson Sirleaf says the country will try to use the lessons learned during the epidemic to strengthen its health system. She spent 9 May shaking hands—a practice discouraged during the epidemic—with survivors and family members of those who died.

AROUND THE WORLD

Nobelists defend animal research

BRUSSELS | Sixteen Nobel laureates have added their voices to a chorus of 149 science organizations defending existing E.U.-wide rules for animal research. In an open letter published last week, the group warns that repealing the current rules, as a citizens' initiative has proposed, would harm biomedical research in Europe. More than 1 million citizens from 26 countries have formally urged the European Commission to scrap a 2010 directive that regulates the use of animals in scientific research. The Stop Vivisection European Citizens' Initiative, submitted to the commission in March, calls for a "paradigm shift in the way biomedical and toxicological research are being conducted." The proponents want the commission to put forward a fresh proposal phasing out animal testing in favor of "more accurate, reliable, human-relevant methods." The commission must now consider turning the proposal into legislation; it has until early June to respond. http://scim.ag/Nobelanimal

White House OKs Arctic drilling

WASHINGTON, D.C. | Royal Dutch Shell has cleared a major hurdle toward its second attempt at oil exploration in the Arctic Ocean. On 11 May, the Obama administration gave conditional approval for the company to resume drilling this summer

Activists in Seattle protest Arctic drilling plans.

in the Chukchi Sea off Alaska's coast. The move comes 3 years after a series of problems, including the grounding of one of its offshore rigs due to rough seas, forced Shell to suspend its operations and embroiled the company in lawsuits by environmental and native groups. Before receiving the go-ahead, Shell must still obtain state and federal drilling permits for six planned exploration wells. Shell must also abide by Arctic-specific safety regulations released by the Bureau of Ocean Energy Management this past February. The administration's decision has angered environmental groups still smarting from a January decision to open up part of the Atlantic coast to drilling (*Science*, 30 January, p. 460). Drilling opponents fear an accident, noting that the Arctic region lacks data on both the fate of oil in the cold environment and the infrastructure for rapid response.

Bioethicists to weigh drug access

NEW BRUNSWICK, NEW JERSEY | Pharmaceutical giant Johnson & Johnson announced last week it will convene a panel of bioethicists to help decide how to respond to patient requests for access to experimental drugs outside of clinical trials. If denied, these appeals can create bad publicity, but granting such requests poses a dilemma for drugmakers, because unapproved treatments have not yet been proven safe or effective and can be costly to supply. The new committee, to be overseen by New York University bioethicist Arthur Caplan, will help the company "better weigh what we know about these therapies against the patient's condition and risk factors," said Amrit Ray, chief medical officer for Johnson & Johnson subsidiary Janssen Pharmaceutical Companies, in a statement. The move could serve as a new model for companies to address "compassionate use," an issue that has recently inspired a series of controversial state laws (*Science*, 20 June 2014, p. 1329).

Pricey drugs on 'essential' list

GENEVA, SWITZERLAND | Several expensive new drugs that treat hepatitis C and some common cancers are on the latest Essential Medicines List (EML) published by the World Health Organization (WHO). An expert committee selects medicines every 2 years for the list based on scientific evidence that the drugs work and are safe and cost-effective. This year's list, released 8 May, includes five new drugs that target the hepatitis C virus (HCV) and 16 new cancer medicines, including

Wrinkles in a baby's foot hold clues to its gestational age.

How old is the baby, really?

Wondering exactly how many weeks a baby was in the womb? There's an app for that. BabyFace, the brainchild of researchers at the University of Nottingham in the United Kingdom, asks new parents to upload photos of their babies' feet, face, and ears, as well as their gestational ages, to an online database that, the scientists hope, will make it easier to gauge a baby's time in the womb. The depth of foot wrinkles and the roundness of eyes are among several subtle clues. The app is designed for babies born between 28 days early and 14 days late, and the eventual goal is to use it to craft a second app, NeoGest, which will assist doctors and families in the developing world who want to gauge a baby's prematurity. The project brings together computer scientists and child health experts at the university and is supported by the Bill & Melinda Gates Foundation.

pricey drugs such as sofosbuvir for HCV and the antileukemia drug Gleevec. "We are trying to use the list as leverage for increasing access and further actions on a global level," says Italian pharmacologist Nicola Magrini, WHO's top overseer of EML. Many developing countries use EML to help determine how much money they invest in different medicines. Magrini describes the list as "a flag" from a neutral party that a "cost-effective" drug is of little use if countries cannot afford it. http://scim.ag/WHOEssMeds

Climate skeptic's center in limbo

SYDNEY, AUSTRALIA | The Australian government's controversial plan to help fund a think tank in collaboration with global warming skeptic Bjørn Lomborg

has unraveled—for now. Last month, the University of Western Australia (UWA) in Perth announced plans to host an Australian Consensus Centre in collaboration with Lomborg's Copenhagen Consensus Center that UWA said would focus on how to prioritize global aid spending, not climate change (*Science*, 24 April, p. 376). But Australia's conservative government outraged scientists already concerned with budget cuts to science funding when UWA announced the government would contribute AU$4 million to start the center and cover a third of its operating costs. In the wake of the uproar, UWA Vice-Chancellor Paul Johnson announced on 8 May with "great regret and disappointment" that he had advised the federal government that the university would cancel the center's contract and

Ground-dwelling birds build complex nests

Living on the ground floor isn't always a bargain—at least when it comes to a bird's nest. A nest can be anything from a few twigs thrown together on a flat space to an elaborately woven hanging orb—but in one family of birds, those species that live lower down tend to build more elaborate nests, scientists report this week in *The Auk: Ornithological Advances*. Although a simple cup-shaped nest suffices for this bearded parrotbill (shown), which lives a meter high among cobweb-laden grass stalks, the parrotbill's ground-based relatives build more elaborate dome-shaped lairs to keep predators away from their young. To understand why birds have such different housing tastes, neurobiologist Zachary Hall of the University of Toronto analyzed nest placement and type across the family tree of 90 species of Old World babblers like the parrotbill. In previous work, Hall had helped establish that birds with more complex nests have more folds in the cerebellum, a part of the motor control section of the brain. Now, he and his colleagues report that for these birds, the more complex domed nests coevolved with the move to the ground.

2.6–2.9
millimeters

Annual rise in global mean sea level from 1993 to 2014, according to a *Nature Climate Change* study. During the 1990s, the rise was slower than previous estimates, suggesting that it is now accelerating.
http://scim.ag/GMSLrise

7.3

Magnitude of another strong earthquake that rocked Nepal on 11 May, just over 2 weeks after a 7.8-magnitude quake struck and killed at least 8000 people.

1.2
million

Hectares of trees lost globally since 2001, threatening species from whooping cranes in Canada to rare Peruvian frogs, according to a recent World Resources Institute analysis.

...would return the money to the government. Australia's education minister has vowed to find a new home for the center.

New science minister in U.K.

In a Cabinet reshuffle after last week's general election that surprisingly left the Conservative Party with a ruling majority in the United Kingdom, **Jo Johnson** has been named the new minister for universities and science. His predecessor, Greg Clark, was promoted to minister for communities and local government. Johnson, a member of Parliament since 2010, studied history at the University of Oxford and worked as a journalist for the *Financial Times* for 13 years. Johnson will oversee higher education, research funding, and related areas. His record on science is scant, but he has taken positions on hot issues for universities, voting to increase tuition fees and supporting enrollment of foreign students.

Drug-resistant typhoid on rise

The world is facing an epidemic of multidrug-resistant typhoid fever, finds the largest study to date of genomes of *Salmonella enterica* Typhi, the bacterium that causes the diseases. Typhoid spreads through contaminated water or food, causing fever, headache, and other symptoms. It can lead to complications like gastrointestinal perforation and can kill up to 20% of patients. Now, a clone of the bacterium that's frequently multidrug-resistant, called H58, is rolling across Asia and Africa, the team found. They analyzed the genomes of 1832 samples from 21 countries in Asia, Africa, and Oceania. H58 likely emerged in South Asia around 1985, picking up resistance genes in the following years before spreading to Southeast Asia and Africa, the scientists report online this week in *Nature Genetics*. They plan to sequence many more typhoid isolates to pin down the origins of H58. http://scim.ag/typhoid

Castro did was very gutsy," Valdés-Sosa says. "This is the beginning of the end of an absurd situation."

Freer travel will aid the handful of U.S. researchers who have used private money in recent years to nurture collaborations in Cuba. Last year, ACC and AAAS (*Science*'s publisher) signed a memorandum of understanding seeking to expand such efforts in areas like neuroscience and infectious disease. One target is chikungunya, a mosquito-borne malady working its way through the Caribbean toward Cuba and the United States. "We have to face this virus together," says Guadalupe Guzmán Tirado, an epidemiologist here at the Institute of Tropical Medicine.

As the awkward pas de deux takes shape, Cuba is seeking to bolster its own scientific capacity. Ever since the revolution, the government's unwavering policy has been to yoke science to societal needs: girding for the consequences of climate change, for example, or bolstering energy supplies. Researchers not pursuing such national priorities have had to fend for themselves. "You can study mathematics or basic science, but there's no money," Llanes-Santiago says. "Everything is for applied science."

That could change with the upcoming establishment of the Cuban NSF. Key details, including its budget and management structure, are still being worked out. But the science ministry has agreed that it will dole out a chunk of its R&D budget—a paltry 90 million pesos ($4 million) in 2015—on competitive grants for basic research. "It's essential to have this fund," Valdés-Sosa says. While most of Cuba's R&D budget will continue to go to "national needs," Clark-Arxer adds, "there must be space for creativity."

Cuba remains a place of outsized ambitions. Castro's eldest son, Fidel Castro Díaz-Balart, for example, is leading an initiative to build a nanotechnology research complex on Havana's southern outskirts. The Center for Advanced Studies of Cuba hopes to carve niches in, for example, drug delivery and solar cells. "We will never be a power in nanoscience," Clark-Arxer acknowledges. "But we have to be proficient." Seemingly defying poverty and the embargo, the center's labs are billed as having "ultralow vibrations without electromagnetic interference," a "powerful computational infrastructure," and "world-class laboratories for nanocharacterization." Work on a nanofabrication facility is slated to begin next year.

Cuba's precision strike into a field dominated by the United States and other powers sounds a lot like guerrilla science. But until the embargo fades, that's the way it has to be, Castro Díaz-Balart says. "This approach," he says, "is consistent with the economy and possibility of Cuba." ∎

Elkhorn coral has vanished in much of the Caribbean but hangs on in Cuban waters.

CUBA'S CORAL EDEN

Scientists rush to study what may be some of the last healthy corals in the Caribbean

By **Elizabeth Pennisi**

Last month, Amy Apprill checked in for a 30-minute flight from Miami to Havana with 17 pieces of luggage stuffed with water filtration pumps, underwater cameras, an ocean acidity probe—even liquid nitrogen. To get anything done in Cuba, the marine microbiologist at Woods Hole Oceanographic Institution in Massachusetts had to bring everything with her. Cash, too: She had $1500 stashed in her backpack to augment the $15,000 that colleagues carried to Havana to pay for diesel fuel and the use of a research vessel.

Those hassles, Apprill hoped, were a small price to pay for an extraordinary opportunity. Thanks to limited development and extensive conservation efforts, Cuba has "the best coral reefs of the region," says Dan Whittle, an attorney in charge of the Cuba program for the Environmental Defense Fund in Raleigh. Many Caribbean reefs are dead or dying, he says, yet Cuba's remain "stunningly beautiful." Apprill wants to know why.

She's not the only one. As Cuba-U.S. relations thaw, scientists are eager to size up the reefs before an anticipated economic boom has a chance to degrade them. "There's a little bit of a stampede to get there," says Clare Fieseler, a graduate student at the University of North Carolina (UNC), Chapel Hill, who made it to Cuba several years ago and hopes to return to visit underexplored reefs. Also fueling a sense of urgency: Cuba's coral reefs may hold the cure for ailing reefs elsewhere in the Caribbean.

Nearly every baby is screened at birth for more than two dozen serious diseases.

BIOMEDICINE

Newborn screening collides with privacy fears

Informed consent requirement may change decades-old program

By **Jennifer Couzin-Frankel**

The wrinkled heel of nearly every baby in the United States is pricked at birth, and a few drops of blood are dabbed on filter paper and shipped off for analysis. Started in the 1960s, this newborn screening program tests for more than 30 rare and serious diseases that are treatable if caught early in life.

Now, many public health experts who help run or advise the program are worried what the future holds. A new law shaped by a coalition of privacy advocates and conservative politicians requires consent for federally funded research on newborn blood spots, which include DNA but no names. Seeking consent sounds innocuous, even welcome. But experts are concerned that the law, which took effect in March, could hamstring not just fundamental research but also the kind of studies that routinely improve screening.

Efforts to improve newborn testing often require studies on hundreds of thousands of stored blood samples; seeking consent for each one would be prohibitive and impractical. When California researchers sought informed consent to test a cutting-edge screening technology on blood spots from 400,000 newborns, for example, overworked hospital staff did not contact nearly half of eligible families, hampering the study. "Do you want genetic privacy at the expense of everything else?" asks David Orren, chief legal counsel of the Minnesota Department of Health in St. Paul.

When it began lumbering through Congress, the Newborn Screening Saves Lives Reauthorization Act of 2014 was unremarkable; it simply updated an expiring 2007 law that provided federal support for state-run newborn screening programs. In early 2014, the bill passed in the Senate—unanimously, and "in about 30 seconds," says Cynthia Pellegrini of the March of Dimes in Washington, D.C., who advocated for the bill.

The controversy began a few days before the House of Representatives voted on the bill last June, when a nurse named Twila Brase, who runs the Citizens' Council for Health Freedom, a nonprofit in St. Paul that presses for medical privacy, reached out to the office of Michele Bachmann, a tea party icon whose district included the northern suburbs of Minneapolis-St. Paul until she retired from Congress earlier this year. Brase, who also opposes the federal mandate for electronic health records and the Affordable Care Act, had been fighting storage and research on newborn blood spots for years.

Brase's contact had its desired effect: When the bill reached the House floor, Bachmann delivered an emotional speech. "This legislation presumes that every parent of every newborn in the United States of America pre-agrees that the government can have their baby's blood sample, which contains their DNA code," she said. "Americans should not see the death of privacy, especially of the most sensitive private information that every American can have."

Bachmann's speech came too late to affect the House vote. The bill passed. But because legislators had added some minor tweaks to the language before voting, the bill had to return to the Senate, so that the two chambers were passing identical text. That gave time for Bachmann's qualms to catch the attention of members of the conservative Senate Steering Committee, including Rand Paul (R–KY) and Patrick Toomey (R–PA). They sought input from her, as well as from officials from the March of Dimes, the National Institutes of Health (NIH), and other research and advocacy groups. After much discussion, the senators settled on the clause mandating informed consent when newborn blood spots were used in federally funded research. It passed both chambers and was signed into law by President Barack Obama a week before Christmas.

At the crux of scientists' and public health advocates' concerns is what fits under the umbrella of "research," which federal regulations define as investigations that "develop or contribute to generalizable knowledge." Does testing a new screening technology qualify as research? What about studies of a test for a disease not currently on a screening panel, to determine whether it should be added?

"There are public health functions that are mixed up with" what might be considered "pure" research, says Logan Spector, an epidemiologist at the University of Minnesota, Twin Cities. And some research that seems unrelated to newborn screening might not be: Probing leukemia's origins, as research-

PHOTO: © ZUMA PRESS INC./ALAMY

ers studying blood spots have done, could also represent nascent steps toward a test for leukemia risk.

Jeffrey Botkin, a pediatrician and bio-ethicist at the University of Utah in Salt Lake City, who is part of a federal advisory panel on newborn screening, worries about the impact of mandating informed consent. But he's sympathetic to its appeal. "It's good to be the subject of much more public dialogue and scrutiny," Botkin says. Many acknowledge that screening programs could do a far better job of educating parents and doctors, ideally before a baby's birth rather than in the distracted hours afterward.

The Office for Human Research Protections is drafting guidelines on the law and plans to define what qualifies as research. In the meantime, scientists and state health departments are trying to anticipate the law's effects. "We've essentially frozen" our repository, says Michael Watson, the executive director of the American College of Medical Genetics and Genomics in Bethesda, Maryland, which runs a virtual bank of dried blood spots. None of the four participating states plans to provide information from blood spots collected after March, when the law took effect. A pilot study to develop a test for detecting Duchenne muscular dystrophy "has been slowed down tremendously," Watson says.

There's also a big question about whether the law is an early jolt of a larger seismic shift in how deidentified samples are handled. Until now, studying such samples, which carry no names or addresses and are not linked to an individual's health records, hasn't required informed consent. But in January, NIH began expecting grantees on genomic research to seek consent before using deidentified samples. The newborn screening law is turning that recommendation into a national requirement, at least for blood spots. (A handful of states already mandate consent.)

Other samples, like tumor tissue or deidentified blood samples from adults, could be next. The Department of Health and Human Services is rewriting its "Common Rule" governing human subject research. An upcoming draft will reveal whether it wants consent for all deidentified samples. Once those regulations are finalized, perhaps within a couple of years, the newborn screening requirement for consent will be subsumed by the Common Rule.

The Common Rule is Brase's next frontier. She plans to comment on the proposed draft rules when they're released, to urge that all deidentified samples be subject to informed consent before scientists can access them. "When researchers decide we're theirs, that sets people up to oppose what's happening in research," she says. ■

AVIAN INFLUENZA

Enigmatic bird flu strain races across the U.S. Midwest

Virologists baffled by the potent strain's continued spread as more than 30 million poultry hit

By **Mara Hvistendahl**, *in Minneapolis, Minnesota*

The United States' largest avian flu outbreak in decades is decimating poultry flocks in the heartland and shaking up old certainties about how highly pathogenic avian flu viruses spread. "All the old dogma about high-path influenza transmission has just gone out the window," says Michael Osterholm, director of the Center for Infectious Disease Research and Policy here at the University of Minnesota (UMN), Twin Cities. "We're in totally uncharted territory."

More than 30 million poultry, mostly chickens and turkeys, have been affected, either infected directly by the lethal H5N2 virus or marked to be sacrificed in massive culls. Three states—Iowa, Minnesota, and Wisconsin—have declared a state of emergency, and the federal government has earmarked at least $330 million in emergency funds. So far, the virus appears to pose no threat to people, unlike some other avian flus. But its transmission route is a mystery, and infection control measures have failed to contain it. "This is an unprecedented outbreak in which influenza doesn't seem to follow the rulebook," says Jeff Bender, an epidemiologist at UMN Twin Cities.

The current outbreak, which has affected 147 backyard and commercial flocks since December, is the third arrival of high-pathogenicity H5N2 to the United States: Different strains walloped Virginia and Pennsylvania in 1983, affecting 17 million poultry, and a single flock of 6600 chickens in Texas in 2004. The latest one evolved from an H5N8 virus found in a migratory bird in Russia in September 2014. The same H5N8 strain later cropped up in Germany, Japan, the Netherlands, and the western United States (*Science*, 6 February, p. 616). Along the way, it swapped genes with a North American avian influenza virus to

David Swayne (*left*), director of USDA's Southeast Poultry Research Laboratory in Athens, Georgia, is heading up efforts to develop a vaccine that would potentially stop H5N2's spread in poultry.

create the new H5N2 strain, says David Swayne, director of the U.S. Department of Agriculture's Southeast Poultry Research Laboratory in Athens, Georgia.

First detected on U.S. soil on 19 December in a backyard poultry flock in Oregon, the virus began infecting birds across the Pacific Northwest, mainly in backyard flocks. By early March, it had infected commercial turkeys in Minnesota's Pope County, presumably carried there by wild birds. From there, it cropped up across the Midwest, hitting 14 states in total. Avian flu outbreaks normally slow as temperatures warm, but this time spring brought no reprieve. Nor do investigators understand why the virus is ravaging turkey farms, threatening so many birds that some industry observers have warned of a turkey shortage this Thanksgiving. Bird flu typically infects chickens more readily, Bender says. But the transmission route is the most troubling mystery.

Some scientists initially guessed that the virus was entering farms on wild bird feces stuck to equipment or workers' clothing. "We were fairly clear that we were seeing

10-kilometer-radius response zones around affected farms for surveillance and testing. Here in Minnesota, the state with the largest number of infected sites, scientists are searching for the virus in wild bird feces, dead birds reported by the public, and wild turkey carcasses felled by hunters.

The Animal and Plant Health Inspection Service, UMN, and the turkey industry are also joining forces on a massive case control study to understand how H5N2 is spreading. Researchers will soon fan out to at least 30 affected turkey farms and an equal number of farms that haven't been hit by the outbreak. They will take stock of farm management practices, the type of feed and equipment used, the presence of wild birds, and the farms' proximity to roads and waterways, among other factors.

The Southeast Poultry Research Laboratory is now testing a candidate poultry vaccine. The U.S. Centers for Disease Control and Prevention (CDC) in Atlanta is also developing candidate vaccine viruses for use in humans in case the disease spreads to people, as some avian flus have in the past. But CDC is "cautiously optimistic that we

Flu in the coop

Though no humans have been infected, the current outbreak is the largest in decades of a highly pathogenic bird flu virus.

PERIOD	STATES INVOLVED	VIRUS	NUMBER OF AFFECTED BIRDS
1924	Connecticut, Indiana, Illinois, Michigan, Missouri, New York, New Jersey, Pennsylvania, West Virginia	H7 strain (then referred to as "fowl plague")	600,000 (New York City only)
1983–84	Pennsylvania, Virginia	H5N2	17 million
2004	Texas	H5N2	6600
2014–2015	Arkansas, California, Indiana, Idaho, Iowa, Kansas, Minnesota, Missouri, Montana, North Dakota, Oregon, South Dakota, Washington, Wisconsin	H5N2	30.7 million

point introductions," says Beth Thompson, assistant director of the Minnesota Board of Animal Health in St. Paul. "These sites weren't connected in any way." Lately, the virus has spread more rapidly through nearby turkey farms, suggesting that it is windborne. "It could be a plume-related effect," Osterholm says, in which a gust carries feathers or dust long distances. Other hypotheses for the virus's spread include lapses in biosecurity and rodents tracking it onto farms.

Animal health officials have implemented stricter biosecurity measures like having workers wash boots and change clothes before entering a barn and mapped

will not see any human cases" because the virus does not currently have genetic markers associated with increased severity in people, CDC's Alicia Fry said at a 22 April press conference.

Another unknown is whether the virus will stick around in wild birds after the outbreak burns out, posing a continuing threat to flocks. "Maintenance of a high-path avian flu virus within wild birds is unprecedented," says David Stallknecht, an epidemiologist at the University of Georgia, Athens. But H5N2 already has a track record of confounding expectations. "We have to keep an open mind," Osterholm says. "The greatest enemy we have right now is dogma." ■

INFECTIOUS DISEASES

Ebola survivors fight back in plasma studies

Trials hope to show whether antibodies from recovered patients can save lives

By **Martin Enserink**, *in Conakry*

Jean-Pé Kolie came down with Ebola on 22 March 2014, the day after a French lab had confirmed that Guinea had been struck by the virus. A medical student, Kolie thinks he got infected 4 days earlier, when he saw a very sick patient at the emergency room of the Kipé hospital, here in the Guinean capital. Kolie, 29, made a full recovery. More than 2300 Guineans did not.

In February of this year, Kolie was the first Ebola survivor to climb into a massive, bright blue bus parked in front of the National Center for Blood Transfusion (CNTS). It was his chance to fight back against the disease. The $350,000 bus, a gift from the Bill & Melinda Gates Foundation, is a sophisticated mobile plasmapheresis center, in which blood plasma is collected from survivors and processed to be given to new Ebola patients as an experimental therapy at the nearby Donka treatment center, run by Doctors Without Borders (MSF). Teeming with antibodies to the virus, the plasma may help boost their defenses. "I hope that my plasma can save the lives of my compatriots," says Kolie, who is encouraging other survivors to board the bus as well.

Ninety people have so far been treated in the study, paid for by the European Union and coordinated by the Institute of Tropical Medicine (ITM) in Antwerp, Belgium, which makes it one of the largest treatment trials for Ebola ever undertaken. Results are due later this year. The study aims to recruit 130 patients, but enrollment has ground to a halt for a happy reason: The last Ebola patient in Conakry was discharged from the Donka center on 28 April. (There were only seven cases in all of Guinea last week.)

The World Health Organization (WHO) started pushing for studies of blood-based therapies in September, when the Ebola epidemic was exploding, experimental drugs like ZMapp and TKM-Ebola weren't ready, and there was a quickly growing pool of

Jean-Pé Kolie was the first donor in Conakry's blue plasmapheresis bus.

Ebola survivors. Animal studies of similar therapies had yielded mixed results, and the findings of a 1995 human study in Kikwit, in what is now the Democratic Republic of the Congo (DRC), were ambiguous. Seven out of eight patients there who received survivors' blood survived themselves, but an analysis later suggested they were on the road to recovery anyway.

Early in the current epidemic, Sierra Leonean doctors treated 44 patients with whole blood from survivors, as had been done in Kikwit; the results have not been published. Three ongoing trials all use plasma instead of blood. This is technically more complex—plasmapheresis was never done before in Guinea, hence the imported bus—but it has several advantages. Survivors can donate every 2 weeks instead of quarterly, because their red blood cells are separated from the plasma and given back. Frozen at −30°C, plasma lasts at least a year, four times longer than blood. It also takes far less time to administer, a major advantage in Ebola treatment centers, where staff time is precious. (The Guinean trial is the largest of three plasma studies; hampered by a waning epidemic, its counterpart in Liberia enrolled only six patients, and the one in Sierra Leone just one.)

The Guinean team worried that recruiting donors would be difficult. "In Guinea, blood is sacred. You don't give it away," says CNTS researcher Alexandre Delamou. "And

there were all kinds of rumors about MSF taking patients' blood and selling it in Europe." The study team kept a low profile in the media but worked hard to establish good relations with members of the Association of Recovered Ebola Patients in Conakry, in which Kolie is active. Carefully explaining that survivors might just be lifesavers can help convince people, Kolie says. Still, some donors keep their participation quiet out of fear of stigmatization.

Administrating the plasma brings its own problems. Because staff at Ebola treatment centers generally can't spend more than an hour wearing their suffocating biohazard suits, it takes four teams: one to explain the study and get written consent, a second to prepare the patient for transfusion, and two more to infuse two 250-milliliter bags of plasma—from different donors, to maximize the chances of success—and watch the patient for acute reactions.

MSF "initially wasn't all that enthusiastic about participating," Delamou says. "They were worried about the safety of their staff, which is understandable." Now, the collaboration is running smoothly, and every confirmed Ebola patient at Donka has so far agreed to participate.

> ## "I hope that my plasma can save the lives of my compatriots."
> **Jean-Pé Kolie**, Ebola survivor

The researchers acknowledge that results from the study will be difficult to interpret. The study has no control arm; both MSF and an ethical panel in Guinea considered it unacceptable to withhold a potentially lifesaving treatment from some of the patients. The team originally assumed that some patients would form natural controls because plasma of some blood types would not be available in sufficient quantities, but that hasn't happened.

The current plan is to compare patients in the study with those who came into the treatment center during the 3 months before it started. But that's far from an ideal control group: Those months included the peak of the epidemic in Conakry, when the center was stretched to its limits and treatment may not have been as good.

Even if the study does not show an overall effect on mortality, finer grained analyses could yield useful data. A lab in France will determine antibody levels in every batch of plasma to see if higher levels are correlated with a better outcome in recipients; investigators will also determine each patient's viral load right before the transfusion and 24 hours later to see if it drops. "We're probably not going to see a definitive answer from these studies," WHO's David Wood says, "but we will know what directions to pursue in the future."

If nothing else, the study has already shown that producing and safely administering plasma during an Ebola epidemic is feasible, says ITM's Johan Van Griensven—although it would be an even bigger challenge in, say, a remote forest village in the DRC than in this port city.

The big blue bus will stay in Conakry after the epidemic is over, says CNTS Director Nyankoye Haba, but what it will do isn't clear. Plasma, or components of it, can be used to treat some other infectious diseases and hemophilia, but a single plasmapheresis session costs about $85 in materials alone, Haba says. In a country where total spending on health per capita is about $67 per year, that price is almost certainly too high. ∎

The fused pair of bones that form a beak in a chick embryo (*left*, arrow) are rounded and unfused in treated chicks (*middle*), like in alligators (*right*).
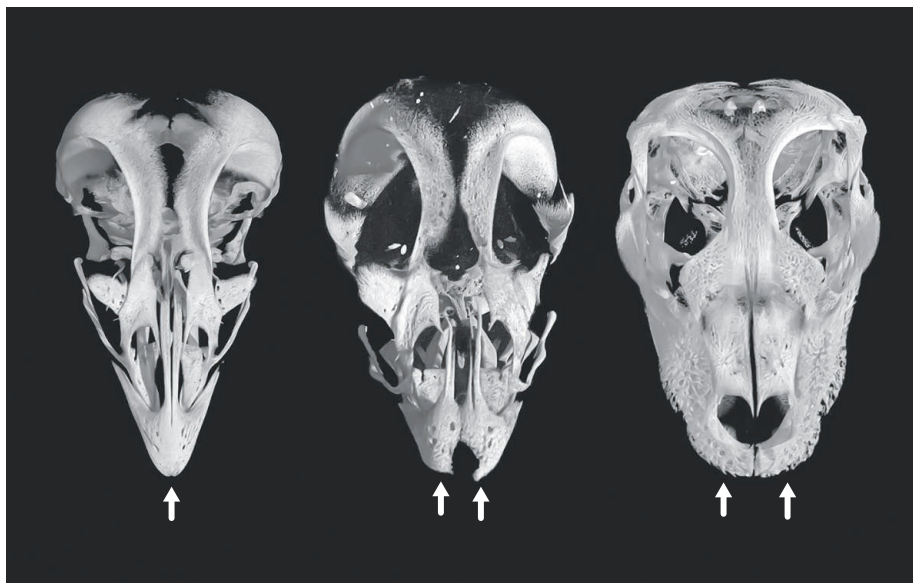
EVOLUTION

How birds got their beaks

Combining fossils and lab studies, researchers home in on genes that transformed a snout into a bill

By **Elizabeth Pennisi**

When birds got their wings, they lost the clawed fingers wielded by their dinosaur relatives. But they evolved a new "finger"—in their face. And what a boon that has been. Agile beaks of all shapes and sizes, from the gulping gape of a pelican to the needle nose of a hummingbird, have enabled the 10,000 avian species to thrive from the Arctic to the tropics, build intricate nests, and eat many different foods.

Now, researchers may have identified genes that transformed an ancestral snout into a bird's bill. By manipulating the genes' proteins, they have seemingly turned back the evolutionary clock, producing snouts in developing chicken embryos that resemble those of alligators today. "We're trying to explain evolution through developmental studies," says Harvard University evolutionary developmental biologist Arhat Abzhanov, who, with colleagues, describes the work this week in *Evolution*.

Their conclusions are at odds with an earlier study. But even those who disagree with the result say Abzhanov and his student Bhart-Anjan Bhullar, now a postdoctoral fellow at the University of Chicago in Illinois, have demonstrated a powerful new approach: pinning down how anatomy changes using fossils, then trying to re-capitulate the changes in the lab by tinkering with genetic signals. "The value of this paper is their ability to blend paleontology with evolutionary developmental biology," says Richard Schneider of the University of California, San Francisco (UCSF), who has linked beak evolution to different genes.

To define just what changed in the face of bird ancestors, Bhullar examined scores of skulls of dinosaur fossils, birds, and alligators and other reptiles, taking hundreds of pictures at different angles. A computer compiled these images into 3D scans and precisely determined differences in bone size, shape, and configuration between the animals.

In ancestral reptiles, a pair of small bones makes up the tip of a snout. In today's birds, those premaxillary bones are long, narrow, and fused, producing the upper bill. The ancient bird *Archaeopteryx* reveals an intermediate step. Its premaxillary bones were not very expanded, but in later avian species the bones are progressively more fused. Other work had also implicated the premaxillary bones in beak evolution.

So Bhullar searched for earlier studies of genetic pathways that control development of these bones. Work in mice and chickens had implicated two sets of signals. A gene called Fibroblast growth factor 8 (*Fgf8*) becomes active in the front part of the face as it takes shape in 3-day-old chick embryos; later, just before bones form, a gene called *WNT* helps drive the proliferation of cells in the middle of the face, where it may prompt expansion of the premaxillary bones. In mammals, lizards, turtles, and alligators, in contrast, activity of the *WNT* gene is highest on the sides of the embryonic face.

To explore these genes' roles, Bhullar and Abzhanov treated bird embryos with inhibitors of the WNT and Fgf8 proteins. When the two signals were most curbed, the premaxillary bones became round and never fused, as in birds' dinosaur relatives, instead of growing long and pointy.

To the pair's surprise, a palatal bone, which makes up the roof of the mouth, also changed dramatically. In many vertebrates, this bone is flat and fused to surrounding bones. But in birds, it's reduced and disconnected, which frees the top part of the bill to move upward, expanding birds' gape. In the treated chick embryos, the palate looked more like it does in other vertebrates: flat and seemingly reconnected to the jaw bones. The studies suggest that *Fgf8* and *WNT* signaling changes allowed skulls of ancient birds "to evolve in a whole new direction" and form a beak, Abzhanov says.

Not everyone agrees. In 2014, UCSF's Nathan Young and Ralph Marcucio, working with Schneider, carried out extensive skull measurements on a variety of embryonic vertebrates and determined the point during development at which the bird face begins to diverge from those of other vertebrates. The work and later experiments supported a 2009 idea proposed by Marcucio that the activity of another gene, *SHH* (for sonic hedgehog), was critical for forming the beak. Unlike *Fgf8*, he says, it's active in the right place and right time in bird embryos.

Marcucio, a developmental biologist, also worries that the changes in facial structure observed by the Harvard team may stem from unintended cell death caused by the inhibitors they used. "Adding the fossil record to this work is really an important step, but I think they are just looking at the wrong pathway," he says. Abzhanov and Bhullar counter that *Fgf8* and *SHH* are often coexpressed and may work together; also, they saw no excess of cell death.

Neutral parties predict this face-off over bird beaks will not be resolved quickly. "There undoubtedly are many more genes involved in these pathways and these will need to be sorted out," says Joel Cracraft, an evolutionary biologist at the American Museum of Natural History in New York City. ∎

Rules of the name

To avoid offense, WHO says no people, places, food, or animals in new disease names

By **Kai Kupferschmidt**

The World Health Organization (WHO) mostly works to reduce the physical toll of disease. But last week it turned to another kind of harm: the insult and stigma inflicted by naming diseases after people, places, and animals. Among the existing monikers that its new guidelines "for the Naming of New Human Infectious Diseases" would discourage: Ebola, swine flu, Rift Valley fever, Creutzfeldt-Jakob disease, and monkeypox. Instead, WHO says names should use more neutral terms, such as severe respiratory disease or novel neurologic syndrome.

Many scientists agree that disease names can be problematic, but they aren't sure the new rulebook is an improvement. "It will certainly lead to boring names and a lot of confusion," predicts Linfa Wang, an infectious disease expert at the Australian Animal Health Laboratory in Geelong. "You should not take political correctness so far that in the end no one is able to distinguish these diseases," says virologist Christian Drosten of the University of Bonn in Germany.

Badly chosen names can stigmatize people, as did gay-related immune deficiency, an early name for AIDS. They can also lead to confusion and hurt tourism and trade. The so-called swine flu, for instance, is not transmitted by pigs, but some countries still banned pork imports or slaughtered pigs after a 2009 outbreak. More recently, some Arab countries were unhappy that a new disease caused by a coronavirus was dubbed Middle East respiratory syndrome (MERS).

Although "it's usually scientists who come up with these names … the WHO gets the diplomatic pressure" if someone takes offense, Drosten says. The new guidelines, released 8 May, aim to smooth the process. "The WHO had to do something to take itself out of the firing line," Drosten says.

"[I]t is important that an appropriate disease name is assigned by those who first report" the disease, notes the WHO guidance. That could "minimize unnecessary negative impact of disease names on trade, travel, tourism or animal welfare, and avoid causing offence to any cultural, social, national, regional, professional or ethnic groups."

To that end, new disease names should not include geographic locations; the names of people, occupations, animals or food; or "terms that incite undue fear" (such as unknown, fatal, and epidemic). Instead, the names should use generic descriptions of symptoms (respiratory disease or watery diarrhea) and specific terms describing patients, epidemiology, or the environment (juvenile, maternal, seasonal, summer, coastal), as well as

A rose as sweet?

Under WHO's new guidance, some existing diseases (left) might have gotten very different names.

EXISTING	COULD HAVE BEEN
Marburg	Filovirus-associated hemorrhagic fever 1
Ebola	Filovirus-associated hemorrhagic fever 2
Hendra	Zoonotic acute encephalitis and respiratory paramyxovirus disease
MERS	BetaCoV-associated SARS 2012
Legionnaires' disease	Atypical pneumonia associated with cooling towers disease
Athlete's foot	Fungal infection of the foot disease

pathogen names and arbitrary identifiers (alpha, beta, 1, 2, 3).

The group that wrote the recommendations met "more than a few times" over a year, says Kazuaki Miyagishima, WHO's director for food safety, zoonoses, and foodborne diseases, and a member of the group. Among the ideas they discussed: naming diseases after Greek gods, using a system similar to that used to name comets, or alternating male and female names as with hurricanes. "But while naming a hurricane Katrina may not offend people, if we do it for a disease, it's not just for one week. It will make its way into the history of human suffering," Miyagishima says.

The guide is well-intentioned, but goes too far, says Ian Lipkin, a virologist at Columbia University. "I don't see how it will be helpful to eliminate names like monkeypox that provide insights into natural hosts and potential sources of infection," he says.

It could also become harder to easily distinguish diseases. For instance, under the new rules, Marburg disease (named after a city in Germany) might have been called filovirus-associated hemorrhagic fever 1, while Ebola (named after a river in Africa) might have been filovirus-associated hemorrhagic fever 2. Such bland names "lose something that is more than just quaint," says Howard Markel, a medical historian at the University of Michigan, Ann Arbor. As for MERS, "would it have been better if we had named it novel betacoronavirus clade C, type 1?" Drosten asks.

The new rules are limiting, "but we think we have left a fairly large area for freedom," Miyagishima says. "We do not want to kill the creativity of researchers completely."

Wang understands naming difficulties. Two decades ago, he named a virus and the disease it causes after Hendra, a suburb of Brisbane, Australia; he still gets angry calls from residents complaining that the name hurts property values. Norwalk virus, named after an Ohio city, raised other sensitivities. A panel of virologists changed the name of the genus from *Norwalk-like virus* to *Norovirus*. But in 2011, a Japanese individual asked the panel to reconsider, because Noro is a common Japanese surname. The panel recommended using the name of the species *Norwalk virus*.

Acronyms may be a good solution, says Ab Osterhaus, a virologist at Erasmus MC in Rotterdam, the Netherlands. They keep names short (another WHO recommendation), and people often forget what the letters mean. But acronyms can cause trouble. In 2003, WHO coined SARS (severe acute respiratory syndrome) to describe a pneumonia spreading in Asia, partly to avoid a name like "Chinese flu." SARS played poorly in Hong Kong, however, which is officially known as an SAR, or special administrative region.

Numbers may be the best way to avoid problems, some say. There is precedent. Growing up in China in the late 1960s, Wang remembers that diseases had digits. "I was really scared of number 5 disease," he recalls. "I don't know why, you just really did not want to get disease number 5." ∎

IN FROM THE COLD

After keeping science alive during decades of scarcity,
Cuba's "guerrilla scientists" are ready to rejoin the world

By **Richard Stone**, *in Havana*

Ernesto Altshuler has a principle for doing science in one of the world's more challenging settings, Cuba. Faced with scant resources and a persistent brain drain, the University of Havana physicist says he became a "guerrilla scientist."

That didn't mean toting a Kalashnikov. "My strategy to survive as an experimental physicist was to violate the boundaries of safe science," Altshuler says, "invading zones where I was not a specialist, looking around for new phenomena with wider eyes, seeing scientific instruments in daily life objects, attacking and retreating from serendipitous findings like a guerrilla." He has used ants to model how panicked people behave, for example, and has studied how bits of tea leaves seem to defy gravity by climbing a stream of tea into a pot's spout. In his studies of granular materials, Altshuler spent about $100 "to obtain the same quality of data" as other researchers who spend millions of dollars on microgravity experiments, says Thorsten Pöschel, a physicist at the Friedrich-Alexander University Erlangen-Nürnberg in Germany. "This should have

At the University of Havana, Ernesto Altshuler spends pennies on his microgravity experiments—and gets million-dollar results.

embarrassed some of our colleagues."

If Che Guevara were alive today, the iconic guerrilla leader of the Cuban revolution surely would applaud how Altshuler and a handful of comrades have kept science alive by cunning and daring in an isolated nation trapped in a time warp. Here in Havana, '50s Chevrolets and Soviet sidecar motorcycles share the rutted roads with sleek Chinese limousine buses whisking tourists to beachside resorts. On a manicured bluff overlooking Havana Harbor behind the Hotel Nacional de Cuba, foreigners and well-heeled Cubans sip mojitos and puff cigars next to Bay of Pigs–era cannon emplacements.

For every expansive mind like Altshuler's, there are scores of researchers working with blinders to the outside world, producing little while being paid less. Cubans blame their penury on "the blockade": the U.S. embargo in place for a half-century. "The embargo is like God. It affects every aspect of life," says Sergio Jorge-Pastrana, foreign secretary of the Academy of Sciences of Cuba (ACC). It

stymies the import of equipment and supplies made in the United States or with U.S. components, and it has turned Cuba into a cyber-backwater with excruciatingly slow Internet speeds. Meanwhile, U.S. travel restrictions hampered academic exchange between the two countries.

But at long last, Cuban science is poised to join the modern world. In a historic rapprochement, Cuban President Raúl Castro and U.S. President Barack Obama announced last December that their nations would strive to overcome mutual hostility and normalize relations. The overture stunned Americans and Cubans alike. "I almost fainted," says ACC President Ismael Clark-Arxer. The pace of détente picked up in April, when Obama struck Cuba from the list of states that sponsor terrorism, paving the way for the two nations to reopen embassies as early as summer. Revised travel rules ease visits to Cuba for U.S. scientists, and the U.S. Commerce Department now allows scientific equipment to be freely donated to Cuba, so long as it does not have potential military applications.

Reforms are taking root on Cuban soil as well. In early 2013, Cuba abolished exit visas and now permits citizens to spend 2 years overseas—up from 11 months—without losing residency rights at home. And in a critical way, Cuba is about to join the scientific mainstream. In the coming months, the government is expected to establish an agency akin to the U.S. National Science Foundation (NSF) that will distribute research funds through competitive, peer-reviewed grants.

Few on either side of the Cuba-U.S. ideological divide anticipate a quick end to a rift that has lasted more than 50 years. Yet Cuba and the United States have shown that they can overcome political differences for the sake of science. A U.S. State Department official says that the United States will not link science engagement with Cuba to progress on human rights, such as free expression, that are still curtailed in Cuba. Already, joint efforts to assess Cuba's coral reefs (see p. 751) and to combat Ebola in West Africa are under way. Science diplomacy, Jorge-Pastrana says, could help Cuba

and the United States lay the foundation of a new relationship.

At the very least, says Luis Montero-Cabrera, a computational chemist at the University of Havana, "we don't want to be a pariah anymore."

PEDRO VALDÉS-SOSA was a 9-year-old Cuban expatriate living in Chicago when Fidel Castro seized power in his homeland in 1959. The ferment filled him with pride. The next year, when his fifth-grade teacher explained that U.S. Army physician Walter Reed first hypothesized that mosquitoes transmit yellow fever, Valdés-Sosa could not contain himself. "I stood up and objected," he says. "The true discoverer, of course, was Carlos Finlay," a Cuban doctor. (Reed himself credited Finlay with discovering the vector.) In 1961, Valdés-Sosa's parents moved the family to Cuba to take part in the socialist experiment. Pedro and his fraternal twin brother, Mitchell, would both become influential neuroscientists here, while remaining lifelong White Sox fans.

Finlay is the founding father of Cuban science. A white marble bust of the epidemiologist sporting a bushy mustache and muttonchops sits on a 3-meter-tall pedestal in a garden across from ACC's headquarters in Old Havana. Finlay's key insight into yellow fever came in 1881, when Cuba still belonged to Spain.

After Cuban independence in 1898, however, intellectual life withered, and the island became known as a winter playground for fast-living U.S. celebrities like Ernest Hemingway, Ava Gardner, and Marlon Brando. A team from the International Bank for Reconstruction and Development that visited Cuba in 1950 reported, "In the field of applied research and labs, there was no development at all in Cuba." The country possessed just three agricultural research stations specializing in sugarcane and tobacco and a single higher education institution, the University of Havana.

Science became a priority again after Cuba's 1959 revolution. In a speech in January 1960, Castro declared, "The future of our country has to be necessarily a future of men of science, of men of thought." Cubans were gobsmacked. "One-fifth of the

Meager resources

$4 million
Science ministry's R&D budget in 2015

$2 million
GDP per peer-reviewed scientific paper, about 3% of U.S. figure

6000
Number of scientists in Cuba

559
Number of Cubans who earned a B.S. in natural sciences or mathematics in 2007–08

$36
How much most scientists in Cuba earn each month

population was illiterate. Everybody thought he was dreaming," Jorge-Pastrana says.

In 1965, the government established the National Center for Scientific Research here, for applied science and engineering. Later that year, ACC, quiescent for decades, began opening institutes in natural sciences. Guevara, as industry minister, launched research centers in mining and metallurgy and in sugarcane byproducts. A stream of students headed overseas, mainly to Eastern bloc countries, for graduate studies.

In 1973, the first Ph.D. was awarded in Cuba, in neuroscience. Cuba now has 63 universities, and roughly one scientist for every 1800 people. Salaries have always been a pittance, but in the heyday of the Soviet bloc they came with scientific perks. High-powered specialists in geology, marine biology, and other fields beat a path to Cuba from the Soviet Union and other communist redoubts with robust scientific traditions. The visitors took aspiring Cuban scientists like Manuel Iturralde-Vinent under their wing.

As a youngster, Iturralde-Vinent loved to explore caves near his hometown of

Manuel Iturralde-Vinent's geological research flourished when a strong Soviet Union aided Cuban science.

Cienfuegos, on Cuba's southern coast. In 1964, when he was 18, the high school dropout parlayed his amateur prowess in speleology into a job as a technician at the newly formed National Institute of Hydraulic Resources. After becoming a department head at the tender age of 22, Iturralde-Vinent turned to mapping water basins with a Russian field geologist. "I treasured him as a father I didn't have. We were speaking in my poor Russian, I was writing in Spanish about karst geology,

and we were drinking vodka all the time."

Iturralde-Vinent joined the Institute of Geology and Paleontology in Havana just as it was gearing up for a massive Eastern bloc effort to map Cuba's geology. Once that was complete, Comecon, the Soviet-led economic assistance body, poured millions of dollars into an effort in the early 1980s to translate the newly acquired geological knowledge on Cuba into data on mineral resources, such as the country's prodigious nickel reserves. "We drilled like crazy," says Iturralde-Vinent, president of the Cuban Geological Society. "For any other country at that time, it would have been impossible."

In many fields Cuba was the junior partner to its socialist big brothers. But in one risky new field it set out to be a pioneer.

BIOTECH BEWITCHED FIDEL CASTRO. On a visit here in 1981, R. Lee Clark, president of the MD Anderson Cancer Center in Houston, Texas, met the fatigue-clad leader and bent his ear about the potential of interferon, an immune-modulating compound, to subdue cancer. Castro dispatched two

Fidel Castro's first-born son foments a nanotech revolution

By **Richard Stone**

The father took care of the politics. The son shepherded some of Cuba's biggest science dreams. In the 1980s, Fidel Castro tapped his eldest son, Fidel Castro Díaz-Balart, to bring nuclear power to Cuba. Fidelito, who had earned a Ph.D. in 1978 from Moscow's Kurchatov Institute, took the reins of a new Cuban Atomic Energy Commission and oversaw the creation of a nuclear research center at Juragua. Construction of the first of two Soviet VVER pressurized-water nuclear power reactors began in 1983.

The reactors were never finished. In 1992, after the collapse of the Soviet Union, Fidel Castro pulled the plug on the project. Castro Díaz-Balart's influence in Cuba waned and he reinvented himself as a science statesman, representing the nation at international forums. When Raúl Castro took power in 2008, Castro Díaz-Balart, who has always been close to his uncle, saw his stock rise. Now, he has discovered a new passion, nanotechnology, and has spent several years laying the groundwork for a nanotech R&D center slated to open later this year in south Havana.

A demicelebrity, Castro Díaz-Balart, 65, landed in

the gossip columns in March when heiress Paris Hilton snapped selfies of herself and a bemused Fidelito during a cigar festival in Havana. The soft-spoken science adviser to Cuba's powerful Council of State and vice president of the Academy of Sciences of Cuba sat down with *Science* in February in the towering José Martí monument, a short walk from his office in the main government complex in Havana. This transcript was edited for clarity and brevity.

Q: Growing up, were you sheltered from politics?
A: The early years were very intense. Due to the aggression and continuous sabotage,

our government policy was oriented to the survival of the revolution. In those years, I was concerned only with science. I was very interested in relativity theory, and how the nucleus worked. When I was a teenager, some of my classmates called me the atomic engineer.

Q: As a student in Moscow, you went by the pseudonym José Raúl Fernandez. Would the Castro name have brought unwanted attention?
A: Due to the conditions, I had that name from high school. Some people saw that as an order from above. It was because I loved chess. I took that name from José Raúl

bright young biologists to Houston in 1981 for a weeklong crash course on interferon in Clark's lab. The duo next did a stint at the State Serum Institute in Helsinki with Kari Cantell, who in the 1970s had been the first to isolate interferon from human white blood cells. Back in Havana, the government gave them a two-building compound to use for lab space; it had been expropriated from a Cuban family that had fled after the revolution. In short order "they isolated the first Cuban interferon," Jorge-Pastrana says. "Within 2 years, they could produce interferon by genetic engineering." Cuba used its interferon widely in the early 1980s to stem internal bleeding in dengue patients.

Emboldened by that success, Cuba decided to get into genetic engineering on the ground floor. "We were not going to miss the biology revolution," Clark-Arxer says. The country spent about $1 billion on biotech in the 1980s and 1990s, he says. Cuba's state-owned biotech industry now employs more than 21,000 people at 32 institutes and enterprises managed by BioCubaFarma, a holding company. Biotech is now the country's second biggest source of revenue, after tourism, earning several hundred million dollars each year from exports of products such as recombinant epidermal growth factor for diabetic ulcers; recombinant erythropoietin for anemia; and a pentavalent vaccine against diphtheria, tetanus, whooping cough, hepatitis B, and *Haemophilus influenzae* B.

Biotech was one of the few areas of Cuban science to survive "the special period," Cuba's existential crisis after the collapse of the Soviet Union, its main financial backer, in 1991. Within 4 years, Cuba's gross domestic product contracted 40%, sinking from third in Latin America to 23rd. "There was no petrol, so there were almost no cars on the streets. And there were food shortages," even malnutrition, Jorge-Pastrana says. Outside of biotechnology, most scientists fell into indigent hibernation. "There was almost no research," says Iturralde-Vinent, who in 1988 had moved to the Museum of Natural History, where he pillaged old data for insights into Caribbean plate tectonics.

Cuba began pulling out of its nosedive around 1996. But the isolation of Cuban science has continued. "The miracle is that we are still competent in some important fields," Clark-Arxer says. One standout is the Cuban Neuroscience Center. In the dark days of the early 1990s, "it didn't have money for toilet paper," says Mark Rasenick, a neuroscientist at the University of Illinois, Chicago, who collaborates with Valdés-Sosa. But the center kept its research going at a slow burn and today, Rasenick says, its brain mapping studies "are really among the best in the world." Adrian Raine, a neuropsychologist at the University of Pennsylvania, agrees. Research in his area, the biological roots of violence, "is being largely transported to countries like Cuba," he says. "They seem to

be well ahead of the United States."

Another miracle is that there's anyone left in Cuba to do good science. "Our biggest problem is a massive emigration of young professionals," Altshuler says. "We could be sucked dry." The country's crumbling buildings and infrastructure tell young scientists that the odds are against a research career. Bright young science students decamp to universities from Argentina to Arkansas. And fewer go into science in the first place. Just 559 students in Cuba earned a B.S. degree in natural sciences and mathematics in 2007 to 2008: less than a sixth of the number who had enrolled in these areas 4 years earlier.

"Some people say the special period is still going on," Iturralde-Vinent says.

UNLIKE MANY OF HIS NEATLY COIFED countrymen, Altshuler wears his wavy graying hair hippie-long. Ingenuity borne of dire straits has, he says, given him "an immense feeling of freedom." A couple of years ago, he designed, for pennies, a system for studying how granular materials respond to different gravitational fields: a free-falling, sand-filled bucket. It plunges 15 meters while a Ping-Pong ball fitted with an accelerometer penetrates the sand. The out-of-this-world rationale, as described in *Geophysical Research Letters* online on 1 May 2014, was to test how spacecraft and other objects settle on granular surfaces in gravities different from Earth's. "In Cuba, we don't have much

---

Capablanca [the Cuban world chess champion from 1921 to 1927]. I have 30 scientific publications with that name.

Q: Considering the geopolitical reality, was Cuba's nuclear program doomed from the start?
A: I don't think so. When we were building the Juragua power plant, we had to develop the nation's infrastructure. It was called the investment of the century. We created an institute to train nuclear scientists and engineers. This effort boosted all of Cuban science and technology.

Q: Tell me about your nanotech ambitions. Can Cuba really compete in this area?
A: Cuba, like many countries, cannot replicate what you have in the United States. We

don't have to develop new materials for planes or rockets like big powers in the world. But we have a critical mass of people with knowledge in this sphere. We're not going to have a Caribbean, tropicalized nanotechnology. We're going to have state of the art.

Nanotechnology is a dis-

ruptive technology. In a small way, we want to take part in this new revolution, the most important in the last 200 years. To create this kind of oasis, we'll have to have good cooperation with first-world countries.

Q: That prospect seems brighter now that the United States and Cuba are normalizing relations.
A: I'm optimistic. We have a lot of common ground. However, a discouraging but a true reality is that most modern hardware and equipment for science and medicine has more than 10% American components. We cannot obtain it because it is subject to the embargo. That is a dark point.

It's true that almost any scientific materials can be put to military use. That is the yin

and yang of science. People raised those questions about our biotechnology in the early 2000s. Experts came to our P3 laboratory [for research on dangerous pathogens] and vaccine facilities to see if there was weaponization. They could understand perfectly well that our research is for the benefit of society.

I'm confident that as scientists, we can put aside differences. You don't have to agree to everything when you have relations with a friend. Healthy disagreement is good. It's time to get past poisoned disagreements.

Q: Do you have political aspirations?
A: [smiles] Maybe in my next life. In this one, I feel very good to be a scientist. ∎

Graying Cuba strains socialist safety net

By **Richard Stone**

At Cuba's Center of Molecular Immunology (CIM), a biotechnology hub on Havana's western edge, Director Agustin Lage points to a country-by-country graph of life expectancy versus health care spending. Many dots are unsurprising: The United States spends a bundle and people tend to live long, whereas Sierra Leone lays out almost nothing and its citizens have an average life expectancy of 46. Then there's Cuba. The impoverished nation spends a pittance on health care, but with a life expectancy of 78 years for both sexes, it's neck and neck with its northern neighbor.

Two big reasons why Cubans live long without prospering are a raft of compulsory childhood immunizations—13, including eight vaccines produced in Havana—and an army of doctors, six per 1000 inhabitants, deployed across the nation. In 2013, Cuba's infant mortality rate was 4.76 per 1000 births—less than a third of Mexico's rate and even better than that of the United States, which recorded 5.9 deaths per 1000 births.

While Cubans live longer, young adults have left the country in droves, and those who stay aren't having babies: Cuba has one of the lowest fertility rates in the world, averaging 9.9 births per 1000 people. "There is no money to raise a family," explains Pedro Valdés-Sosa, research director at the Cuban Neuroscience Center in Havana. Cuba's median age is now 40—far senior to Mexico (27.3) and even older than the United States (37.6)—and continues to rise.

A graying population is straining Cuba's social safety net and its vaunted health system. Studies suggest that roughly 10% of Cuba's population has dementia to varying degrees, Valdés-Sosa says. "It's a huge social problem that we have to start attacking."

Cancer, another disease of the elderly, is also on the rise. CIM is trying to extend the lives of Cuba's cancer patients by broadening the use of therapeutic vaccines, designed to rouse the immune system so that it attacks the tumor, curtailing growth and metastasis. "The goal is to transform cancer into a chronic disease," Lage says.

In the United States and other Western countries, cancer vaccines are still largely experimental. Cuba has been in the cancer vaccine business for nearly 15 years—longer than most countries, says Tania Ramos, director of CIM's clinical research division. "I have no doubt that the Cuban population has received more immunotherapy than any country in the world," she says.

Cuba's willingness to gamble on cancer vaccines is attracting foreign patients with late-stage cancer. Some health experts see parallels with the clinics in Mexico that dispensed dubious treatments with the drug laetrile. But such worries are off target, says Mark Rasenick, a neuroscientist at the University of Illinois, Chicago, because Cuba's cancer vaccines "are based on a solid scientific foundation."

Pedro Valdés-Sosa seeks ways to slow cognitive decline in the elderly.

A colleague with advanced lung cancer recently followed the well-trodden path to Havana for treatment, because, Rasenick says, patients know "you won't be in a control group" that is denied the vaccine.

Starting this year, Cuba is pushing cancer vaccines out of its oncology units and into the hands of primary care doctors. In a trial run, CIM last year began stocking 50 primary care units across the country with two lung cancer vaccines. The center hopes to have the vaccines in all clinics by the end of 2015. Vaccines against breast cancer and other tumor types are on the way. ∎

fancy equipment," Altshuler says, "but we have tons of beautiful sand!"

Altshuler's observation of tea leaves flowing upstream into a teapot led to another case of bargain-basement physics. A few years ago, Troy Shinbrot, a physicist at Rutgers University, New Brunswick, in New Jersey, was intrigued by Altshuler's account of the phenomenon. They collaborated on experiments confirming that bits of matter could climb a 1-centimeter waterfall and move upstream in a meters-long channel— all thanks to surface tension. "It's a pretty cool phenomenon," says Shinbrot, who with Altshuler published their findings online on 3 July 2013 in the *Proceedings of the Royal Society A*.

For the vast majority of Cuban researchers, however, the embargo is a scientific straitjacket. Strolling through the verdant south Havana campus of the Higher Polytechnic Institute José Antonio Echeverría (CUJAE), Cuba's top technical university, research vice-rector Orestes Llanes-Santiago recounts the university's early travails in computing. Barred from buying U.S. computers, scientists with CUJAE—then the technology faculty at the University of Havana—and colleagues formed a crack team to design Cuba's first computer from scratch in the early 1970s.

Cuban industry produced the computer, similar to Digital Equipment Corp.'s PDP-8, until 1990. By then the archaic machines were almost useless, and CUJAE set out to obtain a Sun Microsystems workstation. They got one through a chain of contacts in "five or six countries," Llanes-Santiago says, "to erase the trace." But whenever they tried downloading software or upgrades over the Internet, their Cuban IP address betrayed them. A message would flash on the screen— "You are in a forbidden country"—and the updates were blocked.

Few pieces of Cuba's lab equipment are state of the art. "It's tremendously difficult" to buy genuine reagents and other supplies, says Agustin Lage, director of the Center of Molecular Immunology here. Montero-Cabrera chafes at not being allowed access in Cuba to computational chemistry software. "It's insulting and discriminatory," he fumes. "I'm treated as a terrorist."

The restrictions are maddening, agrees Rasenick, who failed a few years ago to send a functional magnetic resonance imaging machine to Cuba. U.S. officials deemed it to have potential military applications. "I guessed if you dropped it on someone you could hurt them," he says.

THE PROSPECT OF NORMALCY is intoxicating, even though Cuban scientists expect it will be slow in coming. "What Obama and

Castro did was very gutsy," Valdés-Sosa says. "This is the beginning of the end of an absurd situation."

Freer travel will aid the handful of U.S. researchers who have used private money in recent years to nurture collaborations in Cuba. Last year, ACC and AAAS (*Science*'s publisher) signed a memorandum of understanding seeking to expand such efforts in areas like neuroscience and infectious disease. One target is chikungunya, a mosquito-borne malady working its way through the Caribbean toward Cuba and the United States. "We have to face this virus together," says Guadalupe Guzmán Tirado, an epidemiologist here at the Institute of Tropical Medicine.

As the awkward pas de deux takes shape, Cuba is seeking to bolster its own scientific capacity. Ever since the revolution, the government's unwavering policy has been to yoke science to societal needs: girding for the consequences of climate change, for example, or bolstering energy supplies. Researchers not pursuing such national priorities have had to fend for themselves. "You can study mathematics or basic science, but there's no money," Llanes-Santiago says. "Everything is for applied science."

That could change with the upcoming establishment of the Cuban NSF. Key details, including its budget and management structure, are still being worked out. But the science ministry has agreed that it will dole out a chunk of its R&D budget—a paltry 90 million pesos ($4 million) in 2015—on competitive grants for basic research. "It's essential to have this fund," Valdés-Sosa says. While most of Cuba's R&D budget will continue to go to "national needs," Clark-Arxer adds, "there must be space for creativity."

Cuba remains a place of outsized ambitions. Castro's eldest son, Fidel Castro Díaz-Balart, for example, is leading an initiative to build a nanotechnology research complex on Havana's southern outskirts. The Center for Advanced Studies of Cuba hopes to carve niches in, for example, drug delivery and solar cells. "We will never be a power in nanoscience," Clark-Arxer acknowledges. "But we have to be proficient." Seemingly defying poverty and the embargo, the center's labs are billed as having "ultralow vibrations without electromagnetic interference," a "powerful computational infrastructure," and "world-class laboratories for nanocharacterization." Work on a nanofabrication facility is slated to begin next year.

Cuba's precision strike into a field dominated by the United States and other powers sounds a lot like guerrilla science. But until the embargo fades, that's the way it has to be, Castro Díaz-Balart says. "This approach," he says, "is consistent with the economy and possibility of Cuba." ∎

Elkhorn coral has vanished in much of the Caribbean but hangs on in Cuban waters.

CUBA'S CORAL EDEN

Scientists rush to study what may be some of the last healthy corals in the Caribbean

By Elizabeth Pennisi

Last month, Amy Apprill checked in for a 30-minute flight from Miami to Havana with 17 pieces of luggage stuffed with water filtration pumps, underwater cameras, an ocean acidity probe—even liquid nitrogen. To get anything done in Cuba, the marine microbiologist at Woods Hole Oceanographic Institution in Massachusetts had to bring everything with her. Cash, too: She had $1500 stashed in her backpack to augment the $15,000 that colleagues carried to Havana to pay for diesel fuel and the use of a research vessel.

Those hassles, Apprill hoped, were a small price to pay for an extraordinary opportunity. Thanks to limited development and extensive conservation efforts, Cuba has "the best coral reefs of the region," says Dan Whittle, an attorney in charge of the Cuba program for the Environmental Defense Fund in Raleigh. Many Caribbean reefs are dead or dying, he says, yet Cuba's remain "stunningly beautiful." Apprill wants to know why.

She's not the only one. As Cuba-U.S. relations thaw, scientists are eager to size up the reefs before an anticipated economic boom has a chance to degrade them. "There's a little bit of a stampede to get there," says Clare Fieseler, a graduate student at the University of North Carolina (UNC), Chapel Hill, who made it to Cuba several years ago and hopes to return to visit underexplored reefs. Also fueling a sense of urgency: Cuba's coral reefs may hold the cure for ailing reefs elsewhere in the Caribbean.

An abundance of predatory fish like the black grouper may help keep Cuba's corals healthy.

Though roughly the size of Florida, Cuba has four times as much coral reef, and much of its coast is underdeveloped. Cuba's Law 81 is a big factor, scientists say. Adopted after the late explorer Jacques Cousteau visited the island in the 1980s, the law created an environmental agency that set out to protect 25% of Cuba's lands and water—a goal that Cuba claims has been reached for its coastal regions.

The biggest jewel in Cuba's coral necklace may be the Jardines de la Reina, or Gardens of the Queen, a chain of 250 mangrove and coral islands 80 kilometers off southern Cuba. "Diving for 40 years, I have never seen anything like it," says David Guggenheim, a marine scientist and president of Ocean Doctor, a nonprofit in Washington, D.C., which helps U.S. scientists visit Cuba. The Gardens have healthy elkhorn coral, an endangered species that has virtually disappeared elsewhere in the Caribbean.

As a no-take reserve largely off-limits to divers and fishers, the Gardens brim with predatory fish—a rare sight in the region. John Bruno, a marine ecologist at UNC Chapel Hill, and his Cuban postdoc Abel Valdivia have measured 600 grams of fish per square meter, primarily shark, grouper, and snapper. That's six to eight times more fish mass than at most Caribbean reefs. An abundance of predatory fish may help keep the Gardens healthy by reducing populations of fish that hurt corals.

Another protective factor may be the reef's tiniest members. Apprill has teamed up with the U.S-based Cuba Marine Research and Conservation Program, Patricia González of the University of Havana, and other colleagues who last year began comparing Cuban reefs with different tourism and fishing pressures. They have found some that are as impressive as the Gardens. Apprill aims to determine whether healthy reefs have a different array of microbes—their microbiome—than unhealthy reefs in Florida.

As part of the $559,000, 5-year project, the team will drill into corals to extract cores that, like tree rings, enable them to peer back in time at environmental effects on coral growth. One core already in hand turns back the clock 200 years. Correlating growth with nitrogen levels recorded in the reef, for example, may reveal how corals coped with higher nutrient runoff during the Cold War, when the Soviet Union supplied Cuba with large quantities of fertilizer for sugarcane production.

Despite that history, Karl Castillo, a marine ecophysiologist at UNC Chapel Hill, believes that the coral reefs are relatively untouched. He wants to go to Cuba soon to collect his own cores, which he predicts will reveal "the impact of global warming with no impact of humans on coral reef." Castillo hopes to gather data before Cuba's coasts absorb a surge in tourism. "Baseline conditions could be quickly lost," he says.

Not all Cuba's reefs are an oceanic Eden, scientists caution. "There is much hype about the 'pristineness' of Cuba's reefs," Fieseler says. "In areas [of Cuba] that are open to fishing, those reefs are really, really overfished and that has a considerable effect on the health of corals." Even in the Gardens of the Queen, coral cover—a proxy for reef health—is "nothing special," averaging about 18% of the sea floor, compared with a Caribbean average of 16%, Bruno says. (On the best reefs, corals cover half the sea floor.) Staghorn and a stony coral called Montastraea are in trouble or have disappeared, he says, and it seems that few coral larvae are settling within the reserve boundaries.

The bevy of new projects hopes to paint a more nuanced picture of Cuba's reefs. Because the U.S. trade embargo prohibits spending federal funds on research in Cuba, U.S. efforts require private money. Guggenheim is an adept fundraiser—he leads 11-day dive trips running $8000 a person—and promoter, having talked up the reefs on *60 Minutes*, on public radio, and in diver magazines. Ocean Doctor is putting on a fall workshop to take a dozen reef scientists to the Gardens to forge a plan for long-term monitoring of coral resilience.

Les Kaufman, a marine biologist at Boston University, is jumping at the chance to attend. Compared with the rest of the Caribbean, he says, "there's a better chance of Cuba hanging on to its healthy reef." A trip to the Gardens of the Queen, Kaufman says, will be worth the hassle. ∎

Flourishing reefs

Cuba has four reef chains longer than 100 kilometers, including the Gardens of the Queen, the largest marine reserve in the Caribbean.

Colorados Archipelago
Havana
Gardens of the King
Gulf of Batabanó
CUBA
Gulf of Guanahacabibes
Gulf of Ana Maria
Canarreos Archipelago
Gardens of the Queen

CREDITS: (PHOTO) © IMAGEBROKER/ALAMY; (MAP) C. SMITH/*SCIENCE*

PERSPECTIVES

Fisheye view of the Grotta de Fumane.

ANTHROPOLOGY

Chronicling modern human's arrival in Europe

Dental remains elucidate the demise of the Neandertals

By **Nicholas J. Conard**[1] *and* **Michael Bolus**[2]

The Aurignacian, named after the type site of Aurignac in southern France, is the best known cultural group associated with the spread of modern humans across Europe between about 45,000 and 35,000 years ago. The Protoaurignacian is a cultural group that is well represented in southern Europe and has long been viewed as a precursor of the Aurignacian. On page 793 in this issue, Benazzi *et al.* (*1*) use both morphological arguments and ancient DNA to show that

[1]Department of Early Prehistory and Quaternary Ecology and Senckenberg Center for Human Evolution and Paleoenvironment, University of Tübingen, Schloss Hohentübingen, 72070 Tübingen, Germany. [2]Heidelberg Academy of Sciences and Humanities, Research center "The Role of Culture in Early Expansions of Humans" at the University of Tübingen, Rümelinstraße 23, 72020 Tübingen, Germany. E-mail: nicholas.conard@uni-tuebingen.de; michael.bolus@uni-tuebingen.de

two incisors from Protoaurignacian layers at Grotta di Fumane and Riparo Bombrini in Italy are from modern humans and not Neandertals. These results confirm that modern humans were the makers of the Protoaurignacian and thereby help to plot the spread of modern humans across Europe. This process is closely associated with the demise and ultimate extinction of the indigenous Neandertal populations.

Dates from many sites have established that lithic assemblages rich in blades and bladelets, occasional finds of personal ornaments, and organic tools characteristic for the Protoaurignacian are roughly 40,000 years old. However, the two teeth have not been dated directly, and the paleogenetic clock only dates the finds to the broad period between ~78,000 and 19,000 years ago. Critics may question the stratigraphic contexts of the finds, as has been the case at other sites (*2*). Indeed, at many sites, iso-

lated finds of all classes of materials have been attributed to layers much older than the objects themselves. This was, for example, the case with the famous human remains from Vogelherd, which for 70 years were viewed as belonging to the Aurignacian, but were ultimately demonstrated to be intrusive bones from the Neolithic (*3*). Skeptics thus need to be taken seriously.

Nonetheless, the results look reliable. The fieldwork at Fumane is one of the flagship excavations in the European Paleolithic. The site has been excavated carefully for decades (see the photo) and has produced numerous important results about the lifeways of Neandertals and modern humans. Fumane is well dated and has an outstanding stratigraphic sequence that covers the key periods of the Mousterian (universally attributed to Neandertals), the Uluzzian, which has long been viewed as transitional between the Middle and Upper Paleolithic

Two cultures? (**1** to **7**) Protoaurignacian finds from Grotta di Fumane (**1** to **7**) are compared to early Aurignacian finds from Geißenklösterle (**8** to **14**). (**1**) Therianthropic painting on limestone block; (**2**, **3**) points with abrupt retouch; (**4**, **9**, **10**) carinated scrapers; (**5**, **6**) grooved cervid teeth; (**7**, **13**) split-based bone points; (**8**) therianthropic relief carved from ivory; (**11**, **12**) personal ornaments made from ivory; (**14**) bone flute made from a swan radius. Benazzi *et al.* show that dental remains at Grotta di Fumane are from modern humans, thus confirming that modern humans rather than Neandertals made these artifacts.

and has recently been attributed to modern humans (*4*), and the Protoaurignacian (*5*, *6*). Bombrini does not have the same history of research, but the results presented by Benazzi *et al.* are entirely plausible.

These results indicate that the Protoaurignacian was made by modern humans, which will come as little surprise to many researchers. But what exactly is the Protoaurignacian and how does it relate to its apparent sister group the Aurignacian? The report by Benazzi *et al.* raises the question of where research needs to go from here. Aside from an obvious lack of human skeletal material, which can only be remedied by new excavations under high methodological standards and the refinement of techniques of biological anthropology and paleogenetics, much work remains to be done studying

the material culture of late Neandertals and early modern humans in Europe.

The Protoaurignacian was first defined by Laplace in 1966 (*7*) and is said to be distinguishable from the Aurignacian on the basis of lithic and organic artifacts (see the figure) (*8*). The Aurignacian is characterized by distinctive techniques for producing large blades and small bladelets. In contrast, artifacts from Protoaurignacian deposits, often found in Mediterranean Europe, are said

---

"The fieldwork at Fumane is one of the flagship excavations in the European Paleolithic."

---

to be characterized by a single stone knapping sequence to produce both blades and bladelets (*8*). Additionally, the Aurignacian has produced large assemblages of three-dimensionally formed personal ornaments, figurative representations, occasional finds of mythical imagery, and musical instruments, whereas the Protoaurignacian typically has a much more limited range of tools made from bone, antler, and ivory and far fewer symbolic artifacts.

Despite its name, the Protoaurignacian is not always older than the Aurignacian. At least at sites like Geißenklösterle and Willendorf II in the Middle and Upper Danube, the Aurignacian dates back to nearly 43,000 years ago and is slightly older than the Protoaurignacian (*9*, *10*). It now appears unlikely that the Aurignacian evolved out of the Pro-

toaurignacian, although at sites including Le Piage and Isturitz in France, the Protoaurignacian underlies the Aurignacian (*11*, *12*). The best record of early symbolic artifacts in Europe comes from the Swabian Aurignacian and from the Aurignacian of southwestern France and several other regions, and not from the Protoaurignacian.

It is not clear, however, whether the term Protoaurignacian has much meaning. For example, the purported Protoaurignacian assemblage of Krems-Hundssteig has been shown to be a mixed assemblage containing a strong component of artifacts from the Gravettian, an Upper Paleolithic cultural group that postdates the Protoaurignacian by ~10,000 years (*13*). Also, artifacts such as split-based bone points and carinated scapers, often viewed as hallmarks of the Aurignacian, have been found at sites attributed to the Protoaurignacian (see the figure). This is the case with the split-based bone points at Trou de la Mère Clochette, Arbreda, and Fumane (*14*). Similarly, lithic assemblages with mixed signatures have been recovered from Crimea, Romania, and the Basque Country (*15*). The concept of the Protoaurignacian is thus not as robust as the article by Benazzi *et al.* implies.

While the research reported by Benazzi *et al.* is a welcome step forward in establishing the narrative of colonization of Europe by modern humans, the archaeological and human fossil records will almost certainly prove to be more complex and fascinating than our current models suggest. It is only through carefully excavating sites and establishing high-resolution regional signatures of the events and processes of the last glacial cycle that a reliable picture of the spread of modern humans and the extinction of Neandertals will come into focus. ∎

REFERENCES

1. S. Benazzi *et al.*, *Science* **348**, 793 (2015).
2. J. Zilhão, F. d'Errico, *J. World Hist.* **13**, 1 (1999).
3. N. J. Conard *et al.*, *Nature* **430**, 198 (2004).
4. S. Benazzi *et al.*, *Nature* **479**, 525 (2011).
5. M. Peresani *et al.*, *J. Archaeol. Sci.* **35**, 2986 (2008).
6. A. Broglio *et al.*, in *Proceedings of the 13th UISPP Congress, Forlì, 9 to 14 September 1996* (Forlì, Italy, 1998), vol. 2, pp. 495–509.
7. G. Laplace, *Recherches sur l'origine et l'évolution des complexes leptolithiques* (E. de Boccard, Paris, 1966).
8. N. Teyssandier, F. Bon, J.-G. Bordes, *J. Anthropol. Res.* **66**, 209 (2010).
9. T. Higham *et al.*, *J. Hum. Evol.* **62**, 664 (2012).
10. P. R. Nigst *et al.*, *Proc. Natl. Acad. Sci. U.S.A.* **111**, 14394 (2014).
11. J.-G. Bordes, in *Towards a Definition of the Aurignacian*, O. Bar-Yosef, J. Zilhão, Eds. (Trabalhos de Arqueologia, Lisboa, 2006), vol. 45, pp. 147–171.
12. C. C. Szmidt, C. Normand, G. S. Burr, G. W. L. Hodgins, S. LaMotta, *J. Archaeol. Sci.* **37**, 758 (2010).
13. E. M. Wild *et al.*, *Radiocarbon* **50**, 1 (2008).
14. C. C. Szmidt *et al.*, *J. Archaeol. Sci.* **37**, 3320 (2010).
15. V. Sitlivy *et al.*, *Quartär* **59**, 85 (2012).

RNA

Phased piRNAs tackle transposons

Tertiary piRNAs help silence dangerous DNA elements

By **Haruhiko Siomi**[1] *and* **Mikiko C. Siomi**[2]

Transposable elements are dominant inhabitants of the eukaryotic genome. Their ability to mobilize and insert anywhere in the genome can cause mutations that are generally detrimental to the host. This makes them key targets for silencing. Small RNAs called PIWI-interacting RNAs (piRNAs) are one means to attack transposons. They constitute the largest class of small RNAs, but the mechanisms by which they are generated are not completely clear. On pages 812 and 817 of this issue, Mohn *et al.* (*1*) and Han *et al.* (*2*), respectively, propose a revised model for piRNA biogenesis that increases the diversity of piRNA sequences and thereby expands the range of targets they can silence.

In animals, piRNAs are generated in germline cells, which means their effects can be transmitted to offspring. Most piRNAs are derived from genomic regions called piRNA clusters, which also harbor a large number of truncated transposable elements (*3*). In the germ cells of *Drosophila melanogaster*, single-stranded precursor transcripts (antisense) are produced from these clusters (see the figure). This precursor piRNA is then cleaved by an endonuclease Zucchini (Zuc), to generate short primary piRNAs (26 to 31 nucleotides long). The processing of cluster transcripts occurs in the cytoplasm, and mature piRNAs are loaded onto the PIWI proteins Ago3, Aub, and Piwi (*4*). Primary piRNAs have a bias toward having uridine at their 5′ ends (1U bias), are largely antisense with regard to corresponding transposable element sequences, and are loaded onto Aub and Piwi. Aub-bound primary piRNAs, together with Ago3, then initiate a "ping-pong cycle," which generates secondary piRNAs by cleaving complementary targets (both sense and antisense single-stranded RNA). Cleavage not only determines the 5′ end of secondary piRNAs but also consumes transposable element transcripts, thereby silencing transposons (*3*, *5*). Secondary piRNAs loaded onto Ago3 show 10-nucleotide complementarity at their 5′ ends with Aub-bound primary piRNAs and possess a sense bias with adenosine at the 10th nucleotide (10A bias). Piwi does not participate in the ping-pong cycle because once loaded with

piRNAs, it is imported into the nucleus to repress transposable elements by modifying chromatin (*6*). This cycling model amplifies only ping-pong pairs of piRNAs and is therefore insufficient to explain the extraordinary sequence diversity of piRNAs.

Using state-of-the art bioinformatics, Mohn *et al.* and Han *et al.* independently found that Piwi- and Aub-, but not Ago3-bound piRNAs, displayed notable sequence "phasing." By analyzing small RNA populations from *Drosophila* germ cells (from ovaries) that are depleted of Rhino, a factor required for dual strand piRNA cluster transcription (*7–9*), Mohn *et al.* noticed a distinct nucleotide start site in piRNA profiles. These sites may correspond to piRNA biogenesis initiation sites, and the piRNAs that contain them are called "responder piRNAs." Most responder piRNAs occupy Aub and are com-

> ## "...PIWI-interacting RNAs (piRNAs) are one means to attack transposons."

plementary to Ago3-bound piRNAs, with a 10-nucleotide overlap at their 5′ ends. These Ago3-bound secondary piRNAs may trigger production of responder piRNAs. Surprisingly, piRNAs originating downstream of the responder piRNAs, called "trailer piRNAs," mostly associate with Piwi.

Mohn *et al.* observed that the 3′ ends of responder piRNA are immediately followed by 5′ ends of Piwi-bound trailer piRNAs. Remarkably, trailer piRNAs show phasing with a ~27-nucleotide interval, though both the amounts of trailer piRNA and phasing accuracy decrease as the distance from the trigger site increases. Phased trailer piRNAs also show a striking 1U bias. These findings support an intriguing model in which piRNA 3′ ends are defined by a cleavage event that preferentially occurs immediately upstream of a U residue, which corresponds to the 5′ end of the next piRNA.

[1]Department of Molecular Biology, Keio University School of Medicine, Tokyo 160-8582, Japan. [2]Graduate School of Science, The University of Tokyo, Tokyo 113-0032, Japan. E-mail: awa403@keio.jp, siomim@bs.s.u-tokyo.ac.jp
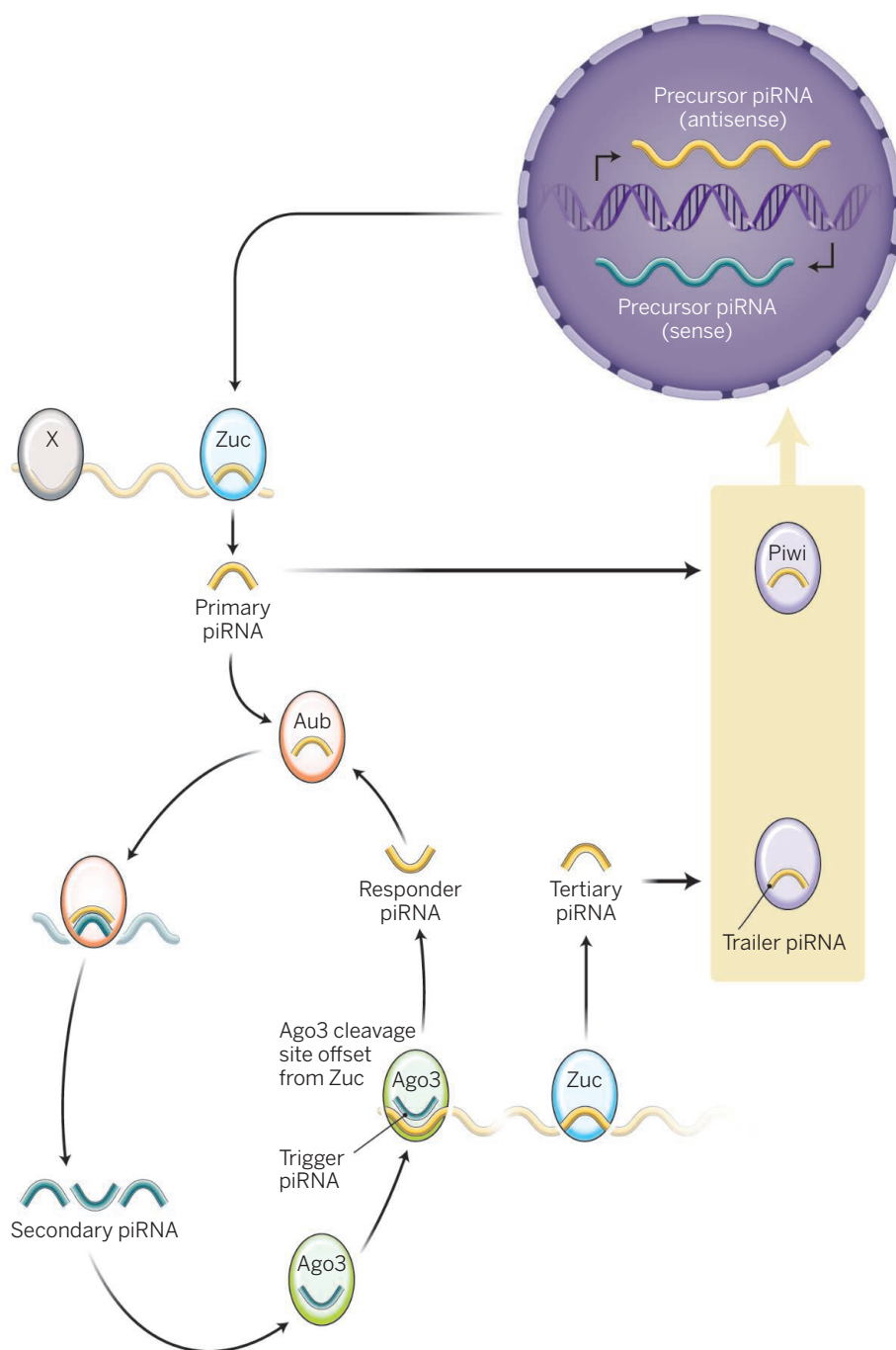
Expanding the piRNA arsenal. In *Drosophila* germ cells, Ago3-bound secondary piRNAs act as triggers to produce responder piRNAs that bind to Aub. This initiates production of trailer piRNAs (through Zuc-dependent phased tertiary RNA production) that mostly bind to Piwi. Protein X may determine piRNA cluster transcripts among cellular RNAs and initiate phased piRNA production by cleaving the cluster transcripts. A similar ping-pong–independent mechanism may also exist in ovarian somatic cells.

scripts: Once a cleaved 3′ transcript with 1U is loaded onto Piwi, it follows repeated rounds of cleavage with a ~27-nucleotide interval. The interval may be determined by a combination of Piwi's footprint, Zuc cleavage of Piwi-bound trail sequences, and the preference of Piwi to bind 1U. Although Zuc-dependent piRNAs are viewed as primary piRNAs, trailer piRNAs, which occupy the vast majority of Piwi, may reasonably be called "tertiary" piRNAs because their production depends on secondary piRNAs. Therefore, primary piRNAs make secondary piRNAs, which make phased "tertiary piR-NAs." What initiates this sequential pathway is Aub-bound antisense primary piRNAs, which produce Ago3-bound sense "trigger piRNAs" in the ping-pong cycle. This raises the question of how such antisense primary piRNAs are selectively produced.

Both Mohn *et al.* and Han *et al.* also observed phased piRNAs in ovarian somatic cells where only the primary piRNA production pathway operates, indicating that Zuc-dependent phasing can be initiated without the ping-pong cycle. Because purified Zuc exhibits no nucleotide preference for its cleavage site (*10*, *11*), ovarian somatic cells may rely on factors replacing the function of Ago3-trigger piRNA complexes to determine piRNA biogenesis initiation sites on particular transcripts. This ping-pong–independent mechanism should also be available in germline cells to supply Aub-bound antisense primary piRNAs that produce Ago3-bound trigger piRNAs.

Mohn *et al.* and Han *et al.* demonstrate that Zuc-mediated 3′ end formation of piRNAs is also evident in mice, suggesting that primary piRNA phasing is mechanistically conserved in mammals. Thus, important future challenges are to identify factors that endow specificity to Zuc both in germline and ovarian somatic cells to trigger 3′-directed and phased piRNA production in the vast array of the transcriptome, and to elucidate the mechanisms that funnel most Zuc-cleaved transcripts onto Piwi. ∎

REFERENCES

1. F. Mohn, D. Handler, J. Brennecke, *Science* **348**, 812 (2015).
2. B. W. Han *et al.*, *Science* **348**, 817 (2015).
3. J. Brennecke *et al.*, *Cell* **128**, 1089 (2007).
4. H. Ishizu, H. Siomi, M. C. Siomi, *Genes Dev.* **26**, 2361 (2012).
5. L. S. Gunawardane *et al.*, *Science* **315**, 1587 (2007).
6. K. Saito *et al.*, *Genes Dev.* **24**, 2493 (2010).
7. C. Klattenhoff *et al.*, *Cell* **138**, 1137 (2009).
8. Z. Zhang *et al.*, *Cell* **157**, 1353 (2014).
9. F. Mohn, G. Sienski, D. Handler, J. Brennecke, *Cell* **157**, 1364 (2014).
10. H. Nishimasu *et al.*, *Nature* **491**, 284 (2012).
11. J. J. Ipsaro, A. D. Haase, S. R. Knott, L. Joshua-Tor, G. J. Hannon, *Nature* **491**, 279 (2012).

Thus, 5′- and 3′-end formation of piRNAs is mechanistically coupled, precluding a 3′-trimming event to form mature piRNAs. Trailer piRNAs are selectively lost in ovaries lacking Zuc, suggesting that Zuc determines both the 3′ and 5′ ends of most germline Piwi-bound piRNAs. By sequencing analysis of cleaved transcripts, Han *et al.* also concluded that production of Piwi- and Aub-bound phased piRNAs depends on Zuc.

The findings of Mohn *et al.* and Han *et al.* also suggest that cleavage in the ping-pong cycle by trigger piRNA (bound to Ago3) produces not only a corresponding ping-pong partner piRNA but also piRNAs from the remaining 3´ portion of the cleaved tran-

GEOPHYSICS

Probing the underbelly of a supervolcano

Seismic imaging of Yellowstone provides a better understanding of large volcanic systems

By **Nikolai M. Shapiro**[1,2]
and **Ivan Koulakov**[3,4]

Human civilization remains vulnerable to volcanic eruptions. For example, the moderate eruption of Eyjafjallajökull volcano in Iceland in 2010 was responsible for the total disruption of air traffic in Europe for several days. The largest eruptions known in human history (such as that of Mount Tambora, Indonesia, in 1815) ejected enormous volumes of volcanic material, ranging from 25 to 150 km³, and caused serious worldwide climate changes, leading to huge loss of life even in countries located far from volcanoes. Even greater eruptions that have spewed out more than 1000 km³ of ash and volcanic gases into the atmosphere have occurred in the recent geological past (*1*). The ash of such supereruptions covered

¹Institut de Physique du Globe de Paris, Sorbonne Paris Cité, CNRS (UMR7154), 1 rue Jussieu, 75238 Paris, cedex 5, France. ²Institute of Volcanology and Seismology FEB RAS, 9 Piip Boulevard, Petropavlovsk-Kamchatsky, Russia. ³Trofimuk Institute of Petroleum Geology and Geophysics, SB RAS, Prospekt Koptyuga, 3, Novosibirsk, 630090, Russia. ⁴Novosibirsk State University, Pirogova, 2, Novosibirsk, 630090, Russia.
E-mail: nshapiro@ipgp.fr, koulakovIY@ipgg.sbras.ru

huge areas, polluted the atmosphere, and caused notable climate changes throughout the world with marked effects on the biosphere (*2*). Evaluating whether such strong volcanic eruptions will occur in the future requires an understanding of the geological processes and physical mechanisms that led to them. Such an understanding can be gained from studies of the volcanic systems known to produce these supereruptions in the near past. On page 773 of this issue, Huang *et al.* (*3*) present a new seismic tomography study of the crust and the uppermost mantle beneath the Yellowstone volcanic field that provides insights into the functioning of supervolcanoes.

Located in North America, this volcanic system is the youngest manifestation of the Yellowstone hotspot (*4*, *5*) and is among the most active supervolcanic sites of the Quaternary period [the other two are Toba in Indonesia (*2*) and Taupo in New Zealand (*6*)]. It is characterized by extensive earthquake activity, episodic ground deformation, high fluxes of heat and CO_2 emission, and a vigorous hydrothermal system. The Yellowstone complex is made of large calderas generated by several explosive eruptions. The three largest eruptions occurred

2.1 million years ago (Ma), 1.3 Ma, and 640,000 years ago, forming the Island Park caldera, the Henry's Fork caldera, and the Yellowstone caldera, respectively. The Island Park caldera supereruption produced the Huckleberry Ridge Tuff and was the largest with ~2500 km³ of ejected material. The younger Henry's Fork caldera is associated with the smaller Mesa Falls Tuff (~280 km³). The latest supereruption formed the Yellowstone caldera and produced the Lava Creek Tuff (~1000 km³).

In comparison, volcanoes fed by the Hawaii hotspot have erupted ~300,000 km³ of lava in the past 5.5 Ma (*7*). Despite the larger output rate compared to Yellowstone, these volcanoes did not generate appreciable explosive eruptions and are characterized by a relatively steady sequence of many thousands of effusive eruptions.

Both the Hawaii and the Yellowstone volcanoes are fed by mafic melts generated in the mantle. Therefore, the reason(s) for the striking difference in their styles of volcanism is not related to the deepest magma sources but must be sought in the structures through which magma passes on its way to the surface. In the case of Hawaii, the hot basaltic melts rise through a thin

Influence of the crust on the style of volcanism. Mafic magmatic fluids remain buoyant within the oceanic crust and traverse it almost without obstacles, leading to a quasi-open system generating the steady effusive volcanism. Within the continental crust, basaltic magmas cannot easily ascend through the low-density felsic rocks and are accumulated in sill complexes at depth. This accumulation leads to a formation of intermediate magma reservoirs and differentiation of silicic magmas that, in turn, ascend to shallow depths and produce explosive eruptions.

and mostly mafic oceanic crust in which they remain relatively buoyant, leading to a fast ascent directly to the surface (see the figure) and an effusive volcanism dominated by basaltic lava flows.

Magma ascent through thick continental crust proceeds in more complex ways. Basaltic melts are denser than most of the felsic rocks that make up the upper crust. They therefore tend to stall within the lower or middle crust, where they form magma reservoirs that grow over many thousands or a few millions of years (8) by accretion of many individual sills (9, 10). Silicic magmas that are enriched in volatiles and cause explosive eruptions are believed to be produced by magma differentiation during the long-term evolution of these crustal reservoirs (11).

In most cases, the information about the origin and evolution of these crustal magmatic reservoirs is deduced from petrological analysis of the erupted volcanic rocks, though their location and size remain poorly known.

Huang *et al.*'s seismic tomography survey of deep parts of the Yellowstone volcanic system combined local and teleseismic data. This information allowed them to unveil a 46-km^3 basaltic reservoir in the lower crust that is a factor of about 4.5 times larger than a shallower rhyolitic reservoir. This lower-crustal reservoir absorbs a large part of the magmas generated by the mantle plume, and only a reduced volume of evolved magmas ascends to the surface and generates large explosive eruptions. The results of Huang *et al.* show that further understanding of the functioning of the largest volcanic systems requires information about their roots in the lower crust that can be obtained via large-scale geophysical studies, including seismic and magnetotelluric (12) imaging. ∎

REFERENCES AND NOTES

1. B. G. Mason, D. M. Pyle, C. Oppenheimer, *Bull. Volcanol.* **66**, 735 (2004).
2. C. A. Chesner, *Quat. Int.* **258**, 5 (2012).
3. H.-H. Huang *et al.*, *Science* **348**, 773 (2015).
4. R. L. Christiansen, *U.S. Geol. Surv. Prof. Pap.* **729-G**, 145 (2001).
5. M. J. Fouch, *Geology* **40**, 479 (2012).
6. C. J. N. Wilson, *J. Volcanol. Geotherm. Res.* **112**, 133 (2001).
7. R. W. Decker, T. L. Wright, P. H. Stauffer, Eds., *Volcanism in Hawaii*, U.S. Geological Survey Professional Paper 1350 (1987).
8. J. E. Gardner, P. W. Layer, M. J. Rutherford, *Geology* **30**, 347 (2002).
9. C. Michaut, C. Jaupart, *Tectonophysics* **500**, 34 (2011).
10. K. Jaxybulatov *et al.*, *Science* **346**, 617 (2014).
11. C. Annen, J.-D. Blundy, R. S. J. Sparks, *J. Petrol.* **47**, 505 (2006).
12. G. J. Hill *et al.*, *Nat. Geosci.* **2**, 785 (2009).

The missing link in oceanic phosphorus cycling?

Rapidly recycled reduced phosphorus compounds play a key role in phosphorus biogeochemistry

By **Claudia Benitez-Nelson**

Nutrient limitation plays a central role in the productivity of marine systems and long-term atmospheric carbon dioxide uptake by the oceans (1). Marine organisms are adept at changing their biochemical physiology to take advantage of scarce resources (2). Thus, changes in the ocean environment affect the biodiversity of organisms within those waters and the efficiency by which material is transported from the surface to the sea floor (3). On page 783 of this issue, Van Mooy *et al.* (4) report their discovery of a large, rapidly recycled pool of reduced phosphorus compounds that play a key role in ocean phosphorus biogeochemistry.

Phosphorus is a critical nutrient for all forms of life (5). Altered environmental conditions associated with human-induced and natural climate dynamics may cause the ocean's plankton community to become increasingly phosphorus-stressed (6, 7). Yet the composition of marine phosphorus and the factors that determine the timing and extent of phosphorus use and storage by marine organisms are incompletely understood. Van Mooy *et al.* now show that oceanic phosphorus is recycled through a previously unrecognized and vast pool of reduced forms of phosphorus at an unprecedented rate.

For decades scientists have assumed, on the basis of thermodynamics and cellular transport across membranes, that organisms only consume phosphorus in the form of phosphate for their cellular requirements. However, organisms can also break down and use a variety of other dissolved phosphorus forms, even when phosphate concentrations are relatively high (5) (see the figure). This dissolved phosphorus is a mixture of phosphate, phosphorus esters, polyphosphate, and phosphonates (8). High concentrations of the reduced phosphorus compound phosphonate in the dissolved phosphorus pool are unexpected, given the energy required to break the C–P bond (5). Yet various heterotrophic bacteria, cyanobacteria, and even archaea are now known to contain the molecular machinery for producing and using phosphonates as well

as another reduced phosphorus compound, phosphite (5, 9). Multiple lines of evidence thus suggest the importance of reduced phosphorus compounds in marine phosphorus biogeochemistry. But one last piece of information has been missing: How rapidly are they produced and used?

Van Mooy *et al.* provide a definitive answer to this question. They show that the production of reduced phosphorus compounds in cells may be as high as 15% of phosphate uptake in biological communities. In some cases, much of this phosphorus is rapidly released to the surrounding environment. Thus, the amount of phosphorus recycled through redox reactions equals or even exceeds oceanic phosphorus inputs via continental and atmospheric sources (see the figure). The rapid synthesis and release of reduced phosphorus

> *"...the amount of phosphorus recycled through redox reactions equals or even exceeds oceanic phosphorus inputs via continental and atmospheric sources..."*

compounds in low-nutrient marine environments helps to explain the large divergence from predicted N:P ratios in marine organisms (10). This redox cycle further explains why phosphonates are present in seawater (8) and how cyanobacteria and archaea can sustain carbon fixation in increasingly stratified, phosphorus-poor waters.

Why organisms produce energetically expensive, reduced phosphorus compounds remains a mystery, particularly given that these compounds are subsequently released to surrounding waters. Van Mooy *et al.* and others have shown that phosphorus recycling is often independent of inorganic and organic phosphorus concentrations

Department of Earth and Ocean Sciences and Marine Science Program, University of South Carolina, Columbia, SC 29208, USA. E-mail: cbnelson@geol.sc.edu
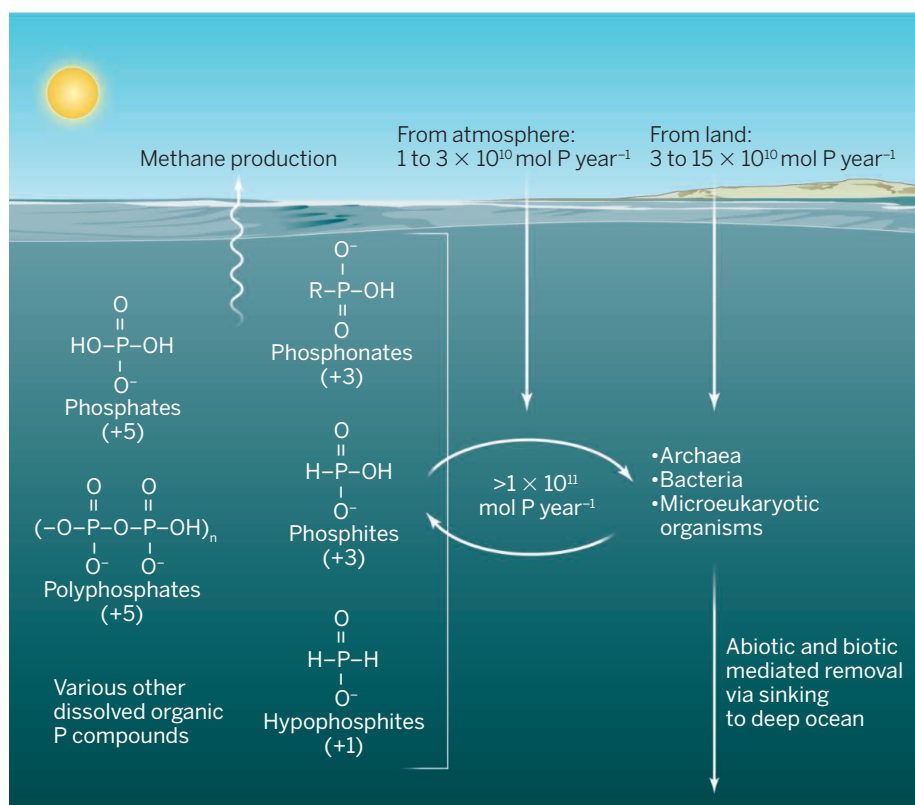
Major forms of marine phosphorus speciation and their cycling in the ocean. Phosphorus oxidation states are given in brackets. The redox recycling rate between dissolved and particulate forms of phosphorus determined by Van Mooy et al. (4) is comparable to the total phosphorus inputs to the ocean from terrestrial and atmospheric sources (15).

and phosphate turnover times (4, 5). Thus, the environmental factors that contribute to the production and release of reduced phosphorus compounds in surface waters remain unknown. Perhaps this redox cycling is related to the evolution of cyanobacteria and archaea more than 3 billion years ago. At that time, phosphorus concentrations in the oceans were very low because high concentrations of ferrous oxides scavenged and removed phosphorus preferentially from the surface ocean (11).

The discovery of such a large redox component in the marine phosphorus cycle is profound. Low-molecular-weight phosphonates have been implicated in both surface and deep water aerobic production of methane, a major greenhouse gas (12). Therefore, increased methane contributions to the atmosphere are directly linked to changes in the oceanic P redox cycle. This cycle is further relevant over geologic time scales, as phosphite played an important role in the evolution of life and the production of oxygen on Earth (13, 14).

For more than half a century, studies of the biogeochemistry of phosphorus have been hampered by a lack of analytical tools with which to delve into the speciation of phosphorus at environmental concentrations. As a result, most analyses focused on the bulk phosphorus pools. New methodologies and instrumentation are now providing insights into a nutrient cycle that was once viewed as rather simple (5). Van Mooy et al.'s findings on the rapid production and release rates of reduced phosphorus compounds in the marine environment are a major advance in phosphorus biogeochemistry. This breakthrough will inspire new research into why organisms participate in such an energetically expensive cycle and will ultimately further our understanding of ocean biogeochemistry and its response to climate change. ∎

REFERENCES

1. C. M. Moore et al., Nat. Geosci. **6**, 701 (2013).
2. P. Martin et al., Proc. Natl. Acad. Sci. U.S.A. **111**, 8089 (2014).
3. T. DeVries, C. Deutsch, Nat. Geosci. **7**, 890 (2014).
4. B. A. S. Van Mooy et al., Science **348**, 783 (2015).
5. D. M. Karl, Annu. Rev. Mar. Sci. **6**, 279 (2014).
6. T. Tyrrell, Nature **400**, 525 (1999).
7. D. M. Karl, R. R. Bidigare, R. M. Letelier, Deep Sea Res. II **48**, 1449 (2001).
8. C. L. Young, E. D. Ingall, Aquat. Geochem. **16**, 563 (2010).
9. W. W. Metcalf et al., Science **337**, 1104 (2012).
10. R. Geider, J. La Roche, Eur. J. Phycol. **37**, 1 (2002).
11. N. J. Planavsky, Nat. Geosci. **7**, 855 (2014).
12. D. M. Karl et al., Nat. Geosci. **1**, 473 (2008).
13. M. A. Pasek, J. P. Harnmeijer, R. Buick, M. Gull, Z. Atlas, Proc. Natl. Acad. Sci. U.S.A. **110**, 10089 (2013).
14. P. Van Cappellen, E. D. Ingall, Science **271**, 493 (1996).
15. C. R. Benitez-Nelson, Earth Sci. Rev. **51**, 109 (2000).

10.1126/science.aab2801

CANCER IMMUNOTHERAPY

Neo approaches to cancer vaccines

A neoantigen-based vaccine elicits T cell responses in cancer patients

By **Lélia Delamarre**, **Ira Mellman**, **Mahesh Yadav**

The recent success of cancer immunotherapies is rapidly changing the face of both cancer care and cancer biology. The excitement has been driven by various antibodies that block so-called "immune checkpoints" to enhance antitumor immune responses (1). Although this approach has produced durable responses for patients across a variety of tumor types, it is also the case that only a minority of patients benefit from these agents. It seems likely that among patients who do not respond or respond poorly to immunotherapies, there will be individuals who lack preexisting antitumor T cell responses. In principle, this situation can be addressed with antitumor vaccines, a strategy that has yet to yield much success despite decades of effort. The recent finding that tumor-specific mutations (neoantigens) may drive potent antitumor responses has provided hope and prompted renewed interest in the field (2). On page 803 of this issue, Carreno et al. (3) report, in a first proof of concept study, that CD8 T cell responses to tumor neoantigens can be enhanced through vaccination in melanoma patients.

Current cancer immunotherapeutic approaches act largely by reinvigorating or expanding preexisting antitumor T cell responses, overcoming a natural homeostatic mechanism designed to prevent T cell overstimulation during infection. This includes inhibiting the immune checkpoint receptors cytotoxic T lymphocyte–associated protein 4 (CTLA-4) and programmed cell death protein 1 (PD-1) on T cells. Over the past year, another conceptual advance suggests that the panoply of mutations that accompany many cancers generate potent neoantigens that provide protective immunity (2).

ILLUSTRATION: P. HUEY/SCIENCE

The potency of these neoantigens reflects the fact that the immune system could not have been tolerized against them during fetal development, enhancing the chance that they will be recognized as "foreign."

Recent studies have shown that CD8 T cells that recognize neoantigens can attack tumors, which suggests that enhancing neoantigen-specific T cell responses could improve antitumor responses (4–6). Because the bulk of mutations are patient-specific, any vaccine would require the development of a personalized approach. This presents some obvious challenges to implementation, such as how to determine what fraction of tumor mutations is immunogenic, which neoantigens should be included in a vaccine, what vaccine platform would be best to deliver neoantigens (see the figure), and whether this approach will work in human tumors as it apparently does in mice (7, 8).

One big challenge is the identification of immunogenic neoantigens. Only a very small fraction of mutations leads to the formation of a neoantigen presented on major histocompatibility complex (MHC) class I molecules (2). Carreno et al. identified several hundred such mutations in each melanoma patient. MHC class I binding affinity, determined from prediction algorithms and biochemical assays or from the affinity differential between the mutant peptide and corresponding wild-type peptide, was used to reduce the number of mutant peptides considered. Potential candidates were further prioritized according to mRNA expression level. Only seven of the possible candidates were included in the vaccine for each patient, and one-third of the selected neoepitopes proved to be immunogenic. The other neoepitopes either failed to stimulate T cells or were not processed or presented by the tumors ("cryptic antigens"). Increasing the efficiency of neoantigen identification and selection will therefore be important to extend the utility of this approach. For example, a more detailed characterization of antigen processing pathways and improved understanding of the biochemical properties of immunogenic peptides (e.g., T cell receptor affinity) should improve prediction algorithms.

The vaccine platform used to elicit immunity is another important variable. Vaccination strategies using dendritic cells generated in vitro, such as that used by Carreno et al., are based on the superior

Genentech, South San Francisco, CA 94080, USA. E-mail: mellman.ira@gene.com

capacity of these cells to induce effective T cell responses (3, 9). Such an approach may be particularly useful when the target antigen is poorly immunogenic or to bypass the risk of developing immune tolerance, as in the case of tumor-associated self-antigens. However, implementing a cell-based vaccine approach may not be needed for strongly immunogenic antigens. A simpler immunization with long synthetic peptides combined with adjuvant or with RNA-based vaccines would be more suited for broader application of a neoantigen-based vaccine and more feasible to implement in the clinic. In mouse tumor models, mutant peptide vaccines elicited potent therapeutic immunity that resulted in tumor regression even in the absence of checkpoint blockade therapy (8). In addition, an RNA-based approach elicits effective antitumor T cell response to mutant antigens (10). Nevertheless, as Carreno et al. demonstrate, neoantigen vaccination not only can amplify existing CD8 T cell clones but also can produce responses that might have been silent prior to vaccination, thus yielding a highly diverse antitumor T cell repertoire more likely to be therapeutically effective.

Because patients underwent resection surgery before vaccination, Carreno et al. could not monitor tumor regression. Important questions remain as to whether such vaccinations will be sufficient or must be accompanied by immune adjuvants, T cell costimulatory agonists, or inhibitors of immune-suppressive mechanisms (including checkpoint inhibitors). With improved T cell monitoring and readouts of clinical efficacy, future studies should soon begin to address these issues. There could, however, be a few possible hurdles to seeing a clini-

cal response despite induction of CD8 T cell responses upon vaccination, such as T cell exclusion from tumor, loss of tumor mutation, and immune suppression. Furthermore, although limited, there is increasing evidence that recognition of MHC class II mutant neoantigens by CD4 T cells occurs in cancer, and it is possible that their potentiation is required to further boost the activity of CD8 T cells targeting neoantigen (10-12). The optimal individualized vaccine may therefore have to include both CD8 and CD4 T cell-specific neoantigens.

Despite decades of study, cancer vaccines have not had a smooth ride and have earned a less than stellar reputation in many quarters. The findings of Carreno et al. and others (10–12) reinvigorate the field and point to new strategies for achieving successful antitumor vaccines. Although there are many problems to be addressed, efficacy to be confirmed, and mechanisms to be understood, neoantigen-specific vaccines merit serious consideration. ∎

Personalized cancer vaccines. Routine identification of tumor-specific mutations is enabling the exploitation of their immunogenicity through vaccination. Challenges to this approach are described in the text.

REFERENCES AND NOTES

1. P. Sharma, J. P. Allison, *Science* **348**, 56 (2015).
2. T. N. Schumacher, R. D. Schreiber, *Science* **348**, 69 (2015).
3. B. M. Carreno et al., *Science* **348**, 803 (2015).
4. N. A. Rizvi et al., *Science* **348**, 124 (2015).
5. M. S. Rooney et al., *Cell* **160**, 48 (2015).
6. A. Snyder et al., *N. Engl. J. Med.* **371**, 2189 (2014).
7. M. M. Gubin et al., *Nature* **515**, 577 (2014).
8. M. Yadav et al., *Nature* **515**, 572 (2014).
9. K. Palucka, J. Banchereau, *Immunity* **39**, 38 (2013).
10. S. Kreiter et al., *Nature* **520**, 692 (2015).
11. C. Linnemann et al., *Nat. Med.* **21**, 81 (2015).
12. E. Tran et al., *Science* **344**, 641 (2014).

Unfortunately, to date, only 64 out of the 196 States Parties to the IHR reported meeting all core-capacity requirements (7). Work must still be done to support the remaining countries in developing their national and local response capabilities.

Because of current shortcomings in response capabilities, suggestions have been made for how best to organize international assistance efforts in the event of an emergency. Some proposals would strengthen WHO's capacities (such as creating a ready-response corps under WHO authority). Others favor bypassing WHO in favor of a new entity—although it is unclear how a new international organization would remain free of bureaucratic and resource constraints that challenge existing ones. Although WHO can establish norms and deploy technical expertise, as well as provide a trusted presence on the ground, it has limited financial mechanisms to help member states prepare for public health emergencies—much less contain an emerging crisis rapidly.

A global funding mechanism for rapid response to public health emergencies may be one of the most positive developments to emerge from the Ebola outbreak. In October

"...how best to organize international assistance efforts in the event of an emergency."

2014, World Bank President Jim Yong Kim called for creation of the $20 billion PEF, to be administered by the World Bank, to allow the UN, the International Monetary Fund, regional development banks, and other donors to combine and coordinate financial contributions for responses to future emergencies (8). The World Bank is meeting with global leaders and regional financing entities to determine the best path forward, focused on two options for financing future outbreak responses through the PEF: work with private insurance partners or long-term pledges from development partners (8, 9).

Such a fund is not a new concept: Article 58 of the WHO Constitution calls for creation of a "special fund," to be used at the discretion of the governing board, to meet "emergencies and unforeseen contingencies" (10). This permanent fund was never created. Specific relief and response efforts rely on ad hoc emergency fund-raising mechanisms (11). A 2013 effort by the WHO African Regional Office to establish a permanent public health emergency fund failed to attract sufficient support from the inter-

national community (12). A response fund within a trusted and globally positioned financial institution—such as the World Bank, with knowledge and oversight for disbursing and managing funds—raises the potential of success for the proposed PEF.

TRIGGERING FINANCE. The declaration of a PHEIC by the WHO Director-General (DG) is one possible signal to initiate PEF financing, but such a declaration may come too late to finance an effective and early response. Fortunately, the IHR (2005)—developed after the severe acute respiratory syndrome (SARS) outbreak in 2003 and recognition of the need for a legal framework to obligate countries to share information and to empower WHO to act on it—contain other mechanisms that could be used.

Article 11 of the IHR (2005) (13) allows WHO to share information with "relevant" intergovernmental organizations (which include the World Bank) as soon as possible, if a public health threat will most likely not be contained without an international response (Article 11, ¶1). Such information would not necessarily be restricted to that from formal States Parties reporting but could also include other sources, including nonstate agencies and the media (Article 9). Crucially, through the IHR, WHO has the legal authority to use information supplied by States Parties for "verification, assessment and assistance purposes" before the declaration of a PHEIC if WHO determines any of the following: WHO has confirmed, according to epidemiological principles that the threat has spread beyond international borders, existing control measures are unlikely to prevent international spread, the affected country lacks the capacity to stop further spread of disease, or the nature of the event requires immediate international control measures (13).

At present, WHO decides on a case-by-case basis whether and with which organizations to share information on events that meet these criteria. Just as Annex 2 of the IHR (2005) provides an algorithm to guide States Parties in assessing whether any public health threat should be reported to WHO as a potential PHEIC, these Article 11 criteria could provide a way for WHO to alert the World Bank of emerging events, without the full weight of a PHEIC declaration. The Bank would need its own mechanism to evaluate WHO Article 11 notifications and to start the process of delivering emergency financing promptly through the proposed PEF or other instruments. This would likely include an internal consultatative process using the Bank's own technical and regional expertise to determine whether the even met specific criteria, such as the ability of affected countries to implement early control measures

without rapid external finance and whether the outbreak is likely to affect household incomes, markets, and health services in the affected country or region.

Under this scheme, an event meeting the criteria of Article 11 would not automatically turn on financing but would prompt WHO to share information with the World Bank and to establish a framework for the Bank to begin making confidential decisions on funding support while WHO's DG decides whether or not to convene an emergency committee for expert advice and/or declare a PHEIC. The emergency committee's technical recommendations could also guide funding priorities.

A regular mechanism for mobilizing assistance systematically—earlier in the time line of an outbreak and with a lower public profile—might alleviate some of the tension surrounding the PHEIC declaration process. It would allow for funding and technical assistance to be released when concerted efforts are more likely to curb transmission and control the outbreak. In 2014, an IHR-linked trigger for mobilization of prearranged funds for the public health emergency response in West Africa might have helped save thousands of lives and billions of dollars. ■

REFERENCES AND NOTES

1. M. Chan, "Report by the Director-General to the special session of the Executive Board on Ebola" (DG WHO, Geneva, 2015); http://bit.ly/1GS7AEU.
2. WHO, "Ebola virus disease in Guinea" (WHO, Geneva, 2014); http://bit.ly/1za6ryH.
3. WHO Regional Office for Africa, "Situation report 1 Ebola virus disease, Guinea, 28 March 2014" (WHO, Brazzaville, Republic of Congo, 2014); http://bit.ly/1GqvW2y.
4. UN Mission for Ebola Emergency Response, "External situation report" (UN, New York, 2015); http://bit.ly/1z7tErF.
5. WHO, OIE, World Bank Group, "WHO-OIE Operational Framework for good governance at the human-animal interface: Bridging WHO and OIE tools for the assessment of national capacities" (WHO, Geneva; OIE, Paris; WBG, Washington, DC, 2014); http://bit.ly/1bMD9IW.
6. WHO, "Implementation of the International Health Regulations (2005): Report of the Review Committee on the Functioning of the International Health Regulations (2005) in relation to pandemic (H1N1) 2009" (WHO, Geneva, 2011); http://bit.ly/whoRepIHR.
7. WHO, "Implementation of the International Health Regulations (2005): Responding to public health emergencies" (WHO, Geneva, 2015); http://bit.ly/whoImplIHR.
8. World Bank Group, "World Bank Group President calls for new global pandemic emergency facility" (WBG, Washington, DC, 2014); http://bit.ly/1q8JAQx.
9. WBG, "Pandemic emergency facility: Frequently asked questions" (WBG, Washington, DC, 2015); http://bit.ly/1bxDzvW.
10. WHO, Constitution of the World Health Organization, (WHO, Geneva, 2006); http://bit.ly/whoConst.
11. O. Jonas et al., Finance Dev. 51, 16 (2014); http://bit.ly/imfMag.
12. WHO Regional Office for Africa, "African Public Health Emergency Fund" (WHO, Brazzaville, Republic of Congo, 2013); http://bit.ly/whoAPHEF.
13. WHO, IHR (2005) (WHO, Geneva, rev. ed., 2008).

BOOKS et al.

SCIENCE LIVES

Pioneers of the final frontier

African Americans and the early days of the space program

We Could Not Fail
The First African Americans in the Space Program
Richard Paul and Steven Moss
University of Texas Press, 2015. 312 pp.

By **Claudia Alexander**

We Could Not Fail presents the biographies of 10 African-American engineers, mathematicians, and technicians who laid the groundwork for the first African-American astronauts through their involvement in the U.S. space program in the 1950s and 1960s.

Authors Richard Paul and Steven Moss explore the premise that NASA's activity in the South precipitated and facilitated that region's transition from an economy based on cotton and other agrarian activities to a more technology-driven economy that improved employment opportunities for African Americans. Paul and Moss maintain that Lyndon Johnson was the driving force behind this transition, an argument that is in keeping with Johnson's ambition for a "Great Society" and represents a natural follow-on to Franklin Roosevelt's New Deal. The authors support this assertion with numerous citations from the Johnson Presidential Library. To achieve Johnson's ambition, NASA would have to tap into the local African-American workforce in the South, a fact that the authors argue would ultimately play a role in forcing necessary social change in the region.

The book confirms and corroborates little-known histories (in many cases oral) of life in the rural South in the years after the "Great Migration" of African Americans from the South to urban areas in the Northeast, Midwest, and West [a phenomenon documented previously in *The Warmth of Other Suns* (*1*)]. One of the areas profiled is the African-American fishing village of Allenhurst, Florida—a "free" community founded by former slaves in 1872. Allenhurst (also known by the more idyllic name "Laughing Waters") was destroyed by NASA to create Cape Canaveral in the early 1960s. One of the pioneers described in the book, Theodis Ray, recalls growing up in Allenhurst. He attributes the liberated attitude enjoyed by inhabitants as an important part of the aspiration that drove him to pursue a career in the aerospace industry, against custom and expectations.

Four members of the Caltech Black Student Union and their adviser (*center*) in 1975.

Because of the parallels with another "free" African-American community in California called Allensworth (*2*), it is unfortunate that the authors didn't spend more time discussing the prevalence of free African-American communities across the country. Nonetheless, documentation of a community like Allenhurst—evidently for the first time in written form—makes the book a valuable resource. The before and after pictures of this community are an especially compelling feature of the book.

Unfortunately, the book's premise that NASA played a significant role in transforming the African-American workforce in the South is not supported by the data tables presented in the appendix, and the defense of this premise in the concluding chapter is lukewarm. In 1973, for example, minority groups made up just 5.6% of the total staff at NASA, while the government workforce, as a whole, averaged 20%. This is not for lack of qualified individuals, as shown in the accompanying photograph, taken of the Black Student Union at Caltech in 1975. All of the students shown were training in a variety of technical fields. If potential hirees were matriculating through quality institutions, albeit in small numbers, one wonders what more NASA could have done to combat institutionalized discrimination and attract more qualified minority candidates. The fact that the book addresses different regions of the South that were plagued by different problems is also not presented with clarity in the concluding section.

Nonetheless, *We Could Not Fail* is hard to put down. Reading about the personal experiences of African Americans with technical expertise before the civil rights era resonated strongly, as it likely will for any reader with African-American ancestors. The book's discussion of free African-American communities also sheds light on an important, but often overlooked, part of American history.

We Could Not Fail is not only a terrific read but also an important historical book, collecting and documenting features of life in the South for African Americans that have not heretofore been recorded. NASA's history is enriched with these stories. Kudos belong to these deserving pioneers and to the authors who dedicated themselves to bringing their stories to light.

REFERENCES

1. I. Wilkerson, *The Warmth of Other Suns* (Random House, New York, 2010).
2. A. Royal, M. Ellinger, S. Braley, *Allensworth: The Freedom Colony* (Heyday Books, Berkeley, CA, 2008).

The reviewer is at the Jet Propulsion Laboratory, Pasadena, CA 91740, USA. E-mail: claudia.j.alexander@jpl.nasa.gov

10.1126/science.aaa8008

PHOTO: THE CALTECH ARCHIVES
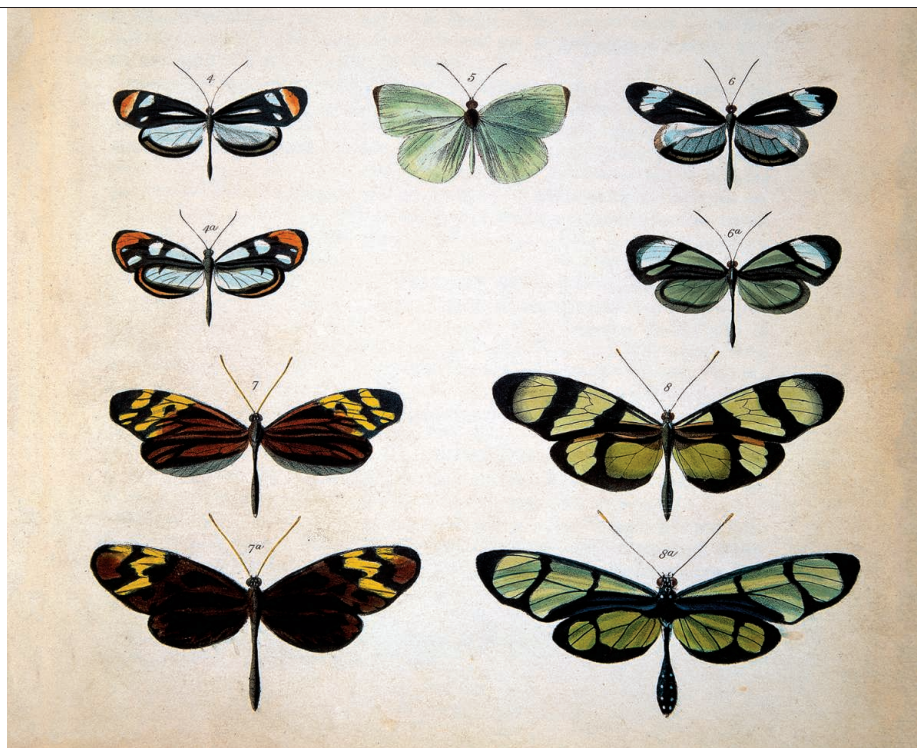
Biological mimicry in butterfly species collected by Henry Walter Bates.

Adventures in the Amazon

For three intrepid Victorian naturalists, exploration and entrepreneurship went hand in hand

By **Sandra Knapp**

To many, the word "explorer" conjures an image of a man with a pith helmet cutting his way through untracked forest. But exploration takes many forms. Alfred Russel Wallace, Henry Walter Bates, and Richard Spruce were not explorers of the pith-helmet school, nor were they independently wealthy ships' naturalists as were Joseph Banks on the *Endeavour* or Charles Darwin on the *Beagle*. They were young, middle-class natural history enthusiasts who set out from their native England to study the diversity of the Amazon in the mid-19th century.

In addition to recording the occurrence and distribution of many organisms new to science, all three men made groundbreaking scientific contributions. Wallace's experiences led to insights on biogeography and evolution by natural selection, Bates showed that mimicry could be a driving force in evolutionary change, and Spruce's collections of *Cinchona* trees—the source of

The reviewer is at the Department of Life Sciences, Natural History Museum, London SW7 5BD, UK.
E-mail: s.knapp@nm.ac.uk

the antimalarial quinine—saved many lives in Southeast Asia.

In *Naturalists in Paradise*, John Hemming uses the stories of these three iconic Victorian explorers to show how the experience of being in the field is intensively individual and as idiosyncratic as the people themselves. There is no one better to explore their journeys than Hemming, who not only is a great scholar of the Amazon and its peoples but also has, himself, trodden in the footsteps of these men, a fact that allows him to empathize charmingly with their individual tales.

Through quotations from their published works and letters home to family and friends, Hemming portrays the personalities of each of these men brilliantly—Wallace the quirky enthusiast, Bates the dependable citizen, and Spruce the quiet adventurer. All three men are depicted in light of their human interactions, not only as natural historians or scientists. A passage describing Spruce's participation in a native celebration in a small town far upriver from Manaus offers a case in point: "We got through the dance triumphantly, and at its close there was a general *viva* and clapping of hands for 'the good white man who did not despise other

people's customs!'" Spruce wrote to a friend. "Once 'in for it' I danced all night."

This open-mindeness about the peoples of the Amazon is an element that Hemming brings out more clearly than anyone who has written about these men before. All three, but particularly Wallace and Spruce, were among the first European voyagers to record anthropological and ethnographic details of the indigenous people of the Amazon in a sympathetic way. They were fascinated by the lives and customs of local communities with whom they came in contact and admired their close relationship with the forest in which they lived. Hemming's own distinguished career has helped to improve our understanding of the plight of indigenous peoples of the Amazon, so his perspective has great resonance.

Wallace, Bates, and Spruce were not mere naturalists; they were also entrepreneurs. All three men collected specimens that they sold to an avid Victorian public. Bates concentrated on insects; Wallace on birds, fish, and insects; and Spruce on plants. All had agents in London who prepared the market by publishing their letters and accounts of their adventures. All the while, sales generated by their collections were used to finance further travel.

I find it hard to even imagine how any of these materials made it back to England at all—no air freight, no sealed boxes to keep ants from eating everything. It is hard enough even today to keep everything together in the field, and I have my own transport, plastic bags, and a waterproof tent. Every specimen collected by these men that is in a museum today represents a triumph of persistence over adversity.

I have always admired Wallace, Bates, and Spruce, but for me, the most striking theme in Hemming's book is the powerful description of the importance of collaboration in field work and in science in general. They collaborated in part because they had to. They had no government backing them or money to buy their way, and they needed to work well with whomever they met. Today's scientists working with biodiversity and ecosystem services could take a cue from these Victorian naturalists who explored with both their eyes and minds open.

LETTERS

Edited by **Jennifer Sills**

Rethinking migration

WE APPLAUD THE Report by C. Montes *et al.* ("Middle Miocene closure of the Central American Seaway," 10 April, p. 226), whose geochemical analysis pushes back the timeframe of the shoaling of the Isthmus of Panama by 10 to 12 million years. This finding establishes a middle Miocene [13

Titanis Terror bird

to 15 million years ago (Ma)] completion of the land bridge between North and South America, marking a substantial shift in our understanding of the merger between these long-isolated landmasses. This has key implications for understanding the mass migration of organisms between these two continents—the so-called Great American Biotic Interchange (GABI).

In light of this new hypothesis, previous inferences about the GABI require a fresh reassessment. For example, although the majority of animal migrations appear to have taken place during the previous estimate of when the land bridge was thought to have been completed (~3.5 Ma), the new date better conforms with evidence of older migrations (10 to 5 Ma) involving flightless animals such as ground sloths, procyonids, gomphotheres, tapirs, peccaries, and flightless terror birds without invoking complicated island-hopping scenarios (*1–3*). For plants, however, the route of migration across the Isthmus region appears to have been used much earlier. In the Barbados cherries, for example, numerous independent migration events from South America to Mexico occurred as early as the middle Eocene (46 Ma) based on phylogenetic inference, but increased six-fold beginning in the lower Miocene (23 Ma), just before the newly estimated date (*4*). Thus, rates of

plant migrations between North and South America appear to have been greatly stimulated by the formation of this land bridge, even before its completion.

This reassessment raises a new conundrum: Why does the migration of animals lag so dramatically behind that of plants? It could be that even if the habitat was suitable, there were geological impediments to reaching it (dispersal limitation). However, the migration of flying birds, which conceivably could have overcome such impediments, appears to be as delayed as that of other animals, relative to plants (*5*). Another possibility is sampling bias in the fossil record. Alternatively, these patterns may hint at ecological, as opposed to geological, barriers underlying biome assembly. Ecological barriers could have included Plio-Pleistocene global climate, as Montes *et al.* suggest, or the need for vegetative changes to establish suitable habitat before the arrival of the animals. To the extent that this scenario applies, it indicates that geological barriers are not the only factor influencing migration at geological time scales and opens exciting new possibilities for exploring the relative importance of ecological factors in the merger of two continental biotas.

Charles G. Willis[1,2]** and Charles C. Davis*[2]**

[1]Harvard University Center for the Environment, Harvard University, Cambridge, MA 02138, USA. [2]Department of Organismic and Evolutionary Biology and Harvard University Herbaria, Harvard University, Cambridge, MA 02138, USA.

*Corresponding authors. E-mail: charleswillis@fas.harvard.edu (C.G.W.); cdavis@oeb.harvard.edu (C.C.D.)

REFERENCES

1. M. O. Woodburne, *J. Mamm. Evol.* **17**, 245 (2010).
2. E. G. Leigh, A. O'Dea, G. J. Vermeij, *Biol. Rev.* **89**, 148 (2014).
3. B. J. MacFadden, J. Labs-Hochstein, R. C. Hulbert, J. A. Baskin, *Geology* **35**, 123 (2007).
4. C. G. Willis, B. F. Franzone, Z. Xi, C. C. Davis, *Front. Genet.* **5**, 1 (2014).
5. J. T. Weir, E. Bermingham, D. Schluter, *Proc. Natl. Acad. Sci. U.S.A.* **106**, 21737 (2009).

The Nobel pulsar

THE SPECIAL ISSUE of *Science* on "General Relativity turns 100" (6 March, p. 1082) gives a wonderful history of the successes of the theory, but I feel that it is important to make a correction pertaining to the binary pulsar PSR B1913+16 and the effect of gravitational waves. There has been no Nobel Prize for relativity. Russell Hulse and Joseph Taylor were deservedly awarded their Nobel Prize "for the discovery of a new type of

pulsar, a discovery that has opened up new possibilities for the study of gravitation" (*1*). Hulse and Taylor clearly understood the importance of this system when it was discovered in 1974 (*2*), as well as its potential for "heretofore unavailable tests of gravitational theories" (*3*). The importance of this system was quickly recognized by others as well (*4*). However, the observation of the decay of the orbit, and the agreement with energy loss from gravitational wave emission, was due to Joseph Taylor and Joel Weisberg (*5*). Subsequent observations (*6*) have confirmed that the orbital decay of PSR B1913+16 is in remarkable agreement with predictions from general relativity, and further tests of gravity in the strong field regime are possible (*7*).

Whether from LIGO-Virgo, pulsar timing, or B-modes in the cosmic microwave background, the coming years should produce further remarkable observations of gravitational waves.   *Nelson Christensen*

Department of Physics and Astronomy, Carleton College, Northfield, MN 55057 USA. E-mail: nchriste@carleton.edu

REFERENCES

1. The Nobel Prize in Physics 1993 (www.nobelprize.org/nobel_prizes/physics/laureates/1993/press.html).
2. R. A. Hulse, J. H. Taylor, *Astrophys. J.* **195**, L51 (1975).
3. J. H. Taylor, R. A. Hulse, L. A. Fowler, G. E. Gullahorn, J. M. Rankin, *Astrophys. J.* **206**, L53 (1976).
4. T. Damour, R. Ruffini, *C. R. Acad. Sci. Paris* **279**, 971 (1974).
5. J. H. Taylor, J. M. Weisberg, *Astrophys. J.* **253**, 908 (1982).
6. J. M. Weisberg, D. J. Nice, J. H. Taylor, *Astrophys. J.* **722**, 1030 (2010).
7. J. H. Taylor, A. Wolszczan, T. Damour, J. M. Weisberg, *Nature* **355**, 132 (1992).

Preparing for disasters

THE NATIONAL INSTITUTE of Environmental Health Sciences (NIEHS) fully supports the development of "A community for disaster science" (M. McNutt, Editorial, 3 April, p. 11). Almost 2 years ago, we created the NIH Disaster Research Response (DR2) Project to facilitate the incorporation of "disaster science" into national response and recovery efforts (*1*). Key components of this project include improving accessibility to health data collection tools and Institutional Review Board (IRB)–approved research protocols, proactive engagement of diverse public and private stakeholders, and fostering the development of a trained cadre of academic researchers who can collect critical information and function in the immediate post-disaster environment without interfering with the emergency response.

The publicly accessible NIH DR2 website now includes more than 165 data collection tools and other information to support disaster science activities (*2*). We have

also sponsored a national workshop and conducted two tabletop exercises that have brought together academia, local community representatives, private industry, emergency responders, and public health, emergency management, and volunteer organizations to discuss the challenges and benefits of conducting post-disaster research and the value of evidence-based decision-making (*3*).

It is clear that disaster response and recovery require an interdisciplinary effort supported by the best evidence available. As such, we have begun to develop a national "Environmental Health Sciences Network for Disaster Response" composed of interested academic centers with diverse expertise to enhance our ability to identify human health threats, prioritize research needs, provide expert consultation, and conduct disaster research. Research and response organizations must work jointly with community partners, first responders, local public health departments, and policymakers to anticipate threats and develop innovative methods to prevent being overwhelmed by unexpected cascading events, such as those following the Great East Japan earthquake, tsunami, and nuclear reactor meltdown in 2011. For a sustained effort, there also needs to be a national framework that supports disaster science research, timely funding that supports a science response, and an interdisciplinary disaster science career path within academic institutions and government entities that nurtures the next generation of disaster researchers.

Aubrey Miller* and Linda Birnbaum

National Institute of Environmental Health Sciences, Research Triangle Park, NC 27709, USA.

*Corresponding author. E-mail: miller.aubrey@nih.gov

REFERENCES

1. N. Lurie, T. Manolio, A. P. Patterson, F. Collins, R. Frieden, *N. Engl. J. Med.* **368**, 1251 (2013).
2. NIH Disaster Research Response (DR2) (http://dr2.nlm.nih.gov).
3. Institute of Medicine, "Enabling rapid and sustainable public health research during disasters: Summary of a Joint Workshop by the Institute of Medicine and the U.S. Department of Health and Human Services" (National Academies Press, Washington, DC, 2014).

TECHNICAL COMMENT ABSTRACTS

Comment on "Morality in everyday life"
Manuel C. Voelkle
In examining morality in everyday life, Hofmann *et al.* (Reports, 12 September 2014, p. 1340) conclude that being the target of (im)moral deeds impacts happiness, whereas committing them primarily affects one's sense of purpose. I point to shortcomings in the analyses and interpretations and caution that, based on the methodological approach, conclusions about everyday life relationships between morality and happiness/purpose are premature.
Full text at http://dx.doi.org/10.1126/science.aaa2409

Response to Comment on "Morality in everyday life"
Wilhelm Hofmann, Daniel C. Wisneski, Mark J. Brandt, Linda J. Skitka
Voelkle challenges our conclusions regarding the relationship between morality and momentary happiness/sense of purpose based on methodological concerns. We show that our main conclusions are not affected by this methodological critique and clarify that the discrepancies between our and Voelkle's effect size estimates can be reconciled by the realization that two different (but compatible) research questions are being asked.
Full text at http://dx.doi.org/10.1126/science.aaa3053

TECHNICAL COMMENT

SOCIAL PSYCHOLOGY

Comment on "Morality in everyday life"

Manuel C. Voelkle[1,2]

In examining morality in everyday life, Hofmann *et al*. (Reports, 12 September 2014, p. 1340) conclude that being the target of (im)moral deeds impacts happiness, whereas committing them primarily affects one's sense of purpose. I point to shortcomings in the analyses and interpretations and caution that, based on the methodological approach, conclusions about everyday life relationships between morality and happiness/purpose are premature.

Hofmann *et al*. (*1*) take the study of morality out of the lab and into real life. They do so by using smartphones to assess momentary happiness and sense of purpose five times a day across 3 days, along with participants' reports on whether they committed, were the target of, witnessed, or learned about moral or immoral acts within the past hour after being signaled. The aim of providing a more ecologically valid picture of moral life in a large sample of $N = 1252$ participants is important and deserves close attention by the scientific community.

The white bars in Fig. 1 show the findings presented in the original article, after correction of a computational error (also corrected online in the original paper). With Cohen's d (*2*) ranging between 0.57 and 1.34, the effects of moral and immoral acts on everyday happiness are impressive and easily surpass effects sizes typically observed in studies on the impact of major life events on subjective well-being (*3*), happiness (*4*), or the effectiveness of positive psychology interventions (*5*). How can simple (im)moral acts, such as assisting a tourist with directions or disrespecting one's mother, have such strong effects on everyday happiness and sense of purpose?

To understand this, a closer look at the data analysis and interpretation of results by Hofmann *et al*. (*1*) is necessary. The analysis was carried out in two steps. First, about 70% of the total responses, in which no morally relevant events were reported, were deleted from the data set. Second, a two (moral versus immoral) by four (perspective:

[1]Humboldt University Berlin, Department of Psychology, Rudower Chaussee 18, 12489 Berlin, Germany. [2]Max Planck Institute for Human Development, Lentzeallee 94, 14195 Berlin, Germany.
Corresponding author. E-mail: voelkle@mpib-berlin.mpg.de
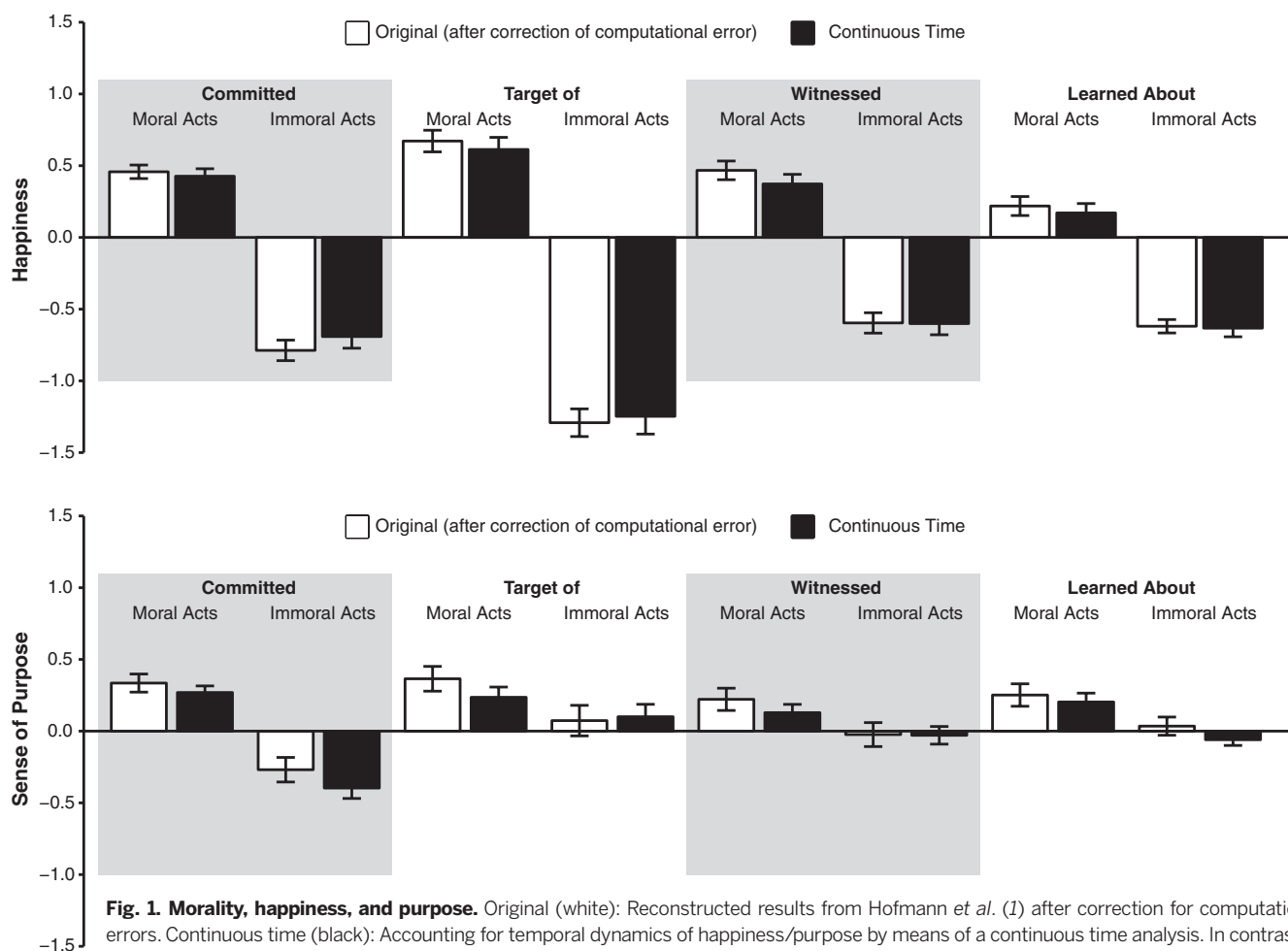
Fig. 1. Morality, happiness, and purpose. Original (white): Reconstructed results from Hofmann *et al*. (*1*) after correction for computational errors. Continuous time (black): Accounting for temporal dynamics of happiness/purpose by means of a continuous time analysis. In contrast to the original findings presented by Hofmann *et al*. (*1*), all effects are centered at the baseline for reasons of comparability.

Table 1. Morality and happiness. Comparison between effect sizes reported by Hofmann *et al.* (*1*) and effect sizes based on a reanalysis that also included morally irrelevant situations. Cohen's (*2*) recommendations on effect size interpretation are provided in parentheses. For these comparisons, effect sizes (f^2) were computed and rounded up or down to the nearest cut-off value. *Parameter estimates were obtained via the plm package (*11*) in R (*12*).

Condition	Original article (*1*): Mean difference in happiness between moral and immoral acts (Cohen's *d*)	Reanalysis: Effect of morality on everyday fluctuations in happiness (R squared)*
Committed	0.85 (large)	0.022 (small)
Target of	1.34 (large)	0.023 (small)
Witnessed	0.73 (large)	0.013 (small)
Learned about	0.57 (medium)	0.022 (small)

committed, target of, witnessed, learned about) factorial linear mixed-effects analysis was carried out on the remaining data. This approach is problematic for two reasons.

First, the deletion of such a large portion of data is unnecessary. Although researchers are often trained to think in terms of fully crossed factorial designs (here, a two by four design), the general linear model is not limited to such designs. By using morally irrelevant situations as baseline, the eight different conditions could have been represented by eight dummy variables, making use of all available information. Furthermore, by limiting the analysis to moral and immoral acts, the authors created a situation that has little to do with morality in everyday life, where most situations encountered by individuals are morally irrelevant. In fact, only 104 participants (9%) ever committed an immoral act directly after a moral act, and only 18 participants (1%) were ever the target of a moral act followed immediately by an immoral act (4% for witnessed; 8% learned about). The large effect sizes reported in the study result from comparing these extreme conditions against each other. The effect sizes thus reflect the fact that, if a group of people encountered a moral situation, we can expect them to be happier than a different group who encountered an immoral situation. For the study of morality in everyday life, however, a measure of the expected difference in happiness/purpose between different groups is misleading, because (i) it ignores the low base-rate of the event, and (ii) it describes an unrealistic scenario because any given individual is most unlikely to ever experience a direct transition from a moral to an immoral situation. Including morally irrelevant situations in the analysis, via the dummy variable approach proposed above, provides a more realistic picture. As is apparent from Table 1, the two dummy variables for moral versus immoral acts explain about 2% of the fluctuations in happiness across all conditions (baseline). According to Cohen's recommendations (*2*), these are consistently small effect sizes, which not only provide a more realistic picture of the effect of everyday morality on everyday happiness but also are better in line with the existing literature (*3–5*).

Second, the linear mixed-effects analysis does not account for temporal dynamics. The assumption that happiness/purpose at time point *t* is independent of happiness/purpose at time point *t* − 1 seems unrealistic and counter to the authors' own theory and analyses on moral dynamics (*1*). Although different methods have been developed to account for such dynamics (*6, 7*), continuous time models (*8, 9*) seem particularly suited because they generalize readily to designs with arbitrary measurement occasions at the individual level. Results of the continuous time analysis are depicted by the black bars in Fig. 1. When comparing different methods for data analysis, it is important to keep in mind that the primary question is not whether parameter estimates are significantly different from each other but whether the methods result in (significantly) different conclusions. This is the case. For example, in absolute terms, the (corrected) effect of committing a moral act on sense of purpose is lower than the effect of being the target of a moral act, which stands in contrast to the conclusion of the original article. Interestingly, though, although not supported by the authors' own analysis, this conclusion is remedied by the continuous time analy-

sis (see Fig. 1). Furthermore, whereas the original analysis suggests a significantly stronger reduction in happiness for people who committed rather than witnessed an immoral act, the continuous time analysis suggests a nonsignificant difference.

The strength of the study by Hofmann *et al.* (*1*) is the ecological approach combined with a panel data structure with individually varying measurement occasions. In principle, such a design holds the potential to use temporal information to uncover causal dynamics of everyday morality at an average within-person level. Unfortunately, however, Hofmann *et al.* (*1*) do not model temporal contingencies at the within-person level. Hence, the data do not show whether "committing moral deeds…boost momentary happiness and sense of purpose" (*1*), and care must be taken to not generalize beyond the observed group mean difference to within-person processes when interpreting results (*10*). However, pursuing Hofmann *et al.*'s (*1*) ecological approach with a higher temporal resolution regarding the ordering of events in time and better methods to analyze the resulting dynamics, as outlined in this comment, may provide a promising avenue for future research on everyday morality.

REFERENCES AND NOTES

1. W. Hofmann, D. C. Wisneski, M. J. Brandt, L. J. Skitka, *Science* **345**, 1340–1343 (2014).
2. J. Cohen, *Psychol. Bull.* **112**, 155–159 (1992).
3. M. Luhmann, W. Hofmann, M. Eid, R. E. Lucas, *J. Pers. Soc. Psychol.* **102**, 592–615 (2012).
4. D. Ballas, D. Dorling, *Int. J. Epidemiol.* **36**, 1244–1252 (2007).
5. L. Bolier *et al.*, *BMC Public Health* **13**, 119 (2013).
6. C. Hsiao, *Analysis of Panel Data* (Cambridge Univ. Press, Cambridge, ed. 2, 2003).
7. K. A. Bollen, P. J. Curran, *Latent Curve Models: A Structural Equation Perspective* (John Wiley, Hoboken, NJ, 2006).
8. M. C. Voelkle, J. H. L. Oud, E. Davidov, P. Schmidt, *Psychol. Methods* **17**, 176–192 (2012).
9. J. H. L. Oud, R. A. R. G. Jansen, *Psychometrika* **65**, 199–215 (2000).
10. P. C. M. Molenaar, *Measurement* **2**, 201–218 (2004).
11. Y. Croissant, G. Millo, *J. Stat. Softw.* **27**, 1–43 (2008). www.jstatsoft.org/v27/i02/paper
12. R Core Team (R Foundation for Statistical Computing, Vienna, 2014).

RESEARCH

The opah, a large deepwater fish, warms both its heart and brain
Wegner et al., *p. 786*

Yellowstone "supervolcano"

VOLCANOLOGY
Yellowstone's missing magmatic link

Yellowstone is an extensively studied "supervolcano" that has a large supply of heat coming from a pool of magma near the surface and the mantle below. A link between these two features has long been suspected. Huang *et al.* imaged the lower crust using seismic tomography (see the Perspective by Shapiro and Koulakov). Their findings provide an estimate of the total amount of molten rock beneath Yellowstone and help to explain the large amount of volcanic gases escaping from the region. — BG

Science, this issue p. 773; see also p. 758

HUMAN BEHAVIOR
Friends and family?

Evolutionary theory stresses the importance of living with kin, not least because they share some of our genes. Nevertheless, a large-scale assessment of contemporary hunter-gatherer societies has established a consistent pattern of unrelated individuals living together. Dyble *et al.* used a modeling approach to suggest that a possible answer to this conundrum is that cohabitation choices are being governed equally by men and women. — GJC

Science, this issue p. 796

3D PRINTING
Mimicking complex shapes of natural shells

What design principles in sea-shells make their mechanical properties so outstanding? Tiwary *et al.* 3D-printed such shapes, based on their understanding of the stress distribution schemes found in seashells. The adoption of Mother Nature's design could have a strong impact on future engineering applications. For instance, the natural shape of a limpet shell reduces stress in the central cavity region, which protects its resident from external loads. — ZHK

Sci. Adv. 10.1126.sciadv. 1400052 (2015).

QUANTUM OPTICS
Tailoring the quantum dynamics of light

The energy levels of a quantum system are determined by the laws of quantum mechanics and the specifics of the physical setting. Light confined to a cavity has energy levels neatly arranged in a "ladder" of equidistant rungs, each rung corresponding to a fixed number of photons. Bretheau *et al.* devised a way to limit the dynamics to only the lowest few rungs by coupling the system to a qubit, which shifted the energy of one of the higher rungs. When they then drove the system at a frequency corresponding to the distance between the rungs, only the states lower in energy than the shifted state could participate. — JS

Science, this issue p. 776

MITOSIS
Chromosomes: Let me be your guide

The correct alignment of chromosomes at the center of the mitotic spindle—the metaphase plate—before cell division is one of the key mechanisms for the maintenance of genomic stability. But is there anything special about the microtubules of the spindle that helps this process? Barisic *et al.* demonstrate that chromosome alignment at the cell equator is controlled by a specific posttranslational modification of selected microtubules
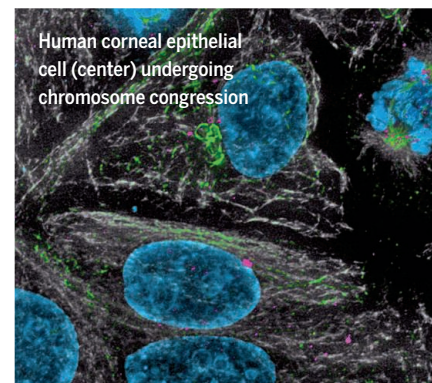
Human corneal epithelial cell (center) undergoing chromosome congression

oriented toward the center of the mitotic spindle. — SMH

Science, this issue p. 799

GALAXY EVOLUTION
In a cluster of protogalaxies far, far away

Astronomers constantly scour the sky for astronomical objects that can provide insight and constrain their models and simulations of galaxy evolution. Hennawi *et al.* surveyed the ancient sky at an epoch when the universe was half its age for nebulae: large clouds of ionized hydrogen. They stumbled across a system containing four active galactic nuclei, or quasars; objects that are thought to be the progenitors of galaxies. Finding a nebula with a rare quadruple quasar system embedded within it allows detailed spectroscopic and motional studies that may help to refine current models of galaxy and galaxy cluster formation. — ISO

Science, this issue p. 779

ARCHAEOLOGY
Cultural prehistory in southern Europe

The Protoaurignacian culture appeared in the southern European archeological record around 42,000 years ago and was characterized by artefacts including personal ornaments and bladelets. Archaeologists have debated whether it was ancestral *Homo sapiens* or Neandertals who made these tools and ornaments. Benazzi *et al.* analyzed dental remains from

PHOTO: © FLPA/ALAMY

two Protoaurignacian sites in Italy and confirm that they were *H. sapiens*. The arrival of this culture may have led to the demise of Neandertals in these areas (see the Perspective by Conard *et al.*). — AMS

Science, this issue p. 793; see also p. 754

CANCER IMMUNOTHERAPY
Giving antitumor T cells a boost

Mutations allow tumors to divide, escape death, and resist treatment. But mutations can also cause tumors to express mutant proteins, which could potentially be exploited to drive antitumor T cell responses. Carreno *et al.* report the results of a small phase I trial seeking to do just this (see the Perspective by Delamarre *et al.*). They vaccinated three patients with advanced melanoma with personalized dendritic cell–based vaccines designed to activate T cells specific for mutations in the patients' cancer. T cells specific for mutant peptides did indeed expand. A next step will be to determine whether this promising strategy improves patient outcomes. — KLM

Science, this issue p. 803; see also p. 760

NEURODEGENERATION
Making aggregation less aggravating

The accumulation of α-synuclein aggregates occurs in certain neurodegenerative disorders, including Parkinson's disease. Daniele *et al.* found that α-synuclein aggregates activated the receptor complex TLR1/2 on primary mouse microglia, leading to the production of proinflammatory cytokines. TLR1/2 antagonists, including a drug approved for treating hypertension, prevented the activation of microglia and cytokine secretion in response to aggregated α-synuclein. Thus, repurposing of drugs that also inhibit TLR1/2 may be beneficial for patients with synucleinopathies. — LKF

Sci. Signal. **8**, ra45 (2015).

IN OTHER JOURNALS

Edited by **Sacha Vignieri** *and* **Jesse Smith**

Larger birds, such as this white-plumed honeyeater, decline in Australian woodlands surrounded by maturing pine plantations

CONSERVATION BIOLOGY
Shaped by your surroundings

Humans are fragmenting natural habitats into relatively pristine patches surrounded by a larger altered landscape patchwork, or matrix. The nature of this matrix can influence which species in the remaining intact habitat will persist. Mortelliti and Lindenmayer report on a large, long-term experiment that measured the impact of landscape change on 64 species of birds found within fragmented native *Eucalyptus* woodlands in Australia. They found that though overall species richness did not change, emerging pine plantations altered communities, favoring smaller birds that move easily through dense vegetation but reducing the presence of larger species. These results suggest that matrix vegetation types can shape selection in such a way that species and communities within native landscape patches are permanently changed. — SNV

Conserv. Biol. 10.1111/cobi.12523 (2015).

EDUCATION
A stopgap laboratory experience

As science education moves toward lab-based courses, what happens to students without access to a lab? One option is peer-led team learning (PLTL), a cooperative-learning strategy that encourages students to actively engage in learning. Snyder *et al.* hypothesized that a PLTL model would lead to increased achievement for students not enrolled in an optional lab course. Non–lab course PLTL students participated in active problem-solving, resulting in this group averaging a letter-grade higher than their nonlab peers without PLTL. This difference
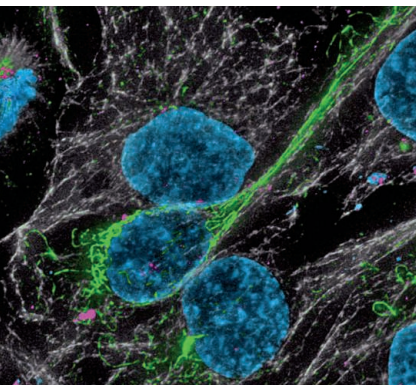
PALEOBIOGEOGRAPHY

Dating the history of a biotic connection

The closure of the Panama isthmus enabled the dispersal of terrestrial organisms between South and Central America and prevented the dispersal of marine creatures between the Caribbean and Pacific oceans. This Great American Biotic Interchange is generally held to have begun about 3.5 million years ago. Bacon *et al.* analyze fossil and molecular sequencing data that indicate some significant and much earlier dispersal events for terrestrial organisms and separation events for marine organisms, at 6 to 7 and 23 to 24 million years ago. Together with recent geological evidence for earlier land emergence, these results suggest a more complex history for the biogeographic events shaping the biota of the Americas. — AMS

Proc. Natl Acad. Sci. U.S.A. 10.1073/pnas.1423853112 (2015).

The land bridge connecting South and Central America may have formed millions of years earlier than thought

was statistically significant, suggesting that PLTL workshops almost entirely closed the achievement gap for students without access to a lab. Although successful, the authors caution against using PLTL workshops as a replacement for laboratory experience. — MM

CBE Life Sci. Educ. **14**:ar2 (2015).

CANCER BIOLOGY

Creating a safe haven for tumor cells

Melanomas with certain mutations often respond dramatically to drugs inhibiting a protein kinase called BRAF. This is because BRAF is part of a signaling pathway that, when mutationally activated, drives melanoma growth. Unfortunately, the response is often short-lived because tumor cells develop resistance to the drugs. Hirata *et al.* make

the surprising observation that melanoma cells do not acquire resistance to BRAF inhibition on their own but rather receive help from neighboring fibroblasts. BRAF inhibitors cause fibroblasts to remodel the extracellular matrix. Signals from the remodeled matrix then reactivate the growth signaling pathway in the melanoma cells. Thus, the tumor microenvironment can provide a safe haven for tumor cells that allows them to tolerate certain drugs. — PAK

Cancer Cell **27**, 574 (2015).
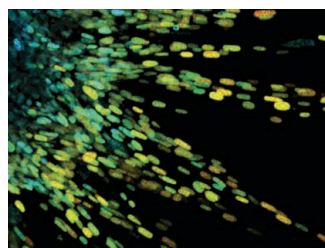
Neighboring fibroblasts help cancer cells tolerate certain drugs

CHEMISTRY

Water helpful but not needed to fold DNA

DNA has found a range of applications in chemistry and materials science, from acting as a link that connects other materials to forming complex structures. DNA structures are formed in water and cannot be transferred to organic solvents without a loss of order or change in helical structure. Gállego *et al.* show that a deep eutectic solvent composed of a 4:1 mixture of glycerol and choline chloride enables DNA assembly under room-temperature conditions. When water was added to the mix to lower the viscosity, the assembly time was reduced from 6 days to 20 min, thus providing a method for kinetic control of the assembled structures. — MSL

Angew. Chem. Int. Ed. 10.1002/anie.201412354 (2015).

SYSTEMS BIOLOGY

Signaling at the heart of blood pressure regulation

Genetic variants, detected in large genome-wide association studies (GWASs) of blood pressure regulation in humans, account for only about 1% of the variability observed between individuals. Thus, better understanding of complex regulatory networks is necessary to find causal events and potential therapeutic targets. Huan *et al.* used integrative analysis that included transcriptional profiling and coexpression network analysis, GWASs, and molecular network modeling to tease out "key driver" genes that are central to regulatory modules that control blood pressure. One of these was SH2B3, a cell signaling adaptor protein previously detected in GWAS studies. The analysis further suggested that SH2B3 may function by altering inflammatory responses and T cell functions. — LBR

Mol. Syst. Biol. 10.15252/msb.20145399 (2015).

MEMBRANE SCIENCE

Probing antifouling by graphene oxide

Graphene oxide (GO) surfaces have antibacterial properties, but they are not due to any known specific physical interactions with cells. Because GO is toxic to bacteria, it has been proposed as an antifouling material for membranes during water purification. To test the hypothesis that GO physically disrupts or binds to cells, Romero-Vargas Castrillón *et al.* measured the physical interactions between GO-coated atomic force microscope probes and *Escherichia coli* cells. Other than occasional lipopolysaccharide binding events, the forces of interaction are mostly repulsive. Other modes of action, such as oxidative stress, therefore are likely to be responsible for GO toxicity. — NW

Environ. Sci. Technol. Lett. 10.1021/acs.estlett.5b00066 (2015).

ALSO IN *SCIENCE* JOURNALS

Edited by **Stella Hurtley**

CELL BIOLOGY
How cells know when they are the right size

Biologists have long recognized that cells exist in a large range of sizes. Cell size is also flexible: Cells can differentiate into another cell type with a very different size. External factors can also influence cell size, but the consistent size of a given cell type shows that cells have mechanisms to measure their own size and adjust their growth rate or rate of cell division to maintain uniformity. Ginzberg *et al.* review recent advances in understanding how cells know when they are at the right size. — LBR

Science, this issue p. 771

PHOSPHORUS CYCLING
The phosphorus redox cycle

Phosphorus in the oceans cycles between +5 and +3 oxidation states. Most of the oceans' phosphorus is present as oxidized bioavailable phosphate (+5) compounds. Reduced organophosphorus compounds are also present but at much lower concentrations. Through field measurements in the western tropical North Atlantic Ocean and a series of laboratory incubations, Van Mooy *et al.* measured fast reduction rates of a small but appreciable amount of phosphates by plankton communities, forming phosphites and phosphonates (see the Perspective by Benitez-Nelson). On a global scale, this phosphorus redox cycle adds as much reduced phosphorus to the oceans as all pre-anthropogenic land runoff. — NW

Science, this issue p. 783;
see also p. 759

NEURODEVELOPMENT
How to maintain a zebrafish brain

Even in the zebrafish brain, which seems better able than the human brain to generate new neurons, regenerative capacity may not be unlimited. Barbosa *et al.* mapped the fates of individual neuronal cells in live zebrafish over time. Seen as glowing dots, neural stem cells sustain the population of neurons, although not quite at full replacement rates. After injury to the brain, more of the stem cells were pulled into neuronal pathways, with fewer remaining to feed future replacement. — PJH

Science, this issue p. 789

NONCODING RNA
Spreading small RNAs to protect the genome

In animals, PIWI-interacting RNAs (piRNAs) are small noncoding RNAs that protect our germ lines from the ravages of transposons. To do this, piRNAs target and cleave transposon RNAs. Synthesis of piRNA is initiated by a cut made in a long, single-stranded precursor RNA. The piRNAs can also undergo a self-perpetuating amplification cycle (see the Perspective by Siomi and Siomi). Han *et al.* and Mohn *et al.* now reveal that piRNA biogenesis can also spread in a strictly phased manner from the site of initial piRNA formation. Spreading piRNA synthesis greatly increases their sequence diversity, potentially helping them to target endogenous and novel transposons more effectively. — GR

Science, this issue p. 817, p. 812;
see also p. 756

ANIMAL PHYSIOLOGY
A cold-water fish with a warm heart

Mammals and birds warm their entire bodies above the ambient temperature. Generally, this ability is lacking in other vertebrates, although some highly active fish can temporarily warm their swim muscles. Wegner *et al.* show that the opah, a large deepwater fish, can generate heat with its swim muscles and use this heat to warm both its heart and brain. This ability increases its metabolic function in cold deep waters, which will help the fish compete with other, colder-blooded species. — SNV

Science, this issue p. 786

CENTROSOMES
A little bit of this and a little bit of that

Centrosomes are the major microtubule-organizing centers in animal cells. Key to this function is the somewhat mysterious pericentriolar material (PCM). Woodruff *et al.* describe the in vitro reconstitution of PCM assembly. In cells, PCM is recruited by centrioles to form centrosomes that nucleate and anchor microtubules. SPD-5, the main component of the PCM matrix in *Caenorhabiditis elegans*, polymerized in vitro to form micrometer-sized porous networks. SPD-5 polymerization was directly controlled by the polo family kinase Plk1 and Cep192/SPD-2, two conserved regulators that control PCM assembly across metazoans. — SMH

Science, this issue p. 808

MULTIPLE SCLEROSIS
Rethinking the role of reactive T cells

In patients with multiple sclerosis (MS), damage to the nerve-insulating myelin sheath blocks the ability of neurons to conduct messages. Although the injury is thought to be caused by the body's own immune system, myelin-restricted immune cells exist in comparable numbers in MS patients and healthy controls. Now, Cao *et al.* report functional differences between myelin-reactive T cells from MS patients—which are proinflammatory—and those in healthy controls—which secrete more of the immunoregulatory cytokine interleukin-10. Thus, functional divergence in selected immune cells may contribute to disease development — ACC

Sci. Transl. Med. **7**, 287ra74 (2015).

DEVELOPMENT ECONOMICS
Attacking the problem of extreme poverty

A persistent concern about well-intentioned efforts to improve living standards for the 1.2 billion people who survive (if it can be called that) on less than $1.25 US per day is figuring out what works. A second concern is figuring out whether what works in one setting can be made to work in another. Banerjee *et al.* describe encouraging results from a set of pilot projects in Ethiopia, Ghana, Honduras, India, Pakistan, and Peru encompassing 11,000 households. Each project provided short-term aid and longer-term support to help participants graduate to a sustainable level of existence. — GJC

Science, this issue p. 772

REVIEW SUMMARY

CELL BIOLOGY

On being the right (cell) size

Miriam B. Ginzberg,[1]* Ran Kafri,[2]* Marc Kirschner[1]*†

BACKGROUND: How do the different cell types in our bodies maintain their distinctive and characteristic sizes? Although much is known about the signaling networks that stimulate or suppress cell growth, such as the mammalian target of rapamycin (mTOR) pathway, this central question remains: How do a common set of pathways precisely specify the appropriate size for any given cell type and physiological condition? The precision with which size is controlled is demonstrated by the uniformity in cell size typically seen in tissues. Most epithelial tissues, for example, display a striking regularity in the size and morphology of cells, whereas size heterogeneity can be a sign of neoplastic growth.

Most work on the subject of how cell size is regulated has explored the control of cell growth and proliferation by extracellular signals, such as growth factors and cytokines. However, although these signals can dictate the mean size of cells, individual cells will inevitably deviate from that mean. Variability in cell size can arise from variability in growth rate

and cell-cycle length or asymmetry in cell division. These sources of variation raise the question of whether they are counteracted by cellular mechanisms that act to increase size homogeneity. Size variation can only be reduced with processes that differentially affect cells of different sizes, despite the fact that they share the same environment. This kind of control requires that individual cells measure their own size and adjust their behavior as necessary to achieve a common target size.

ADVANCES: In this Review, we present a growing body of evidence that suggests that animal cells autonomously measure and adjust their individual sizes to maintain uniformity within a population. We discuss possible mechanisms by which this can be achieved, including the size-dependent adjustment of cell-cycle length and/or growth rate, as well as the limitations of these strategies. We summarize the progress that has been made thus far in identifying the cell's size control machinery and highlight important unanswered questions.

The presence of mechanisms ensuring precise size specification suggests that there may be an optimal cell size for a particular cell's function. Here, we address the question of whether cells function most efficiently when at the "right" size by examining cases in which cell size was altered naturally or experimentally. Some tissues seem to easily compensate for cell-size changes, whereas in others, cells appear to perform best at their appropriate size. We highlight examples of cell types, such as pancreatic β cells and adipocytes, in which a relationship between cell size and cell function has been observed.

OUTLOOK: We conclude by discussing the gaps in our understanding of how cell size is regulated, stressing the questions that have been most neglected. Throughout this Review, we point out the experimental challenges that have hindered progress in this field and emphasize recent technological advances that may allow us to overcome these obstacles. Last, we pose the questions that we anticipate will guide this field in the upcoming years. ∎
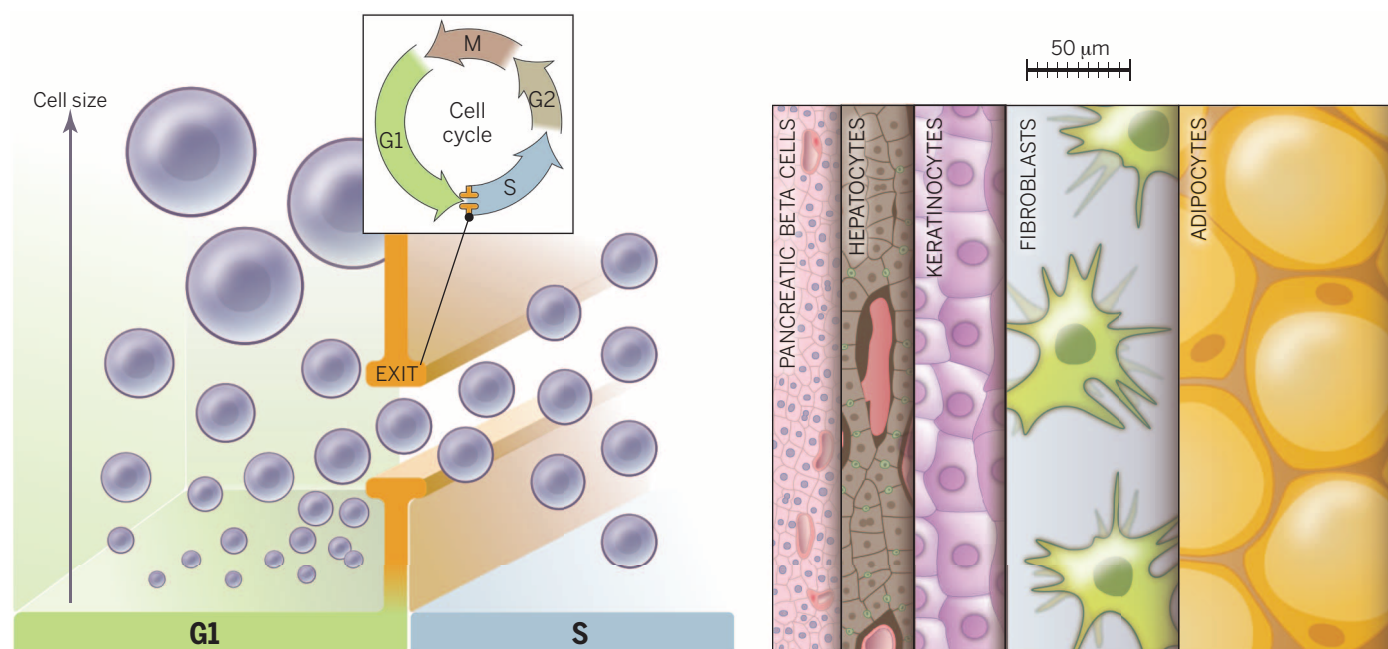
How is cell size specified? (**Left**) In populations of proliferating cells, size uniformity may be ensured by linking the processes of growth and cell-cycle progression. One way this can be accomplished is by restricting progress through a particular cell-cycle stage (for example, the G₁/S transition) to cells that have reached a specific "target" size. (**Right**) Typical sizes of various human cell types. Cells are drawn to scale: pancreatic β cells, hepatocytes, keratinocytes, fibroblasts, and adipocytes.

REVIEW

On being the right (cell) size

Miriam B. Ginzberg,[1]* Ran Kafri,[2]* Marc Kirschner[1]*†

Different animal cell types have distinctive and characteristic sizes. How a particular cell size is specified by differentiation programs and physiology remains one of the fundamental unknowns in cell biology. In this Review, we explore the evidence that individual cells autonomously sense and specify their own size. We discuss possible mechanisms by which size-sensing and size-specification may take place. Last, we explore the physiological implications of size control: Why is it important that particular cell types maintain a particular size? We develop these questions through examination of the current literature and pose the questions that we anticipate will guide this field in the upcoming years.

Early cytologists found that within a species, it is the number of cells, rather than the size of the cells, that makes one individual larger than another; cell size is relatively constant (*1*). Although this seems to downgrade the question of cell size in favor of proliferative potential, it raises the curious question of how cells of a common cell type achieve such a uniform size yet are capable of changing their size by orders of magnitude during differentiation or in response to physiological stimuli. For example, pancreatic β cells are surrounded by acinar cells that are roughly twice their size, and chondrocytes increase their volume by 10- to 20-fold during hypertrophic bone growth (*2*). These examples, among others (Fig. 1), demonstrate that a cell's size is not the result of physical constraints but rather is adaptively regulated. What, then, specifies a particular cell's size?

Much work on this subject has focused on identifying extracellular factors (and their intracellular responsive pathways) that elicit changes in cell size. These studies found that the size of a cell is largely controlled by its cell-surface receptors and the combinations of growth factors, mitogens, and cytokines in its environment. In the 1980s, Zetterberg and co-workers distinguished between factors, such as insulin-like growth factor 1 (IGF-1) and insulin, that primarily initiate cell growth and factors such as epidermal growth factor (EGF) that primarily drive cell-cycle progression, even in the absence of growth (*3*, *4*). In Schwann cells, for example, IGF-1 functions primarily as a growth factor increasing cell mass, whereas glial growth factor (GGF) acts as a mitogen, inducing proliferation (*5*, *6*). Consequently, Schwann cell size can be manipulated through adjustment of the relative concentrations of IGF-1 and GGF in their environment. These findings caused some to conclude that in proliferating animal cells, growth and cell-cycle progression are independent pro-

cesses, each governed by extracellular cues. According to this view, size itself is not actively controlled but merely results from the independent control of the rates of cell growth and cell division.

Although it is clear that extracellular growth factors and mitogens can trigger changes in cell size, such cues do not account for how cell-size variance is constrained to achieve the uniformity in cell size that is typically seen in tissues (Fig. 2). These extracellular signals can dictate the mean size of cells, but individual cells will still deviate from that mean. Variability in cell size can arise from variability in growth rate and cell-cycle length, or asymmetry in cell division. These sources of inevitable variation raise the question of whether there are cellular mechanisms that might act to increase size homogeneity. Size variation can only be reduced with processes that differentially affect cells of different sizes, despite the fact that they share the same environment. Such a process could reduce heterogeneity by eliminating cells that deviate widely from the mean, through cell death or differentiation. Alternatively, a size-discriminatory process could force large cells to accumulate less mass than small ones, in response to identical extracellular signals. This kind of control requires a mechanism by which individual cells measure their own size and adjust their cell-cycle length, growth rate, or both, as necessary to achieve a common target size. In

this Review, we will discuss a growing body of evidence that such mechanisms exist and address the following questions: (i) Do animal cells have mechanisms to autonomously measure and adjust their individual sizes? (ii) Does the presence of such mechanisms indicate that there is an optimal cell size for a particular cell's function?

Our discussion of cell-size control will focus on proliferating populations of cells, which have been more extensively studied in this context, although many of the issues raised are relevant in nonproliferating tissues as well.

Ways to limit heterogeneity in cell size

In proliferating cells, size variability can be constrained if cells progress through the cell cycle in a size-dependent manner (Fig. 3A). Cells that are born small would have more time to grow before their next division, as compared with oversized cells, which would divide more quickly. Several groups have suggested that mammalian cells have a size threshold for exit from the G_1 phase of the cell cycle (*7*–*9*), as has been observed in budding yeast (*10*). In order for a size threshold to work, cell size must be reported to the processes regulating the cell cycle. The "signal" could be the amount of a particular protein or protein modification, the distance between cytoskeletal features, or even the number or size of the cell's neighbors.

Instead of (or in addition to) changing their cell-cycle length in a size-dependent manner, cells could also reach their target size by adjusting their growth rate, so that small cells grow quickly and large cells grow slowly (Fig. 3B). This growth rate adjustment could be modulated by the sort of signals described above. Alternatively, the growth rate, and the final cell size, could be determined by a "balance point" of synthesis and degradation. If, for example, cells synthesize proteins at a fixed rate but degrade them at a rate that is proportional to their total cell size, net growth would slow as cell size increases. This is not a trivial condition because it requires that degradation depend on the total amount of protein in the cell, rather than the protein concentration.

Evidence for cell-autonomous size measurement

There is increasing evidence that cells autonomously regulate their size to reduce cell-size
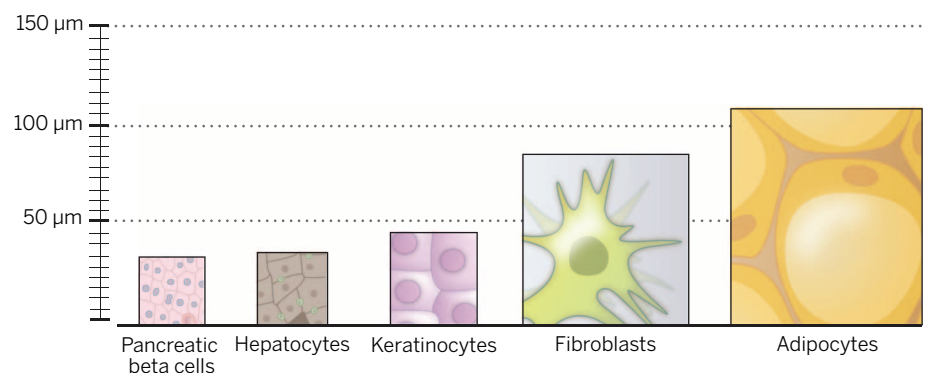
[1]Department of Systems Biology, Harvard Medical School, Boston, MA, USA. [2]The Hospital for Sick Children, Toronto, Canada.
*These authors contributed equally to this work. †Corresponding author. E-mail: marc@hms.harvard.edu

Fig. 1. Typical sizes of various human cell types. Cells are drawn to scale. Pancreatic β cells, hepatocytes, keratinocytes, fibroblasts, and adipocytes.

variation. In 1965, Killander and Zetterberg used interferometric microscopy to measure the dry mass of individual fibroblasts as a function of time since division (7). They reported that cells that had recently entered S phase were less variable in size than those in early G_1 (8). S phase entry appeared to be more heavily dependent on a cell's size than its age; cells entered S phase at similar sizes, whereas their age at S phase entry varied widely. These results suggested that there might be a cell-size threshold gating G_1 exit in animal cells. Killander et al. also showed that cells split into separate culture dishes often displayed slight difference in phenotypes, including cell size (7). When comparing cell size and cell-cycle distributions of different cultures, they noticed that populations with smaller average birth sizes had longer average G_1 lengths, so that cells exited G_1 at a similar size in all populations. They concluded that a critical cell mass is required for S phase entry (Fig. 4).

A dependence of G_1 length on cell size was also observed by Dolznig et al. (9). They engineered avian erythroblasts to proliferate in the absence of cytokines, under control of a viral constitutively active EGF-R1, v-ErbB. When v-ErbB signaling was blocked with an EGF-R inhibitor, and the cells were supplied with the appropriate cytokines, they proliferated under the control of their physiological receptors, c-Kit and EpoR. Cells were substantially larger when driven by v-ErbB than they were during c-Kit/EpoR–driven proliferation. Dolznig et al. monitored the cell-cycle distribution after switching cells from v-ErbB– to c-Kit/EpoR–driven proliferation. They reasoned that if there is a size threshold that is lowered in c-Kit/EpoR–driven proliferation, the first cell cycle after the switch should be shorter than subsequent cycles. This expectation was fulfilled, suggesting that there is a size threshold at G_1 exit that is influenced by extracellular conditions. Whereas the results of Killander and Zetterberg can be explained by a correlation between G_1 length and size at any point in G_1, Dolznig's work suggests that a true size threshold restricts G_1 exit. Notably, Echave et al. (11) transferred Schwann cells from 3% serum (in which they maintain a large size) to serum-free medium (in which they are small) and failed to see a shortening of the first cell cycle. This discrepancy may be attributable to differences in experimental conditions or cell type.

Kafri et al. provided evidence of a size-discriminatory process that reduces variability in cell mass (assayed by protein staining) at G_1 exit in several normal and transformed cell lines (12). To reveal the coordination of growth and cell-cycle progression, using fixed unsynchronized cell preparations, they applied a fundamental statistical principle: In an unsynchronized population of cells, the proportion of cells characterized by a certain property or phenotype is a function of the duration of the events during the cell cycle in which that phenotype is expressed. Specifically, if cells of a given size and cell cycle position are underrepresented in the population, those cells must either grow or progress through that stage of the cell cycle more rapidly. On the

basis of this "ergodic rate analysis" (ERA) of large populations captured in a single image, they detected a prominent fingerprint of feedback regulation. In late G_1, large cells are distinguished from small cells in a process that causes large cells to accumulate less mass than smaller ones, decreasing size heterogeneity in the population. Their conclusions were consistent with either of two possibilities: a faster growth rate or a longer duration of G_1 for smaller cells.

A major source of variation in size is variation in the rates at which individual cells grow. Growth rates of individual cells are very hard to measure, requiring methods for resolving small differences

in mass (a fraction of the mass of a single cell). To address this problem, Manalis and colleagues developed a microfluidic resonator that measures the buoyant mass of single cells with exquisite accuracy, enabling measurement of the instantaneous growth rate of a cell with a resolution of ~3 min (13). Their experiments on mouse lymphocyte precursors provided the first highly accurate, direct measurements of growth curves of single cells (14). They observed a convergence of the variable growth rates of individual cells as they approach the end of G_1. At birth, there are large disparities in growth rate among individual cells in the population, and as cells progress
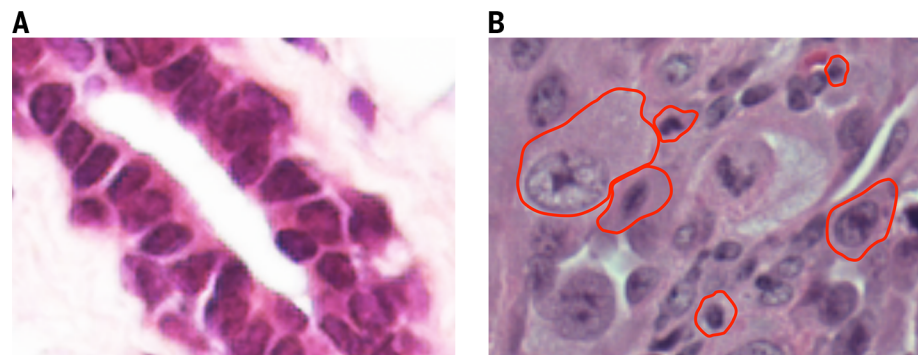
Fig. 2. Cell-size uniformity in a healthy mammary epithelium compared with a pleomorphic mammary tumor. (**A**) Hematoxylin-and-eosin staining across a duct of a normal mouse mammary gland illustrates the uniformity in cell size that is typical of epithelial tissues. [Image courtesy of S. Wang and E. Zacksenhaus (Toronto General Hospital)] (**B**) A pleomorphic mammary tumor exhibits extreme disparities in cell size. Tumor section was collected from a xenograft of mammary epithelial cells transformed with LT, hTERT, and H-rasV12. To highlight the size heterogeneity in the pleomorphic tumor, borders of several cells varying in size were manually outlined (red).
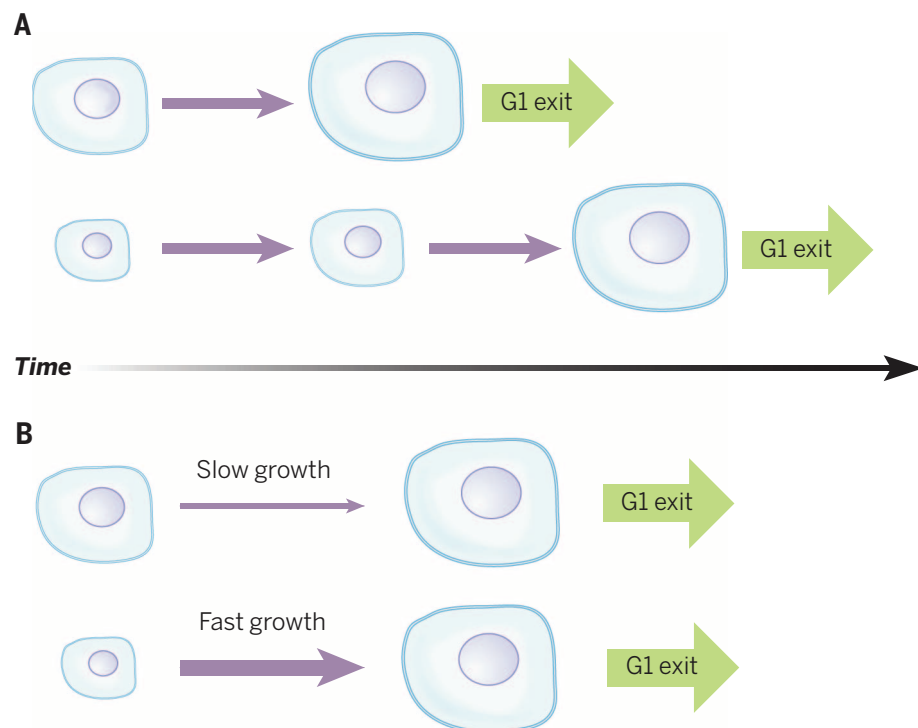
Fig. 3. Size control strategies. To exit G_1 with the appropriate size, cells can adjust either (**A**) the amount of time spent in G_1 or (**B**) the rate at which they grow.

through the cell cycle, their growth rates continuously increase, creating more disparity. However, in these cells G$_1$ length is inversely proportional to a cell's initial rate of growth, not size. Slower growing cells are held in G$_1$, allowing them more time to accelerate their growth, so that all cells exit G$_1$ with similar growth rates. These results suggest that a growth-rate threshold gates G$_1$ exit. Such a mechanism would reduce the rate at which variation builds up during cell growth by both allowing slower growing cells more time to grow between divisions and reducing growth-rate disparities. An alternative possibility consistent with these observations is that cells measure not their rate of growth, but the amount of mass accumulated since birth. This possibility is supported by recent studies of bacterial cell growth (15).

For many investigators in the past few decades, the question of whether cells regulate their own size was tied to another, more abstract question: Do cells grow with linear or exponential kinetics (16–20)? At first glance, the latter question may seem to have little biological relevance. But upon closer examination, a distinction between these models carries major implications. With exponential growth, larger cells grow faster than do smaller cells, amplifying any existing size disparities in proliferating populations. Therefore, evidence that cells grow exponentially, and are expected to diverge in size, would suggest that regulatory mechanisms exist to counterbalance this effect and maintain size homeostasis.

Despite the elegance of this claim, to actually distinguish exponential from linear kinetics requires measurements of cell size with an error smaller than 6% (21), a resolution that was technologically unavailable until recently. Ingeniously circumventing this challenge, in 1963 Collins and Richmond (22) published a method to calculate growth kinetics from three static size distributions: a distribution of newborn cells, dividing cells, and an unsynchronized population. Intuitively, if one observes very few cells in the unsynchronized population with a particular size, this might be because (i) cells of this size grow very quickly (and spend very little time at this

volume), (ii) most newborn cells are larger than this, or (iii) most cells divide before reaching this size. By comparing the three size distributions in the Collins-Richmond relation, the effects of (ii) and (iii) can be estimated, and one can infer the average growth rate for cells of any given size. The most difficult aspect of applying the Collins-Richmond method is measuring the sizes of newborn and dividing cells. This challenge was overcome in 2009 (21) by culturing mouse lymphoblasts that were loosely attached to a membrane, so that one daughter cell from every mitosis was released, and the volumes of these newborn cells were measured via Coulter counter. The size distribution of dividing cells was inferred by assuming that the volume of a cell just before division is the same as the total volume of the two resulting newborns.

Applying the Collins-Richmond equation to the measured cell-volume distributions revealed that growth kinetics are more complex than either the linear or the exponential models. Overall, lymphoblast growth rates do increase with cell size, upholding the exponential growth model, although this trend is reversed in the very largest of cells. Additionally, during early G$_1$ the growth of all cells accelerates faster than predicted by either model. The extent of this complexity was further revealed by the newly developed methods described above (12, 14), which detailed how growth kinetics vary over the course of the cell cycle.

The finding that growth is size-dependent during much of the cell cycle suggested that lymphoblasts must have a robust size-control mechanism. To investigate this possibility, the authors tracked the size distribution of a synchronized population of cells over several cycles. They found that for cells of equal age, the larger is more likely to divide. Similarly, for two cells of equal size the older cell is more likely to divide. This implies that lymphoblast division is regulated by both cell size and age—that both a "sizer" and a "timer" are involved.

How can a cell measure its own size?

Although changes in cell size are easily induced by extracellular conditions, such as growth factor

levels, cells of different types in a common environment display characteristic and distinctive sizes. It is clear that different cell types respond to the same signals in different ways, so that their size distinction is preserved. The combination of a cell's differentiation state and the composition of its environment specify the particular target size it will maintain. The uniformity in cell size of most cell types suggests that single cells sense their individual size in relation to this target size. Perhaps the most intriguing aspect of such a regulatory mechanism is that both the cell's target size and its actual size must be evaluated on absolute rather than relative scales. This type of absolute size measurement has been proposed to occur in keratinocytes, which differentiate only at diameters between 12 and 14 μm (23).

How can individual cells assess their size on an absolute, rather than a relative, scale? Researchers studying size control in the fission yeast, *Schizosaccharomyces pombe*, proposed that a physical basis for size sensing is an intracellular gradient of the mitotic inhibitor Pom1, whose concentration is high at the cell ends and decreases toward the cell center (24–26). As the *S. pombe* cell grows by elongation, a Pom1-depleted region is established at its center and plays a role in triggering mitosis. The concentration profile of intracellular Pom1 was proposed to serve as a ruler marking the distance between the cell tips. More recent work, showing that cells maintain size homeostasis even in the absence of Pom1, led others to conclude that the Pom1 gradient is not the direct size sensor responsible for the negative correlation between cell size at birth and cell-cycle length (27). However, Pom1 does modulate the absolute size for mitotic entry, possibly by preventing mitosis near cell ends, ensuring a minimum cell length. In this example, the link between cell-cycle progression and cell size is thought to be the kinetics of a reaction-diffusion system. Despite the fact that most cells lack the morphological simplicity of the rod-shaped *S. pombe*, it is possible that such intracellular gradients serve as cellular "rulers" in many contexts.

The observation that growth rates of lymphocyte precursors converge at G$_1$ exit raises the possibility that a target growth rate, and not a target size, is required for cell-cycle progression, and that individual cells measure their own rates of growth. There is evidence that this type of mechanism is active in the budding yeast *Saccharomyces cerevisiae*, in which cells must achieve a threshold protein synthesis rate before progressing through G$_1$ to S phase. There is a well-established link between growth and G$_1$/S progression in *S. cerevisiae* [a comprehensive review is availabe in (28)], which is reflected in the negative correlation between cell size at birth and G$_1$ duration (29). Di Talia *et al.* showed that size control is imposed during the earlier part of G$_1$ and depends on the G$_1$ cyclin Cln3, whereas the late events of G$_1$ are size-independent (29). In small cells, G$_1$ is lengthened, allowing cells to approach a "size threshold" before passing "Start" and subsequently exiting G$_1$. In *S. cerevisiae* cells, growth rate is proportional to size (29), so a growth-rate threshold

Fig. 4. In populations of proliferating cells, size uniformity may be ensured by linking the processes of growth and cell-cycle progression. One way this can be accomplished is by restricting progress through a particular cell-cycle stage (for example, the G$_1$/S transition) to cells that have reached a specific "target" size.
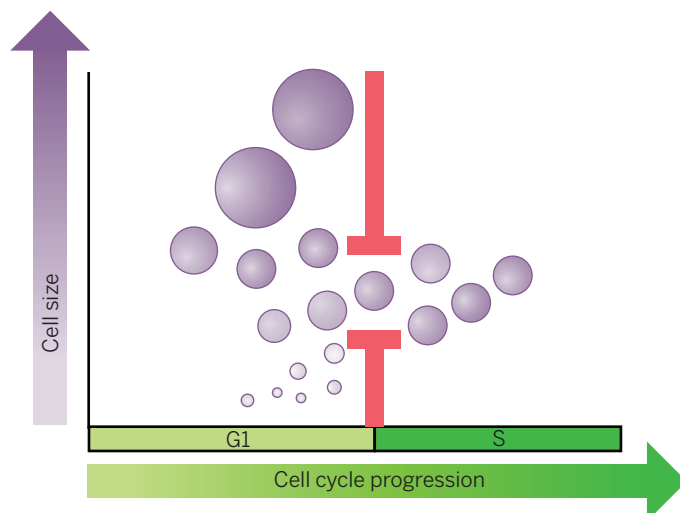
gating G_1 exit would give the appearance of a size threshold.

Cln3 has been implicated as a sensor of the rate of protein synthesis (30, 31). Cln3 is a rate-limiting determinant of G_1 exit; mutants with highly abundant Cln3 have a shorter G_1 and smaller size than that of wild-type cells (32). The link between cell growth and G_1 exit may lie in the CLN3 5′ untranslated region, where an open reading frame allows appreciable Cln3 synthesis only when there are sufficient ribosomes to bypass the block. Because this leaky scanning mechanism is inefficient, Cln3 synthesis requires a minimum rate of protein translation (30). Because Cln3 is highly unstable (32), its abundance at any given time is indicative of the current translation rate. This work suggests that in budding yeast, cell-cycle entry is regulated by a threshold on the overall rate of protein synthesis. A similar threshold has been proposed to regulate mitotic entry. Both cdc25 (a dosage dependent activator of mitosis) and the G_2/M cyclin cdc13 mRNAs have long 5′ untranslated regions containing open reading frames, rendering their levels particularly sensitive to the rate of translation initiation (33).

Cln3 promotes cell-cycle progression by relieving inhibition of the transcription factor SBF (SCB binding factor), activating the transcription of many cell-cycle genes, including downstream G_1 cyclins Cln1 and Cln2. These cyclins further activate SBF, triggering a positive feedback loop that ensures an irreversible commitment to the cell cycle ("Start") (34–36). Among its other modes of action, Cln3 localizes to SBF binding sites in the CLN2 promoter, where it releases SBF inhibitor Whi5 (31). Titration of Cln3 against the fixed number of SBF binding sites in the genome may be the means by which the cell senses the total amount of Cln3, despite the increasing volume of the cell that is expected to stabilize Cln3 concentration (31).

In vertebrate systems, cyclin E is functionally homologous to the yeast Cln3. Expression of human cyclin E can compensate for loss of Cln3 in yeast lacking all G_1 cyclins (37). Active cyclin E activates Cdk2, promoting G_1 exit and the onset of the cell-division cycle. In line with its roles in the cell cycle, cyclin E overexpression shortens G_1, resulting in a decreased cell size (38, 39).

The idea that cyclin E might serve as sensor of protein translation rate, analogous to Cln3, was first proposed by Edgar and Neufeld (39) in their work on growth of the *Drosophila* wing disc. Like Cln3, the *Drosophila* cyclin E contains several open reading frames in its 5′ untranslated region (40). Ras activation, which increases cell size and growth rates, was found to cause a posttranscriptional increase in cyclin E levels, promoting G_1/S progression (41).

Similarly, in mammalian hepatocytes cyclin E abundance correlates more strongly with cell growth than with cell-cycle progression (42–44). Transfecting hepatocytes with cyclin D causes proliferation 1 day after treatment. Six days later, hepatocytes show little proliferation but increased growth. Although the amount of cyclin E mRNA is highly increased during the earlier proliferative phase, a large increase in the cyclin E protein abundance occurs only later, with cell growth. The fact that translation, but not transcription, of cyclin E is correlated with cell growth suggests that it might serve as a translation rate sensor. However, because of the correlative nature of these findings, further investigation is still needed to determine whether cyclin E truly links cell growth to cell-cycle progression. Another potential translation rate sensor is the E2F1 transcription factor. E2F1 drives endocycles in *Drosophila* salivary cells by promoting cyclin E expression and S phase entry, and translational control of E2F1 was found to couple rates of endocycle progression to cellular growth rates (45).

Physiological consequences of cell size

Why would cells need a mechanism with which to specify and fine-tune their individual sizes? For certain cells, there is an obvious association between a cell's function and its physical dimensions. Neurons, for example, must span the distance across which they relay information. Yet for the majority of cell types, whether epithelial or mesenchymal, the advantage of a specific size is not obvious. A famous 1945 study by Fankhauser documents the effects of the increased cell size in polyploid salamander larvae on the formation of various multicellular structures, such as pronephric tubules (46). In many organs, the shape and dimensions of these structures are unchanged, with a decrease in cell number compensating for the increase in cell size. In pentaploid larvae, this compensation meant that the circumference of pronephric tubules and ducts was often spanned by just a single cell. The fact that normal structures could be formed even with large alterations in cell size suggested that for many cell types, a cell's size is not imposed by its role as the structural unit of the organism. Notable exceptions to this trend include the observation that cell size influences the size and morphological complexity of the brain (47).

There is some indication that a cell's size is commonly related to its physiology; some cells change their size in response to external cues. For example, kidney epithelial cells modulate their size in response to rates of fluid flow in the nephron ducts, sensed by mechanical shear on the primary cilium (48). Cell size also often changes during differentiation. Lymphocytes, for instance, rapidly grow to a larger size after exposure to cytokines or Toll-like receptor stimulation (49). However, in these cases it is not clear whether size is the target of regulation or a by-product of some other adaptation.

A change in organ size, when demanded by physiology, can be accomplished through a change in cell number, a change in cell size, or both. The choice of modulating organ growth through cell growth or proliferation is often context-dependent. Pancreatic β cells, for example, increase their size by over 25% during pregnancy, in response to increased insulin demand (50). However, the insulin demand resulting from β cell death leads to increased proliferation of β cells, without changing their size (50). Similarly, liver size increases during pregnancy through hepatocyte hypertrophy, whereas liver regeneration after surgical resection occurs through increased hepatocyte proliferation. These examples suggest that under particular physiological conditions, it might be advantageous for a specific cell to have a specific size. This raises the question, do cells function most efficiently when at the "right" size?

Because cells have multiple roles, a cell's "function" is hard to define, and its functional efficiency is hard to quantify. Another difficulty is that for most cell types, size has not been a primary focus of investigation. Consequently, literature that systematically quantifies cell size and relates it to cell behavior is sparse. An exception to this rule is the case of the pancreatic β cell. Insulin secretion is associated with β cell mass, so the size of β cells has been the subject of much research. To a simple approximation, a β cell may be described as a device that performs one main function—secretion of insulin in response to increases in blood glucose—and this process can be measured quantitatively. For these reasons, we will examine the evidence of a size-function relationship in β cells, with the hope that this discussion will stimulate similar investigations of other cell types.

Giordano *et al.* found that the rate of insulin production of individual rat β cells is more strongly correlated with cell size than with metabolic activity as assayed by means of NADPH (reduced form of nicotinamide adenine dinucleotide phosphate) fluorescence (51). In fact, in cultured rat β cells, insulin secretion, metabolic activity, and global rates of protein production are all correlated with cell size. These correlations are further reinforced in transgenic mice harboring mutations that affect cell size. For example, β cells of mice lacking S6K1 are reduced in size (52, 53). These small β cells secrete less insulin per cell than do normal β cells, possibly because of the reduction in membrane surface available, leading to hypoinsulinemia. In contrast, rapamycin treatment of wild-type β cells, which reduces S6K1 activity but does not change β cell size, does not affect insulin secretion, indicating that the reduced insulin secretion results from a size defect rather than the absence of S6K1 (52).

Additional studies suggest that there is an optimal size for maximum efficiency of insulin secretion. Like mice in which S6K1 has been knocked out, mice expressing only a mutant, nonphosphorylatable ribosomal protein S6 have small β cells (54–56). However, in these mutants, the cell-size defect is compensated by increased cell number, so that their total β cell mass is similar to that of wild-type mice. Despite this rough conservation of bulk mass, these mutants are still hypoinsulinemic, suggesting that small cells are disproportionately less efficient insulin producers than are normal-sized cells. Furthermore, mice expressing constitutively active protein kinase Akt1 have larger β cells than those of wild-type mice and an increased rate of insulin secretion (57). However, insulin secretory capacity per unit of β cell mass is lower. A persistent hyperinsulinemia in these transgenic mice may indicate inefficiency in hormone regulation. These results suggest that β cell function may be impaired in cells

that are either larger or smaller than their target size. A caveat to this interpretation comes from the pleiotrophic effects of pathways such as mammalian target of rapamycin (mTOR), mitogen-activated protein kinase (MAPK), and phosphatidylinositol 3-kinase (PI3K), pathways that, in addition to affecting cell size, can regulate many other functions. Hence, it is hard to know whether a change in size actually causes a change in function or is simply correlated with it.

Another case in which evidence may suggest an optimal cell-size criterion is that of mammalian adipocytes. Clear differences in gene expression between large and small adipocytes suggest that cell size influences adipocyte biology (58, 59). One explanation for this effect is that cellular enlargement, by increasing cell surface area and modifying interactions between the cell and its extracellular matrix, activates the β_1-integrin/extracellular signal–regulated kinase (ERK) signaling pathway that modulates several transcription factors (59). Large adipocytes display a marked increase in the activity of fatty acid synthase and lipoprotein lipase. These changes are further manifested in the altered metabolic activity of large adipocytes. For example, Smith et al. compared large and small adipocytes isolated from the same specimen of human adipose tissue (60, 61) and found that large adipocytes have higher rates of lipid synthesis. This increase in lipogenesis rate is still evident when measurements are normalized to cell size, meaning that large cells are disproportionally more productive than are small cells. Changes in cell size have also been linked to transcriptional and metabolic changes in other cell types, including hepatocytes and erythrocytes (62–65).

However, the increased metabolic efficiency of large adipocytes comes at a price. Larger cells are less sensitive to the stimulating effects of insulin on glucose uptake, the oxidation of glucose to CO_2 (66), and the uptake of triglyceride fatty acids (67). These defects may result from the stress of adipocyte enlargement against the physical constraints imposed by collagen and the extracellular matrix (68). The balance between metabolic capacity that scales positively with adipocyte size and insulin sensitivity that scales negatively with size implies an optimal adipocyte size. Supporting this idea, increased adipocyte size, rather than total body fat, is associated with insulin resistance in obesity and is a risk factor for development of type II diabetes mellitus (69).

Several lines of research have suggested an interesting link between the regulation of cell-size variability and the pathology of cancer, although the systematic studies needed to confirm this link are still lacking. Although cancer is a disease of deregulated proliferation, in clinical histology it is the size of cancer cells that renders their appearance distinct from the surrounding tissue (70). Malignant tumor cells are both larger and more variable in size than normal cells. Pleomorphism, the increased variability in cell size and shape, is a histological characteristic of many malignant lesions (71–73) and is sometimes used as a criterion for the determination of histologic grade. The loss of cell-size regularity in cancer cells also occurs when cell lines of normal and neoplastic origin are grown in matching culture conditions, indicating that the increased size variability in cancer is cell-autonomous and not a product of the tumor microenvironment (74). Furthermore, when epidermoid carcinoma cell lines were classified according to cell-size variability, only the highly heterogeneous lines initiated tumors upon heterotransplatation into mice (74). These experiments raise the question of whether aberrant regulation of cell size has a role in tumorigenesis, although increased cell size variability may also be a mere correlate of tumor biology (perhaps the result of aneuploidy), and further experiments are warranted to resolve this conflict.

Questions, challenges, suggestions

Early cell-cycle research featured a debate over whether the cell cycle was the result of a linear cascade of interdependent events, with early events providing substrates essential for later ones, or whether there was an independent master regulator of the cell cycle—a cell cycle clock (75). Investigations of cell size now face a similar dilemma. Is the size of a cell simply the by-product of its rate of growth and frequency of division? Or is there a master regulator that independently specifies cell size on the basis of a cell's function and physiological needs? The evidence reviewed above suggests that there is a separate and at least partially independent pathway for cell-size regulation.

Almost exclusively, studies of size regulation have focused on the possibility of a size checkpoint, an event that regulates either G_1 exit or cell division on the basis of cell size. The checkpoint model posits that the size of a cell is specified by adjusting the amount of time during which it grows. Lengthening G_1 would increase the amount of time in which a cell grows, resulting in an increased cell size. This possibility is grounded in observations from yeast biology (10). Yet, there is also an alternative class of mechanisms that can just as easily dictate cell size. Instead of regulating the amount of time during which they grow, cells may regulate the rate at which they accumulate mass. To limit size disparity, small cells could accelerate their growth rate, or large cells could decelerate it. This alternative has remained unexplored, largely because of the difficulty of making precise measurements of cell growth.

If individual cells were to specify their size by modulating their growth rates rather than their cell-cycle length, a cell's overall synthetic machinery would have to be fine-tuned to reflect its size. In other words, there would have to be feedback linking a cell's physical dimensions to its anabolic control. The identification of such a mechanism would substantially alter the way we understand growth control. We would need to expand the simple and intuitive model of a discrete size checkpoint to include the continuous modulation of growth rates.

It has been over 150 years since Virchow wrote, "omnis cellula e cellula," giving us a very modern concept of the cell; since that time, the problem of how cell size is regulated has been staring us in the face. Today, we have only achieved a partial phenomenological explanation of cell-size homeostasis. Why has it been so difficult? Despite the simplicity of size as a phenotype, its study is inherently challenging. The specific size of a cell is an outcome of numerous and diverse processes. Accumulation of cell mass is directly related to a cell's metabolic and anabolic activity, as well as protein turnover and autophagy. In proliferating populations, cell size reflects a balance between growth and division. In some cases, size is also affected by a cell's state of differentiation and physiological conditions. For this reason, it is hard to establish whether a mutation or chemical perturbation that affects cell size is associated with size control per se. In a screen for cell-size mutants, Jorgensen et al. pointed out this problem, stating that an increase in the mean cell size in a population could reflect a shift to later cell-cycle stages, rather than abnormal growth (76). Additionally, a change in rates of cell division could increase or decrease cell size, even if growth rates remain unchanged. In retrospect, chemical composition yielded to biochemical investigation more readily than did integrated mechanisms such as growth, shape, motility, and behavior. Whereas genetics could point us to processes that affect size, it could not easily disentangle contributions from nutrition, biogenesis, differentiation, and cell division. But most importantly, we had only the crudest quantitative measures for the very processes we wished to study at the single-cell level: growth and size.

The advances in recent years, summarized above, have provided evidence that growth and cell-cycle progression are coordinated in proliferating cells. Confident that we are not merely studying the wake behind the boat, but that real circuits exist to precisely specify cell size, we can confront the underlying molecular circuitry and explore its biological consequences. We have interesting questions to address. How is the mean cell size established for each lineage? How do cells adapt to external stimuli to change the set point for their size? How does each cell measure its size and assess its deviation from the mean? By what mechanism do proliferating cells alter their rates of growth or passage through the cell cycle to prevent the natural accumulation of size variability? How do size changes affect cell function, and do certain cells function best at a given size? What role does cell size play in pathology and senescence? Haldane reminded us of the importance of size at the organism level in his lively essay, " On being the right size" (77). Biologists who have reveled in the qualitative complexity of cells might take new inspiration from the simple process of size control; it is certain to have deep consequences and fascinating explanations.

REFERENCES AND NOTES

1. E. B. Wilson, *The Cell in Development and Heredity* (Macmillan, New York, ed. 3, 1925), p. xxxvii.
2. K. L. Cooper et al., Multiple phases of chondrocyte enlargement underlie differences in skeletal proportions.

Nature **495**, 375–378 (2013). doi: 10.1038/nature11940; pmid: 23485973

3. A. Zetterberg, W. Engström, E. Dafgård, The relative effects of different types of growth factors on DNA replication, mitosis, and cellular enlargement. *Cytometry* **5**, 368–375 (1984). doi: 10.1002/cyto.990050413; pmid: 6380994

4. A. Zetterberg, O. Larsson, Coordination between cell growth and cell cycle transit in animal cells. *Cold Spring Harb. Symp. Quant. Biol.* **56**, 137–147 (1991). doi: 10.1101/SQB.1991.056.01.018; pmid: 1819483

5. I. J. Conlon, G. A. Dunn, A. W. Mudge, M. C. Raff, Extracellular control of cell size. *Nat. Cell Biol.* **3**, 918–921 (2001). doi: 10.1038/ncb1001-918; pmid: 11584274

6. M. N. Hall, M. C. Raff, G. Thomas, *Cell Growth: Control of Cell Size* (Cold Spring Harbor Laboratory Press, Cold Spring Harbor, NY, 2004), pp. xii.

7. D. Killander, A. Zetterberg, A quantitative cytochemical investigation of the relationship between cell mass and initiation of DNA synthesis in mouse fibroblasts in vitro. *Exp. Cell Res.* **40**, 12–20 (1965). doi: 10.1016/0014-4827(65)90285-5; pmid: 5838935

8. D. Killander, A. Zetterberg, Quantitative cytochemical studies on interphase growth. I. Determination of DNA, RNA and mass content of age determined mouse fibroblasts in vitro and of intercellular variation in generation time. *Exp. Cell Res.* **38**, 272–284 (1965). doi: 10.1016/0014-4827(65)90403-9; pmid: 14284508

9. H. Dolznig, F. Grebien, T. Sauer, H. Beug, E. W. Müllner, Evidence for a size-sensing mechanism in animal cells. *Nat. Cell Biol.* **6**, 899–905 (2004). doi: 10.1038/ncb1166; pmid: 15322555

10. G. C. Johnston, J. R. Pringle, L. H. Hartwell, Coordination of growth with cell division in the yeast *Saccharomyces cerevisiae*. *Exp. Cell Res.* **105**, 79–98 (1977). doi: 10.1016/0014-4827(77)90154-9; pmid: 320023

11. P. Echave, I. J. Conlon, A. C. Lloyd, Cell size regulation in mammalian cells. *Cell Cycle* **6**, 218–224 (2007). doi: 10.4161/cc.6.2.3744; pmid: 17245129

12. R. Kafri *et al.*, Dynamics extracted from fixed cells reveal feedback linking cell growth to cell cycle. *Nature* **494**, 480–483 (2013). doi: 10.1038/nature11897; pmid: 23446419

13. T. P. Burg *et al.*, Weighing of biomolecules, single cells and single nanoparticles in fluid. *Nature* **446**, 1066–1069 (2007). doi: 10.1038/nature05741; pmid: 17460669

14. S. Son *et al.*, Direct observation of mammalian cell growth and size regulation. *Nat. Methods* **9**, 910–912 (2012). doi: 10.1038/nmeth.2133; pmid: 22863882

15. S. Taheri-Araghi *et al.*, Cell-size control and homeostasis in bacteria. *Curr. Biol.* **25**, 385–391 (2015).

16. I. Conlon, M. Raff, Differences in the way a mammalian cell and yeast cells coordinate cell growth and cell-cycle progression. *J. Biol.* **2**, 7 (2003). doi: 10.1186/1475-4924-2-7; pmid: 12733998

17. I. Conlon, M. Raff, Control and maintenance of mammalian cell size: Response. *BMC Cell Biol.* **5**, 36 (2004). doi: 10.1186/1471-2121-5-36; pmid: 15458578

18. S. Cooper, Control and maintenance of mammalian cell size. *BMC Cell Biol.* **5**, 35 (2004). doi: 10.1186/1471-2121-5-35; pmid: 15456512

19. H. E. Kubitschek, K. B. Clay, A second growth state for *Schizosaccharomyces pombe*. *Exp. Cell Res.* **165**, 243–254 (1986). doi: 10.1016/0014-4827(86)90548-3; pmid: 3709687

20. E. C. Anderson, G. I. Bell, D. F. Petersen, R. A. Tobey, Cell growth and division. IV. Determination of volume growth rate and division probability. *Biophys. J.* **9**, 246–263 (1969). doi: 10.1016/S0006-3495(69)86383-6; pmid: 5764232

21. A. Tzur, R. Kafri, V. S. LeBleu, G. Lahav, M. W. Kirschner, Cell growth and size homeostasis in proliferating animal cells. *Science* **325**, 167–171 (2009). doi: 10.1126/science.1174294; pmid: 19589995

22. J. F. Collins, M. H. Richmond, Rate of growth of *Bacillus cereus* between divisions. *J. Gen. Microbiol.* **28**, 15–33 (1962). doi: 10.1099/00221287-28-1-15; pmid: 13880594

23. Y. Barrandon, H. Green, Cell size as a determinant of the clone-forming ability of human keratinocytes. *Proc. Natl. Acad. Sci. U.S.A.* **82**, 5390–5394 (1985). doi: 10.1073/pnas.82.16.5390; pmid: 2410922

24. S. G. Martin, Geometric control of the cell cycle. *Cell Cycle* **8**, 3643–3647 (2009). doi: 10.4161/cc.8.22.9891; pmid: 19844171

25. S. G. Martin, M. Berthelot-Grosjean, Polar gradients of the DYRK-family kinase Pom1 couple cell length with the cell cycle. *Nature* **459**, 852–856 (2009). doi: 10.1038/nature08054; pmid: 19474792

26. J. B. Moseley, A. Mayeux, A. Paoletti, P. Nurse, A spatial gradient coordinates cell size and mitotic entry in fission yeast.

Nature **459**, 857–860 (2009). doi: 10.1038/nature08074; pmid: 19474789

27. E. Wood, P. Nurse, Pom1 and cell size homeostasis in fission yeast. *Cell Cycle* **12**, 3228–3236 (2013). doi: 10.4161/cc.26462; pmid: 24047646

28. J. J. Turner, J. C. Ewald, J. M. Skotheim, Cell size control in yeast. *Curr. Biol.* **22**, R350–R359 (2012). doi: 10.1016/j.cub.2012.02.041; pmid: 22575477

29. S. Di Talia, J. M. Skotheim, J. M. Bean, E. D. Siggia, F. R. Cross, The effects of molecular noise and size control on variability in the budding yeast cell cycle. *Nature* **448**, 947–951 (2007). doi: 10.1038/nature06072; pmid: 17713537

30. M. Polymenis, E. V. Schmidt, Coupling of cell division to cell growth by translational control of the G1 cyclin CLN3 in yeast. *Genes Dev.* **11**, 2522–2531 (1997). doi: 10.1101/gad.11.19.2522; pmid: 9334317

31. H. Wang, L. B. Carey, Y. Cai, H. Wijnen, B. Futcher, Recruitment of Cln3 cyclin to promoters controls cell cycle entry via histone deacetylase and other targets. *PLOS Biol.* **7**, e1000189 (2009). doi: 10.1371/journal.pbio.1000189; pmid: 19823669

32. M. Tyers, G. Tokiwa, R. Nash, B. Futcher, The Cln3-Cdc28 kinase complex of *S. cerevisiae* is regulated by proteolysis and phosphorylation. *EMBO J.* **11**, 1773–1784 (1992). pmid: 1316273

33. R. R. Daga, J. Jimenez, Translational control of the cdc25 cell cycle phosphatase: A molecular mechanism coupling mitosis to cell growth. *J. Cell Sci.* **112**, 3137–3146 (1999). pmid: 10462529

34. G. Charvin, C. Oikonomou, E. D. Siggia, F. R. Cross, Origin of irreversibility of cell cycle start in budding yeast. *PLOS Biol.* **8**, e1000284 (2010). doi: 10.1371/journal.pbio.1000284; pmid: 20887490

35. L. Dirick, K. Nasmyth, Positive feedback in the activation of G1 cyclins in yeast. *Nature* **351**, 754–757 (1991). doi: 10.1038/351754a0; pmid: 1829507

36. J. M. Skotheim, S. Di Talia, E. D. Siggia, F. R. Cross, Positive feedback of G1 cyclins ensures coherent cell cycle entry. *Nature* **454**, 291–296 (2008). doi: 10.1038/nature07118; pmid: 18633409

37. D. J. Lew, V. Dulic, S. I. Reed, Isolation of three novel human cyclins by rescue of G1 cyclin (Cln) function in yeast. *Cell* **66**, 1197–1206 (1991).

38. T. P. Neufeld, A. F. de la Cruz, L. A. Johnston, B. A. Edgar, Coordination of growth and cell division in the *Drosophila* wing. *Cell* **93**, 1183–1193 (1998). doi: 10.1016/S0092-8674(00)81462-2; pmid: 9657151

39. T. P. Neufeld, B. A. Edgar, Connections between growth and the cell cycle. *Curr. Opin. Cell Biol.* **10**, 784–790 (1998). doi: 10.1016/S0955-0674(98)80122-1; pmid: 9914170

40. H. E. Richardson, L. V. O'Keefe, S. I. Reed, R. Saint, A *Drosophila* G1-specific cyclin E homolog exhibits different modes of expression during embryogenesis. *Development* **119**, 673–690 (1993). pmid: 8187637

41. D. A. Prober, B. A. Edgar, Ras1 promotes cellular growth in the *Drosophila* wing. *Cell* **100**, 435–446 (2000). doi: 10.1016/S0092-8674(00)80679-0; pmid: 10693760

42. L. K. Mullany *et al.*, Akt-mediated liver growth promotes induction of cyclin E through a novel translational mechanism and a p21-mediated cell cycle arrest. *J. Biol. Chem.* **282**, 21244–21252 (2007). doi: 10.1074/jbc.M702110200; pmid: 17517888

43. C. J. Nelsen *et al.*, Induction of hepatocyte proliferation and liver hyperplasia by the targeted expression of cyclin E and skp2. *Oncogene* **20**, 1825–1831 (2001). doi: 10.1038/sj.onc.1204248; pmid: 11313930

44. C. J. Nelsen, D. G. Rickheim, N. A. Timchenko, M. W. Stanley, J. H. Albrecht, Transient expression of cyclin D1 is sufficient to promote hepatocyte replication and liver growth in vivo. *Cancer Res.* **61**, 8564–8568 (2001). pmid: 11731443

45. N. Zielke *et al.*, Control of *Drosophila* endocycles by E2F and CRL4(CDT2). *Nature* **480**, 123–127 (2011). doi: 10.1038/nature10579; pmid: 22037307

46. G. Fankhauser, Maintenance of normal structure in heteroploid salamander larvae, through compensation of changes in cell size by adjustment of cell number and cell shape. *J. Exp. Zool.* **100**, 445–455 (1945). doi: 10.1002/jez.1401000310; pmid: 21010861

47. G. Roth, J. Blanke, D. B. Wake, Cell size predicts morphological complexity in the brains of frogs and salamanders. *Proc. Natl. Acad. Sci. U.S.A.* **91**, 4796–4800 (1994). doi: 10.1073/pnas.91.11.4796; pmid: 8197137

48. C. Boehlke *et al.*, Primary cilia regulate mTORC1 activity and cell size through Lkb1. *Nat. Cell Biol.* **12**, 1115–1122 (2010). doi: 10.1038/ncb2117; pmid: 20972424

49. A. K. Abbas, A. H. Lichtman, S. Pillai, *Cellular and Molecular Immunology*. (Elsevier/Saunders, Philadelphia, ed. 7, 2012), pp. x.

50. S. Dhawan, S. Georgia, A. Bhushan, Formation and regeneration of the endocrine pancreas. *Curr. Opin. Cell Biol.* **19**, 634–645 (2007). doi: 10.1016/j.ceb.2007.09.015; pmid: 18061427

51. E. Giordano *et al.*, B-cell size influences glucose-stimulated insulin secretion. *Am. J. Physiol.* **265**, C358–C364 (1993). pmid: 8368265

52. M. Pende *et al.*, Hypoinsulinaemia, glucose intolerance and diminished beta-cell size in S6K1-deficient mice. *Nature* **408**, 994–997 (2000). doi: 10.1038/35050135; pmid: 11140689

53. M. C. Fabian, J. R. Lakey, R. V. Rajotte, N. M. Kneteman, The efficacy and toxicity of rapamycin in murine islet transplantation. In vitro and in vivo studies. *Transplantation* **56**, 1137–1141 (1993). doi: 10.1097/00007890-199311000-00017; pmid: 8249114

54. I. Ruvinsky *et al.*, Ribosomal protein S6 phosphorylation is a determinant of cell size and glucose homeostasis. *Genes Dev.* **19**, 2199–2211 (2005). doi: 10.1101/gad.351605; pmid: 16166381

55. I. Ruvinsky *et al.*, Mice deficient in ribosomal protein S6 phosphorylation suffer from muscle weakness that reflects a growth defect and energy deficit. *PLOS ONE* **4**, e5618 (2009). doi: 10.1371/journal.pone.0005618; pmid: 19470038

56. I. Ruvinsky, O. Meyuhas, Ribosomal protein S6 phosphorylation: From protein synthesis to cell size. *Trends Biochem. Sci.* **31**, 342–348 (2006). doi: 10.1016/j.tibs.2006.04.003; pmid: 16679021

57. E. Bernal-Mizrachi, W. Wen, S. Stahlhut, C. M. Welling, M. A. Permutt, Islet beta cell expression of constitutively active Akt1/PKB alpha induces striking hypertrophy, hyperplasia, and hyperinsulinemia. *J. Clin. Invest.* **108**, 1631–1638 (2001). doi: 10.1172/JCI200113785; pmid: 11733558

58. C. Farnier *et al.*, The signaling pathway for beta1-integrin/ERKs is involved in the adaptation of adipocyte functions to cell size. *Ann. N. Y. Acad. Sci.* **973**, 594–598 (2002). doi: 10.1111/j.1749-6632.2002.tb04706.x; pmid: 12485934

59. C. Farnier *et al.*, Adipocyte functions are modulated by cell size change: Potential involvement of an integrin/ERK signalling pathway. *Int. J. Obes. Relat. Metab. Disord.* **27**, 1178–1186 (2003). doi: 10.1038/sj.ijo.0802399; pmid: 14513065

60. U. Smith, Effect of cell size on lipid synthesis by human adipose tissue in vitro. *J. Lipid Res.* **12**, 65–70 (1971). pmid: 4322518

61. U. Smith, B. Jacobsson, Studies of human adipose tissue in culture. II. Effects of insulin and of medium glucose on lipolysis and cell size. *Anat. Rec.* **176**, 181–183 (1973). doi: 10.1002/ar.1091760206; pmid: 4711443

62. T. R. Gregory, A bird's-eye view of the C-value enigma: Genome size, cell size, and metabolic rate in the class aves. *Evolution* **56**, 121–130 (2002). doi: 10.1111/j.0014-3820.2002.tb00854.x; pmid: 11913657

63. T. P. Miettinen *et al.*, Identification of transcriptional and metabolic programs related to mammalian cell size. *Curr. Biol.* **24**, 598–608 (2014). doi: 10.1016/j.cub.2014.01.071; pmid: 24613310

64. S. Maciak, E. Bonda-Ostaszewska, M. Czarnołęski, M. Konarzewski, J. Kozłowski, Mice divergently selected for high and low basal metabolic rates evolved different cell size and organ mass. *J. Evol. Biol.* **27**, 478–487 (2014). doi: 10.1111/jeb.12306; pmid: 24417348

65. M. A. Monnickendam, M. Balls, The long-term organ culture of tissues from adult *Amphiuma*, the Congo eel. *J. Cell Sci.* **11**, 799–813 (1972). pmid: 4675179

66. L. B. Salans, S. J. Knittle, J. Hirsch, The role of adipose cell size and adipose tissue insulin sensitivity in the carbohydrate intolerance of human obesity. *J. Clin. Invest.* **47**, 153–165 (1968). doi: 10.1172/JCI105705; pmid: 16695937

67. P. J. Nestel, W. Austin, C. Foxman, Lipoprotein lipase content and triglyceride fatty acid uptake in adipose tissue of rats of differing body weights. *J. Lipid Res.* **10**, 383–387 (1969). pmid: 5797524

68. T. Khan *et al.*, Metabolic dysregulation and adipose tissue fibrosis: Role of collagen VI. *Mol. Cell. Biol.* **29**, 1575–1591 (2009). doi: 10.1128/MCB.01300-08; pmid: 19114551

69. A. Guilherme, J. V. Virbasius, V. Puri, M. P. Czech, Adipocyte dysfunctions linking obesity to insulin resistance and type 2 diabetes. *Nat. Rev. Mol. Cell Biol.* **9**, 367–377 (2008). doi: 10.1038/nrm2391; pmid: 18401346

70. D. W. Kufe, *Cancer Medicine 6 Review: A Companion to Holland-Frei Cancer Medicine-6.* (B.C. Decker, Hamilton, Ontario, 2003), pp. x.
71. G. Majno, I. Joris, *Cells, Tissues, and Disease: Principles of General Pathology* (Oxford Univ. Press, New York, ed. 2, 2004), pp. xxviii.
72. F. Moinfar, *Essentials of Diagnostic Breast Pathology: A Practical Approach* (Springer, New York, ed. 1, 2007).
73. E. Rubin, H. M. Reisner, *Essentials of Rubin's Pathology* (Wolters Kluwer Health/Lippincott Williams & Wilkins, Philadelphia, ed. 6, 2014), pp. xii.
74. T. Caspersson, G. E. Foley, D. Killander, G. Lomakka, Cytochemical differences between mammalian cell lines of normal and neoplastic origins. Correlation with heterotransplant-ability in Syrian hamsters. *Exp. Cell Res.* **32**, 553–565 (1963). doi: 10.1016/0014-4827(63)90193-9; pmid: 14099824
75. A. W. Murray, M. W. Kirschner, Dominoes and clocks: The union of two views of the cell cycle. *Science* **246**, 614–621 (1989). doi: 10.1126/science.2683077; pmid: 2683077
76. P. Jorgensen, J. L. Nishikawa, B. J. Breitkreutz, M. Tyers, Systematic identification of pathways that couple cell growth and division in yeast. *Science* **297**, 395–400 (2002). doi: 10.1126/science.1070850; pmid: 12089449
77. J. B. S. Haldane, *Possible Worlds and Other Essays* (Chatto & Windus, London, 1927), pp. viii.

RESEARCH ARTICLE SUMMARY

DEVELOPMENT ECONOMICS

A multifaceted program causes lasting progress for the very poor: Evidence from six countries

Abhijit Banerjee, Esther Duflo, Nathanael Goldberg, Dean Karlan,* Robert Osei, William Parienté, Jeremy Shapiro, Bram Thuysbaert, Christopher Udry

INTRODUCTION: Working in six countries with an international consortium, we investigate whether a multifaceted Graduation program can help the extreme poor establish sustainable self-employment activities and generate lasting improvements in their well-being. The program targets the poorest members in a village and provides a productive asset grant, training and support, life skills coaching, temporary cash consumption support, and typically access to savings accounts and health information or services. In each country, the program was adjusted to suit different contexts and cultures, while staying true to the same overall principles. This multipronged approach is relatively expensive, but the theory of change is that the combination of these activities is necessary and sufficient to obtain a persistent impact. We do not test whether each of the program dimensions is individually necessary.

Instead, we examine the "sufficiency" claim: A year after the conclusion of the program, and 3 years after the asset transfer, are program participants earning more income and achieving stable improvements in their well-being?

RATIONALE: We conducted six randomized trials in Ethiopia, Ghana, Honduras, India, Pakistan, and Peru with a total of 10,495 participants. In each site, our implementing partners selected eligible villages based on being in geographies associated with extreme poverty, and then identified the poorest of the poor in these villages through a participatory wealth-ranking process. About half the eligible participants were assigned to treatment, and half to control. In three of the sites, to measure within village spillovers, we also randomized half of villages to treatment and half to control. We conducted a baseline survey on all eligible participants, as well as an endline at the end of the intervention (typically 24 months after the start of the intervention) and a second endline 1 year after the first endline. We measure impacts on consumption, food security, productive and household assets, financial inclusion, time use, income and revenues, physical health, mental health, political involvement, and women's empowerment.

RESULTS: At the end of the intervention, we found statistically significant impacts on all 10 key outcomes or indices. One year after the end of the intervention, 36 months after the productive asset transfer, 8 out of 10 indices still showed statistically significant gains, and there was very little or no decline in the impact of the program on the key variables (consumption, household assets, and food security). Income and revenues were significantly higher in the treatment group in every country. Household consumption was significantly higher in every country except one (Honduras). In most countries, the (discounted) extra earnings exceeded the program cost.

CONCLUSION: The Graduation program's primary goal, to substantially increase consumption of the very poor, is achieved by the conclusion of the program and maintained 1 year later. The estimated benefits are higher than the costs in five out of six sites. Although more can be learned about how to optimize the design and implementation of the program, we establish that a multifaceted approach to increasing income and well-being for the ultra-poor is sustainable and cost-effective. ∎

Pooled average intent-to-treat effects, endline 2 at a glance

This figure summarizes the average treatment effects in each country for the 10 primary outcomes. All treatment effects are presented as standardized z-score indices and 95% confidence intervals.
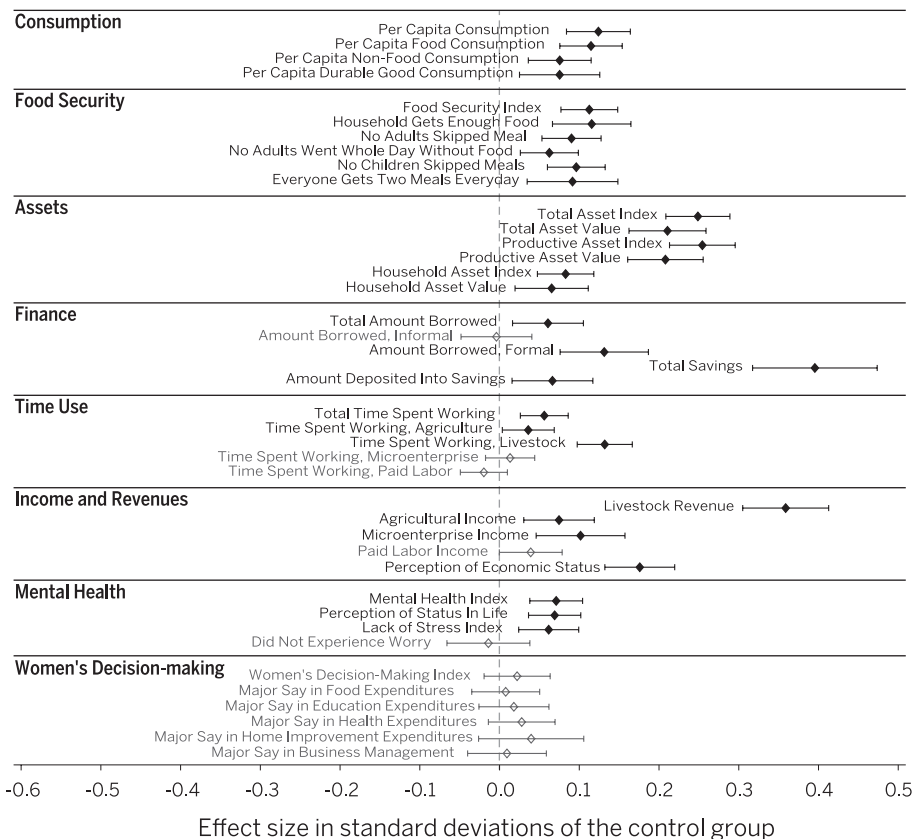
Effect size in standard deviations of the control group

DEVELOPMENT ECONOMICS

A multifaceted program causes lasting progress for the very poor: Evidence from six countries

Abhijit Banerjee,[1,2,3,4] Esther Duflo,[1,2,3,4] Nathanael Goldberg,[5] Dean Karlan,[2,3,4,5,6]*
Robert Osei,[7] William Parienté,[4,8] Jeremy Shapiro,[9]
Bram Thuysbaert,[5,10] Christopher Udry[2,3,4,6]

We present results from six randomized control trials of an integrated approach to improve livelihoods among the very poor. The approach combines the transfer of a productive asset with consumption support, training, and coaching plus savings encouragement and health education and/or services. Results from the implementation of the same basic program, adapted to a wide variety of geographic and institutional contexts and with multiple implementing partners, show statistically significant cost-effective impacts on consumption (fueled mostly by increases in self-employment income) and psychosocial status of the targeted households. The impact on the poor households lasted at least a year after all implementation ended. It is possible to make sustainable improvements in the economic status of the poor with a relatively short-term intervention.

More than one-fifth of the world's population lives on less than purchasing power parity (PPP) US$1.25 a day, and there is an emerging international consensus that this share should (and can) be driven close to zero by 2030 (*1, 2*). Reaching this objective will require enabling the poorest families, who are often the most marginalized within their villages, to shift from insecure and fragile sources of income to more sustainable income-generating activities. One possible avenue, popular with both development organizations and governments, is to promote self-employment activities (such as cow rearing or petty trading). Past efforts to reduce poverty by encouraging these types of activities among the poor, however, have often been plagued by implementation problems and been deemed failures (*3*). For example, India's Integrated Rural Development Program (IRDP) is believed to have been both poorly targeted and ineffective (*4, 5*). However, in recent years, several large nongovernmental organizations (prominent international northern NGOs such as Oxfam, World Vision, and Heifer, as well as many local NGOs) have gone back to this "livelihood" approach. This past experience raises the question: Is it actually pos-

sible to reliably improve the livelihoods of the poorest households by giving them access to self-employment activities, or is this entire approach flawed? In particular, is it possible to come up with a model for doing so that can be implemented by a wide variety of organizations and works in a wide range of geographic, institutional, and cultural contexts?

We present results from randomized control trials (RCTs) in six countries of a particular approach to foster self-employment activities among the very poor. Originally designed and implemented by BRAC, a large Bangladeshi NGO that runs several country-wide programs, the "Graduation" program provides a holistic set of services, including the grant of a productive asset, to the poorest households in a village (referred to by BRAC as the "ultra-poor"). The beneficiaries are identified through a participatory process in a village meeting, followed by a verification visit by the organization's staff. Selected beneficiaries are then given a productive asset that they choose from a list, training and support for the asset they have chosen, as well as general life skills coaching, weekly consumption support for some fixed period, and typically access to savings accounts and health information or services. These different activities (plus regular interactions with the households over the course of a year) are designed to complement each other in helping households to start a productive self-employment activity. The idea is to provide a "big push," over a limited period of time, with the hope of unlocking a poverty trap. The program costs per household average 100% (range from 62 to 145%) of baseline household consumption. Although the program may initially be relatively expensive (compared to

just providing training, coaching or a cash transfer), the thinking behind the program is that the combination of these activities is necessary and sufficient to obtain a persistent impact on a large fraction of the beneficiaries.

We address the "sufficiency" claim: Is the Graduation approach effective and cost-effective, and can it be implemented at scale and in different contexts and cultures? Whether all the ingredients of the program are individually necessary is not tackled here and will need to be dealt with in future work.

A key feature of the BRAC approach is that, while comprehensive, it is well codified, scalable, and replicable. BRAC has already implemented the program at scale in Bangladesh. As of 2011, BRAC had reached close to 400,000 households, and a further 250,000 were scheduled to be reached between 2012 and 2016 (*6*). It has now also been replicated in about 20 countries, including the six countries that are studied here. A high-quality RCT, conducted independently but simultaneously with this study, has shown the BRAC program in Bangladesh to be very effective (*6*). Two years after graduation, households have expanded their self-employment activities, diversified out of agriculture and livestock, reduced casual labor, and increased consumption. Previous nonrandomized studies of the BRAC program (*7–9*) found similar impacts.

Between 2007 and 2014, we conducted a multisite RCT of the Graduation program. The sites were chosen as part of an effort led by the Ford Foundation and Consultative Group to Assist the Poor (CGAP), referred to here as the Graduation Program Consortium. The programs were implemented by six different organizations in six countries (Ethiopia, Ghana, Honduras, India, Pakistan, and Peru), but overall planning on the programs and evaluation were coordinated from the onset (*10*). Treatment was randomly assigned among eligible households. Data were collected at baseline and immediately after the programs ended, 2 years later ("endline 1"), and again 1 year after the programs ended, i.e., about 3 years after the beginning of the programs ("endline 2"). We report pooled results from all the sites (21,063 adults in 10,495 households), as well as site-by-site results.

The main contribution of this study is the evaluation of the cost-effectiveness of the same potentially important intervention across a diverse set of contexts. The sites span three continents, and different cultures, market access and structures, religions, subsistence activities, and overlap with government safety net programs. This diversity should give us a high level of confidence in the robustness of the impact to variations in both the context and implementation agency. The core components of the program are similar in substance and magnitude, although the program design includes adjustments as are necessary for local contexts. For example, country-specific market analysis was conducted to determine viable livelihoods to promote, rather than simply promoting the same livelihood in every context. In addition, because the study was conceived from

[1]Massachusetts Institute of Technology (MIT), Cambridge, MA, USA. [2]Center for Economic and Policy Research (CEPR), Washington, DC, USA. [3]National Bureau of Economic Research (NBER), Cambridge, MA, USA. [4]Jameel Poverty Action Lab (J-PAL), MIT, Cambridge, MA, USA. [5]Innovations for Poverty Action (IPA), New Haven, CT, USA. [6]Yale University, New Haven, CT, USA. [7]University of Ghana–Legon, Accra, Ghana. [8]Institut de Recherches Economiques et Sociales (IRES), Université Catholique de Louvain, Louvain-La-Neuve, Belgium. [9]Princeton University, Princeton, NJ, USA. [10]Ghent University, Ghent, Belgium.
*Corresponding author. E-mail: dean.karlan@yale.edu

the onset as one multisite study, variables were collected in a comparable manner on a broad array of outcomes. Finally, households were surveyed over 3 years, including 1 year after the end of the program, which directly speaks to the sustainability of the changes we observe.

The program: Commonalities and variations

The basic approach of the program is to combine six different activities designed to complement each other to help households start, and continue with, a self-employment activity. The core of the program is a productive asset transfer, but the premise of the program is that the support has to be sufficiently broad and long-lasting to ensure that households continue to benefit from that asset into the future.

Following identification of the beneficiary households through a participatory process in the village, the six activities are:

1. Productive asset transfer: a one-time transfer of a productive asset

2. Consumption support: a regular transfer of food or cash for a few months to about a year (*11*)

3. Technical skills training on managing the particular productive assets

4. High-frequency home visits

5. Savings: access to a savings account and in some instances a deposit collection service and/or mandatory savings

6. Some health education, basic health services, and/or life-skills training

The Graduation Program Consortium organized global learning events at which staff from each of the sites, along with researchers, gathered to discuss site-specific design considerations. The Consortium also hosted a dedicated website to foster ongoing knowledge exchange between sites and a wider community of practice. There were five global learning events between 2008 and 2014, plus several regional workshops. The first two global meetings featured exposure visits to the BRAC program in Bangladesh and the Bandhan program in India. Each partner thus participated in at least two field visits, with some additional exchange visits arranged on an ad hoc basis (e.g., the Ghana team visited the Ethiopia site as they designed their program).

We now detail the core components of the program. We first discuss the commonalities across all sites, and then discuss the important variations across sites. Table 1 has a detailed description of the program features in each site.

Targeting

The Graduation program is intended to serve the poorest of the poor within villages. The targeting process starts with selection of a poor region based on national survey data, and a list of villages within the target area (often selected in consultation with program staff). At most program sites, ultrapoor households are then identified using a Participatory Wealth Ranking (PWR) during which villagers create an economic ranking of all village households. In Indonesia, Alatas *et al.* (*12*) find that a PWR used to identify recipients of a gov-

ernment program successfully identified the poorer households. The households selected for the Graduation program through the PWR are then visited by field officers from the implementing organizations to verify their poverty status with an asset checklist [often the Progress out of Poverty (PPI) scorecard (*13*)]. Of the selected households, 48% have daily per capita consumption below PPP US$1.25, compared to 19% of the population at-large in these countries (table S1a).

A fraction of households in the resulting list are then randomly assigned to receive the program and are invited to participate. In all sites but India, all intended beneficiaries enrolled. We provide more discussion of take-up in the India program below.

Productive-asset transfer

The asset transfer is the core component of the program and also one of its largest costs. Each household chose, in consultation with the field officer, one of the assets (or asset bundle options) in a list proposed by the implementing organization (often, this list was created after hiring local experts to analyze markets and the viability of livelihood options). Common choices included raising livestock (sheep, goats, chicken, cattle, etc.) and petty trade, and are detailed in Table 1. The value of assets varied between sites, ranging from PPP US$437 to PPP US$1228 per household. The differences in transfer costs partially reflect the differences in local livestock prices: All but one site (Peru) transferred productive assets worth between four to eight goats at local prices (see Table 1 for exact figures). Furthermore, although the asset type differed across countries, the principle in choosing the asset was consistent. In four of the six sites, the asset transferred was the most or the second most commonly held asset at baseline. In Peru and Ethiopia, the most commonly transferred assets were guinea pigs, and sheep and goats, respectively, because they were believed to be more profitable than the most commonly held assets. Different assets generated quite different cash flow patterns: Some produced immediate revenue (e.g., petty trade), whereas others (like cows) produced far more delayed and lumpy revenue flows.

The asset transfer generally happened between 0 and 15 months, largely depending on the site, after the identification of the beneficiaries and the baseline survey. In Pakistan, where the intervention was run by several organizations, it took several months, and in some cases a year or more, to complete all rounds of asset transfers. Honduras also had delays in starting the program. In Ethiopia, the transfers were spread out over 6 months.

Consumption support

Consumption support—generally a cash stipend—was distributed typically weekly or monthly. The purpose of the consumption stipend is both to immediately improve and stabilize consumption, and to reduce incentives to sell (or eat up) the productive assets being distributed. The distribution of consumption support lasted between 4 and 13 months, depending on the site, and

ranged from PPP US$24 to PPP US$72 per month (*14*). This variation partly reflects the fact that the PPP in each country is not based on the bundle of goods purchased by the poor: In all sites but Ethiopia (where the consumption support was part of an existing program), the transfer corresponds roughly to the monetary equivalent of between 2,402 and 5,142 calories per day (or roughly a kilogram of rice at local price) (*15*).

Consumption support was provided everywhere, but in two sites (Ethiopia and Peru), a form of consumption support already existed before the program started, so it was available for all (Ethiopia) or part (Peru) of the control group, as well. In Ethiopia, both treatment and control households received benefits from the Productive Safety Net Programme (PSNP), a food-for-work program for food-insecure households. For this reason, the program did not offer any additional consumption support to treatment households. In Peru, a conditional cash transfer program, Juntos, was active in 51 of the 86 project villages. Juntos provides PEN 200 (PPP US$143.33) every 2 months, on the condition that female heads of households meet the following conditions: obtain identity cards for their children, take children under 5 to health check-ups, and send children to school. In the non-Juntos villages, the treatment households received a "Juntos-like" consumption support: PEN 100 (PPP US$71.96) per month for 9 months, conditional on children attending school and receiving health check-ups. In our sample, 57% of control households report receiving support from Juntos during the baseline survey, whereas all the treatment households receive either Juntos or the replacement. Thus, Peru is an intermediate case between Ethiopia and the other sites.

Honduras implemented its consumption support by providing a one-time food transfer intended to cover the 6-month lean season.

Training

Before receiving their assets, households were provided with training on running a business and managing their chosen livelihood. For example, those selecting livestock received information on how to rear the livestock, including vaccinations, feed, and treatment of diseases.

High-frequency home visits

Households received regular training and coaching from a field officer throughout the 2-year program. The visits were intended to provide accountability (i.e., making sure that the households carry out the tasks necessary to maintain and grow their livelihood into a stable income-generating activity), as well as to be encouraging (e.g., helping households believe that they can have control of their lives and put themselves on a path out of extreme poverty) (*16*). During the home visits, field staff provided health education and financial capabilities coaching. In Peru, where traveling to the villages proved to be logistically challenging, visits happened only every 6 weeks, and in Pakistan, similar difficulties led the implementing NGOs to shift gradually to biweekly or monthly visits.

Table 1. Implementation summary.

	Ethiopia	Ghana	Honduras	India	Pakistan	Peru
Location	Kilte Awlaelo district in Tigray	Northern and Upper East regions	Lempira department	Murshidabad, a district north of Kolkata	Sindh region	13 districts of the provinces of Canas and Acomayo, in the department of Cusco
Implementing NGO	Relief Society of Tigray (REST)	Presbyterian Agricultural Services (PAS) and Innovations for Poverty Action (IPA); program called Graduation from Ultra Poverty (GUP)	Proyecto MIRE, a partnership between PLAN International Honduras and Organización de Desarollo Empresarial Feminino Social (ODEF), a Honduran microfinance institution	Bandhan	Pakistan Poverty Alleviation Fund, Aga Khan Planning and Building Services Pakistan, Badin Rural Development Society, Indus Earth Trust, Sindh Agricultural and Forestry Workers Coordinating Organization	Asociación Arariwa; PLAN International Peru
Type of NGO	Local NGO	Local NGO	Local NGO; international NGO	Local MFI	Local NGOs	Local NGO; international NGO
Financial institution partner	Dedebit Credit and Savings Institution (DECSI), an Ethiopian microfinance institution (MFI)	Services provided by PAS	Services provided by ODEF	Services provided by Bandhan	None	Services provided by Arariwa
Eligibility requirements	Participant in food-for-work program, at least one member capable of work, no loans taken out by household	Exclusion criteria included: (i) ownership of >30 small ruminants or >50 fowl; (ii) member found to be alcoholic or drug addict; (iii) no strong, able-bodied adult; (iv) did not have a female member; (v) did not have a member between the ages of 18 and 65	Household must have (i) monthly income of less than or equal to HNL 600 (PPP US$67.82); (ii) lived in community for at least 3 years; (iii) not received a loan in last year; (iv) not a benificiary of cash or food transfer program (excluding government conditional cash transfer); (v) at least one child (under 18). Households must satisfy two of the following three criteria: (i) one manzana or less of cultivated land; (ii) children in the household work; (iii) not participating in development program	Household has able-bodied female member, households are not associated with any MFI and receive below a certain threshold of aid from the government. Meet three of the following criteria: primary source of income is informal labor or begging, land holdings are below 0.2 acres, household has no productive assets other than land, no able-bodied males in the household, school-age children work instead of attending school	Households meet at least three of the five selection criteria: no ownership of productive assets, no active male member in the households, income less than INR 25 (PPP US$1.74) per day, livelihood at risk, and no member working on salaried employment.	Household must (i) have head or spouse 60 years old or less; (ii) have at least one child under 18; (iii) have head not away from household for 6 months or more in a year; (iv) not borrow money from a formal financial institution; (v) not have a second home outside of the community; (vi) neither the head nor spouse has formal employment
Method of identifying participants	Chosen by local community's food security task force	Participatory Wealth Ranking at village level	Participatory Wealth Ranking at village level; followed by verification survey	Participatory Rural Appraisal, followed by NGO verificiation	Participatory Rural Appraisal, followed by NGO verification	Participatory Wealth Ranking at village level; followed by verification survey

Continued on next page

	Ethiopia	Ghana	Honduras	India	Pakistan	Peru
Savings component	Households had bank accounts opened at DECSI, required to regularly deposit savings. In total, households required to save ETB 4724 (PPP US$1227.87) over the 2 years of the program; households were unable to withdraw funds until they reached this threshold	Half of GUP households received savings accounts (savings collected during weekly visits by field agents, households receive passbooks to log deposits)	Female heads of household are required to open savings accounts with ODEF and are randomly assigned to two savings treatments: (i) savings matching biannually equal to 50% of the avereage account balance, (ii) monthly direct savings transfers [both get savings incentives of up to HNL 800 (PPP US$90.42)]	Households required to save approximately INR 10 (PPP US$0.97) per week at weekly meeting with Bandhan staff	Households encouraged to save money at home, in boxes, or with Rotating Savings and Credit Associations (ROSCAs)	Participant households encouraged to join community savings groups; participants could also open passbooks with Banco de Nacion or deposit group savings with Arariwa Microfinance
Health component	None	Health and nutrition education. Beneficiaries were enrolled in the National Health Insurance Scheme.	Trainings in health, nutrition and hygiene	Health discussed at weekly meetings	Lady health visitors provided basic health services including checkups, health and hygiene training, and medicine. More difficult and serious cases were referred to the nearest doctor.	Health discussed at trainings (three modules: nutrition, healthy practices, prenatal health)
Asset transfer	June 2010–Jan 2011	July 2011–July 2012	August 2009–August 2010	February 2007–March 2008	December 2008–May 2010	February 2011–June 2011
Value of asset transfer	ETB 4724 (PPP US$1227.87)	GHS 300 (PPP US$451.38)	HNL 4750 (PPP US$536.89)	INR 4500 (PPP US$437.31)	PKR 15000 (PPP US$1043.33)	PEN 1200 (PPP US$853.97)
Value of asset transfer, in terms of local goat prices	7.98 goats	6.00 goats	4.75 goats	6.53 goats	3.75 goats	17.14 goats
Most common asset chosen	Sheep and goats (62%)	Goats and hens (44%)	Chickens (83%)	Goats (52%)	Goats (56%)	Guinea pigs (64%)
Second most common asset chosen	Oxen (24%)	Goats and maize inputs (27%)	Pigs (6%)	Cows (30%)	Shops (11%)	Hens (24%)
Third most common asset chosen	Bees (10%)	Shea nuts and hens (6%)	Fish (5%)	Nonfarm micro-enterprise inventory (11%)	Hens (10%)	Cattle (4%)
Consumption Support	Both treatment and control households received food support through food-for-work program through the duration of the program; 5 days of work (which can be completed once per month) earns 15 kg of wheat, 0.66 kg of chickpeas, and 0.4 liters of oil, worth approximately ETB 100 (PPP US$25.99)	Treatment households received weekly cash transfers of GHS 4 to 6 (PPP US$6.02 to 9.03) (amount dependent on household size) during lean season	Treatment houeholds received one-time food transfer worth HNL 1920 (PPP US$217.02), intended to cover the 6- month lean season	Treatment households received weekly cash transfers of INR 90 (PPP US$8.76) for 13 to 40 weeks, depending on the asset chosen (13 weeks for nonfarm enterprise, 30 weeks for goats, and 40 weeks for cows)	Treatment households received monthly cash transfers of PKR 1000 (PPP US$69.56) for the first year in the program	Treatment households that were not enrolled in a government conditional cash transfer program (Juntos) received monthly cash transfers of PEN 100 (PPP US$71.96). Treatment and control households enrolled in Juntos received bimonthly cash transfers of PEN 200 (PPP US$143.33)

	Ethiopia	Ghana	Honduras	India	Pakistan	Peru
Consumption support, measured in calories of cereals that could be purchased for the household if transfer were in cash	2,402	5,142	3,854	3,928	3,149	4,993
Baseline daily per capita consumption, measured in number of buyable calories of cereals	4,389	7,885	4,929	4,179	6,000	7,099
Consumption support provided to control households	Yes	No	No	No	No	Yes, in 51 of 86 project villages
Frequency of household visits from local NGO	Weekly, over 24 months	Weekly, over 24 months	Weekly, over 24 months	Weekly, over 18 months	Weekly, over 24 months, with gradual shift to biweekly or monthly in some cases	Every 6 weeks, over 24 months
Support provided from village assistance committees	No	Yes	Yes	Yes	No	No

Savings

Households were encouraged (and in some sites, required) to save in order to improve their ability to cope with shocks. This is one component that varied from site to site. Four sites (Ethiopia, Honduras, India, and Peru) partnered with microfinance institutions able to provide access to savings accounts. In Pakistan, households were encouraged to save through savings groups, and in Ghana, households received savings accounts. In India and Ghana, individuals were able to save at program meetings or with a visit by a field agent, but in the other four sites, households had to make deposits at the financial institution.

In Honduras, savings were further encouraged through financial incentives. Beneficiary households opened a savings account and were randomized into two groups: (i) savings matching semi-annually equal to 50% of the average account balance, or (ii) monthly direct savings transfers. Both groups received savings incentives equal to a maximum value of HNL 800 (PPP US$90.42). We do not analyze this experimental variation in this paper.

Ethiopia had a strong forced savings component. The government prohibited unconditional transfers to the poor. To satisfy this prohibition but still implement the program, the implementing partner, Relief Society of Tigray (REST) and the government agreed to allow the asset transfers to be described as "like" a loan, as recipients had to make deposits into a savings account in exchange for receiving the asset. Households were not able to withdraw their savings from the account until they saved an amount equal to ETB

4724 (PPP US$1228), the value of the asset transfer. However, once households achieved the required savings threshold, they had full access to their deposits and could withdraw from their accounts as they saw fit. Furthermore, if they failed to make the deposits, they did not forfeit their asset. Compliance with the deposits was very high, with only 15 households (out of 458) not fulfilling the commitment.

Health and other services

Finally, all sites but one (Ethiopia) included a health component such as health, nutrition, and hygiene training. Some sites also facilitated access to health care, either as direct services from community health workers, referring them to government or NGO health clinics, or by enrolling beneficiaries in national health insurance. Several of the sites organized support from village assistance committees comprising village leaders who helped advise the households, mediated problems, and connected beneficiaries with additional services.

Experimental methods

Experimental design

Of the six experiments, three are individual randomized trials with randomization at the household level within each village (India, Ethiopia, and Pakistan) and three are clustered randomized trials, with randomization at both the village and household level (Ghana, Honduras, and Peru). In the countries with clustered randomization,

villages were randomly selected to be treatment or control villages, and then treatment households were randomly selected within the set of eligible households in treatment villages. The goal of this design was to be able to measure spillovers. For the main analysis in this paper, we ignore possible externalities and include all control households (within villages or across villages). In the Results section, we provide a discussion of whether any spillovers within the sample may bias our results. Randomization was carried out either remotely by the research team (using a computer), or on-site via a public lottery.

One site (Ghana) had a more complex design with two additional treatment groups (savings only, and productive asset grant only) to "unpack" those aspects of the intervention. In this paper, we are using only the group that received the pooled intervention. This is because none of the other studies systematically tried to unpack the effects, and therefore even with the full Ghana results we would have just one "data-point" and would not be able to answer the unpacking questions with anything approaching the degree of confidence that we have about the overall program effect.

The sample size used in the analysis varies from 925 households (Ethiopia) to 2,606 households (Ghana) from site to site. The overall sample size pooling all sites is 10,495 households.

Table 2 provides details by site of key experimental design features, including sample sizes; Fig. 1 provides a timeline for the typical implementation of both the program and the data collection; and figs. S1a to S1f provide a timeline for each site.

Table 2. Research design.

	Ethiopia	Ghana	Honduras	India	Pakistan	Peru
Location	Tigray Region	Northern Region	Lempira Department	West Bengal State	Sindh Region	Cusco Department
Sample Size	925	2,606	2,403	978	1,299	2,284
Number of households chosen in randomization	458	666	800	512	660	785
Number of households accepting entry into program	458	666	800	266	660	785
Short consumption surveys	No	Yes, three rounds	Yes, five rounds	No	No	Yes, eight rounds
Spillover research design	No	Yes, GUP Villages	Yes	No	No	Yes
Multiple treatment arms	No	GUP savings, GUP no savings, SOUP matched, SOUP unmatched, Asset only	No	No	No	No
Unit of randomization	Individual household randomization	Village-level randomization, followed by individual household randomization within treatment villages	Village-level randomization, followed by individual household randomization within treatment villages	Individual household randomization	Individual household randomization	Village-level randomization, followed by individual household randomization within treatment villages
Method of randomization	One public lottery in each of 10 tabias (administrative subunits). In each tabia, 50 were selected for treatment status, 50 for control	Randomization done remotely by research team	Randomization done remotely by research team	Randomization done remotely by research team	Public lottery	Randomization done remotely by research team
Stratification variables used in block randomization procedure	10 tabia	155 villages (among those not selected as pure control villages)	40 villages (among those not selected as pure control villages)	119 hamlets	4 partner NGOs; 66 villages	43 villages (among those not selected as pure control villages)
Stratification variables to verify orthogonality, used in rerandomization procedure	None	Household size, asset ownership index, household owns business, total surface area of land owned, livestock ownership index, distance to closest market, number of compounds in village	Household size, number of children, female headed household, adult in household of prime working age (18 to 60), number of durable goods owned, income per capita, cell phone ownership	None	None	Household size, total PPI score, education level of household head, population in village, distance from nearest town
Number of months between midpoint of baseline survey and midpoint of asset transfers	6	10	15	0	11	7
Number of months between midpoint of asset transfer and midpoint of endline 1	21	18	25	23	25	29

Continued on next page

	Ethiopia	Ghana	Honduras	India	Pakistan	Peru
Number of months between end of household visits (i.e., end of program interaction with households) and midpoint of endline 1	1	1	3	5	Varied by partner	2
Number of months between midpoint of endline 1 and midpoint of endline 2	13	12	13	15	7	12

Cross-site timeline
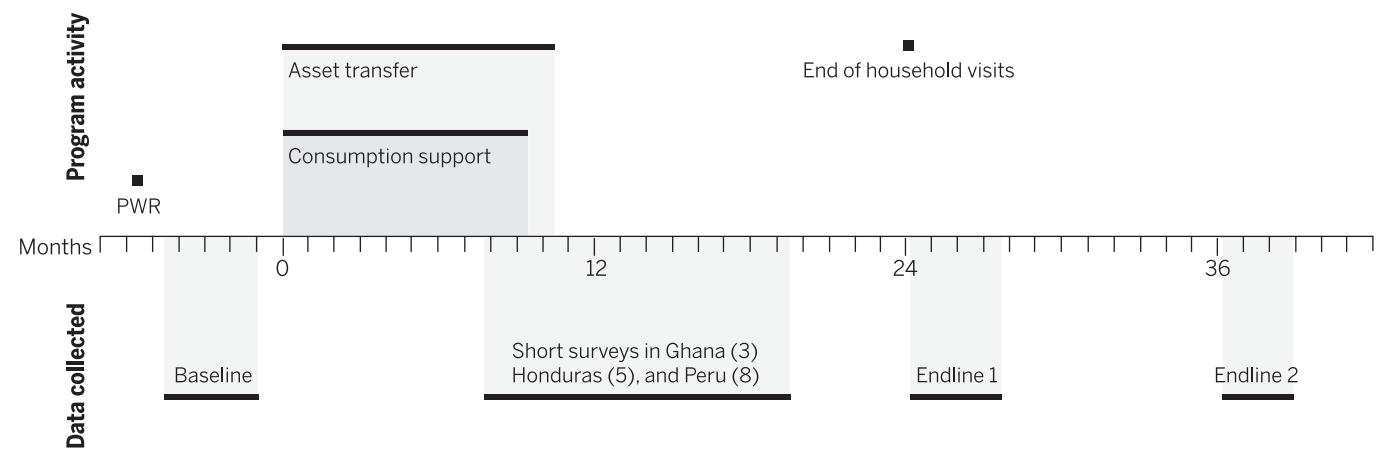
Fig. 1. Cross-site timeline. PWR, participatory wealth ranking. Only short surveys that occurred within 12 months of endline 1 are used in endline 1 analysis.

Integrity of the experimental design

Balance

Table S1b presents baseline data for the same variables and indices used as the primary outcome measures. Panel A presents the mean comparisons and t tests for equality of means. At baseline, we fail to reject at the 5% level the equality of means of treatment and control groups for any of the 10 primary outcome measures. Panel B presents similar analysis, but with a regression framework that includes fixed effects by country, and finds similar balances. The aggregate test, reported in panel C, finds that we are not able to reject equality of means across all 10 measures (p-value = 0.689). Tables S1c to S1e, present similar results for each country. Overall, the sample balance was good in every individual country.

Survey attrition

Table S1f presents an analysis of survey attrition for both endlines 1 and 2. The follow-up rate was excellent. We resurveyed 94% of baseline respondents in endline 1, and 91% in endline 2 (panel A). Panel B presents analysis on the type of people that were more likely to be resurveyed.

Panel C presents a test of whether the treatment affected the type of person who completed the endline surveys, i.e., whether the treatment caused a sample composition bias. The p-values on a full set of baseline characteristics interacted with treatment are 0.75 (endline 1) and 0.17 (endline 2), thus supporting the contention that the survey attrition did not lead to a different sample frame across treatment and control groups ([17]). Tables S1g and S1h present similar results for each country. At 17%, attrition was the worst in India in endline 1; Pakistan was the worst at endline 2, at 21%. In neither country was attrition differential in the treatment group.

Compliance with treatment assignment

In all sites but one, the experimental design was strictly adhered to: No control received the program, and all treatment households received the program. The India site was the only site in which some individuals refused participation: 52% of those selected in the randomization participated in the program. According to Bandhan, the implementing organization, 35% of households declined the offer, for two unrelated reasons: First, in some villages, a section of villagers held the

(erroneous) belief that Bandhan was a Christian organization trying to convert beneficiaries, and acceptance of the livestock constituted agreeing in some way to participating in Christian rituals. Second, some wives were worried that their husband would mishandle the asset and they would lose face in front of their village. A further 13% were deemed ineligible by Bandhan because they were participating in microcredit or self-help group activities. The analysis below is an "intent-to-treat" (ITT): We compare households assigned to control to those assigned to treatment, irrespective of whether they received treatment or not.

Analysis methods for pooled results

Following standard practice in the analysis of multi-site trials, we estimate a single model, with strata and country dummies. Each column of each table represents the results of a separate ordinary least squares (OLS) regression of the form

$$Y_i^k = \alpha + \beta_1 assignment_i + \beta Z_i^k + T_{\text{country}} + U_{\text{shortsurveys}} + V_{\text{stratification}} + \varepsilon_i \qquad (1)$$

where Y_i^k is the outcome k of interest for either household or adult i (details of the variable constructions are presented in the supplementary

text 1 to 3), $assignment_i$ is an indicator for having been randomly selected into the program, Z_i^k is the household or adult's baseline value of the outcome variable k (coded as zero, with an indicator for missing baseline, whenever it was not available), $T_{country}$ is a vector of dummy variables for each of the countries in the study, $U_{shortsurveys}$ is a vector of dummy variables indicating whether or not the household was surveyed in a short survey round (in some countries, data were collected through both long and short surveys), and $V_{stratification}$ is the vector of all variables included in stratification in each of the six countries (*18*).

In the main analysis of the pooled sample, no adjustments are made to reflect the differences in sample sizes between countries; every observation is weighted equally. Again, this follows standard practice in the analysis of multisite RCTs. Regressions that instead weigh each country equally generate similar results. For each variable that we report, we also present the result of a test for equality of the effects across sites (which we discuss in the next subsection).

Because of the comprehensive nature of the program, a large number of outcome variables are reported. Therefore, we expect some of the variables to show significant results due to chance. To avoid overemphasis on any single significant result, we take several steps. First, following Kling *et al.* (*19*), for each "family" of outcomes, we report an index of all of the outcomes taken together, which we report in Table 3. This is our main results table. We construct indices first by defining each outcome Y_{ijl}^k (outcome k, for observation i in family j, within country l) so that higher values correspond to better outcomes. Then we standardize each outcome into a z-score, by subtracting the country control group mean at the corresponding survey round and dividing by the country l's control group standard deviation (SD) at the corresponding survey round. We then average all the z-scores, and again standardize to the control group within each country and round (*20*).

Second, given that multiple families of outcomes are being reported, we correct for the potential issue of simultaneous inference using multiple inference testing. We calculate q-values using the Benjamini-Hochberg step-up method (*21*) to control for the false discovery rate (FDR). We follow the procedure outlined in Anderson (*22*), and test α at all significance levels (1.000, 0.999, 0.998... 0.000). Our q-value is the smallest α at which the null hypothesis is rejected. It is reported in Table 3 (*23*).

Results

Pooled sample

Table 3 (both endlines), fig. S2 (endline 1), and Fig. 2 (endline 2) present an overview of the results pooled across all sites. Table 3 shows the results aggregated by "families," including q-values corrected for the fact that we are presenting the results from 10 indices (*24*).

At endline 1 (year 2 of the study, just after the end of the program in most sites), all the families of outcomes have improved in the treatment group

(compared to the control group). We use two outcome measures for consumption: Per capita consumption increases by 0.12 SDs (q-value 0.001), which is equivalent to PPP US$4.55 per capita per month, or roughly 5% of control group mean of PPP US$78.80; and an index of food security increases by 0.11 SDs (q-value 0.001). An index of productive and household assets increases by 0.26 SDs (q-value 0.001). Household income and revenues increase by 0.38 SDs (q-value 0.001). There are also improvements in personal lives: Physical health improves by 0.034 SDs (q-value 0.078), and mental health improves by 0.10 SDs (q-value 0.001). Political involvement increases by 0.064 SDs (q-value 0.001), and women's empowerment by 0.046 SDs (q-value 0.049).

By endline 2 (year 3 of the study, typically 1 year after the program ended), all the effects on economic variables are still significant, and usually similar to or larger than after endline 1. It is striking that there is no evidence of mean reversion in the per capita consumption, food security, or assets. The gains in financial inclusion, total time spent working, income and revenue, and mental health have declined but are still positive and statistically significant. The gains in physical health and women's empowerment have declined and are no longer statistically significant.

Figure S2 and Fig. 2, which present the variable-by-variable results at a glance, tell a similar story: The indices are not driven by specific variables. Most individual variables show significant impacts at endline 1. At endline 2, most variables stay significant, and the various variables in the women's decision-making families and the mental health families have either declined or become not significant.

Tables S2a to S2h, contain the detailed variable-by-variable results for the entire sample.

In table S2a, we see that food consumption increases more than nonfood consumption, both in absolute value and in proportion (specifically, food consumption increases 7.5% from a control group mean of $51.60, and nonfood consumption increases 2.4% from a control group mean of $25.30). The elasticity of food consumption to overall expenditure appears to be greater than 1, a striking result given prior estimates of well below 1 (*25*). Durable goods expenditures do not increase significantly in either time period, but we do see that treatment households have more household assets than the control households in both periods (table S2c), so the expenditure variable may fail to pick up some durable goods expenditures. The consequence of the increase in food expenditure is a greater sense of food security (table S2b), which is as strong in endline 2 as in endline 1 (for example, 14% reported at least one person not eating at all for an entire day, compared to 17% in the control group; table S2b, column 3).

In table S2c, we see that households have statistically significantly more assets both in endline 1 and in endline 2. The asset index we construct in all countries is 0.26 SDs larger in endline 1 and 0.25 SDs larger in endline 2. Likewise, the effect size for productive assets (those

used in household self-employment activities) does not change between endlines 1 and 2, with an effect size of 0.27 SDs at endline 1 and 0.25 SDs at endline 2. There is an increase both in household and productive assets, but the increase in productive assets is larger in both years (productive asset value increases by 15.1 and 13.6% compared to control group means of PPP US$1964 and PPP US$1576 in endline 1 and 2, respectively). Row 12 of Table 4 compares the value of the assets held by households by year 3 to the value of the asset that was transferred to them. The impact of the program on asset values is lower than the cost of the assets. However, the program impact on asset holdings is stable from year 2 to year 3 (Table 3), so after the households made an initial adjustment to asset holdings, there was no further decline.

The increase in asset holding does not come at the expense of more borrowing or less savings. Instead, we see in table S2d large increase in savings in both endlines (PPP US$151, or 155.5% of control mean in endline 1, and PPP US$75, or 95.7% of control means in endline 2). Savings was mandatory during the first year in many sites, so it is not entirely surprising that we see an increase at endline 1. But continued savings was not required after the program, and the increase in net savings is still large.

These productive assets are being put to use: Adult labor supply increases by 17.5 min per adult per day (10.4% increase over control households) at endline 1, and 11.2 min (6.1% increase) at endline 2 (table S2e). The increase is concentrated on livestock and agricultural activities, consistent with the assets chosen by most people. More assets and more labor translate into increased revenue from livestock (table S2f, column 1) (*26*) and net income from agriculture (column 2). At endline 1, the revenue from livestock is 41.6% larger, compared to a control group mean of PPP US$73.50). At endline 2 it is 37.5% larger, compared to a control group mean of PPP US$80.60. The households also feel better off economically: 0.33 points improvement on a scale of 1 to 10 at endline 1 (control group mean = 3.74), and 0.30 points improvement at endline 2 (control group mean = 3.65). All of the gains to income and revenue persist 1 year after the end of the program, including the increase in self-reported economic status.

Table S2g presents the detailed health and mental health results. The only significant positive impact on physical health seen at either endline at the 5% level is on the activities of daily living score at endline 1. At endline 1, the mental health index is 0.10 SDs higher, driven by the overall self-reported happiness and lack of symptoms of mental distress (*27*). By endline 2, the positive impact on the mental health index has declined to 0.071 SDs, but it remains significantly positive and continues to be driven by both self-reported happiness and lack of stress. This minor decrease in the treatment effect may be another instance of the well-known "hedonic treadmill" (*28*).

Table S2h presents results on political and social empowerment, and women's empowerment

Table 3. Indexed family outcome variables and aggregates.

	Endline 1			Endline 2		
	(1)	(2)	(3)	(4)	(5)	(6)
Indexed outcomes	**Standardized mean treatment effect**	*q*-value for all 10 hypotheses	*F*-test of equality of coefficients across sites, with *q*-values	**Standardized mean treatment effect**	*q*-value for all 10 hypotheses	*F*-test of equality of coefficients across sites, with *q*-values
Total per capita consumption, standardized	0.122*** (0.023)	0.001	3.207 0.009	0.120*** (0.024)	0.001	5.307 0.001
Food security index (five components)	0.107*** (0.022)	0.001	1.670 0.139	0.113*** (0.022)	0.001	2.405 0.050
Asset index	0.258*** (0.023)	0.001	14.26 0.001	0.249*** (0.024)	0.001	23.90 0.001
Financial inclusion index (four components)	0.367*** (0.030)	0.001	55.33 0.001	0.212*** (0.031)	0.001	10.70 0.001
Total time spent working, standardized	0.090*** (0.018)	0.001	7.520 0.001	0.054*** (0.018)	0.004	2.644 0.038
Incomes and revenues index (five components)	0.383*** (0.036)	0.001	12.05 0.001	0.273*** (0.029)	0.001	5.82 0.001
Physical health index (three components)	0.034* (0.019)	0.078	3.825 0.003	0.029 (0.020)	0.159	0.776 0.630
Mental health index (three components)	0.099*** (0.022)	0.001	5.189 0.001	0.071*** (0.020)	0.001	1.781 0.142
Political Involvement index (four components)	0.064*** (0.018)	0.001	4.176 0.002	0.064*** (0.019)	0.002	2.624 0.038
Women's empowerment index (five components)	0.046** (0.023)	0.049	1.803 0.121	0.022 (0.025)	0.385	0.469 0.800

Notes: 1. Results presented are mean standardized intent-to-treat estimates, including country dummies and controls for every variable used in both block stratification and in rerandomization procedures. All indices are standardized with respect to the control group in that same time period. 2. Dummy variables are included in endline 1 regressions for wave of data, i.e., for whether observation was from endline 1 or one of the short surveys conducted prior to endline 1. 3. See supplementary text 2 for the components of each index 4. Endline 1 was conducted immediately following the end of the household visits, which was typically 2 years after the transfer of productive assets. 5. Endline 2 was conducted 12 months after endline 1, i.e., 1 year after the end of all program activities. 6. Indices measured at the household level are total per capita consumption, food security, assets, financial inclusion, and incomes and revenues. For these indices, our sample size ranges from 9,613 to 9,785 for endline 1, and from 9,482 to 9,508 at endline 2. Use of time, physical health, mental health, and political involvement are asked of adults in each household (normally one or two adults, but as many as seven in India). Sample sizes for these indices range from 12,493 to 15,662 at endline 1 and from 14,051 to 15,136 at endline 2. Pakistan did not include a mental health module in endline 1. India did not include a women's empowerment module in endline 2. 7. For both household- and adult-level indices, standard errors are clustered at the unit of randomization.

within the household. Beneficiaries, who are at the outset often marginalized within their village, become more likely to be involved in political activity (except voting) and village-level actions. This improvement is true both immediately after the program ends and 1 year later. At endline 1, treatment women report having a greater say in decisions within the household related to health expenditures and home improvements. However, this gain in empowerment does not persist over time.

In table S3, we present bounds for our treatment effects, depending on different assumption with respect to attrition, using Horowitz-Manski-Lee bounds (*29*, *30*). The conclusions are robust to this exercise, with all lower bounds except that

for women's empowerment significantly positive at endline 1.

Country-by-country variation

There are too many countries and too many variables to comment on the country-by-country and variable-by-variable results in detail, though the tables are all available in the supplementary materials. Figure S3 (endline 1) and Fig. 3 (endline 2) have a format similar to that of fig. S2 and Fig. 2, but they present the country-by-country results for the summary indices. Tables S4a through S4f present the impacts on the 10 indexed family outcomes, one table per country. Tables S5a-1 through S5h-2 present the impacts on each of the components in each of the coun-

tries, one table per family of outcomes per endline. Here, we highlight some particularly relevant information from this analysis.

The first and most important point is that the results are not driven by any one country. The differences across countries can be seen in fig. S3 and Fig. 3. We present tests for the hypothesis that the results are the same for all countries for each outcome variable. The hypothesis is rejected for almost all pooled outcomes (Table 3), which suggests that there is significant site-by-site variation (and enough data to pick it up), which would be important to study in future work. However, in endline 1, the program appears to have positive impacts on most indices for most countries (tables S4a to S4f). An exception is

Pooled Average Intent-to-Treat Effects, Endline 2 at a Glance
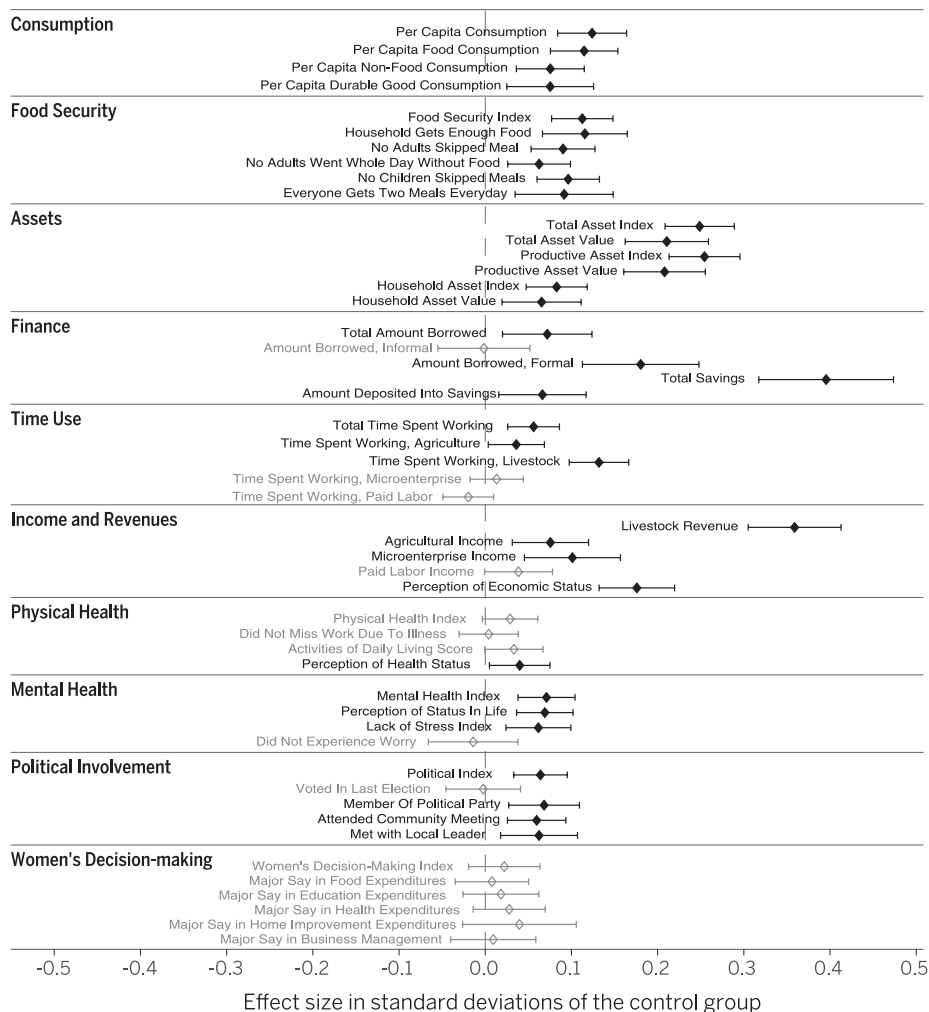
Fig. 2. Pooled average intent-to-treat effects, endline 2 at a glance. This figure summarizes treatment effects presented in tables S2a to S2h. Treatment effects on continuous variables are presented in SD units. Each entry shows the OLS estimate and 95% confidence interval for that outcome. (♦) Statistically significant, 5% level; (◊) not statistically significant, 5% level.

Peru, where we see 3 results out of 10 statistically significant at the 5% level. In endline 2, four of the countries (Ethiopia, Ghana, India, and Pakistan) continue to have statistically significant and positive impacts on most variables, but Honduras and Peru have weaker results, with positive and statistically significant impacts on 3 out of 10 and 4 out of 10 families of outcomes before multiple hypothesis adjustments, respectively (and Honduras also has a negative, and statistically significant prior to multiple hypothesis adjustment, impact on assets).

Turning to the key variables, the gains in per capita consumption, for example, are statistically significant for both endlines in every country except Honduras and Peru. However, we do find a statistically significant increase in food consumption for Honduras in endline 1 and Peru in endline 2 (tables S5a-1 and S5a-2). Likewise, there is an increase in livestock revenues (live-

stock was the most frequently chosen asset in all sites) in all countries by endline 2. There is significant improvement in assets in all countries except Honduras (where it actually declines by endline 2). When looking at the variables individually, some results are different from country to country, no doubt partly due to local specificities and probably partly due to pure luck, but the overall bottom line is that the program appears to be effective in most places. Even in Peru, where we see gains on fewer variables than in other countries, the gains in food expenditures per capita, assets, livestock revenues, physical health, and mental health are all positive and significant.

Second, although it is dangerous to rationalize the Honduras results ex-post, there is a relatively simple explanation for the pattern of results we observe, with generally positive results in endline 1 declining by endline 2. Most households were

given chickens. In both endlines we do see an increase in revenue coming from chickens, as well as a significant increase in food consumption. However, a large fraction of the chickens died due to illness. By the time households were interviewed at endline 2, the households had lost most of their productive asset (leading to a negative and statistically significant impact on the asset index by endline 2) and were not consuming more.

Third, the India results, which come from West Bengal, an area of India that is directly abutting Bangladesh and shares a language and a culture, are strikingly similar, down to most details, to the results in the RCT of the impact of BRAC reported in Bandiera *et al.* (*6*). In particular, as they do, we find that there is an increase in nonagricultural, nonlivestock income by endline 2 in West Bengal (table S5f-2). None of these were promoted through the program, yet they materialized as the household's well-being improved (*31*). This result suggests a pathway—income diversification—through which the results might persist over time.

Fourth, the strongest positive results across the board are obtained in Ethiopia. The Ethiopia case is interesting, because it is the one country where all of the control group also received the basic consumption support that, in other sites, is only provided to the treatment groups (in Peru, half of the control group was also on a government cash transfer program, Juntos). Because it is only one country, we have no counterfactual to what would have happened in Ethiopia if the control group had not received consumption support, but this design at least tells us that the consumption support on its own is not responsible for the entire impact of the program. Note, however, that the productive asset transfer in Ethiopia (equivalent to 7.98 goats) was also larger than in Ghana (6.00 goat equivalents), India (6.53 goat equivalents), or Pakistan (3.75 goat equivalents), so to the extent that assets are liquid, the larger asset transfer in Ethiopia may have compensated for the difference in consumption support.

Effects on distribution of outcomes

Table 5 shows quantile regression estimates at the 10th, 25th, 50th, 75th and 90th percentiles of the distribution of the outcomes. There are several notable results. First, we see positive and significant impacts on income, consumption, and assets, at all tested quantiles. This is encouraging, in that it shows that the program did not push the poorest toward an activity that they did not have the means to manage successfully. Second, for the other variables, the pattern of results is what standard theory would predict. For example, we see impacts on food security only toward the bottom (at the 25th percentile): Those are the households that frequently miss meals and thus likely use any income gains to buy more food. On the other hand, we see impacts on financial inclusion only for the top quantiles (median and above at both endlines): If either access to credit or savings requires meeting some threshold of resources, the poorest of the

Table 4. Cost-benefit analysis.

Panel A: Program costs per household, USD PPP 2014	Ethiopia	Ghana	Honduras	India	Pakistan	Peru
Direct transfer costs	1228	680	724	700	2048	1095
(1) Asset cost	1228	451	537	437	1043	854
Food stipend	0	229	187	263	911	241
Total supervision costs	1900	2832	1633	407	–	3357
Salaries of implementing organization staff	347	1994	801	297	–	2477
Materials	33	119	112	1	–	55
Training	850	44	121	19	–	111
Travel costs	174	293	210	17	–	55
Other supervision expenses	496	382	388	73	–	660
Total direct costs	3127	3513	2356	1107	4680	4452
Start-up expenses	43	133	104	38	–	45
Indirect costs	421	1026	209	112	470	462
Total costs, calculated as if all incurred immediately at beginning of year 0	3591	4672	2670	1257	5150	4960
(2) Total costs, inflated to year 3 at 5% annual discount rate	4157	5408	3090	1455	5962	5742
Exchange rate to PPP adjustment scalar	3.41	2.19	1.90	3.52	4.44	1.84

Panel B: Benefits per household, USD PPP, all values inflated or deflated to year 3 at 5% annual social discount rate

	Ethiopia	Ghana	Honduras	India	Pakistan	Peru
(3) Year 1 annual nondurable consumption ITT, assuming treatment effect equal to year 2	451	293	66	344	613	339
(4) Year 2 annual nondurable consumption ITT treatment effect	451	293	66	344	613	339
(5) Year 3 household asset ITT treatment effect	63	15	−20	6	7	37
(6) Year 3 nondurable annual consumption ITT treatment effect	424	332	−218	251	451	263
(7) Year 4 onward total consumption ITT treatment effect, assuming year 3 gains persist in perpetuity	9417	6241	−6011	5354	8994	7402
(8) Total benefits: (3) + (4) + (5) + (6) + (7) = (8)	10805	7175	−6118	6298	10678	8380
(9) Year 3 productive asset ITT treatment effect	851	118	32	171	163	59
(10) Year 3 savings balance ITT treatment effect	272	11	32	9	7	45

Panel C: Benefit/cost ratios

	Ethiopia	Ghana	Honduras	India	Pakistan	Peru
(11) Total benefits/total costs ratio: (8)/(2) = (11)	260%	133%	−198%	433%	179%	146%
Increase in asset value in year 3						
(12) (Household, productive and financial)/cost of asset transfers: [(5) + (9) + (10)]/(1) = (12)	97%	32%	8%	43%	17%	16%
(13) Increase in asset value/transfers, 10th percentile	56%	5%	−3%	1%	2%	7%
(14) Increase in asset value/transfers, 25th percentile	72%	12%	8%	10%	7%	8%
(15) Increase in asset value/transfers, 50th percentile	85%	20%	15%	23%	15%	7%
(16) Increase in asset value/transfers, 75th percentile	123%	29%	20%	58%	45%	16%
(17) Increase in asset value/transfers, 90th percentile	175%	37%	32%	131%	52%	7%
Sensitivity analysis						
(18) Internal rate of return (IRR)	13.3%	6.9%	–	23.4%	9.5%	7.5%
(19) Annual rate of dissipation of the treatment effect such that costs = benefits	10.3%	1.8%	–	31.1%	5.0%	2.6%
(20) Benefit/cost ratio, at discount rate of 7%	182%	93%	−132%	306%	127%	102%
(21) Benefit/cost ratio, at discount rate of 10%	124%	63%	−84%	211%	88%	69%

Notes: 1. Costs: The implementing partner in Honduras initially allocated all start-up costs and indirect costs into their direct supervision line items. We assume that 5% of costs were committed to start-up and 10% to indirect costs, while preserving the total costs equal to the organization's full budget for the project. In Pakistan, there were five implementing partners, each with different allocations of the nondirect costs. The total represents the average across these organizations. Staff costs associated with the selection of the beneficiaries (identifying the district and poorest individuals, and screening are included in the staff costs. The (nonstaff) costs associated with the identification process are included in "other supervision expenses." In India, note that the compliance rate was 52.0%; the cost-benefit conservatively uses the per-person cost of those who received the program (rather than the total costs divided by the number of all people selected in the randomization). 2. Benefits: In India and Ghana, individuals do not provide an estimate of the value of all assets. We use the relative value of assets across sites and the average purchase prices available in each country (e.g. goats and cattle in both sites) to provide an estimate of the asset ITT. In India and Pakistan, we do not directly ask about the savings balance. We use an OLS regression from the other four countries, with savings balance as our dependent variable and cumulative deposit amount as our independent variable, to predict the ITT of savings balance in those two countries. We calculate nondurable consumption equal to the total of columns (2) and (3) in tables S5a-1 and S5a2 (i.e., total consumption less durable good expenditures) multiplied by the average household size in the country times 12. The average household sizes in Ethiopia, Ghana, Honduras, India, Pakistan, and Peru are 5.59, 8.34, 5.88, 3.96, 6.29, and 5.20 in endline 1, respectively, and 5.59, 8.48, 5.91, 3.79, 6.58, and 5.24 in endline 2, respectively. 3. Benefit/cost: To estimate the break-even dissipation rate (i.e., the rate of decline of the impact on consumption from one time period to the next), we calculate the net present value of consumption in perpetuity beginning in year 4 with the equation {[ITT consumption × (1 − dissipation rate)]/1.05}/(discount rate + dissipation rate). We then solve for the level of dissipation such that the net present value of the costs equals the net present value of the benefits. We do not offer a calculation for Honduras because the costs exceed the benefits even when assuming there is no dissipation. 4. See supplementary text 5 for more details on the cost-benefit calculations. 5. Table S7 replicates Panel A of this table but using exchange rate conversions rather than PPP conversions

Average Intent-to-Treat Effects by Country, Endline 2 at a Glance
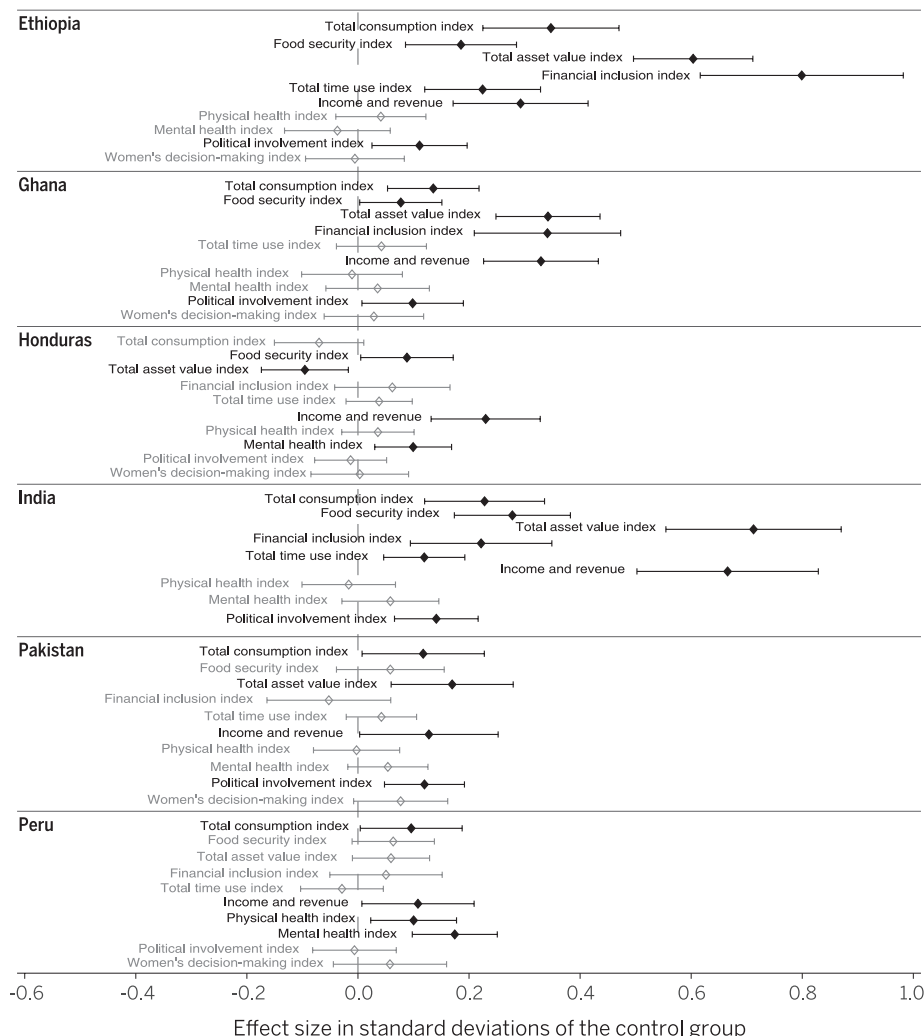
Fig. 3. Average intent-to-treat effects by country, endline 2 at a glance. This figure summarizes the treatment effects presented in tables S3a to S3f. Treatment effects are presented as z-score indices, standardized to the control group at endline 2. Each entry shows the standardized index outcome and its 95% confidence interval. (◆) Statistically significant, 5% level; (◇) not statistically significant, 5% level.

poor may not have met that threshold even with the program. Third, the effects on consumption per capita and the income and revenues index are all increasing with the quantiles: for example, at endline 1, the 10th percentile of consumption (income and revenue index) increases by 0.027 SD (0.005 SD), whereas the 90th percentile increases by 0.491 SD (0.079 SD). Finally, we do see much larger asset growth at higher quantiles (0.038 SD for the 10th quantile versus 0.357 for the 90th quantile).

Are spillovers biasing the results?

In supplementary text 4 and tables S6a and S6b, we examine spillover results in Ghana, Honduras, and Peru. These three sites employed a randomization at both the village and household levels to permit comparisons of control individuals in treatment villages to control individuals in control villages. Overall, these results suggest

that neither externalities nor general equilibrium effects within villages substantially affect our outcomes. This finding implies that it is appropriate to pool the control households in treatment villages with the households in control villages to form the control group.

Discussion

The experiment, conducted in six countries on three continents, shows that the ultrapoor Graduation program improves the lives of the very poor along many dimensions. The program's primary goal, to increase consumption, is achieved by the conclusion of the program and maintained 1 year later. Furthermore, the pattern of impacts on intermediate and downstream outcomes accords with the theory of change: Productive assets, income, and revenue go up. Although results vary across countries, the general pattern of positive effects that persist for at least a year after

the program concludes is common across all countries, with weaker impacts in Honduras and Peru.

Cost-benefit analysis

Naturally the benefits should not be considered without also considering the costs. Table 4, panel A presents costing details, broken down by direct costs (direct transfer and supervision costs), start-up expenses, and indirect costs (including local and international overhead costs). The total program costs for the full duration of the program (inflated to year 3 equivalent PPP dollars, using 5% as the social discount rate, range from PPP US$1455 per household (India) to PPP US $5962 (Pakistan). We use 5% as the social discount rate to harmonize with the joint World Bank and International Monetary Fund policy (*32*), but also calculate internal rates of return and show sensitivity to 7 and 10%. There is no single driver of costs to explain the differences; some of it can be attributed to in-country operating cost differences and some is presumably due to variations in the actual program design. Peru, for example, is a much richer country than Pakistan, so the wages paid to the implementing staff were a lot higher. It is not possible to precisely assign labor costs to specific activities; however, the majority of supervision costs in each country are likely attributable to the household visits and training activities. The asset costs and food stipends, by contrast, required little labor to distribute.

Table 4, Panel B summarizes the consumption gains and asset value changes attributable to the program, all inflated to year 3 equivalent PPP dollars. We assume that the (unmeasured) year 1 ITT effect on per capita consumption is equal to that estimated for year 2, and we assume that the estimated impact on year 3 consumption continues indefinitely into the future (we then relax this assumption, below, as a sensitivity check). The overall impact of the program on consumption expenditure, reported in row 8, is the sum of the impact on the year 3 stock of household durables and the total impact on each year's nondurable consumption (in year 3 equivalent dollars). Rows 9 and 10 of Panel B also report the impact of the programs on the stock of productive assets and savings.

As noted previously, the increase in assets held by the households is lower than the value of the asset in all countries but Ethiopia. On average, households have drawn down part of the asset transfer in the first year, but there is no further decline between year 1 and year 2, and the consumption gains (the final objective of the programs) persist over time. The decline in asset holding in the first year, followed by a stable pattern in both assets and consumption, is somewhat surprising, as economic theory would suggest a slower adjustment to a steady-state level of assets (even if the initial transfer was larger than the optimal steady-state level of assets). We may capture imperfectly some informal assets or liabilities (such as debt or loans to or from other households in the village, which may be labeled as gifts or alms). We also do not capture the value of human capital, which has increased as a result of better nutrition,

Table 5. Quantile treatment effects, indexed family outcomes.

	Endline 1					Endline 2				
	(1)	(2)	(3)	(4)	(5)	(6)	(7)	(8)	(9)	(10)
Indexed outcomes	10th percentile	25th percentile	50th percentile	75th percentile	90th percentile	10th percentile	25th percentile	50th percentile	75th percentile	90th percentile
Total per capita consumption, standardized	0.065*** (0.014)	0.067*** (0.013)	0.045** (0.019)	0.099*** (0.032)	0.140** (0.058)	0.053*** (0.013)	0.061*** (0.014)	0.079*** (0.019)	0.105*** (0.030)	0.206*** (0.063)
Food security index (five components)	0.013 (0.029)	0.073** (0.034)	0.000 (0.000)	0.000 (0.006)	0.000 (0.002)	0.000 (0.020)	0.032** (0.015)	0.000 (0.010)	0.000 (0.006)	0.000 (0.002)
Asset index (productive and household assets)	0.038*** (0.007)	0.072*** (0.010)	0.172*** (0.017)	0.288*** (0.028)	0.357*** (0.064)	0.023*** (0.007)	0.062*** (0.009)	0.135*** (0.014)	0.251*** (0.026)	0.329*** (0.054)
Financial inclusion index (four components)	0.000 (0.001)	0.000 (0.001)	0.153*** (0.010)	0.322*** (0.023)	0.587*** (0.072)	0.000 (0.002)	0.000 (0.002)	0.033*** (0.011)	0.213*** (0.028)	0.418*** (0.095)
Total time spent working, standardized	0.000 (0.006)	0.000 (0.005)	0.084*** (0.018)	0.078** (0.034)	0.000 (0.028)	0.000 (0.006)	0.000 (0.005)	0.038* (0.021)	0.045* (0.027)	0.022 (0.039)
Incomes and revenues index (five components)	0.027*** (0.005)	0.053*** (0.008)	0.098*** (0.014)	0.314*** (0.034)	0.491*** (0.079)	0.001 (0.006)	0.029*** (0.009)	0.171*** (0.020)	0.307*** (0.034)	0.538*** (0.070)
Physical health index (three components)	0.000 (0.033)	0.000 (0.024)	0.012 (0.019)	0.000 (0.007)	0.000 (0.006)	0.000 (0.035)	0.000 (0.022)	0.000 (0.016)	0.000 (0.008)	0.000 (0.006)
Mental health index (three components)	0.108*** (0.038)	0.005 (0.025)	0.112*** (0.027)	0.082*** (0.026)	0.000 (0.015)	0.000 (0.020)	0.000 (0.018)	0.000 (0.018)	0.000 (0.011)	0.000 (0.009)
Political involvement index (four components)	0.000 (0.014)	0.000 (0.010)	0.000 (0.007)	0.000 (0.008)	0.000 (0.006)	0.000 (0.004)	0.000 (0.003)	0.000 (0.010)	0.000 (0.009)	0.000 (0.006)
Women's empowerment index (five components)	0.000 (0.014)	0.000 (0.009)	0.000 (0.008)	0.000 (0.000)	0.000 (0.023)	0.000 (0.014)	0.000 (0.015)	0.000 (0.008)	0.000 (0.008)	0.000 (0.009)

Notes: 1. Regressions include baseline controls, country dummies, and controls of the variables used to ensure balance in rerandomizations at baseline. They do not include block stratification variables. 2. The 0's as coefficients reflect the fact that several of our indices relied either partially our entirely upon categorical variables. Although the distributions of results differ at some points, at each percentile measured there is no treatment effect 3. We perform a Komolgorov-Smirnov test for the equality of distributions between treatment and control households for each indexed outcome in both endlines. The *p*-value for each of these 20 tests is 0.000.

physical and mental health: Spending on better food and needed health expenditures early in the program may have been a valuable investment.

The ultimate goal of the program is to durably increase consumption, not merely to increase asset holding. Using total consumption as the measure for benefits, the total benefit-cost ratios presented in row 11 indicate that with the exception of Honduras, the programs all have benefits greater than their costs (ranging from 133% in Ghana to 433% in India).

We explore the sensitivity of this conclusion to some of our crucial assumptions. First, we calculate the internal rate of return, to assess at what social discount rate costs equal benefits. They are 13.3% (Ethiopia), 6.9% (Ghana), not applicable (Honduras), 23.4% (India), 9.5% (Pakistan), and 7.5% (Peru). Second, we calculate in row 19 the rate at which nondurable consumption must dissipate after year 3 (rather than persist into the future) in order for benefits to equal costs. Third, in the subsequent two rows, 20 and 21, we show the sensitivity of the benefit-cost ratio to alternative social discount rates of 7 and 10%. Benefits con-

tinue into the future while the costs are front-loaded, so the benefit-cost ratios decline with increases in the assumed social discount rate. See supplementary text 5 for details on the cost-benefit analysis calculations.

Mechanisms

As mentioned, the results are similar to the positive results of the evaluation of the BRAC program in Bangladesh (*6*). Two other studies of cash transfers and support for self-employment, both in Uganda, find similar results. Blattman *et al.* (*33*) find that a program that provided a $150 grant (PPP US$401) toward a nonfarming self-employment activity along with training and follow-up guidance to very poor women in conflict-affected regions increased consumption, cash earnings, labor supply, and nonfarm self-employment. Blattman *et al.* (*34*) find that a program that provided both training and support and a cash grant to youth increased business assets by 57%, work hours by 17%, and earnings by 38%. The programs that we studied differ from those reported on in (*33*) and (*34*)

on a few dimensions: choice of sample frame (representative ultrapoor, versus unemployed young men or poor women); the level of intervention [household, versus group-level investments as in (*34*)]; and the integration of other components (health and access to savings). Nevertheless, these studies add to an emerging picture from a variety of countries that these types of programs can be effective.

Although we see impacts on all outcomes, more work is needed on the mechanisms that underlie the positive impacts. The core fact is that a time-limited big push led to a sustained increase in consumption and income. One common way to think about the effect of a big push is through the lens of the large, primarily theoretical, literature on poverty traps (*35*). In such models, the combination of constraints and incentives faced by the poor act to keep them in place, ensuring that any small improvement in their well-being quickly dissipates. Only a big push that appreciably relaxes those constraints can set off a virtuous cycle where the beneficiaries move to an entirely different trajectory.

The fact that the effects of the program seem durable supports the interpretation that the program unlocked a poverty trap. Nevertheless, the average effects are not very large and do not correspond to our intuitive sense of what it would mean to be liberated from the trap of poverty. There are several possible ways to resolve this tension:

First, it could be that there is no trap—but rather what one might call a "poverty flat," a world in which small changes persist but neither unleash continued improvement, thus leading to large longer term changes, nor dissipate rapidly.

Second, it is possible that this particular trap is small—the beneficiaries have gotten out of it, only to join the broader mass of the poor, who might be in some other, bigger, trap.

Third, it is worth recalling that the theory predicts that the effect of a push will be heterogeneous, unless the push is simply enormous. Those who are closer to the edge of the trap will exit, but the rest will just slowly fall back in. Perhaps this is what happened—the heterogeneity in the impacts that we see across the distribution lends some support to this hypothesis. Even among the very poor households targeted by these programs, the impacts on income and revenues and consumption, though positive everywhere, are lower at the bottom of the distribution. Because everyone was offered the same menu of assets, under the standard assumptions of constant or decreasing returns to the assets and homotheticity of preferences, we would expect those impacts to be either constant or decreasing. Instead, it appears that the poorest of the poor either have a lower return to the asset, or that they chose to consume more of it, or both. The differences in terms of final asset accumulation are very large: by endline 2, the point estimate of the impact of the program at the 90th percentile of the asset index is more than 10 times that at the 10th percentile.

Fourth, another source of heterogeneity, the level of patience or return on investment, could also help to explain why the average impact is both durable and yet not very large. The more patient or productive would use the asset transfer as a springboard to accumulate more assets and permanently be on a different consumption trajectory, whereas the others would sell off some part of the transferred assets to consume more than they earn, and perhaps eventually end up where they started. In rows 13 to 17 of Table 4, we use quantile treatment effects to generate the total gain in assets at different quantiles and present them relative to value of the original transfer. The ratio of the asset gain to the cost of the transfer is less than 1 at all tested quantiles in every country except Ethiopia (above 1 for the 75th and 90th percentiles) and India (above 1 for the 90th percentile), suggesting that the general pattern of eating into assets holds at every quantile. Therefore, we do not find strong evidence for this kind of heterogeneity.

But what would be the specific nature of a trap? One standard narrative for a poverty trap essentially says that poor people remain poor because they cannot afford enough food to make them strong enough to be productive (36). This theory has been discounted in recent years on grounds of empirical plausibility—essentially most poor people can afford to spend more on food if that were a priority for them (37). However, this may be a case where that theory does apply, at least to some participants in the program, because these people are poorer than most poor people and may actually not be able to afford enough food (Table 1 reports the daily per capita calories that could be purchased if baseline expenditures were allocated solely to staple grains). As noted, for the very poor, we do see large increases in food security. Moreover, the elasticity of food consumption is greater than 1 in the overall experimental population. However, this is driven by the food expenditure responses in Ghana, Honduras, and Peru. In the three other countries, the proportional increase in nonfood consumption is either similar to or greater than the proportional increase in food consumption, and we see a persistent effect there as well. Moreover, we see even larger and persistent impact even at the quantiles where there is no impact on food security (although it could still be that they are eating more nutritional food). So nutrition cannot be the whole story, although it may well be a part.

An alternative view of the poverty trap emphasizes underinvestment by the poor, either because they are unable to borrow enough to be able to make the necessary investment or because they find it too risky (35, 38, 39). For the poorest within our study, we do not find an impact on financial inclusion, and we find a weaker impact on assets. This is consistent with the need to satisfy some asset threshold before being eligible for credit, one of the key ingredients for a credit-based poverty trap. Again, however, the evidence for the existence of such traps is not very strong. There is a growing body of evidence on microcredit that was intended to improve credit access among the segment of the population only slightly less poor than our targeted group. For example, Banerjee et al. (40) review six randomized studies of microcredit in six different countries (41–46) and conclude that although microcredit loans sometimes lead to an increase in business activity, the effect on average business profits is much more muted, and there is no effect of an impact on consumption over a 1- to 3-year time period. That is, for the average poor person, better access to microcredit does not seem to generate the kind of sustained consumption gains that we see with this program, suggesting that credit alone is not the explanation.

The programs that we analyze are different from microcredit in multiple ways. Here, households did not need to repay. This might have encouraged them to take more risks and genuinely invest themselves in the activity. Or it could be the training and personal encouragement that produced this effect on their behavior. Or these people may be in a different economic position—the microcredit borrowers already have an occupation and an income and are merely trying to expand, not start a new activity. The participants in the Graduation programs are starting new activities, more or less from nothing. These are all important possibilities that deserve exploration.

But perhaps we need to go beyond these standard theories. There are now behavioral theories of poverty traps that give an important role to positive expectations of the future (47, 48). We do see some improvement in the self-reported well-being of the beneficiaries, which, at endline 1, are visible at all level of the distribution except for the 90th percentile. Much more detailed psychological measurement would be necessary to fully understand this result and its underlying mechanisms. Perhaps this program worked by making the beneficiaries feel that they mattered, that the rest of society cared about them, that with this initial help they now had some control over their future well-being, and, therefore, the future could be better.

These positive results leave us with a number of important questions. First, is it better to deliver physical assets and support, rather than pure cash transfers? There is evidence—from an RCT evaluation of the GiveDirectly program in Kenya, which transferred on average PPP US $720 to poor households, either monthly or in one lump sum—that pure cash transfers also have positive impacts on consumption, food security, asset holdings in the short run (including productive assets), and on psychological well-being (49). Similarly, de Mel et al. (50) find that a cash (or in-kind) transfer to existing self-employed individuals in Sri Lanka has a persistent positive effect on self-employment profits 4.5 to 5.5 years later. Because it is cheaper and easier to just deliver cash rather than physical assets and training, and the initial consumption increases from Kenya seem to be higher than what we observe after 2 and 3 years, it would be useful to have a direct comparison of the effects of these programs. The Ghana experimental design does include a comparison of the Graduation program to merely an asset transfer, and the results are forthcoming.

However, the Kenya results are unfortunately not quite comparable, because the time to follow-up was much shorter (4 months). The Kenya study did employ random variation in survey timing to try to examine persistence of the impact, and found that the estimated treatment effect was reduced by about half from 1 month after the transfer to 7 months; however, this reduction was not statistically significant. We observe no decline in the gain in consumption per capita almost 3 years after the asset transfer. If the effects of one-time transfers dissipate rapidly in one case and are permanent in the other, this obviously has major consequences for the comparative cost-benefit analyses of the two programs. The evolution of the impacts over time over a longer horizon thus needs to be further explored, both for pure cash transfer programs and for these broader programs.

Second, how important was the training and coaching as a component in the full intervention? This is a particularly important component

to test, because its costs are on average twice that of the direct transfer costs, and because operating at scale requires quality hiring, training, and staff supervision. As discussed above, we do not have experimental variation with which to test this question. Evidence from elsewhere suggests that the household visits, which are a large expenditure, may not be a cost-effective component. In Blattman *et al.* (*33*), for example, variation between zero and five household visits did not generate, after 9 months, large differences in income outcomes (but did lead to higher investment). Furthermore, a meta-analysis of self-employment training programs has found mixed but rarely transformative impacts from training (*51*).

This brings us to the next key question: How long will these results persist? This will not be known until some participants are followed for a longer period of time, but there are a number of encouraging signs. First, the effect on consumption does not decline over time as one would have expected had the program not led to long-term increases in income. Similarly, the increase in consumption was not generated by merely spending down the asset provided (*52*). Second, treatment households have more productive assets and have increased their labor supply 1 year after the program ends, and in some countries have diversified out of the original asset that was provided. Finally, in Bangladesh (*3*), households were followed for 2 more years after the end of the period of support, and the study continues to find robust impacts on consumption, productive assets, and earnings.

Another issue is the potential for externalities or general equilibrium effects, both positive and negative, from the program. Transferring (often) the same productive asset to many households in a small village may generate a negative externality on other asset owners, if, for example, the transfers result in a fall in the price of cows or milk. On the other hand, the benefits that accrue to the treatment households may be shared with others, as has been observed from a conditional cash transfer program in Mexico (*53*). It is worth pointing out that the program is designed to serve few people (the poorest) within each village, and in that sense, the current design probably picks up a fair share of the possible externalities. In endline 2, the evidence from the three sites where randomization allowed the examination of spillover shows no effects on primary economic outcomes such as consumption and income, and no significant effects at the 5% level on any variable after accounting for multiple hypothesis testing.

These questions will become ever more important as these programs scale. The programs studied here were implemented at relatively small scale, and typically by NGOs. Moving forward, to reach the largest numbers of very poor households, either governments will have to implement the programs, or governments will fund implementation via subcontracts to local NGOs. Note that implementing the program at larger scale will mainly require increasing geographic coverage, rather than increasing the proportion of households reached in each village. This suggests

that the smallish general equilibrium effects observed here are probably also representative of what one would expect from a larger program. Hence, the positive impacts generated by these programs are likely to be predictive of what a government could expect, if implemented similarly but at larger scale.

REFERENCES AND NOTES

1. World Bank, "The World Bank Annual Report 2013" (Washington, DC, 2013); https://openknowledge.worldbank.org/handle/10986/16091).
2. "A new global partnership: Eradicate poverty and transform economies through sustainable development" (United Nations High Level Panel, 2013); www.un.org/sg/management/pdf/HLP_P2015_Report.pdf.
3. S. D. Ashley, S. J. Holden, P. B. S. Bazeley, Livestock in Development (Organisation), *Livestock in Poverty-Focused Development* (Livestock in Development, Crewkerne, UK, 1999); www.theidlgroup.com/documents/IDLRedbook_000.pdf.
4. J. Dreze, Poverty in India and the IRDP Delusion. *Econ. Polit. Wkly.* 25 (29 September 1990); www.epw.in/review-agriculture/poverty-india-and-irdp-delusion.html.
5. R. V. Pulley, Making the poor creditworthy: A case study of the Integrated Rural Development Program. *World Bank Discuss. Pap.* 58 (1989); www-wds.worldbank.org/external/default/WDSContentServer/IW3P/IB/2000/06/28/000178830_98101903572627/Rendered/PDF/multi_page.pdf.
6. O. Bandiera, R. Burgess, S. Gulesci, I. Rasul, M. Sulaiman, Can entrepreneurship programs transform the economic lives of the poor? *LSE Work. Pap.* (2013); http://sticerd.lse.ac.uk/dps/eopp/eopp43.pdf.
7. A. U. Ahmed, M. Rabbani, M. Sulaiman, N. C. Das, The impact of asset transfer on livelihoods of the ultra poor in Bangladesh. *BRAC Res. Monogr. Ser.* 39 (2009); http://research.brac.net/new/component/k2/livelihoods.
8. M. S. Emran, V. Robano, S. C. Smith, Assessing the Frontiers of Ultrapoverty Reduction: Evidence from Challenging the Frontiers of Poverty Reduction/Targeting the Ultra-poor, an Innovative Program in Bangladesh. *Econ. Dev. Cult. Change* 62, 339–380 (2014). doi: 10.1086/674110
9. N. C. Das, F. A. Misha, Addressing extreme poverty in a sustainable manner: Evidence from CFPR programme. *BRAC CFPR Work. Pap.* 19 (2010); http://research.brac.net/reports/cfpr_wp19.pdf.
10. In total, 10 sites were identified and programs implemented. Four are not included here for the following reasons: Yemen conducted a randomized evaluation, but has been delayed due to the civil conflict; a second India site, implemented by the microlender SKS, also conducted a randomized evaluation, but by a different set of researchers. It has not been included due to lack of comparability of data. They find no impact, due either to mistargeting individuals engaged in the labor markets, thus the grants generated substitution away from other income-generating activity; portfolio reallocation, in which productive asset grants were sold to pay down debt; or other data issues leading to lack of conclusive evidence (*21*). Two sites (Haiti, implemented by Fonkoze, and a second in West Bengal, India, implemented by Trickle-Up) did not employ experimental methods to measure their impact and are thus not reported here. Ford and CGAP also coordinated ethnographic research in several of the sites.
11. In Ghana, households received consumption support during the 6-month lean season for both years. They therefore received consumption support over the course of 2 years, but the total duration of support received was 14 months.
12. V. Alatas, A. Banerjee, R. Hanna, B. A. Olken, J. Tobias, Targeting the poor: Evidence from a field experiment in Indonesia. *Am. Econ. Rev.* 102, 1206–1240 (2012). doi: 10.1257/aer.102.4.1206; pmid: 25197099
13. Grameen Foundation, PPI Construction; www.progressoutofpoverty.org/ppi-construction.
14. All exchange rates used in this paper are in PPP terms. We convert all monetary figures from local currency to USD PPP, at the year of the program's inception for cost data, and the year of the relevant survey for our results data. We then convert from USD PPP for that year to 2014 USD by multiplying by the ratio of the 2014 U.S. Consumer Price Index (CPI) to the U.S. CPI for the year in question. We use the following PPP rates: for Ethiopian Birr (ETB) in 2010, 2012, and 2013, 4.18, 6.45, and 6.66, respectively; for Ghanaian Cedis

(GHS) in 2011, 2012, and 2014, 0.70, 0.79, and 0.91, respectively; for Honduran Lempiras (HNL) in 2009, 2012, and 2013, 9.77, 10.13, and 10.15, respectively; for Indian Rupees in 2007, 2009, and 2010, 11.76, 13.20, and 14.21, respectively; for Pakistan Rupees (PKR) in 2008, 2011, and 2013, 15.84, 24.35, and 26.83, respectively; for Peruvian Nuevo Soles (PEN) in 2011, 2013, and 2014, 1.48, 1.53, and 2.03, respectively. The U.S. CPIs used for 2007 to 2014 are, respectively, 207.3, 215.303, 214.537, 218.056, 224.939, 232.957, and 236.9111.
15. A. Deaton, O. Dupriez, Purchasing power parity exchange rates for the global poor. *Am. Econ. J. Appl. Econ.* 3, 137–166 (2011). doi: 10.1257/app.3.2.137
16. J. B. Rotter, Generalized expectancies for internal versus external control of reinforcement. *Psychol. Monogr.* 80, 1–28 (1966). doi: 10.1037/h0092976; pmid: 5340840
17. We present bounds for our treatment effects, depending on different assumption with respect to attrition, discussed in Results section.
18. In all countries, individuals were grouped into geographic block strata, which are included here as dummies for each block. In Honduras, Peru, and Ghana, rerandomization was performed to ensure balance on a set of variables. These variables are included as controls.
19. J. Kling, J. Liebman, L. Katz, Experimental analysis of neighborhood effects. *Econometrica* 75, 83–119 (2007). doi: 10.1111/j.1468-0262.2007.00733.x
20. The ITT estimators can thus be interpreted as effect sizes relative to the control group.
21. J. Morduch, S. Ravi, J. Bauchet, "Failure vs. Displacement: Why an Innovative Anti-Poverty Program Showed No Net Impact" (CEI Working Paper Series 2012–05, Center for Economic Institutions, Institute of Economic Research, Hitotsubashi University, Tokyo, 2012); www.ier.hit-u.ac.jp/primced/documents/No32-dp_up_Pdf_2012_000.pdf.
22. M. Anderson, Multiple inference and gender differences in the effects of early intervention: A reevaluation of the Abecedarian, Perry Preschool, and Early Training Projects. *J. Am. Stat. Assoc.* 103, 1481–1495 (2008). doi: 10.1198/016214508000000841
23. The significance levels reported in Table 3 (* 10%, ** 5%, *** 1%) correspond to the naïve *p*-values, which can be inferred from the coefficient and standard errors.
24. Mental health questions were not asked in Pakistan in endline 1, whereas in India, women's empowerment was not asked about in endline 2, and so in both cases the correction is for only 9 outcome families when reporting country-specific indexed family outcomes in tables S3a to S3f . However, it is for 10 families in all other cases.
25. S. Subramanian, A. Deaton, The demand for food and calories. *J. Polit. Econ.* 104, 133–162 (1996). doi: 10.1086/262020
26. This is gross livestock revenue, not income or net profit. On the expenditure side, it does not include fodder costs, which were not measured everywhere and were measured with considerable noise even where they were measured. On the profit side, it does not include unrealized capital gains (for example, as more calves are born, if they are not sold).
27. In some sites, individuals were shown a 10-rung ladder and asked, "How would you describe your satisfaction with life? If the top rung of this ladder (10) represents very satisfied and the lowest rung (1) represents very dissatisfied, where would you place yourself?" In others, individuals were shown five images of faces, and asked, "Which picture describes the current satisfaction level with your life, if the smiling face is the most satisfied and the crying/frowning face is the least satisfied?" In the latter case, the question was also scaled 1 to 10.
28. P. Brickman, D. T. Campbell, Hedonic relativism and planning the good society. *Adapt.-Level Theory*, 287–305 (1971).
29. J. Horowitz, C. Manski, Nonparametric analysis of randomized experiments with missing covariate and outcome data. *J. Am. Stat. Assoc.* 95, 77–84 (2000). doi: 10.1080/01621459.2000.10473902
30. D. S. Lee, Training, wages, and sample selection: Estimating sharp bounds on treatment effects. *Rev. Econ. Stud.* 76, 1071–1102 (2009). doi: 10.1111/j.1467-937X.2009.00536.x
31. Bandhan is also probably the organization that has the strongest links to BRAC, and the Bandhan program may have been run more similarly to BRAC's than the others. BRAC staff trained Bandhan staff at the onset of the program, for example.
32. The World Bank, "Staff guidance note on the application of the joint bank-fund debt sustainability framework for low-income countries" (82566, The World Bank, 2013), pp. 1–64.

33. C. Blattman, E. Green, J. Annan, J. Jamison, The returns to cash and microenterprise support among the ultra-poor: A field experiment. *Columbia Univ. Work. Pap.* (2014); http://papers.ssrn.com/sol3/papers.cfm?abstract_id=2439488.

34. C. Blattman, N. Fiala, S. Martinez, Generating skilled self-employment in developing countries: Experimental evidence from Uganda. *Q. J. Econ.* **129**, 697–752 (2014). doi: 10.1093/qje/qjt057

35. A. V. Banerjee, The two poverties. *Nord. J. Polit. Econ.* **26**, 129–141 (2000).

36. P. Dasgupta, D. Ray, Inequality as a determinant of malnutrition and unemployment: Theory. *Econ. J.* **96**, 1011–1034 (1986). doi: 10.2307/2233171

37. A. Banerjee, A. V. Banerjee, E. Duflo, *Poor Economics: A Radical Rethinking of the Way to Fight Global Poverty* (PublicAffairs, New York, 2011).

38. O. Galor, J. Zeira, Income distribution and macroeconomics. *Rev. Econ. Stud.* **60**, 35–52 (1993). doi: 10.2307/2297811

39. A. Banerjee, A. Newman, Occupational choice and the process of development. *J. Polit. Econ.* **101**, 274–298 (1993). doi: 10.1086/261876

40. A. Banerjee, D. Karlan, J. Zinman, Six randomized evaluations of microcredit: Introduction and further steps. *Am. Econ. J. Appl. Econ.* **7**, 1–21 (2015). doi: 10.1257/app.20140287

41. M. Angelucci, D. Karlan, J. Zinman, Microcredit impacts: Evidence from a randomized microcredit program placement experiment by Compartamos Banco. *Am. Econ. J. Appl. Econ.* **7**, 151–182 (2015). doi: 10.1257/app.20130537

42. O. Attanasio, B. Augsburg, R. De Haas, E. Fitzsimons, H. Harmgart, The impacts of microfinance: Evidence from joint-liability lending in Mongolia. *Am. Econ. J. Appl. Econ.* **7**, 90–122 (2015). doi: 10.1257/app.20130489

43. B. Augsburg, R. De Haas, H. Harmgart, C. Meghir, The impacts of microcredit: Evidence from Bosnia and Herzegovina. *Am. Econ. J. Appl. Econ.* **7**, 183–203 (2015). doi: 10.1257/app.20130272

44. A. Banerjee, E. Duflo, R. Glennerster, C. Kinnan, The miracle of microfinance? Evidence from a randomized evaluation. *Am. Econ. J. Appl. Econ.* **7**, 22–53 (2015). doi: 10.1257/app.20130533

45. B. Crépon, F. Devoto, E. Duflo, W. Pariente, Estimating the impact of microcredit on those who take it up: Evidence from a randomized experiment in Morocco. *Am. Econ. J. Appl. Econ.* **7**, 123–150 (2015). doi: 10.1257/app.20130535

46. A. Tarozzi, J. Desai, K. Johnson, The impacts of microcredit: Evidence from Ethiopia. *Am. Econ. J. Appl. Econ.* **7**, 54–89 (2015). doi: 10.1257/app.20130475

47. A. Banerjee, S. Mullainathan, The shape of temptation: Implications for the economic lives of the poor. *Natl. Bur. Econ. Res.* **15973** (2010); www.nber.org/papers/w15973.

48. B. D. Bernheim, D. Ray, S. Yeltekin, Poverty and self-control. *Natl. Bur. Econ. Res.* **18742** (2013); www.nber.org/papers/w18742.

49. J. Haushofer, J. Shapiro, Welfare effects of unconditional cash transfers: Evidence from a randomized controlled trial in Kenya. *MIT Work. Pap.* (2013) http://www.princeton.edu/~joha/publications/Haushofer_Shapiro_UCT_2013.pdf).

50. S. de Mel, D. McKenzie, C. Woodruff, One-time transfers of cash or capital have long-lasting effects on microenterprises in Sri Lanka. *Science* **335**, 962–966 (2012). pmid: 22363007

51. D. McKenzie, C. Woodruff, What are we learning from business training and entrepreneurship evaluations around the developing world? *World Bank Policy Res. Work. Pap.* **6202** (2012).

52. Nor is the consumption increase simply the permanent income hypothesis in operation. If a household were capable of smoothing the income shock from the transfer perfectly, the increased long-term consumption would simply be the interest rate times the value of the assets transferred. The consumption increases we are observing are considerably higher than that.

53. M. Angelucci, G. De Giorgi, Indirect Effects of an Aid Program: How Do cash transfers affect ineligibles' consumption? *Am. Econ. Rev.* **99**, 486–508 (2009). doi: 10.1257/aer.99.1.486

ACKNOWLEDGMENTS

SUPPLEMENTARY MATERIALS

www.sciencemag.org/content/348/6236/1260799/suppl/DC1
Supplementary Text 1 to 4
Figs. S1 to S3
Tables S1 to S8

REPORTS

VOLCANOLOGY

The Yellowstone magmatic system from the mantle plume to the upper crust

Hsin-Hua Huang,[1,2]* Fan-Chi Lin,[1] Brandon Schmandt,[3] Jamie Farrell,[1] Robert B. Smith,[1] Victor C. Tsai[2]

The Yellowstone supervolcano is one of the largest active continental silicic volcanic fields in the world. An understanding of its properties is key to enhancing our knowledge of volcanic mechanisms and corresponding risk. Using a joint local and teleseismic earthquake P-wave seismic inversion, we revealed a basaltic lower-crustal magma body that provides a magmatic link between the Yellowstone mantle plume and the previously imaged upper-crustal magma reservoir. This lower-crustal magma body has a volume of 46,000 cubic kilometers, ~4.5 times that of the upper-crustal magma reservoir, and contains a melt fraction of ~2%. These estimates are critical to understanding the evolution of bimodal basaltic-rhyolitic volcanism, explaining the magnitude of CO_2 discharge, and constraining dynamic models of the magmatic system for volcanic hazard assessment.

The interaction of the North American Plate moving southwestward across a mantle plume created the Snake River Plain, a bimodal basalt-rhyolite volcanic system dating to 16.5 million years ago (Ma) (1). The Yellowstone volcanic field that sits at the eastern end of the plain is the youngest manifestation of the hotspot and is characterized by extensive earthquakes (2, 3), episodic ground deformation (4), high heat flux averaging 2000 mW m^{-2} (2, 5), and the largest continental hydrothermal system in the world (6, 7). The most recent cataclysmic eruption occurred at 0.64 Ma and created the 40 km × 60 km Yellowstone caldera, which is filled with rhyolitic lava flows as young as 70,000 years (Fig. 1). Earlier teleseismic studies have imaged a west-northwest–dipping plume extending into the top of the lower mantle (8–11). Local earthquake tomography and waveform modeling studies have revealed an upper-crustal magma reservoir between 5 and 16 km depth (3, 12, 13), of which the shallowest portion correlates with the largest area of hydrothermal activity and extends 15 km northeast of the caldera (3). Even with a large volume of >4000 km^3 and a high melt fraction of up to 32% (2, 3, 13), this upper-crustal reservoir cannot account for the large CO_2 flux of 4.5×10^7 kg daily and requires additional input of basaltic magma invading the lower to middle crust (6, 7). Moreover, it is unclear how the mantle plume interacts with the crustal volcanic system. The connection between the shallow magma reservoir (above 16 km depth) and the deep mantle plume (below 60 km depth) is therefore a critical component to understand the entire Yellowstone magmatic system but has never been imaged distinctly, despite other geophysical and geologic

[1]Department of Geology and Geophysics, University of Utah, Salt Lake City, UT 84112, USA. [2]Seismological Laboratory, California Institute of Technology, Pasadena, CA 91125, USA. [3]Department of Earth and Planetary Sciences, University of New Mexico, Albuquerque, NM 87131, USA.
*Corresponding author. E-mail: hsinhua.huang@utah.edu
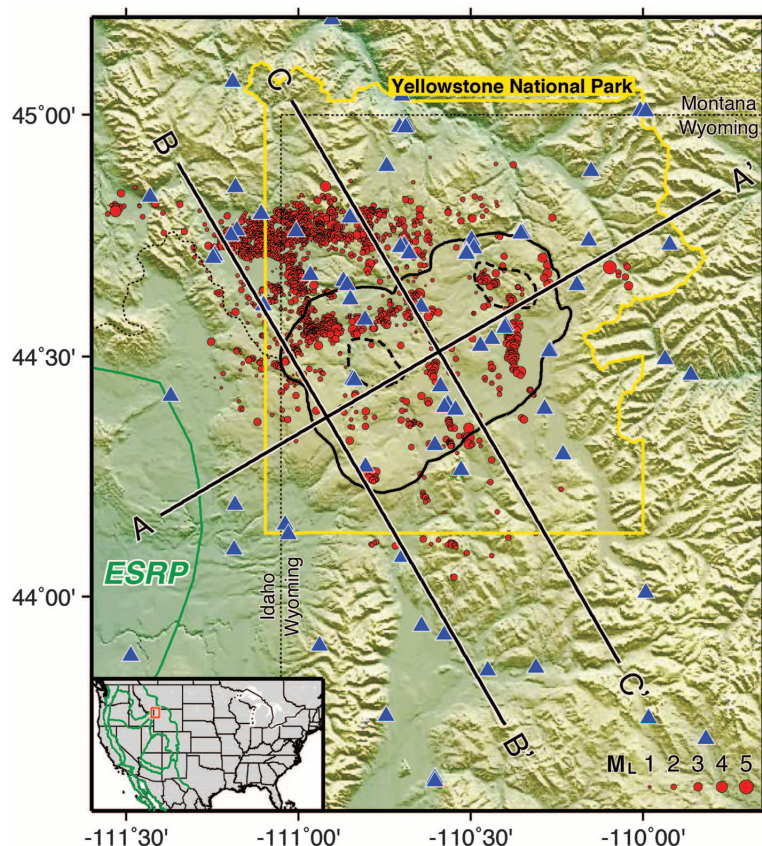
Fig. 1. Map of the seismic stations used in this study and the P-wave velocity cross-section locations in the Yellowstone area. Stations and earthquakes are denoted by blue triangles and red dots, respectively. Black solid and dashed lines outline the Late Quaternary Yellowstone caldera and resurgent domes. Green lines represent the tectonic division of the Eastern Snake River Plain (ESRP). Yellow and thin dotted lines are the border of Yellowstone National Park and the surrounding state borders, respectively. Locations of the cross sections in Fig. 3 are shown by thick black lines with labels. The inset map shows the location of the Yellowstone area (red box) and the major tectonic boundaries (green lines) in the western United States.
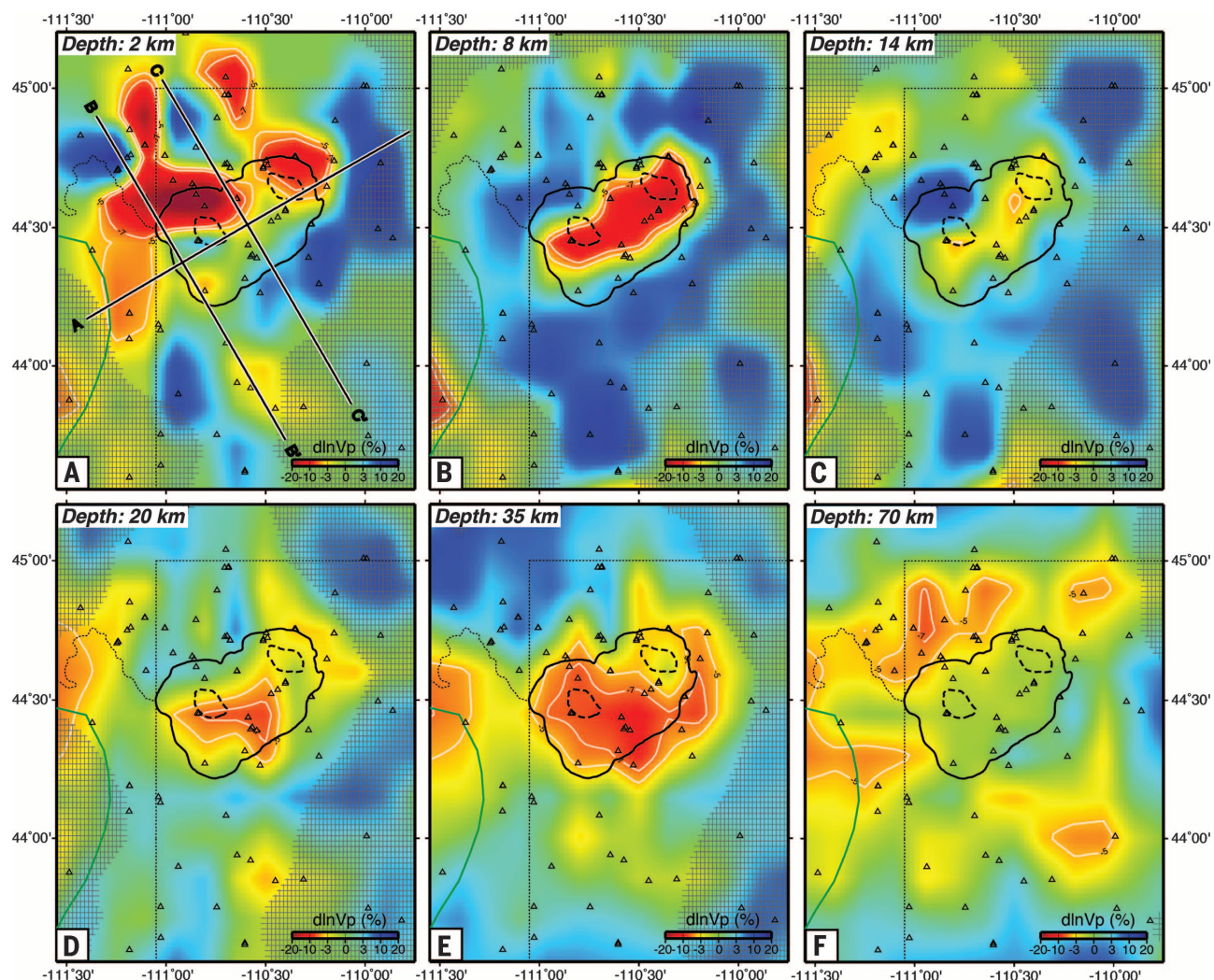
Fig. 2. Depth slices of the Yellowstone tomographic *P*-wave model. (**A** to **E**) Crustal velocity structures; (**F**) upper-mantle velocity structure. Black solid and dashed lines outline the 0.64 Ma caldera and resurgent domes. The green line is the northeast end of the Eastern Snake River Plain. White lines denote the 5% and 7% *P*-wave velocity reduction contours. Poorly resolved areas are shaded according to the index of resolvability, *R*, converted from the checkerboard test results (*25*).
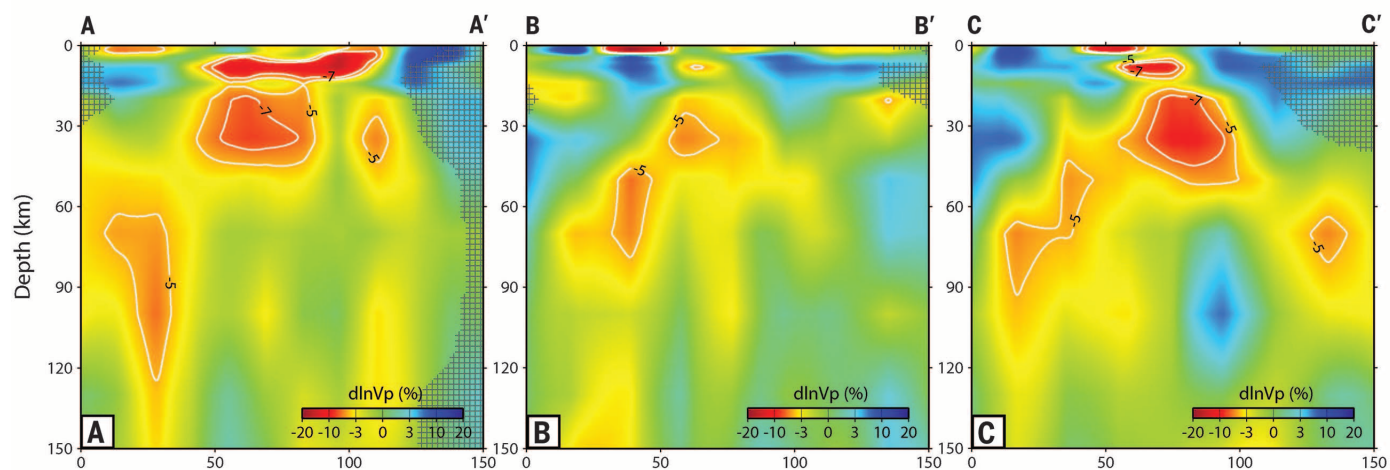
Fig. 3. Cross sections of the Yellowstone tomographic *P*-wave model. (**A** to **C**) The crustal magmatic reservoirs and the mantle plume are demonstrated in northeast-southwest (A) and northwest-southeast [(B) and (C)] directions, respectively. Map-view locations of the cross sections are shown in Fig. 1. White lines denote the 5% and 7% *P*-wave velocity reduction contours. Poorly resolved areas are shaded according to the index of resolvability, *R*, converted from the checkerboard test results (*25*).

evidence that hypothesizes the presence of a continuous crustal magma body (2, 5, 7).

Imaging the position and size of the entire volcanic plumbing system is also important to constrain magmatic dynamics modeling for further hazard assessment (14). Many local seismic array experiments have been conducted on volcanoes such as Askja, Iceland (15); Axial, Juan de Fuca mid-ocean ridge (16); Kilauea, Hawaii (17); and Mount St. Helens, Washington (18). A common observation of these experiments is an imaged shallow low-velocity body (LVB) at depths of 5 to 10 km, which is often interpreted as a magma reservoir. Several of these studies also image the top of a second LVB at greater crustal depths (18, 19); however, they usually quickly lose resolution with depth because of the limited array aperture and the shallowly distributed earthquakes (often less than ~10 km depth). Large arrays for teleseismic tomography can only focus on mantle images and poorly resolved crustal structures. A complete framework of the mantle-crust volcanic system under volcanoes has not yet been elucidated.

By combining data from the dense seismic arrays of the Yellowstone, Teton, and Snake River Plain (SRP) regional seismic networks, the NOISY array (20), and the wide-aperture EarthScope Transportable Array (Fig. 1), we present an image of the entire volcanic plumbing system beneath the Yellowstone caldera and reveal a large basaltic magma reservoir in the lower to middle crust by using a joint tomographic inversion of local and teleseismic earthquake data (21–23). The seismic data used in this study were compiled from previous studies (3, 24) and consist of 47,815 P-wave first arrivals from 4520 local earthquakes and 4605 relative arrival times from 329 teleseismic earthquakes. A local earthquake inversion is first conducted to obtain a three-dimensional initial crustal model and reduce the dominance of the local data prior to the joint inversion (25).

We found a large east-northeast–west-southwest elongated LVB beneath the Yellowstone caldera (Fig. 2, A to C, and Fig. 3A) at depths shallower than 20 km, consistent with previous studies (3, 25). However, at depths of 20 to 50 km, another larger LVB with >5% P-wave velocity (V_P) reduction also emerges in our model (Fig. 2, D and E, and Fig. 3, A and C). From cross section AA´ (Fig. 1 and Fig. 3A), it is clear that this deeper LVB is immediately beneath the shallow LVB. The existence of the lower-crustal LVB and the separation between the two imaged crustal LVBs are validated through characteristic-model synthetic tests and finite-frequency analysis (25), indicating that the deep crustal LVB is a separate magma reservoir in the middle to lower crust, based on a Moho depth of ~45 km in this area (26). The LVB separates into two zones northwest and southeast of the caldera at mantle depths of ~70 km (Fig. 2F). The orientation of the northwestern portion agrees with the extension of the SRP in a northeast-southwest direction, implying the track of the North American Plate across the Yellowstone plume (2, 10). In cross sections BB´ and CC´, this low-velocity zone that dips ~60° northwestward is consistent with the plume geometry determined in previous studies (8–10). In contrast, the southeastern low-velocity zone is relatively smaller and localized, terminating at a depth of 100 km (Fig. 3C).

The V_P reduction of >5% within the imaged crustal LVBs is difficult to explain by temperature and composition alone and implies the presence of melts (25). We assume a 5% V_P reduction as being diagnostic of partial melt (3) to quantitatively estimate the volume of crustal melt. Weaker anomalies may also be partly explained by partial melt, but tradeoffs with temperature or composition variations and tomographic resolution prevent these weaker anomalies from being robustly interpreted as melt. Using this conservative proposition results in volume estimates of ~46,000 km^3 for the lower-crustal LVB and ~10,000 km^3 for the upper-crustal LVB. These estimates agree well with the sizes and depths of the basaltic and rhyolitic magma reservoirs interpreted by geochemical studies (6, 7, 27). The melt fraction of the upper-crustal LVB has been previously estimated to range from 5 to 32% (2, 3, 13). With an average V_P of 5.21 km/s calculated over the volume of the upper-crustal LVB, we estimate a melt fraction of ~9% (25), based on a velocity-melt fraction relation derived for the Yellowstone granite-rhyolite-melt system (13). For the lower-crustal LVB, we assume similar elastic properties between the lower crust and the uppermost mantle and use previously proposed partial derivatives of V_P with respect to melt fraction for a peridotite-basalt-melt system (table S2). Given the calculated average V_P reduction of 6.56%, a ~2% fraction of basaltic partial melts is preferred (25). Multiplying the melt fraction of each LVB by its volume gives ~900 km^3 of rhyolitic melts and also ~900 km^3 of basaltic partial melts. These estimates provide an overall volume estimate that is comparable to the explosive material volumes of the last three Yellowstone giant eruptions at 2.1 Ma (2500 km^3), 1.3 Ma (280 km^3), and 0.64 Ma (1000 km^3) (1). Although lower-crustal basaltic melts are not expected to contribute to the caldera-forming eruptions, and the upper-crustal melts are unlikely to erupt at one time, both melt volumes can feed smaller eruptions. Assuming a CO_2 degassing rate of 4.5×10^7 kg per day, 50% of which comes from subsurface magma discharge (28), the addition of a basaltic lower-crustal reservoir can provide a sufficient influx (25) for the reported ~15,000-year history of the intensive hydrothermal degassing system (29).

Our seismic images depict characteristics of the entire Yellowstone magmatic system from the upper mantle to the crust (Fig. 4) in which the west-northwest–dipping plume is the magmatic source that generates the mafic/basaltic partial melts that intrude into the lower crust, fractionate, and melt the crust to produce more silicic magma, and then intermittently ascend to shallower depths to form the dominantly rhyolitic reservoir at depths of 4 to 14 km beneath the Yellowstone caldera. Because volcanic sills act as traps that accumulate upward-migrating magmatic fluids to form a magma reservoir (2, 3, 6, 30–32), the two large LVBs observed in our model suggest the presence of two sill complexes in the upper and lower crust that are likely linked by dikes. This layered structure of basaltic intrusions was also suggested for the volcanic crustal structure in the nearby eastern Snake River Plain (33). This model may thus be representative of other bimodal basaltic-rhyolitic volcanoes around the
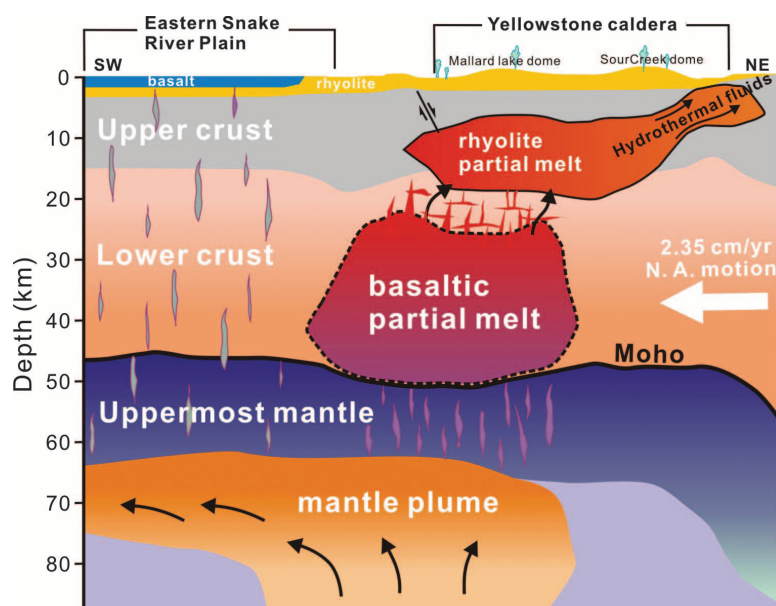
Fig. 4. Schematic model for the Yellowstone crust–upper mantle magmatic system. The orientation of the model is along the cross section AA´ in Fig. 3. The geometry of the upper- and lower-crustal magma reservoirs is based on the contour of 5% V_P reduction in the tomographic model. The dashed outline of the lower-crustal magma reservoir indicates the larger uncertainties in its boundaries relative to that of the upper reservoir (25). The white arrow indicates the North American plate motion of 2.35 cm/year.

world. The estimates of volume and geometry of crustal magma reservoirs may also be critical for realistic modeling magmatic system dynamics (*14*) that in turn could provide further information for volcanic hazard models.

REFERENCES AND NOTES

1. R. L. Christiansen, *U.S. Geol. Surv. Prof. Pap. 729-G*, 145 (2001).
2. R. B. Smith *et al.*, *J. Volcanol. Geotherm. Res.* **188**, 26–56 (2009).
3. J. Farrell, R. B. Smith, S. Husen, T. Diehl, *Geophys. Res. Lett.* **41**, 3068–3073 (2014).
4. W. L. Chang, R. B. Smith, C. Wicks, J. M. Farrell, C. M. Puskas, *Science* **318**, 952–956 (2007).
5. K. R. DeNosaquo, R. B. Smith, A. R. Lowry, *J. Volcanol. Geotherm. Res.* **188**, 108–127 (2009).
6. J. B. Lowenstern, S. Hurwitz, *Elements* **4**, 35–40 (2008).
7. S. Hurwitz, J. B. Lowenstern, *Rev. Geophys.* **52**, 375–411 (2014).
8. H. Yuan, K. Dueker, *Geophys. Res. Lett.* **32**, L07304 (2005).
9. M. Xue, R. M. Allen, *J. Geophys. Res.* **115**, B07303 (2010).
10. M. Obrebski, R. M. Allen, F. Pollitz, S. H. Hung, *Geophys. J. Int.* **185**, 1003–1021 (2011).
11. B. Schmandt, K. Dueker, E. Humphreys, S. Hansen, *Earth Planet. Sci. Lett.* **331–332**, 224–236 (2012).
12. S. Husen, R. B. Smith, G. P. Waite, *J. Volcanol. Geotherm. Res.* **131**, 397–410 (2004).
13. R. Chu, D. V. Helmberger, D. Sun, J. M. Jackson, L. Zhu, *Geophys. Res. Lett.* **37**, L01306 (2010).
14. M. Paulatto *et al.*, *Geochem. Geophys. Geosyst.* **13**, Q01014 (2012).
15. M. A. Mitchell, R. S. White, S. Roecker, T. Greenfield, *Geophys. Res. Lett.* **40**, 5040–5046 (2013).
16. M. West, W. Menke, M. Tolstoy, S. Webb, R. Sohn, *Nature* **413**, 833–836 (2001).
17. E. M. Syracuse *et al.*, *J. Geophys. Res.* **115**, B10310 (2010).
18. G. P. Waite, S. C. Moran, *J. Volcanol. Geotherm. Res.* **182**, 113–122 (2009).
19. I. Koulakov *et al.*, *J. Volcanol. Geotherm. Res.* **263**, 75–91 (2013).
20. K. J. Seats, J. F. Lawrence, *Geophys. Res. Lett.* **41**, 8277–8282 (2014).
21. S. W. Roecker *et al.*, *J. Geophys. Res.* **98**, 15779 (1993).
22. D. Zhao, A. Hasegawa, H. Kanamori, *J. Geophys. Res.* **99**, 22313–22329 (1994).
23. H.-H. Huang *et al.*, *Geophys. Res. Lett.* **41**, 10.1002/2014GL061115 (2014).
24. B. Schmandt, F. C. Lin, *Geophys. Res. Lett.* **41**, 6342–6349 (2014).
25. See supplementary materials on *Science* Online.
26. W. Shen, M. H. Ritzwoller, V. Schulte-Pelkum, *J. Geophys. Res.* **118**, 262–276 (2013).
27. S. M. White, J. A. Crisp, F. J. Spera, *Geochem. Geophys. Geosyst.* **7**, Q03010 (2006).
28. C. Werner, S. Brantley, *Geochem. Geophys. Geosyst.* **4**, 1061 (2003).
29. R. O. Fournier, *Annu. Rev. Earth Planet. Sci.* **17**, 13–53 (1989).
30. K. Jaxybulatov *et al.*, *Science* **346**, 617–619 (2014).
31. C. Annen, J. D. Blundy, R. S. J. Sparks, *J. Petrol.* **47**, 505–539 (2006).
32. A. Gudmundsson, *Tectonophysics* **500**, 50–64 (2011).
33. J. W. Shervais, S. K. Vetter, B. B. Hanan, *Geology* **34**, 365 (2006).

QUANTUM OPTICS

Quantum dynamics of an electromagnetic mode that cannot contain N photons

L. Bretheau, P. Campagne-Ibarcq, E. Flurin, F. Mallet, B. Huard*

Electromagnetic modes are instrumental in building quantum machines. In this experiment, we introduce a method to manipulate these modes by effectively controlling their phase space. Preventing access to a single energy level, corresponding to a number of photons N, confined the dynamics of the field to levels 0 to N – 1. Under a resonant drive, the level occupation was found to oscillate in time, similarly to an N-level system. Performing a direct Wigner tomography of the field revealed its nonclassical features, including a Schrödinger cat–like state at half period in the evolution. This fine control of the field in its phase space may enable applications in quantum information and metrology.

The manipulation of a quantum system usually involves the control of its Hamiltonian in time. An alternative route consists in effectively tailoring its Hilbert space dynamically. This can be done by restricting the system evolution to a subset of possible states. When even a single energy level is disabled, the system evolution is deeply modified and is ruled by the so-called quantum Zeno dynamics (QZD) (*1–5*). As the name suggests, the level blockade can be realized by repeatedly checking whether the level is occupied, owing to the inherent back action of quantum measurements (*1, 2, 6*). Alternatively, as in the present experiment, QZD can be achieved by blocking the level using a strong, active coupling to an ancillary quantum system (*3–5*), without any measurement (*7*). These ideas have recently been demonstrated for atoms, using either Rb Bose-Einstein condensates (*8*) or Rydberg atoms (*9*). However, the dynamics of these systems are intrinsically confined to a finite number of energy levels. Here, using a circuit quantum electrodynamics architecture, we implement QZD of light. With its large number of energy levels and ease of control, a single electromagnetic mode offers a wider and more controllable phase space than atoms and two-level systems.

The principle of our experiment is shown in Fig. 1. One cavity mode of frequency f_c is coupled to a qubit of frequency f_q. For a large enough detuning, their evolution can be described by the dispersive Hamiltonian $hf_c a^\dagger a + hf_q |e\rangle\langle e| - h\chi a^\dagger a |e\rangle\langle e|$, where h is Planck's constant, $a^\dagger$ is the ladder operator, and $|e\rangle$ is the excited state of the qubit. The last term describes the frequency shift of the cavity (qubit) $-\chi$, which occurs when the qubit (cavity) is excited by one extra quantum of energy. Owing to this shift, a tone at frequency $f_q - N\chi$ addresses only the transition between states $|N\rangle \otimes |g\rangle$ and $|N\rangle \otimes |e\rangle$ for level widths smaller than χ (*10*); here, $|g\rangle$ is the ground state of the qubit. These levels then hybridize and repel each other. Their splitting is given by the Rabi frequency Ω_R, at which the qubit population would oscillate in the case where the cavity is in state $|N\rangle$ (Fig. 1). Any transition to level N is now forbidden when the cavity is driven at resonance. Schematically, level N has been moved out of the harmonic ladder (Fig. 1). Then, starting from the ground state, the electromagnetic mode is confined to levels 0 to $N – 1$, whereas the qubit remains in its ground state. The field dynamics is dramatically changed, resembling that of an N-level system, and nonclassical states similar to "Schrödinger cat states" develop.

In the experiment, we use the fundamental mode of a three-dimensional (3D) microwave cavity made out of bulk aluminum, which resonates at $f_c = 7.804$ GHz. This mode is off-resonantly coupled to a superconducting qubit (*11*) with bare frequency $f_q = 5.622$ GHz and dispersive frequency shift $\chi = 4.63$ MHz. The cavity exit rate $\gamma_c = (1.3 \, \mu s)^{-1}$ is dominated by the coupling rate to two transmission lines connected to the cavity, which are used for both driving and the readout of the system. The relaxation rate $\gamma_1 = (11.5 \, \mu s)^{-1}$ and decoherence rate $\gamma_2 = (8.9 \, \mu s)^{-1}$ of the ancillary qubit are an order of magnitude smaller.

The experiment is performed by first turning on the blocking tone at $f_q - N\chi$. For the level blockade to be effective, we choose $\Omega_R = 6.24$ MHz, much larger than the level frequency width, which is about γ_c. Then, the cavity is driven at frequency $f_d \approx f_c$ for a time t varying up to a few µs. The drive power is fixed throughout the experiment and would lead to an amplitude displacement rate ε_d of about 3 µs^{-1} in the cavity, were there neither damping nor nonlinearities. At time t, both the blocking signal and the cavity drive are turned off, and the field state is measured. Two measurement schemes are used to characterize the cavity state. Both methods use as a probe the same qubit that is used to provide the level blockade.

The first method consists in measuring the probability P_k for the field to host k photons. To do so, a selective π pulse is applied to the qubit at frequency $f_q - k\chi$ so that it gets excited if k photons are in the cavity. Measuring

Laboratoire Pierre Aigrain, Ecole Normale Supérieure–PSL Research University, CNRS, Université Pierre et Marie Curie–Sorbonne Universités, Université Paris Diderot–Sorbonne Paris Cité, 24 Rue Lhomond, 75231 Paris Cedex 05, France.
*Corresponding author. E-mail: benjamin.huard@ens.fr

the probability to find the qubit in the excited state hence gives P_k (12). This direct measurement relies on the qubit being initially in the ground state, which is not always the case in our experiment. To account for this, two spurious effects need to be considered. First, the qubit has a residual thermal population of 22%. Second, imperfections of the blockade induce a parasitic excitation of the qubit, which was measured in time and remains below 18%. Taking these effects into account leads to an accurate determination of the conditional probability $\tilde{P}_k$ of measuring k photons given the qubit being initially in the ground state (13).

The resulting probabilities are shown in Fig. 2 as a function of time for several photon numbers k and for N from 2 to 5. Levels with more than N photons are unoccupied, as expected from Hilbert space blockade. Early in the evolution, the occupation of the levels $k \geq 1$ rises in the order of increasing energy, similarly to a coherent state of increasing amplitude (fig. S3C). Later, the level distribution "bounces" off a wall at $k = N$, so that

the probabilities start to oscillate. The period of the oscillations increases with N as expected, because it takes more time to reach $N - 1$ photons with a constant drive as N increases. The case $N = 2$ is straightforward as it implements an effective qubit (8). The time traces of Fig. 2 correspond to Rabi oscillations of a two-level system. For larger N, the evolution is similar to that of a resonantly driven N-level system, as seen in Rydberg atoms (9). In particular, at half period, $\tilde{P}_0$ displays plateaus all the more pronounced as N gets larger. Finally, the $N - 1$ level occupation evolves in opposition to level 0, with a maximum at half period.

The evolution of the field can be modeled with the Hamiltonian of the cavity

$$H = ih\varepsilon_d(a_N^\dagger - a_N)/2\pi + h(f_c - f_d)a_N^\dagger a_N - h\lambda(a_N^\dagger)^2 a_N^2 \quad (1)$$

written in the frame rotating at the drive frequency f_d. These three terms describe the coherent drive, its detuning, and the nonlinearity of

the cavity, respectively. The blockade at level N suppresses transitions to and from $|N\rangle$. This is entirely modeled by an effective annihilation operator

$$a_N = a - \sqrt{N}|N - 1\rangle\langle N| - \sqrt{N + 1}|N\rangle\langle N + 1| \quad (2)$$

for which these forbidden transitions are removed. Finally, the relaxation at rate γ_c is modeled using a master equation of Lindblad form (13).

Using this model, one can reproduce with good agreement the photon number probabilities $\tilde{P}_k$ (Fig. 1), with the displacement rate ε_d, the drive detuning $f_c - f_d$, and the cavity anharmonicity λ as the fit parameters. The displacement rate ε_d, which directly determines the period of oscillations in the level occupation (Fig. 1), is found to be finely tuned between 2.83 and 3.05 μs^{-1} for each blocked level N. The anharmonicity $\lambda = -70$ kHz is negative, as confirmed by independent measurements (fig. S2). This negativity is in contradiction to all reported transmon qubit and 3D transmon models such as those in (14–16). At last, we attribute the origin of the detuning $f_c - f_d$ to an energy shift of the levels caused by the blocking tone. It was found to be −0.1 MHz for $N > 2$ and −0.4 MHz for $N = 2$. These values are consistent with the system being more strongly disturbed by the blocking field at $N = 2$ than for larger N.

These measurements demonstrate how the cavity is transformed into an N-level system by dynamically inducing a blockade at an arbitrary level N. A full characterization of the field, which goes beyond measuring only photon number probability, requires tomography. The Wigner function is a complete representation of the quantum state of the field in continuous variables. It can be expressed as $W(\alpha) = \langle D_\alpha \mathcal{P} D_\alpha^\dagger\rangle$, where $D_\alpha = e^{\alpha a^\dagger - \alpha^* a}$ is the field displacement operator and $\mathcal{P} = e^{i\pi a^\dagger a}$ is the photon parity operator. A direct Wigner tomography of the field is thus performed by first displacing it by a complex amplitude α and then measuring the average photon parity. This can be realized by mapping even and odd photon numbers on the qubit ground and excited states (17–19). In practice, this is performed in three steps. The qubit is first prepared in state $(|g\rangle + |e\rangle)/\sqrt{2}$ using a pulse at the qubit frequency. The $\pi/2$ pulse bandwidth is designed to be larger than 10χ so as to succeed regardless of the cavity state. Then, the qubit is left to evolve freely during a time τ, where it acquires a phase shift that depends on the cavity state owing to the evolution operator $e^{i2\pi\chi\tau a^\dagger a|e\rangle\langle e|}$. The waiting time is chosen to be $\tau = 1/2\chi = 108$ ns, so that the qubit phase increases by $k\pi$ when the cavity state is $|k\rangle$ (fig. S4). Finally, another broadband $\pi/2$ pulse is applied in order to flip the qubit to the excited (ground) state in case of an even (odd) number of photons. Measuring the qubit state then directly leads to the Wigner function, in contrast to indirect reconstruction procedures such as maximum likelihood.

The measured Wigner functions for the field state are shown in Fig. 3 at various times during the first oscillation period for blocked levels $N = 3$
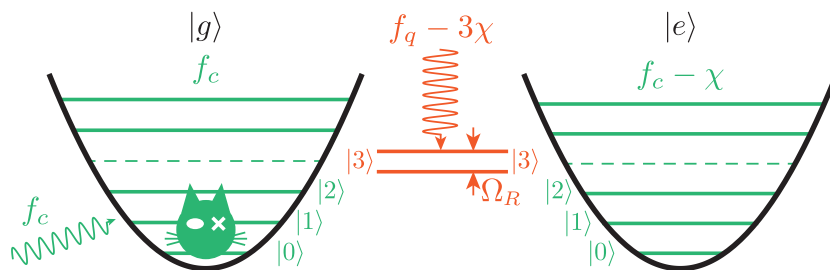
Fig. 1. Principle of the experiment. Combined energy level diagram of the cavity coupled to the ancillary qubit. Each state is labeled as $|k\rangle \otimes |g/e\rangle$ for k photons in the cavity and the qubit either in the ground (g) or excited (e) states. The level $N = 3$ is dynamically blocked by driving the qubit transition at $f_q - N\chi$ (red wavy line). This drive hybridizes the states $|N\rangle \otimes |g\rangle$ and $|N\rangle \otimes |e\rangle$ and shifts their energy. A coherent excitation at the cavity frequency f_c (green wavy line) induces a periodic evolution of the field confined to the first N levels. At half period, a nonclassical state similar to a Schrödinger cat is produced.
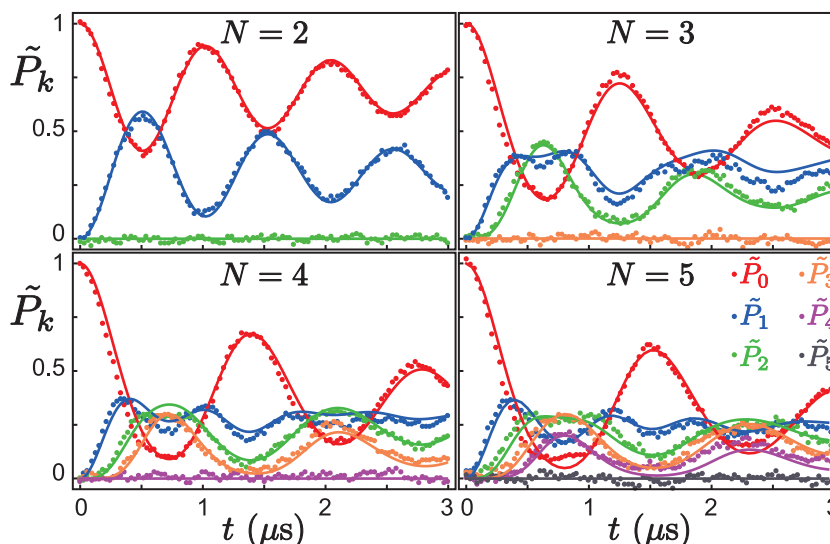
Fig. 2. Evolution of the photon number probabilities. Measured (dots) and theoretical (solid lines) photon number state probabilities $\tilde{P}_k$ as a function of time t. The blocked level N ranges from 2 to 5 and is indicated on each panel. The standard deviation, estimated from the curve $\tilde{P}_N(t)$, is below 1.7%.
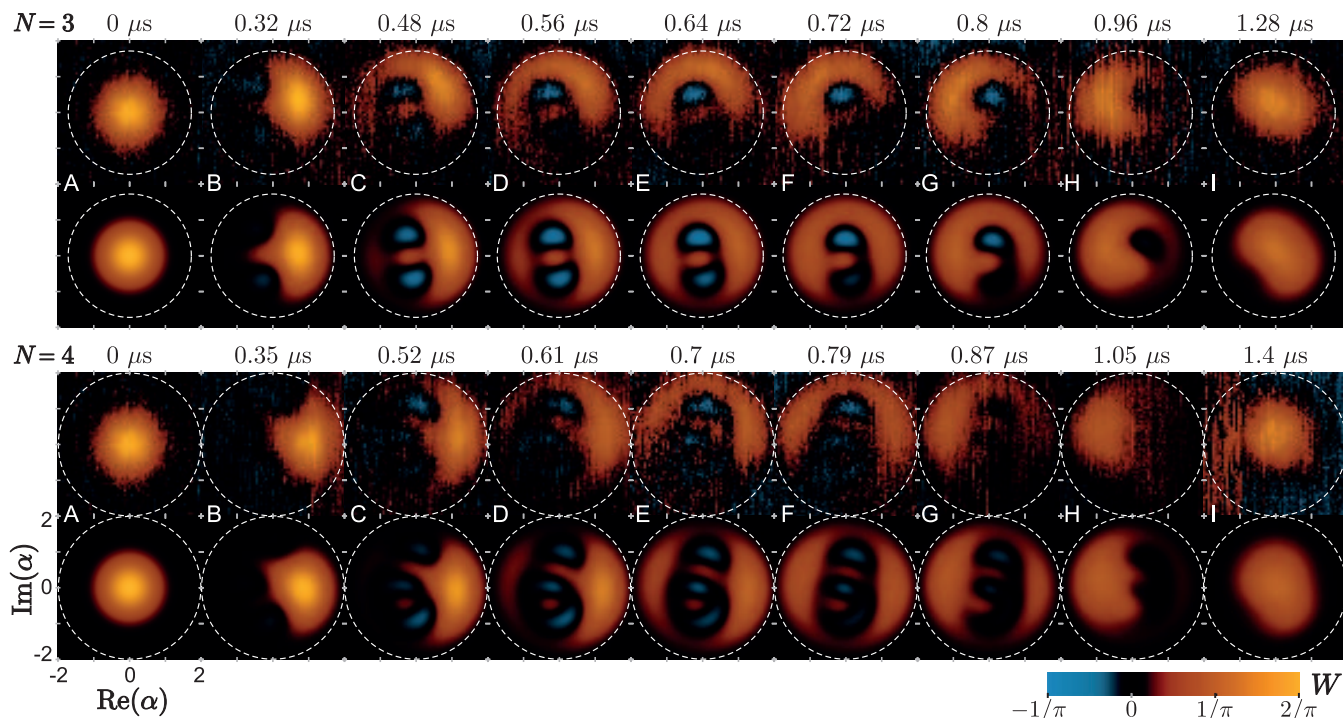
Fig. 3. Time evolution of the Wigner function of a quantum mode of light under QZD. Measured (top rows) and calculated (bottom rows) Wigner functions $W(\alpha)$ as a function of the displacement amplitude α, for a blockade at $N = 3$ (top panel) and $N = 4$ (bottom panel). The time t (nonlinear scale) for the frames shown in (**A**) to (**I**) is given above each panel. The field is confined in phase space by a barrier at amplitude $|\alpha| = \sqrt{N}$ (white dashed circle). Negative values of the Wigner function, in blue, demonstrate the nonclassical nature of the field produced under QZD. The model used is the same as for Fig. 1. Wigner functions are directly measured here and not reconstructed.

and $N = 4$. At time zero (Fig. 3A), the cavity is in the vacuum state and the Wigner function is a positive Gaussian distribution centered at $\alpha = 0$, with a width reflecting zero point fluctuations. As time increases, the resonant drive displaces the Wigner function along the real and positive axis. Without the blockade, and neglecting losses and anharmonicity, the vacuum state observed at time 0 would simply get displaced by $\alpha = \varepsilon_d t$. In the presence of the blockade at level N, all levels with $k \geq N$ remain empty so that the field cannot be in a coherent state, and the distribution gets distorted. Indeed in Fig. 3B, the quasi–probability distribution seems to hit a wall in phase space at an amplitude $\sqrt{N}$. There, it undergoes a rapid counterclockwise evolution (Fig. 3, C to H) along the corresponding barrier (white dashed circle). After a full oscillation period (Fig. 3I), the cavity goes back to a state close to the vacuum state of Fig. 3A. These snapshots of the field state are close to the ones predicted in (5) for light under QZD and similar to the one observed in the levels of a Rydberg atom (9).

Besides confirming the confined and periodic evolution of the field under QZD, this tomography reveals the formation of nonclassical field states, as indicated by the appearance of negative values in the Wigner function. These negative values develop while the field undergoes a transition along the barrier in phase space. At half period, the state is close to an equal superposition of positive and negative field amplitudes at $\pm\sqrt{N - 1}$. The quantum nature of this superposition manifests itself

by the appearance of interference fringes in the Wigner function. These characteristic patterns can be compared for all blockade levels $2 \leq N \leq 5$ in Fig. 4. The photon parity is that of the highest allowed level, $N - 1$, which is also the number of negative fringes. These properties are reminiscent of a quantum superposition between two coherent states of amplitude $\pm\sqrt{N - 1}$, so-called Schrödinger cat state (20). The evolution of the Wigner function can be predicted using the

Fig. 4. Wigner tomography at half period. Measured (top row) and calculated (bottom row) Wigner functions of the cavity field for various blockade levels N from 2 to 5, taken at half period ($t = 0.51$ μs, 0.64 μs, 0.7 μs, and 0.75 μs). The color scale is rescaled compared with Fig. 2 by $A = 0.7$. Similarly to Schrödinger cat states, these states exhibit fringes with alternating positive and negative values.

model above. The calculated distributions are shown below each measurement frame in Figs. 3 and 4. The observed asymmetry between positive and negative imaginary amplitudes is attributed to drive detuning, losses, and anharmonicity (12, 20). The model reproduces qualitatively the measured Wigner functions for all times and values of N.

Our work could be extended to allow evolution outside of the exclusion circle, where the barrier

acts as a peculiar scatterer in phase space (5). Other cat-like states and squeezed states could then be produced. Tailoring the Hilbert space in time is an important new resource for quantum control. Our experiment enables the realization of various protocols based on QZD, such as generation and protection of entanglement (21–23), and quantum logic operations (24). Moreover, by turning on and off in time the blockade level and combining it with fast amplitude displacements, which is feasible by improving the cavity decay rate by an order of magnitude, it would be possible to realize phase space tweezers for light (4, 5). A possible and important outcome would then be the manipulation of Schrödinger cat states in a unique way and the quantum error correction of cat-qubits, which are a promising quantum computing paradigm (25).

REFERENCES AND NOTES

1. P. Facchi, V. Gorini, G. Marmo, S. Pascazio, E. C. G. Sudarshan, *Phys. Lett. A* **275**, 12–19 (2000).
2. P. Facchi, S. Pascazio, *Phys. Rev. Lett.* **89**, 080401 (2002).
3. P. Facchi, D. Lidar, S. Pascazio, *Phys. Rev. A* **69**, 032314 (2004).
4. J. M. Raimond et al., *Phys. Rev. Lett.* **105**, 213601 (2010).
5. J. M. Raimond et al., *Phys. Rev. A* **86**, 032120 (2012).
6. B. Misra, E. C. G. Sudarshan, *J. Math. Phys.* **18**, 756 (1977).
7. Originally, QZD corresponded to quantum evolutions restricted by measurement; the name was later extended to any quantum dynamics in a restricted Hilbert space (3).
8. F. Schäfer et al., *Nat. Commun.* **5**, 3194 (2014).
9. A. Signoles et al., *Nat. Phys.* **10**, 715–719 (2014).
10. D. I. Schuster et al., *Nature* **445**, 515–518 (2007).
11. H. Paik et al., *Phys. Rev. Lett.* **107**, 240501 (2011).
12. G. Kirchmair et al., *Nature* **495**, 205–209 (2013).
13. Materials and methods are available as supporting materials on *Science* Online.
14. S. E. Nigg et al., *Phys. Rev. Lett.* **108**, 240502 (2012).
15. J. Bourassa, F. Beaudoin, J. M. Gambetta, A. Blais, *Phys. Rev. A* **86**, 013814 (2012).
16. F. Solgun, D. Abraham, D. P. DiVincenzo, *Phys. Rev. B* **90**, 134504 (2014).
17. L. Lutterbach, L. Davidovich, *Phys. Rev. Lett.* **78**, 2547–2550 (1997).
18. P. Bertet et al., *Phys. Rev. Lett.* **89**, 200402 (2002).
19. B. Vlastakis et al., *Science* **342**, 607–610 (2013).
20. S. Haroche, J. M. Raimond, *Exploring the Quantum* (Oxford Univ. Press, Oxford, 2006).
21. S. Maniscalco, F. Francica, R. L. Zaffino, N. Lo Gullo, F. Plastina, *Phys. Rev. Lett.* **100**, 090503 (2008).
22. X.-B. Wang, J. Q. You, F. Nori, *Phys. Rev. A* **77**, 062339 (2008).
23. Z. C. Shi, Y. Xia, H. Z. Wu, J. Song, *Eur. Phys. J. D* **66**, 127 (2012).
24. X.-Q. Shao, L. Chen, S. Zhang, K.-H. Yeon, *J. Phys. B* **42**, 165507 (2009).
25. M. Mirrahimi et al., *New J. Phys.* **16**, 045014 (2014).

SUPPLEMENTARY MATERIALS

www.sciencemag.org/content/348/6236/776/suppl/DC1
Materials and Methods
Supplementary Text
Figs. S1 to S4
References (26–32)

GALAXY EVOLUTION

Quasar quartet embedded in giant nebula reveals rare massive structure in distant universe

Joseph F. Hennawi,[1]* J. Xavier Prochaska,[2] Sebastiano Cantalupo,[2,3] Fabrizio Arrigoni-Battaia[1]

All galaxies once passed through a hyperluminous quasar phase powered by accretion onto a supermassive black hole. But because these episodes are brief, quasars are rare objects typically separated by cosmological distances. In a survey for Lyman-α emission at redshift $z \approx 2$, we discovered a physical association of four quasars embedded in a giant nebula. Located within a substantial overdensity of galaxies, this system is probably the progenitor of a massive galaxy cluster. The chance probability of finding a quadruple quasar is estimated to be $\sim 10^{-7}$, implying a physical connection between Lyman-α nebulae and the locations of rare protoclusters. Our findings imply that the most massive structures in the distant universe have a tremendous supply ($\approx 10^{11}$ solar masses) of cool dense (volume density ≈ 1 cm^{-3}) gas, which is in conflict with current cosmological simulations.

C osmologists do not fully understand the origin of supermassive black holes (SMBHs) at the centers of galaxies and how they relate to the evolution of the underlying dark matter, which forms the backbone for structure in the universe. In the current paradigm, SMBHs grew in every massive galaxy during a luminous quasar phase, making distant quasars the progenitors of the dormant SMBHs found at the centers of nearby galaxies. Tight correlations between the masses of these local SMBHs and both their host galaxy (1) and dark-matter halo masses (2) support this picture, further suggesting that the most luminous quasars at high redshift (z) should reside in the most massive galaxies. It has also been proposed that quasar activity is triggered by the frequent mergers that are a generic consequence of hierarchical structure formation (3, 4). Indeed, an excess in the number of small-separation binary quasars (5, 6), as well as the mere existence of a handful of quasar triples (7, 8), support this hypothesis. If quasars are triggered by mergers, then they should preferentially occur in rare peaks of the density field, where massive galaxies are abundant and the frequency of mergers is highest (9).

Following these arguments, one might expect that at the peak of their activity, $z \sim 2$ to 3, quasars should act as signposts for protoclusters, the progenitors of local galaxy clusters and the most massive structures at that epoch. However, quasar clustering measurements (10, 11) indicate that quasar environments at $z \sim 2$ to 3 are not extreme: These quasars are hosted by dark-matter halos with masses $M_{halo} \sim 10^{12.5} M_\odot$ (where $M_\odot$ is the mass of the Sun), too small to be the progenitors of local clusters (12). But the relationship between quasar activity and protoclusters remains unclear, owing

to the extreme challenge of identifying the latter at high redshift. Indeed, the total comoving volume of even the largest surveys for distant galaxies at $z \sim 2$ to 3 is only $\sim 10^7$ Mpc^3, which would barely contain a single rich cluster locally.

Protoclusters have been discovered around a rare population of active galactic nuclei (AGNs) powering large-scale radio jets, known as high-redshift radio galaxies (HzRGs) (13). The HzRGs routinely exhibit giant ~ 100 kpc nebulae of luminous Lyman-α (Lyα) emission $L_{Ly\alpha} \sim 10^{44}$ erg s^{-1}. Nebulae of comparable size and luminosity have also been observed in a distinct population of objects known as Lyα blobs (LABs) (14, 15). The LABs are also frequently associated with AGN activity (16–18), although lacking powerful radio jets, and appear to reside in overdense protocluster environments (15, 19, 20). Thus, among the handful of protoclusters (21) known, most appear to share two common characteristics: the presence of an active SMBH and a giant Lyα nebula.

We have recently completed a spectroscopic search for extended Lyα emission around a sample of 29 luminous quasars at $z \sim 2$, each the foreground (f/g) member of a projected quasar pair (22). Analysis of spectra from the background (b/g) members in such pairs reveals that quasars exhibit frequent absorption from a cool, metal-enriched, and often optically thick medium on scales of tens to hundreds of kiloparsecs (22–28). The ultraviolet radiation emitted by the luminous f/g quasar can, like a flashlight, illuminate this nearby neutral hydrogen and power a large-scale Lyα-emission nebula, motivating our search. By construction, our survey selects for exactly the two criteria that seem to strongly correlate with protoclusters: an active SMBH and the presence of a large-scale Lyα emission nebula.

Of the 29 quasars surveyed, only SDSSJ0841+3921 exhibited extended large-scale ($\gtrsim 50$ kpc) Lyα emission above our characteristic sensitivity limit of 6×10^{-18} erg s^{-1} cm^{-2} arc sec^{-2} (2σ). We designed a custom narrow-band filter tuned to

[1]Max-Planck-Institut für Astronomie, Heidelberg, Germany. [2]University of California Observatories–Lick Observatory, University of California Santa Cruz, Santa Cruz, CA, USA. [3]ETH Zurich, Institute for Astronomy, Zurich, Switzerland. *Corresponding author. E-mail: joe@mpia.de

Fig. 1. Narrow- and broadband images of the field surrounding SDSSJ0841+3921 (A) Continuum-subtracted, narrow-band image of the field around f/g quasar. The color map and the contours indicate the Lyα surface brightness (upper color bar) and the signal-to-noise ratio per arc sec² aperture (lower color bar), respectively. This image reveals a giant Lyα nebula on the northern side of the f/g quasar and several compact bright Lyα

emitters in addition to the f/g quasar. Three of these have been spectroscopically confirmed as AGNs at the same redshift. (**B**) Corresponding V-band continuum image of the field presented at left with the locations of the four AGNs marked. The AGNs are roughly oriented along a line coincident with the projected orientation of the Lyα nebula. We also mark the position of the b/g quasar, which is not physically associated with the quadruple AGN system but whose absorption spectrum probes the gaseous environment of the f/g quadruple AGN and protocluster (Fig. 4).
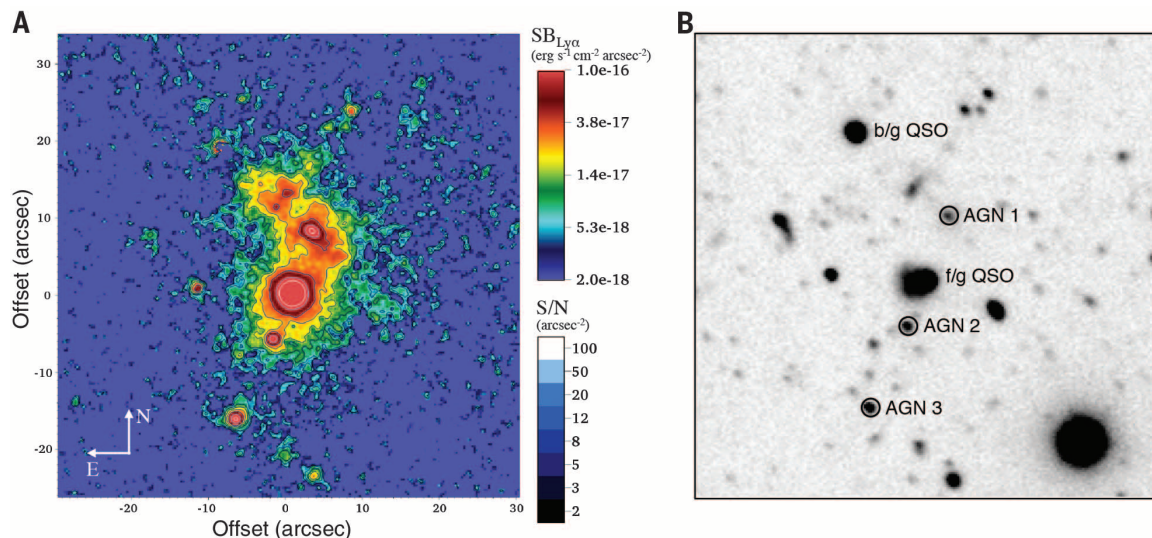
the wavelength of Lyα at the f/g quasar redshift $z = 2.0412$ (central wavelength = 3700 Å, full width at half maximum = 33 Å), and imaged the field with the Keck/LRIS imaging spectrometer for 3 hours on UT 12 November 2012. The combined and processed images reveal Lyα emission from a giant filamentary structure centered on the f/g quasar and extending continuously toward the b/g quasar (Fig. 1). This nebulosity has an end-to-end size of 37″, corresponding to 310 kpc, and a total line luminosity $L_{Ly\alpha} = 2.1 \times 10^{44}$ erg s⁻¹, making it one of the largest and brightest nebulae ever discovered.

The giant nebula is only one of the exceptional properties of SDSSJ0841+3921. Our images reveal three relatively compact candidate Lyα-emitting sources with faint continuum magnitudes $V \simeq 23$ to 24, embedded in the Lyα filament and roughly aligned with its major axis. Followup spectroscopy reveals that the sources labeled AGN1, AGN2, and AGN3 are three AGNs at the same redshift as the f/g quasar [see the right panel of Fig. 1 and (29)], making this system the only quadruple AGN known. Adopting recent measurements of small-scale quasar clustering (30), we estimate that the probability of finding three AGNs around a quasar with such small separations is ~10⁻⁷ (31). Why then did we discover this rare coincidence of AGNs in a survey of just 29 quasars? Did the giant nebula mark the location of a protocluster with dramatically enhanced AGN activity?

To test this hypothesis, we constructed a catalog of Lyα-emitting galaxies (LAEs) and computed the cumulative overdensity profile of LAEs around SDSSJ0841+3921, relative to the background number expected based on the LAE luminosity function (32) (Fig. 2). To perform a quantitative comparison to other giant Lyα nebulae, many of which are known to coincide with protoclusters, we measured the giant nebulae–LAE cross-correlation

Fig. 2. Characterization of the protocluster environment around SDSSJ0841+3921. The data points indicate the cumulative overdensity profile of LAEs δ(<R) as a function of impact parameter R from the f/g quasar in SDSSJ0841+3921, with Poisson error bars. The red curve shows the predicted overdensity profile, based on our measurement of the giant nebulae–LAE cross-correlation function determined from a sample of eight systems—six HzRGs and two LABs—for which published data were available in the literature. Assuming a power-law

form for the cross-correlation $\xi_{cross} = (r/r_0)^{-\gamma}$, we measured the correlation length $r_0 = 29.3 \pm 4.9\ h^{-1}$ Mpc, for a fixed value of $\gamma = 1.5$. The gray-shaded region indicates the 1σ error on our measurements based on a bootstrap analysis, where both r_0 and γ are allowed to vary. The solid blue line indicates the overdensity of Lyman break galaxies (LBGs) around radio-quiet quasars based on recent measurements (10), with the dotted blue lines the 1σ error on this measurement. On average, the environment of HzRGs and LABs hosting giant Lyα nebulae is much richer than that of radio-quiet quasars (10), confirming that they indeed reside in protoclusters. SDSSJ0841+3921 exhibits a dramatic excess of LAEs as compared to the expected overdensities around radio-quiet quasars (blue curve). Its overdensity even exceeds the average protocluster (red curve) by a factor of ≳20 for R < 200 kpc, decreasing to an excess of ~3 on scales of R ≃ 1 Mpc, and exhibits a much steeper profile.

function for a sample of eight systems—six HzRGs and two LABs—for which published data was available in the literature (33). In Fig. 2, we compare the overdensity profile around SDSSJ0841+3921 to this giant nebulae–LAE correlation function. On average, the environment of HzRGs and LABs

hosting giant Lyα nebulae (red line) is much richer than that of radio-quiet quasars (10) (blue line), confirming that they indeed reside in protoclusters. Furthermore, the clustering of LAEs around SDSSJ0841+3921 has a steeper overdensity profile and exceeds the average protocluster
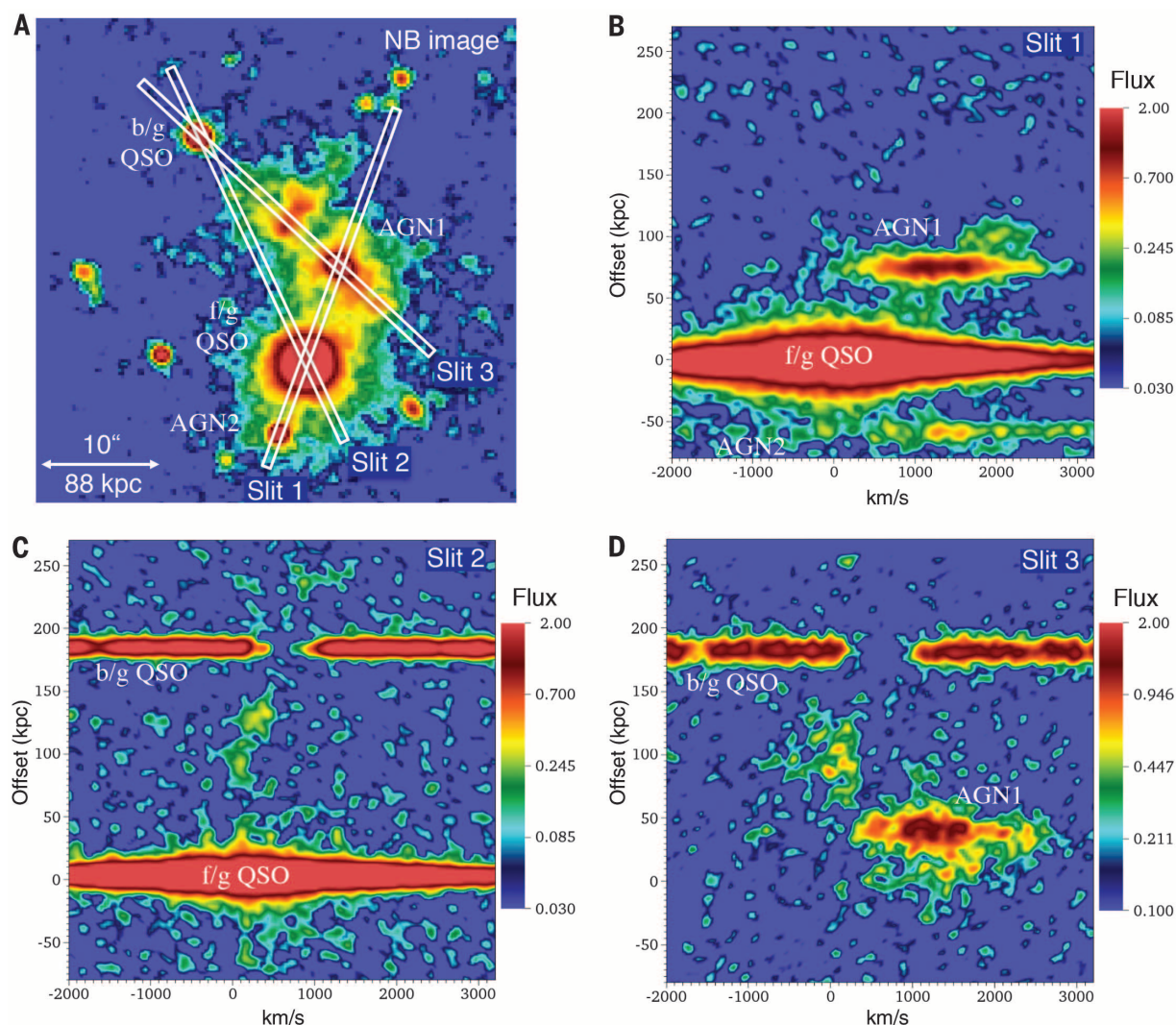
Fig. 3. Lyα spectroscopy of the giant nebula and its associated AGNs. (A) The spectroscopic slit locations (white rectangles) for three different slit orientations are overlaid on the narrowband image of the giant nebula. The locations of the f/g quasar (brightest source), b/g quasar, AGN1, and AGN2 are also indicated. Two-dimensional spectra for slit1 (**B**), slit2 (**C**), and slit3 (**D**) are shown in the accompanying panels. In the upper right and lower left panels, spatial coordinates refer to the relative offset along the slit with respect to the f/g quasar. Spectra of AGN1 are present in both slit 1 (upper right) and slit 3 (lower right) at spatial offsets of 75 and 25 kpc, respectively, whereas the Lyα spectrum of AGN2 is located at a spatial offset −60 kpc in slit 1 (upper right).

The b/g quasar spectra are located in both slit 2 (lower left) and slit 3 (lower right) at the same spatial offset of 176 kpc. The spectroscopic observations demonstrate the extreme kinematics of the system: AGN1 has a velocity of +1300 ± 400 km s^{-1} relative to the f/g quasar, and the Lyα emission in the nebula exhibits motions ranging from −800 km s^{-1} (at ≈100 kpc offset in slit 3, lower right) to +2500 km s^{-1} (at ≈100 kpc in slit 1, upper right). A 3 × 3 pixel boxcar smoothing, which corresponds to 120 km s^{-1} × 0.8″, has been applied to the spectra. In each two-dimensional spectrum, the zero velocity corresponds to the systemic redshift of the f/g quasar. The color bars indicate the flux levels in units of erg s^{-1} cm^{-2} arc sec^{-2} Å^{-1}.

by a factor of ≳20 for $R < 200$ kpc and by ~ 3 on scales of $R \simeq 1$ Mpc. In addition to the overdensity of four AGNs, the high number of LAEs surrounding SDSSJ0841+3921 make it one of the most overdense protoclusters known at $z \sim 2$ to 3.

The combined presence of several bright AGNs, the Lyα emission nebula, and the b/g absorption spectrum provides an unprecedented opportunity to study the morphology and kinematics of the protocluster via multiple tracers, and we find evidence for extreme motions (*34*). Specifically, AGN1 is offset from the precisely determined systemic redshift (*35*) of the f/g quasar by +1300 ± 400 km s^{-1}. This large velocity offset cannot be explained by Hubble expansion [the miniscule

probability of finding a quadruple quasar in the absence of clustering $P \sim 10^{-13}$ (*31*) and the physical association between the AGN and giant nebula demand that the four AGNs reside in a real collapsed structure] and thus provides unambiguous evidence for extreme gravitational motions. In addition, our slit spectra of the giant Lyα nebula reveal extreme kinematics of diffuse gas (Fig. 3), extending over a velocity range of −800 to +2500 km s^{-1} from systemic. Furthermore, there is no evidence for the double-peaked velocity profiles characteristic of resonantly trapped Lyα, which could generate large velocity widths in the absence of correspondingly large gas motions. Absorption line kinematics of the metal-enriched

gas, measured from the b/g quasar spectrum at an impact parameter of $R_\perp = 176$ kpc (Fig. 4), show strong absorption at ≈+650 km s^{-1}, with a significant tail to velocities as large as ≃1000 km s^{-1}. It is of course possible that the extreme gas kinematics, traced by Lyα emission and metal-line absorption, are not gravitational but rather arise from violent large-scale outflows powered by the multiple AGNs. Although we cannot completely rule out this possibility, the large velocity offset of +1300 km s^{-1} between the f/g quasar and the emission redshift of AGN1 can only result from gravity.

One can only speculate about the origin of the dramatic enhancement of AGNs in the SDSSJ0841+ 3921 protocluster. Perhaps the duty cycle for

AGN activity is much longer in protoclusters, because of frequent dissipative interactions (5, 6), or an abundant supply of cold gas. A much larger number of massive galaxies could also be the culprit, as AGNs are known to trace massive halos at $z \sim 2$. Although SDSSJ0841+3921 is the only example of a quadruple AGN with such small separations, previously studied protoclusters around HzRGs and LABs also occasionally harbor multiple AGNs (13, 36). Regardless, our discovery of a quadruple AGN and protocluster from a sample of only 29 quasars suggests a link between giant Lyα nebulae, AGN activity, and protoclusters, similar to past work on HzRGs and LABs, with the exception that SDSSJ0841+3921 was selected from a sample of normal radio-quiet quasars. From our survey and other work (37), we estimate that ≈10% of quasars exhibit comparable giant Lyα nebulae. Although clustering measurements imply that the majority of $z \sim 2$ quasars reside in moderate overdensities (10–12), we speculate that this same 10% trace much more massive protoclusters. SDSSJ0841+3921 clearly supports this hypothesis, as does another quasar-protocluster association (10, 38), around which a giant Lyα nebula was recently discovered (39, 40).

Given our current theoretical picture of galaxy formation in massive halos, an association between giant Lyα nebulae and protoclusters is completely unexpected. The large Lyα luminosities of these nebulae imply a substantial mass (~$10^{11}\,M_\odot$) of cool ($T \sim 10^4$ K) gas (41), whereas cosmological hydrodynamical simulations indicate that already by $z \sim 2$ to 3, baryons in the massive progenitors ($M_{halo} \gtrsim 10^{13}\,M_\odot$) of present-day clusters are dominated by a hot shock-heated plasma $T \sim 10^7$ K (42, 43). These hot halos are believed to evolve into the x-ray–emitting intracluster medium observed in clusters, for which absorption-line studies indicate negligible ≲1% cool gas fractions (44). Clues about the nature of this apparent discrepancy come from our absorption line studies of the massive ≈$10^{12.5}\,M_\odot$ halos hosting $z \sim 2$ to 3 quasars. This work reveals substantial reservoirs of cool gas ≳$10^{10}\,M_\odot$ (22–28), manifest as a high covering factor ≈50% of optically thick absorption, several times larger than predicted by hydrodynamical simulations (42, 43). This conflict most likely indicates that current simulations fail to capture essential aspects of the hydrodynamics in massive halos at $z \sim 2$ (27, 42), perhaps failing to resolve the formation of clumpy structure in cool gas (41).

If illuminated by the quasar, these large cool gas reservoirs in the quasar circumgalactic medium (CGM) will emit fluorescent Lyα photons, and we argue that this effect powers the nebula in SDSSJ0841+3921 (45). But according to this logic, nearly every quasar in the universe should be surrounded by a giant Lyα nebula with size comparable to its CGM (~200 kpc). Why then are these giant nebulae not routinely observed?

This apparent contradiction can be resolved as follows. If this cool CGM gas is illuminated and highly ionized, it will fluoresce in the Lyα line with a surface brightness scaling as $SB_{Ly\alpha} \propto N_H n_H$, where N_H is the column density of cool

clouds that populate the quasar halo, and n_H is the number density of hydrogen atoms inside these clouds. The total cool gas mass of the halos scales as $M_{cool} \propto R^2 N_H$, where R is the radius of the halo (45). Given our best estimate for the properties of the CGM around typical quasars ($n_H \sim 0.01$ cm^{-3} and $N_H \sim 10^{20}$ cm^{-2} or $M_{cool} \simeq 10^{11}\,M_\odot$) (22, 26, 27), we expect these nebulae to be extremely faint $SB_{Ly\alpha} \sim 10^{-19}$ erg s^{-1} cm^{-2} arc sec^{-2} and beyond the sensitivity of current instruments (22). One comes to a similar conclusion based on a full radiative transfer calculation through a simulated dark-matter halo with mass $M_{halo} \approx 10^{12.5}\,M_\odot$ (41). Thus the factor of ~100 times larger surface brightness observed in the SDSSJ0841+3921 and other protocluster nebulae arises from either a higher n_H, N_H (and hence higher M_{cool}), or both. The cool gas properties required to produce the SDSSJ0841+3921 nebula can be directly compared to those deduced from an absorption line analysis of the b/g quasar spectrum (46).

The b/g quasar sightline pierces through SDSSJ0841+3921 at an impact parameter of $R_\perp = $ 176 kpc, giving rise to the absorption spectrum shown in Fig. 4. Photoionization modeling of these data constrains the total hydrogen column density to be $\log_{10} N_H = 20.4 \pm 0.4$ (45), implying a substantial mass of cool gas $1.0 \times 10^{11}\,M_\odot < M_{cool} < 6.5 \times 10^{11}\,M_\odot$ within $r = 250$ kpc. Assuming that the Lyα emitting gas has the same column density as the gas absorbing the b/g sightline, reproducing the large fluorescent Lyα surface brightness requires that this gas be distributed in compact $r_{cloud} \sim 40$ pc clouds at densities characteristic of the interstellar medium $n_H \simeq 2$ cm^{-3}, but on ~100-kpc scales in the protocluster.

Clues to the origin of these dense clumps of cool gas come from their high enrichment level, which we have determined from our absorption line analysis (46) to be greater than 1/10th of the solar value. At first glance, this suggests that strong tidal interactions due to merger activity or
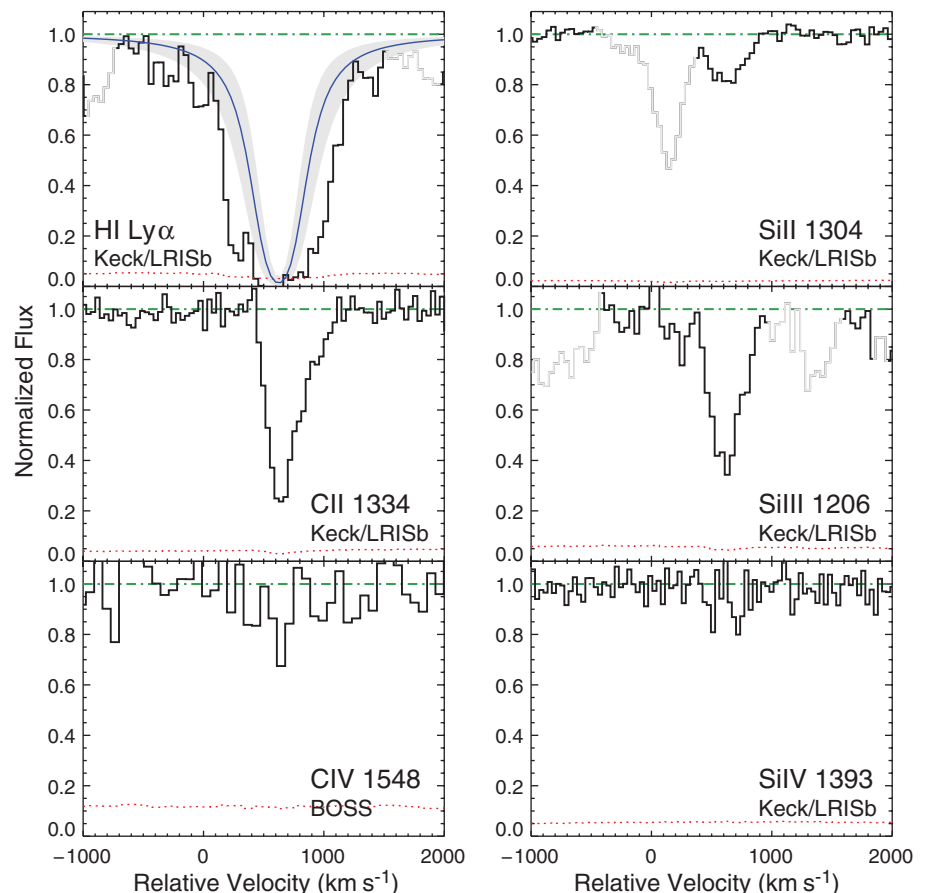
Fig. 4. Absorption line spectrum of cool gas in SDSSJ0841+3921. The spectrum of the absorbing gas detected in the b/g quasar sightline at an impact parameter of 176 kpc from the f/g quasar is shown. The gas shows strong HI and low-ionization–state metal absorption, offset by ≈650 km s^{-1} from the f/g quasar's systemic redshift. The CII absorption in particular exhibits a significant tail to velocities as large as ≈1000 km s^{-1}, providing evidence for extreme gas kinematics. We modeled the strong HI Lyα absorption with a Voigt profile (blue curve with gray band indicating uncertainty) and estimate a column density $\log N_{HI}$ = 19.2 ± 0.3. The strong low and intermediate ion absorption (SiII, CII, and SiIII) and correspondingly weak high ion absorption (CIV and SiIV) indicate that the gas is not highly ionized, and our photoionization modeling (45) implies $\log_{10} x_{HI} = -1.2 \pm 0.3$ or $\log_{10} N_H = 20.4 \pm 0.4$. We estimate a conservative lower limit on the gas metallicity to be 1/10th of the solar value. Spectral regions contaminated by other unassociated absorption are indicated in light gray.

outflows due to powerful AGN feedback are responsible for dispersing dense cool gas in the protocluster. However, the large cool gas mass $\sim 10^{11}\,M_\odot$ and high velocities ~ 1000 km s^{-1} imply an extremely large kinetic luminosity $L_{\rm wind} \sim 10^{44.6}$ for an AGN-powered wind, making the feedback scenario implausible (25). An even more compelling argument against a merger or feedback origin comes from the extremely small cloud sizes $r_{\rm cloud} \sim$ 40 pc implied by our measurements. Such small clouds moving supersonically ~ 1000 km s^{-1} through the hot $T \sim 10^7$ K shock-heated plasma predicted to permeate the protocluster will be disrupted by hydrodynamic instabilities in $\sim 5 \times 10^6$ years and can thus only be transported ~ 5 kpc (47). These short disruption time scales instead favor a scenario where cool dense clouds are formed in situ, perhaps via cooling and fragmentation instabilities, but are short-lived. The higher gas densities might naturally arise if hot plasma in the incipient intracluster medium pressure-confines the clouds, compressing them to high densities (48, 49). Emission line nebulae from cool dense gas have also been observed at the centers of present-day cooling flow clusters (50, 51), albeit on much smaller scales $\lesssim 50$ kpc. The giant Lyα nebulae in $z \sim 2$ to 3 protoclusters might be manifestations of the same phenomenon, but with much larger sizes and luminosities, reflecting different physical conditions at high redshift.

The large reservoir of cool dense gas in the protocluster SDSSJ0841+3921, as well as those implied by the giant nebulae in other protoclusters, appear to be at odds with our current theoretical picture of how clusters form. This is likely to be symptomatic of the same problem of too much cool gas in massive halos already highlighted for the quasar CGM (27, 42, 43). Progress will require more cosmological simulations of massive halos $M \gtrsim 10^{13}\,M_\odot$ at $z \sim 2$, as well as idealized higher-resolution studies. In parallel, a survey for extended Lyα emission around ~ 100 quasars would uncover a sample of ~ 10 giant Lyα nebulae, likely coincident with protoclusters, possibly also hosting multiple AGNs, and enabling continued exploration of the relationship between AGNs, cool gas, and cluster progenitors.

REFERENCES AND NOTES

1. J. Magorrian et al., Astron. J. 115, 2285–2305 (1998).
2. L. Ferrarese, Astrophys. J. 578, 90–97 (2002).
3. J. N. Bahcall, S. Kirhakos, D. H. Saxe, D. P. Schneider, Astrophys. J. 479, 642–658 (1997).
4. M. G. Haehnelt, M. J. Rees, Mon. Not. R. Astron. Soc. 263, 168–178 (1993).
5. S. Djorgovski, The Space Distribution of Quasars, D. Crampton, Ed., vol. 21 of Astronomical Society of the Pacific Conference Series (Astronomical Society of the Pacific, San Francisco, 1991), pp. 349–353.
6. J. F. Hennawi et al., Astron. J. 131, 1–23 (2006).
7. S. G. Djorgovski et al., Astrophys. J. 662, L1–L5 (2007).
8. E. P. Farina, C. Montuori, R. Decarli, M. Fumagalli, Mon. Not. R. Astron. Soc. 431, 1019–1025 (2013).
9. C. Lacey, S. Cole, Mon. Not. R. Astron. Soc. 262, 627–649 (1993).
10. R. F. Trainor, C. C. Steidel, Astrophys. J. 752, 39 (2012).
11. M. White et al., Mon. Not. R. Astron. Soc. 424, 933–950 (2012).
12. N. Fanidakis, A. V. Macciò, C. M. Baugh, C. G. Lacey, C. S. Frenk, Mon. Not. R. Astron. Soc. 436, 315–326 (2013).
13. B. P. Venemans et al., Astron. Astrophys. 461, 823–845 (2007).
14. P. J. Francis et al., Astrophys. J. 457, 490 (1996).
15. C. C. Steidel et al., Astrophys. J. 532, 170–182 (2000).
16. A. Dey et al., Astrophys. J. 629, 654–666 (2005).
17. R. A. Overzier et al., Astrophys. J. 771, 89 (2013).
18. M. K. M. Prescott, I. Momcheva, G. B. Brammer, J. P. U. Fynbo, P. Møller, Astrophys. J. 802, 32 (2015).
19. M. K. M. Prescott, N. Kashikawa, A. Dey, Y. Matsuda, Astrophys. J. 678, L77–L80 (2008).
20. Y. Yang, A. Zabludoff, C. Tremonti, D. Eisenstein, R. Davé, Astrophys. J. 693, 1579–1587 (2009).
21. Y.-K. Chiang, R. Overzier, K. Gebhardt, Astrophys. J. 779, 127 (2013).
22. J. F. Hennawi, J. X. Prochaska, Astrophys. J. 766, 58 (2013).
23. J. F. Hennawi et al., Astrophys. J. 651, 61–83 (2006).
24. J. F. Hennawi, J. X. Prochaska, Astrophys. J. 655, 735–748 (2007).
25. J. X. Prochaska, J. F. Hennawi, Astrophys. J. 690, 1558–1584 (2009).
26. J. X. Prochaska, J. F. Hennawi, R. A. Simcoe, Astrophys. J. 762, L19 (2013).
27. J. X. Prochaska et al., Astrophys. J. 776, 136 (2013).
28. J. X. Prochaska, M. W. Lau, J. F. Hennawi, Astrophys. J. 796, 140 (2014).
29. See supplementary text S2.
30. I. Kayo, M. Oguri, Mon. Not. R. Astron. Soc. 424, 1363–1371 (2012).
31. See supplementary text S3.
32. R. Ciardullo et al., Astrophys. J. 744, 110 (2012).
33. See supplementary text S4.
34. See supplementary text S6.
35. See supplementary text S5.
36. B. D. Lehmer et al., Astrophys. J. 691, 687–695 (2009).
37. See supplementary text S7.
38. R. E. Mostardi et al., Astrophys. J. 779, 65 (2013).
39. D. C. Martin et al., Astrophys. J. 786, 106 (2014).
40. See supplementary text S8.
41. S. Cantalupo, F. Arrigoni-Battaia, J. X. Prochaska, J. F. Hennawi, P. Madau, Nature 506, 63–66 (2014).
42. M. Fumagalli et al., Astrophys. J. 780, 74 (2014).
43. C.-A. Faucher-Giguere et al., Mon. Not. R. Astron. Soc. 449, 987–1003 (2015).
44. S. Lopez et al., Astrophys. J. 679, 1144–1161 (2008).
45. See supplementary text S9.
46. See supplementary text S10.
47. N. H. M. Crighton et al., Mon. Not. R. Astron. Soc. 446, 18–37 (2015).
48. A. H. Maller, J. S. Bullock, Mon. Not. R. Astron. Soc. 355, 694–712 (2004).
49. H. J. Mo, J. Miralda-Escude, Astrophys. J. 469, 589 (1996).
50. T. M. Heckman, S. A. Baum, W. J. M. van Breugel, P. McCarthy, Astrophys. J. 338, 48 (1989).
51. M. McDonald, S. Veilleux, D. S. N. Rupke, R. Mushotzky, Astrophys. J. 721, 1262–1283 (2010).

PHOSPHORUS CYCLING

Major role of planktonic phosphate reduction in the marine phosphorus redox cycle

B. A. S. Van Mooy,[1]* A. Krupke,[1] S. T. Dyhrman,[2] H. F. Fredricks,[1] K. R. Frischkorn,[2] J. E. Ossolinski,[1] D. J. Repeta,[1] M. Rouco,[2] J. D. Seewald,[1] S. P. Sylva[1]

Phosphorus in the +5 oxidation state (i.e., phosphate) is the most abundant form of phosphorus in the global ocean. An enigmatic pool of dissolved phosphonate molecules, with phosphorus in the +3 oxidation state, is also ubiquitous; however, cycling of phosphorus between oxidation states has remained poorly constrained. Using simple incubation and chromatography approaches, we measured the rate of the chemical reduction of phosphate to P(III) compounds in the western tropical North Atlantic Ocean. Colonial nitrogen-fixing cyanobacteria in surface waters played a critical role in phosphate reduction, but other classes of plankton, including potentially deep-water archaea, were also involved. These data are consistent with marine geochemical evidence and microbial genomic information, which together suggest the existence of a vast oceanic phosphorus redox cycle.

Phosphorus is an essential element for life, and in nature it is almost exclusively present at an oxidation state of +5. It is in this state that phosphorus forms phosphoester bonds in essential biochemicals such as phospholipids, nucleic acids, and nucleotides. In most of the oceans, variably protonated dissolved phosphate species of +5 oxidation state (primarily HPO_4^{2-}) are effectively the sole form of phosphorus (1). However, the notable exception to this is the surface water of the ocean's oligotrophic gyres, where dissolved organic phosphorus (DOP)

compounds may exceed phosphate by as much as a factor of 10 (2). About 5 to 10% of DOP is in the form of phosphonates (C–P bonds), which are organic molecules with phosphorus in an oxidation state of +3 (3). Thus, concentrations of dissolved phosphonates can potentially rival those of phosphate in the oligotrophic surface ocean.

Since the discovery of phosphonates (4), much information on the biological origin and biogeochemical roles of these molecules has emerged. The nitrogen-fixing cyanobacterium *Trichodesmium*, a denizen of oligotrophic gyres, contains ~10% of its cellular phosphorus in the form of phosphonates (5). Several classes of planktonic cyanobacteria, heterotrophic bacteria, and archaea appear to carry genes for the synthesis, processing, and/or uptake of phosphonates, including the low–molecular weight (LMW) phosphonate molecules methylphosphonic acid (MPn) and 2-aminoethylphosphonic acid (2-AEP) (6–12). Direct synthesis of MPn by a representative deep-ocean archaeon has also been shown (7). *Trichodesmium* is able to grow with phosphonates as the sole source of phosphorus (13, 14), and the degradation of MPn by these and other microorganisms is thought to fuel the aerobic production of methane in the ocean gyres (10, 12, 15). In addition to phosphonates, variably protonated phosphite species, which also contain phosphorus in the +3 oxidation state, might also play a role in the biogeochemistry of the oligotrophic gyres. Strains of cyanobacteria within the *Prochlorococcus* genus, which together compose the single most abundant group of phytoplankton in oligotrophic gyres, are capable of growing on phosphite as their sole phosphorus source (11). These organisms also carry the genes for phosphite uptake and oxidation to phosphate, as does *Trichodesmium* (11, 16).

To provide direct quantitative information on the cycling rates of phosphorus between the +5 and +3 oxidation states, common experimental approaches and analytical techniques were combined and applied (fig. S1) in the oligotrophic surface waters of the western tropical North Atlantic (17). Natural samples of plankton, either samples of the whole planktonic community from raw seawater or *Trichodesmium* colonies concentrated from seawater, were incubated in the presence of ^{33}P-phosphate. Preparative ion chromatography (IC) was then employed to isolate fractions from intracellular extracts that corresponded with the elution times of LMW P(III) compounds, including phosphite, MPn, and 2-AEP (Fig. 1A and figs. S2 and S3). IC has been applied in a number of previous studies of reduced-P compounds in natural samples (18–20). Finally, these fractions were combined and their radioactivity was measured by liquid scintillation counting (Fig. 1B). We express the yield of ^{33}P-labeled P(III) compounds from the chemical reduction of ^{33}P-phosphate as a percentage of the total uptake of ^{33}P-phosphate

[1]Department of Marine Chemistry and Geochemistry, Woods Hole Oceanographic Institution, Woods Hole, MA 02543, USA. [2]Department of Earth and Environmental Science and Lamont-Doherty Earth Observatory, Columbia University, New York, NY 10027, USA.
*Corresponding author. E-mail: bvanmooy@whoi.edu

into biomass, which was determined independently in parallel ^{33}P-phosphate incubations of identical design. Data were obtained on a cruise from Bermuda to Barbados (Fig. 2A), which spanned a range of surface-dissolved phosphate concentrations from below our limit of quantification (<2 nmol liter^{-1}) to 13 nmol liter^{-1}.

We observed that a substantial fraction of ^{33}P-phosphate uptake could be assigned to the production of intracellular P(III) compounds (Figs. 2B and 3). In surface waters, the production of P(III) compounds by the whole planktonic community was 3.4% ($n = 1$ individual incubation) of phosphate incorporation at station 5, whereas at station 9 values ranged from 0.7 to 1.7% ($n = 3$) (Fig. 3). If these percentages are representative of phosphate uptake by plankton throughout the ocean (21), then on the order of 10^{11} moles of phosphate per year are reduced by plankton in the surface ocean. This is probably a conservative estimate because our method does not capture the production of high–molecular weight P(III) compounds. For comparison, the preanthropogenic riverine input of phosphate to the ocean is on the order of 10^{10} moles P per year (22).

We also repeated our incubations with the whole community at depths of 40 and 150 m at station 5, yielding P(III) compound production of 1.5 to 2.8% ($n = 3$) and 15.3 to 16.5% ($n = 3$) of phosphate uptake, respectively. Thus, it appears that chemical phosphate reduction becomes an even more important component of phosphorus physiology within the planktonic community as depths increase and approach the mesopelagic zone, where archaea compose nearly 40% of the planktonic community (23). Estimating the role of deep-ocean archaea by ascribing all of the observed P(III) compound production at 150 m to archaea (7), applying an estimate of archaeal carbon fixation (24), and assuming a C:P stoichiometry of 100:1 yields an additional 10^{11} moles of chemical phosphate reduction per year in the deep ocean.

In *Trichodesmium* colonies, we found that 0.9 to 16.0% of the phosphate that was taken up was reduced to P(III) compounds intracellularly (Fig. 2B). The percentages at stations 5 and 9 were considerably greater than the concomitant percentage of the whole planktonic community in surface waters at these same locations (Fig. 3). Thus, *Trichodesmium* colonies appear to be sites of particularly intense intracellular chemical phosphate reduction, which is in agreement with previous work (5, 8, 10, 13, 14). The *Trichodesmium* data showed no meaningful correlations with phosphate concentrations, phosphate turnover times, or DOP concentrations. Thus, at the present time, the environmental factors that contribute to the regulation of phosphate reduction to P(III) compounds in surface waters remain unknown.

Calculating the absolute intracellular chemical phosphate reduction rates requires accurate data on phosphate concentrations, and phosphate concentrations were below our limit of quantification (< 2 nmol liter^{-1}) in the surface waters at stations 5 and 9. However, we were able to accurately quantify phosphate concentrations at 40 and
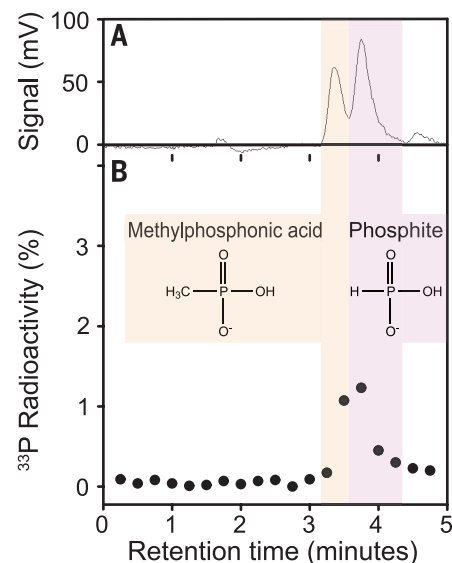
Fig. 1. ^{33}P radioactivity of P(III) compounds. (**A**) Conductivity IC chromatogram of an intracellular extract from *Trichodesmium* at station 19, which shows the elution of the methylphosphonic acid [P(III); highlighted in orange] and phosphite [P(III); highlighted in purple] internal recovery standards. (**B**) ^{33}P-radioactivity of fractions that eluted from the IC. The graph shows a peak in the P(III) fraction that is clearly indicative of the chemical reduction of ^{33}P-phosphate. Hydrolyzable phosphate-containing species and phosphate itself [P(V) compounds; figs. S2 and S4] eluted later than the P(III) compounds. Fractions were not collected at a time resolution that was fine enough to distinguish methylphosphonic acid and phosphite (fig. S3); thus, they were combined and are reported as "P(III) compounds."

150 m at station 5, which enabled us to calculate absolute rates of 18.0 to 42.2 pmol liter^{-1} hour^{-1} and 1.6 to 5.9 pmol liter^{-1} hour^{-1}, respectively. Degradation rates of MPn in surface waters of the North Pacific subtropical gyre were previously reported to be ~0.01 pmol liter^{-1} hour^{-1} (15). The greater rates we report suggest that the redox cycle of phosphate is more extensive than prior methods were able to detect. Possible explanations are that LMW P(III) compounds other than MPn were produced in our incubations or that MPn could be residing only briefly in the LMW form before being incorporated into the reservoir of high–molecular weight phosphonates (15).

We conducted an additional set of experiments to quantify the amount of phosphate reduction that results in the release of extracellular P(III) compounds by *Trichodesmium*. To do this, we took an aliquot of the seawater from the incubations with ^{33}P-labeled phosphate and then isolated the LMW P(III) compounds by preparative IC, as mentioned above (17). We did this at station 7, a location where phosphate concentrations were fortuitously high (13 nmol liter^{-1}), and found extracellular production rates of P(III) compounds that ranged from 7.5 to 13.3 pmol colony^{-1} day^{-1}. The intracellular production rates
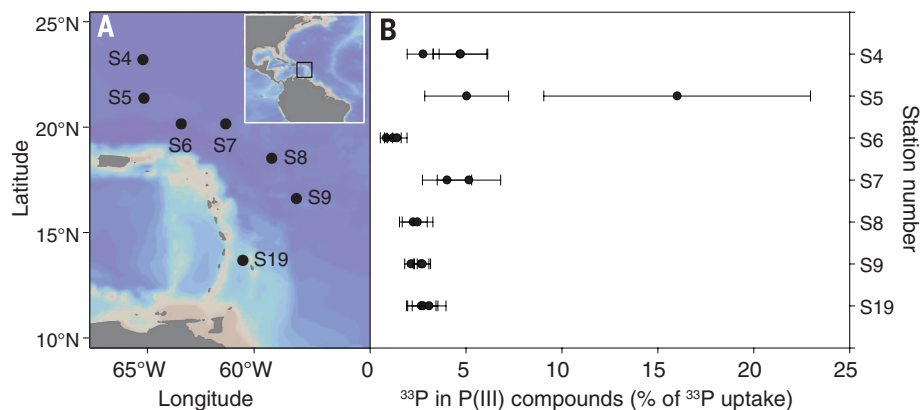
Fig. 2. Sampling locations and synthesis of P(III) compounds by *Trichodesmium* colonies. (**A**) Map of the tropical western North Atlantic Ocean showing station locations. The inset shows the broader western Atlantic. (**B**) Yield of ^{33}P-labeled P(III) compounds from the chemical reduction of ^{33}P-phosphate as a percentage of the total uptake of ^{33}P-phosphate into biomass in *Trichodesmium* colonies. Error bars represent the propagated errors of the IC blank subtraction and the total ^{33}P-phosphate uptake rate. The exceptionally high data point (16.0%) at station 5 (S5) underscores the potential heterogeneity in the rates of phosphate reduction in *Trichodesmium* colonies.
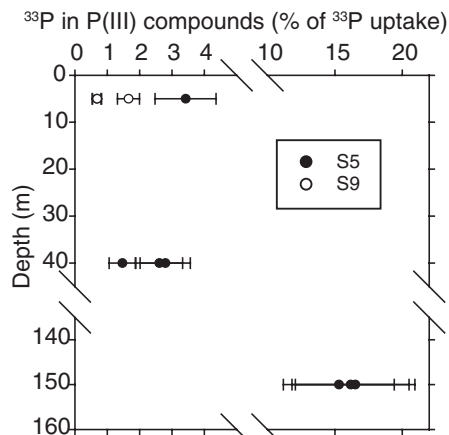
Fig. 3. Synthesis of P(III) compounds in the water column. The relative amount (percentage) of ^{33}P-phosphate incorporated into intracellular P(III) compounds by the whole planktonic community at station 5 (S5) and station 9 (S9). Error bars are as in Fig. 2. Note that two of the data points from S9 at 5 m are directly on top of one another: 0.67 ± 0.13% and 0.68 ± 0.14%.

by *Trichodesmium* at the same location were only 0.5 to 1.1 pmol colony^{-1} day^{-1}, which suggests that the vast majority of phosphate reduced by *Trichodesmium* colonies was released into the environment. Phosphorus has been implicated as a limiting nutrient for *Trichodesmium* in the tropical North Atlantic (*25, 26*), and thus this result is unexpected. Because colonies contain both *Trichodesmium* and epibiotic bacteria that appear to cooperate in the cycling of phosphorus (*27, 28*), we suggest that P(III) compounds could act as a phosphorus currency that is rapidly cycled between *Trichodesmium* and other microorganisms that live in association with the colony. With dissolved phosphonate concentrations in the range of 500 pmol liter^{-1} (*5*) and *Trichodesmium* abun-

dances approaching 10 colonies liter^{-1} in our study area (*29, 30*), *Trichodesmium* alone could drive the turnover of the entire dissolved P(III) reservoir in critical P-stressed regions of upper ocean on the time scale of a few days.

We also measured phosphite uptake by *Trichodesmium* at station 9. Phosphite was recently detected in rivers and estuaries using IC (*20*) but was below our detection limits in the oligotrophic waters of the western tropical North Atlantic. We synthesized ^{33}P-labeled phosphite (*17, 31*) and measured phosphite uptake in incubation experiments of the same design as those used to measure ^{33}P-phosphate uptake. However, unlike the ^{33}P-phosphate incubations, in which the radiotracer amendment represented a vanishingly small addition of phosphate (6 pmol liter^{-1}) (*7*), the specific radioactivity of the ^{33}P-phosphite was fairly low (0.1 Ci mol^{-1}). Thus, an amendment of ~1.5 μmol liter^{-1} was necessary to achieve a sufficient signal of uptake. Phosphite uptake rates ranged from to 307 to 925 pmol colony^{-1} hour^{-1} (*n* = 3) in *Trichodesmium*, probably representing maximum uptake rates indicative of saturated transmembrane phosphite transport or surface adsorption.

Overall, our study suggests that the production of phosphonates and/or phosphite contributes to a globally vast phosphorus redox cycle that exceeds the magnitude of phosphate inputs to the ocean. Phosphorus atoms are therefore likely to pass between +5 and +3 oxidation states on numerous occasions over the course of their ~20,000- to 100,000-year residence time in the ocean (*22*). The attendant changes in the chemical properties of phosphorus are likely to have major effects on the biogeochemical cycling of this critical bioactive element.

REFERENCES AND NOTES

1. D. M. Karl, *Annu. Rev. Mar. Sci.* **6**, 279–337 (2014).
2. K. Björkman, A. L. Thomson-Bulldis, D. M. Karl, *Aquat. Microb. Ecol.* **22**, 185–198 (2000).
3. C. L. Young, E. D. Ingall, *Aquat. Geochem.* **16**, 563–574 (2010).
4. L. L. Clark, E. D. Ingall, R. Benner, *Nature* **393**, 426 (1998).
5. S. T. Dyhrman, C. R. Benitez-Nelson, E. D. Orchard, S. T. Haley, P. J. Pellechia, *Nat. Geosci.* **2**, 696–699 (2009).
6. J. F. Villarreal-Chiu, J. P. Quinn, J. W. McGrath, *Front. Microbiol.* **3**, 19 (2012).
7. W. W. Metcalf *et al.*, *Science* **337**, 1104–1107 (2012).
8. S. T. Dyhrman *et al.*, *Nature* **439**, 68–71 (2006).
9. A. Martinez, G. W. Tyson, E. F. Delong, *Environ. Microbiol.* **12**, 222–238 (2010).
10. D. M. Karl *et al.*, *Nat. Geosci.* **1**, 473–478 (2008).
11. A. Martínez, M. S. Osburne, A. K. Sharma, E. F. DeLong, S. W. Chisholm, *Environ. Microbiol.* **14**, 1363–1377 (2012).
12. P. Carini, A. E. White, E. O. Campbell, S. J. Giovannoni, *Nat. Commun.* **5**, 4346 (2014).
13. A. White, D. Karl, K. Björkman, L. Beversdorf, R. Letelier, *Limnol. Oceanogr.* **55**, 1755–1767 (2010).
14. L. J. Beversdorf, A. E. White, K. M. Björkman, R. M. Letelier, D. M. Karl, *Limnol. Oceanogr.* **55**, 1768–1778 (2010).
15. D. A. del Valle, D. M. Karl, *Aquat. Microb. Ecol.* **73**, 93–105 (2014).
16. R. Feingersch *et al.*, *ISME J.* **6**, 827–834 (2012).
17. Materials and methods are available as supplementary materials on *Science* Online.
18. H. Pech *et al.*, *J. Chromatogr. Sci.* **49**, 573–581 (2011).
19. M. M. McDowell *et al.*, *J. Chromatogr. A* **1039**, 105–111 (2004).
20. M. A. Pasek, J. M. Sampson, Z. Atlas, *Proc. Natl. Acad. Sci. U.S.A.* **111**, 15468–15473 (2014).
21. T. DeVries, J. H. Liang, C. Deutsch, *Biogeosciences* **11**, 5381–5398 (2014).
22. A. Paytan, K. McLaughlin, *Chem. Rev.* **107**, 563–576 (2007).
23. M. B. Karner, E. F. DeLong, D. M. Karl, *Nature* **409**, 507–510 (2001).
24. C. Wuchter *et al.*, *Proc. Natl. Acad. Sci. U.S.A.* **103**, 12317–12322 (2006).
25. M. M. Mills, C. Ridame, M. Davey, J. La Roche, R. J. Geider, *Nature* **429**, 292–294 (2004).
26. S. A. Sañudo-Wilhelmy *et al.*, *Nature* **411**, 66–69 (2001).
27. B. A. S. Van Mooy *et al.*, *ISME J.* **6**, 422–429 (2012).
28. L. R. Hmelo, B. A. S. Van Mooy, T. J. Mincer, *Aquat. Microb. Ecol.* **67**, 1–14 (2012).
29. E. J. Carpenter, A. Subramaniam, D. G. Capone, *Deep-Sea Res. Part I* **51**, 173–203 (2004).
30. M. Rouco, H. J. Warren, D. J. McGillicuddy Jr., J. B. Waterbury, S. T. Dyhrman, *Limnol. Oceanogr.* **59**, 1899–1909 (2014).
31. N. Zhang, J. E. Casida, *J. Org. Chem.* **66**, 327–329 (2001).

SUPPLEMENTARY MATERIALS

www.sciencemag.org/content/348/6236/783/suppl/DC1
Materials and Methods
Figs. S1 to S4
Tables S1 to S3
References (*32–37*)

30 January 2015; accepted 3 April 2015
10.1126/science.aaa8181

ANIMAL PHYSIOLOGY

Whole-body endothermy in a mesopelagic fish, the opah, *Lampris guttatus*

Nicholas C. Wegner,[1]* Owyn E. Snodgrass,[2] Heidi Dewar,[1] John R. Hyde[1]

Endothermy (the metabolic production and retention of heat to warm body temperature above ambient) enhances physiological function, and whole-body endothermy generally sets mammals and birds apart from other animals. Here, we describe a whole-body form of endothermy in a fish, the opah (*Lampris guttatus*), that produces heat through the constant "flapping" of wing-like pectoral fins and minimizes heat loss through a series of counter-current heat exchangers within its gills. Unlike other fish, opah distribute warmed blood throughout the body, including to the heart, enhancing physiological performance and buffering internal organ function while foraging in the cold, nutrient-rich waters below the ocean thermocline.

The ability of an organism to conserve metabolic heat and maintain its body temperature above that of the surrounding environment (endothermy) increases reaction rates, muscle power output, and the capacity for sustained aerobic performance. This process provides distinct benefits, particularly for organisms that inhabit environments of low or variable temperature (*1*, *2*). As such, endothermic organisms demonstrate a higher capacity for niche expansion and often gain a competitive advantage over organisms that thermoconform to their environment (such as in predator-prey interactions) (*2–5*). Because of the high heat capacity of water, the retention of body heat in aquatic habitats is extremely challenging, even for mammals, and thus only a small number of highly active fish species (<0.1% of described fishes) have acquired the ability to retain some internally produced heat (*6–9*). These fishes are termed "regional endotherms" because unlike mammals and birds, they are only able to increase the temperature of specific tissues or organs.

The regionally endothermic tunas (family Scombridae) and lamnid sharks (family Lamnidae) (which warm their aerobic swimming musculature as well as other regions in some species) (*6–12*) and the billfishes (families Istiophoridae and Xiphiidae, which warm the eye and brain region only) (*13*, *14*) are often termed "high-performance" fishes because of their increased physiological function associated with regional heat retention (*8*, *15*). However, these fishes fall far short of whole-body endothermy because much of the body (including vital organs such as the heart) remains at ambient temperature, which ultimately puts limits on aerobic performance in cold water (*16*, *17*). This limitation is linked to mechanisms used by these groups to reduce heat loss. Although conductive heat loss to the water is minimized by the location of heat-producing tissues near the body midline and insulation from the surrounding tissues, the main challenge to fish endothermy is the convective loss of heat as blood comes in close contact with the water at the gill lamellae (site of respiratory gas exchange). To reduce convective loss of heat, these fishes have retia mirabilia or "wonderful nets" of blood vessels that form counter-current heat exchangers com-

posed of densely packed arterioles and venules running in opposing directions, in which warm venous blood returning from the heat-production site transfers its heat to the cold arterial blood arriving from the gills (*18*). To date, these retia in fish have only been observed in connection with specific muscle groups or organs, leaving the heart and many other tissues at ambient water temperature.

This study presents morphological, temperature, and behavioral data that demonstrate an independent evolution of a more whole-body form of endothermy present in the opah, *Lampris gutattus*—a poorly studied, large, mesopelagic fish with a circumglobal distribution. We show that unlike other fishes, the opah has putative heat-conserving retia located inside the gills, thus isolating the primary site of heat loss from the rest of the body. In situ temperature measurements acquired for freshly sacrificed opah landed during fisheries surveys reveal that the entire body core (pectoral swimming musculature, viscera, and heart) and cranial region (Table 1) are all significantly warmer than the environment. A representative superimposed thermal profile for a 40.0-kg opah reconstructed from more than 35 temperature measurements taken 4 to 5 cm beneath the skin over the entire animal (Fig. 1A) shows the general distribution of elevated temperatures. Elevated in situ temperatures were confirmed with in vivo measurements obtained by using a thermocouple implanted in the pectoral musculature of swimming opah released from our fishing vessel and tethered to a surface float for recapture. These fish had an average pectoral muscle temperature elevated 4.8 ± 1.2°C above ambient (Table 1) when swimming between depths of 50 to 300 m at water temperatures of 7.8 to 10.8°C (data for a 39.0-kg opah are shown in Fig. 1B).

In opah, the bulk of metabolic heat appears to be produced by the dark red aerobic pectoral musculature, which is used during continuous swimming (*19*) and is insulated from the water by a 0.88 ± 0.21–cm-thick layer of fatty connective tissue (mean thickness $\pm$ SD from 16 opah, 22.0 to 67.5 kg) (fig. S1). Unlike most fishes that use body undulation to achieve forward thrust during swimming, opah primarily use pectoral fin oscillation (movie S1). The aerobic pectoral musculature in opah comprises 16% of their total mass (37% of the total

[1]Fisheries Resources Division, Southwest Fisheries Science Center, National Marine Fisheries Service (NMFS), National Oceanic and Atmospheric Administration (NOAA), La Jolla, CA 92037, USA. [2]Ocean Associates, Southwest Fisheries Science Center, NMFS, NOAA, La Jolla, CA 92037, USA.
*Corresponding author. E-mail: nick.wegner@noaa.gov

Table 1. Regional body-temperature measurements (means $\pm$ SD) taken from freshly captured and free-swimming opah.

Body region	Mean temperature (°C)	Temperature elevation above ambient (°C)	Number of fish (*n*)
In situ measurements (decked fish)			
Pectoral muscle	13.8 ± 1.5	3.8 ± 0.8	22
Cranial region	16.1 ± 3.9	6.0 ± 3.0	22
Viscera	13.5 ± 1.6	3.5 ± 1.0	21
Heart	13.2 ± 1.7	3.2 ± 0.7	19
In vivo measurements (free-swimming fish)			
Pectoral muscle	14.4 ± 0.4	4.8 ± 1.2	4
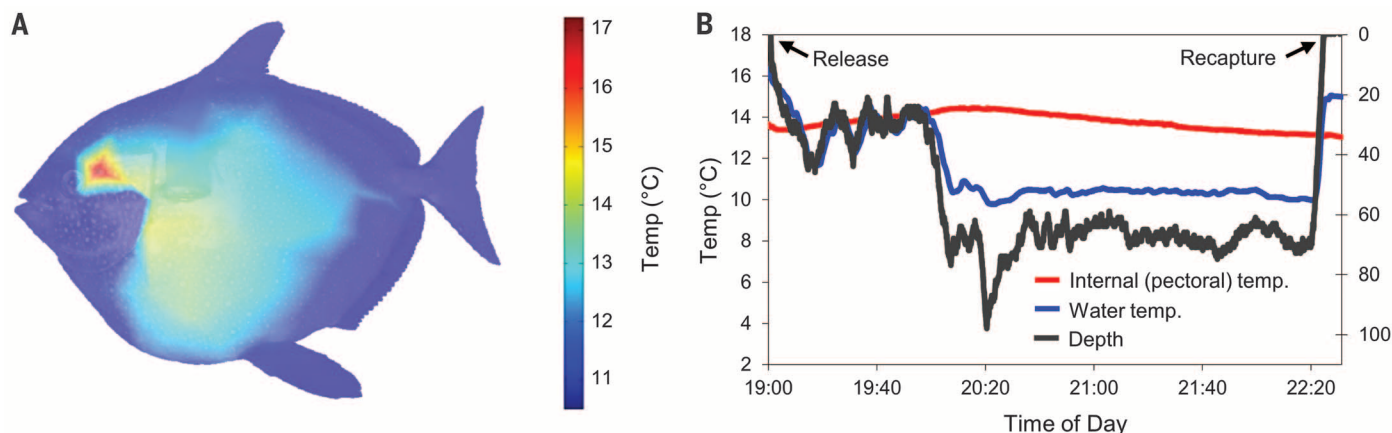
Fig. 1. Body temperature in the opah, *L. guttatus.* (**A**) In situ internal temperature profile (measurements taken ~4 to 5 cm below the skin) for a 98.0-cm fork length (40.0 kg) opah, with an ambient reference temperature of 10.5°C. (**B**) In vivo pectoral muscle temperature for a 96.4-cm (39.0 kg) opah swimming at depth.
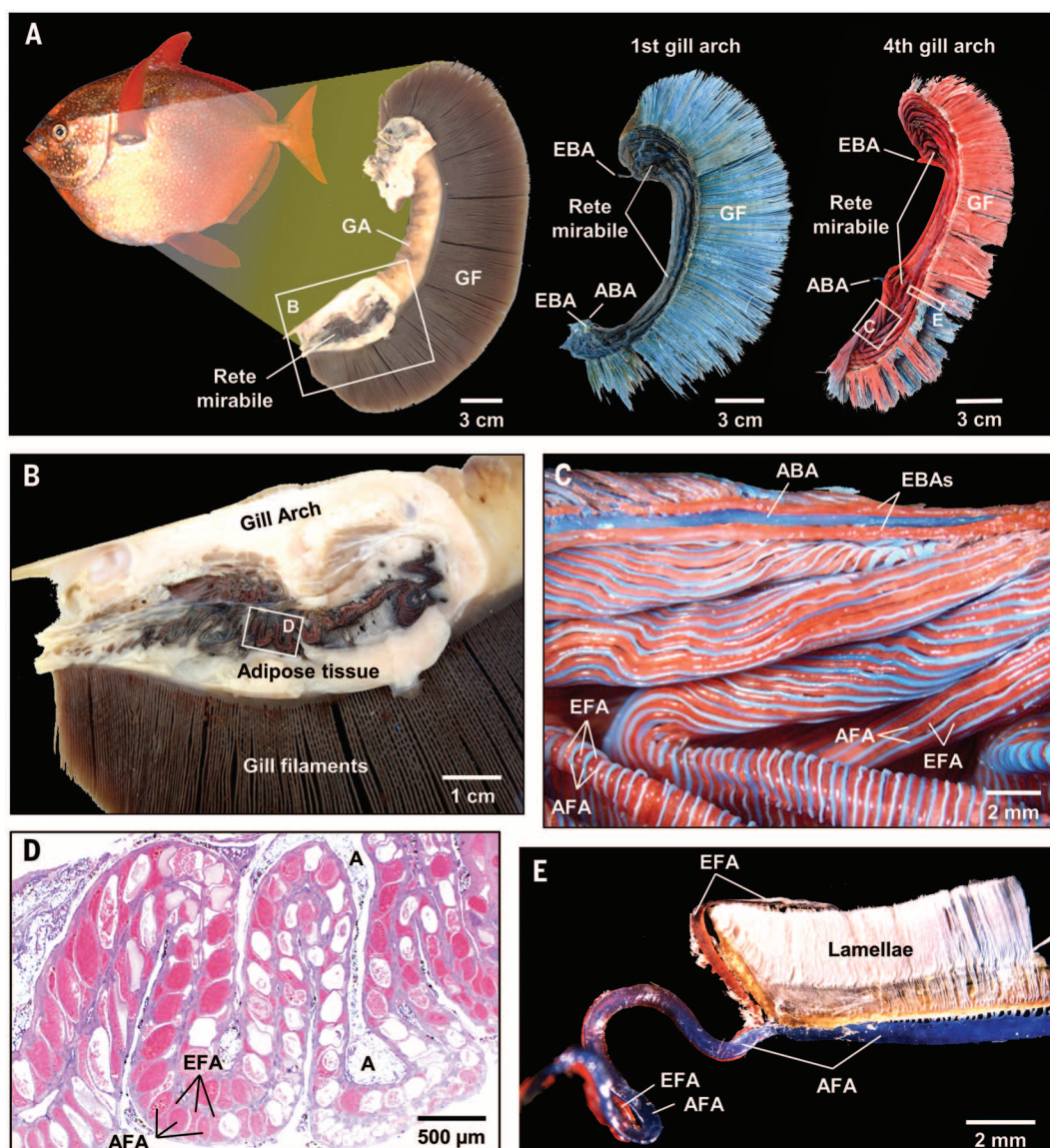
Fig. 2. Anatomy and vasculature of the opah gill. (**A**) Opah with enlarged fixed gill arch (left) and examples of vascular casts of the first gill arch (blue casting material only; center) and fourth arch (blue and red casting material; right). (**B**) Enlarged view of box "B" in (A) showing blood vessels of the rete mirabile surrounded by adipose tissue within the gill arch. (**C**) Enlarged view of box "C" in (A) showing the convoluted alternating afferent (blue, deoxygenated) and efferent (red, oxygenated) filament arteries forming the rete mirabile. (**D**) Magnified image of box in (B) showing a cross section through the rete with two rows of blood vessels (one associated with each gill hemi-branch) containing alternating afferent and efferent filament arteries. (**E**) Gill filament extracted from box "E" in (A) showing the tight coupling of the afferent filament artery (blue, delivering deoxygenated blood to the gas-exchanging lamellae) with the efferent filament artery (red, returning with oxygenated blood). A, adipose tissue; ABA, afferent branchial artery; AFA, afferent filament artery; EBA, efferent branchial artery; EFA, efferent filament artery; GA, gill arch; GF, gill filaments.

propulsive musculature) (*19*), which is among the highest ratio reported for any fish and 25 to 800% more than that of the regionally endothermic tunas and lamnid sharks that warm their aerobic myotomal swimming musculature (table S1).

What is exceptional about the opah is its arrangement of counter-current retia mirabilia located inside each thick, fat-insulated gill arch (Fig. 2), which thermally isolate the respiratory exchange surfaces from the rest of the body. Vascular casts of the gills (Fig. 2, A, C, and E) reveal that unlike other fishes, extensions of the afferent and efferent filament arteries (which deliver and collect blood immediately pre– and post–gas exchange at the gill lamellae) are embedded within each gill arch in a tightly bundled and contorted manner to form an arterio-arterial rete. Specifically, the afferent and efferent arteries of each individual filament are closely coupled (Fig. 2E) and stacked in an alternating pattern within the arch (Fig. 2, C and D) so that the cold oxygenated blood of each efferent vessel (returning from the respiratory exchange surfaces) should be warmed by the conduction of heat from the warm de-oxygenated blood in the afferent filament arteries on either side (which are carrying blood to the gas exchange surfaces). As a result, oxygenated blood leaving the respiratory exchange surfaces should be warmed before entering into efferent branchial arteries for distribution to the rest of the body.

Although these arterio-arterial retia should allow warm blood to be circulated throughout the body, the cranial region is warmer than the body core (Table 1 and Fig. 1), indicating an additional heat source associated with the brain and extraocular muscles (the muscles that move the eye during swimming). Previous work suggests that heat may be produced by the proximal region of the paired lateral rectus muscles that attach at the base of the skull (immediately ventral to the brain) and conserved by small retia associated with the lateral and superior rectus muscles (*20*).

Of particular importance is the capacity of opah to increase the temperature of the heart, which receives warm blood from both the coronary arteries and the systemic venous return and is insulated from the opercular cavities by a 0.56 ± 0.07–cm-thick fat layer (mean thickness from 15 opah, 22.0 to 67.5 kg). For the regionally endothermic tunas and lamnid sharks (which cannot warm the heart), both aerobic performance and foraging dives into cold water are thought to be largely limited by heart function, with weaker cardiac excitation–contraction (E-C) coupling leading to reduced cardiac outputs at lower temperatures (*16, 17, 21, 22*), which likely causes most species to return to surface waters to warm in between deep, cold water dives. Although some regionally endothermic species such as the salmon shark, *Lamna ditropis*, that spend considerable time in cold waters show enhanced expression of E-C coupling proteins to help mitigate the effect of low temperatures, cardiac function is still greatly reduced at colder temperatures (*22*). Evidence of an increased thermal tolerance in opah comes from satellite tracking data showing that opah spend most of their time below the mixed surface layer at depths between 50 and 400 m (Fig. 3)

(*23*) without regular visits to surface waters to warm.

With a warm body core and heart, and even warmer cranial region, opah have the capacity for enhanced physiological function in their deep, cold habitat. The elevated body temperature of opah should increase muscle power output and capacity for sustained performance, enhance temporal resolution and neural conductance for the eye and brain, increase the rates of food digestion and assimilation in the digestive tract, and reduce the impact of cold ambient temperatures and temperature changes on cardiac and other organ performance. Supporting its endothermic ability and increased aerobic performance, the opah has a relatively large heart and gill surface area, high hematocrit level, and an unusually large aerobic muscle mass (table S1), all of which are similar to characteristics of high-performance predators such as tunas and lamnid sharks, and in stark contrast to those of other fishes from its order (order Lampridiformes), which tend to be slow-moving ambush predators.

In many respects, the opah has converged with regionally endothermic fishes such as tunas and lamnid sharks for increased aerobic capacity. However, unlike these active, more surface-oriented predators that are thought to be derived from tropical ancestors and to use regional endothermy to expand their thermal tolerance or habitat utilization into deep and colder waters (*6, 7*), the opah's evolutionary history is likely tied to greater oceanic depths, with all but the most basal lineage of the Lampridiformes inhabiting the mesopelagic zone (200 to 1000 m depth) (*24*). Therefore, rather than using regional endothermy to dive below the thermocline during temporary forages, the opah (with its more whole-body form of endothermy) is distinctively specialized to exploit cold, deeper waters while maintaining elevated levels of physiological performance. The discovery of this form of endothermy, coupled with the recent finding of several distinct opah species inhabiting different regions of the world's oceans (*25*) (including the subpolar southern opah, *L. immaculatus*), sets the stage for future comparative studies to further explore this key evolutionary innovation.

Fig. 3. Depth distribution of an opah in comparison with that of the regionally endothermic albacore tuna, *Thunnus alalunga*, as determined through archival tags. (**Left**) Opah. (**Right**) Albacore tuna. The percentage of time each species spent above 50 m (dotted gray line indicates the estimated mean depth of the bottom of the warm mixed surface layer) is shown for both daylight and nighttime hours. [Data for albacore tuna are from (*26*).]

REFERENCES AND NOTES

1. A. F. Bennett, *Am. J. Physiol.* **247**, R217–R229 (1984).
2. B. K. McNab, *The Physiological Ecology of Vertebrates: A View from Energetics* (Comstock, Ithaca, NY, 2002).
3. A. F. Bennett, J. A. Ruben, *Science* **206**, 649–654 (1979).
4. W. J. Hillenius, J. A. Ruben, *Physiol. Biochem. Zool.* **77**, 1019–1042 (2004).
5. J. Ruben, *Annu. Rev. Physiol.* **57**, 69–95 (1995).
6. K. A. Dickson, J. B. Graham, *Physiol. Biochem. Zool.* **77**, 998–1018 (2004).
7. B. A. Block, J. R. Finnerty, A. F. R. Stewart, J. Kidd, *Science* **260**, 210–214 (1993).
8. D. Bernal, K. A. Dickson, R. E. Shadwick, J. B. Graham, *Comp. Biochem. Physiol.* **129**, 695–726 (2001).
9. F. G. Carey, J. M. Teal, J. W. Kanwisher, K. D. Lawson, J. S. Beckett, *Am. Zool.* **11**, 137–145 (1971).
10. D. Bernal, J. M. Donley, R. E. Shadwick, D. A. Syme, *Nature* **437**, 1349–1352 (2005).

11. J. M. Donley, C. A. Sepulveda, P. Konstantinidis, S. Gemballa, R. E. Shadwick, *Nature* **429**, 61–65 (2004).
12. J. B. Graham, K. A. Dickson, in *Tuna: Physiology, Ecology and Evolution*, B. A. Block, E. D. Stevens, Eds. (Academic Press, San Diego, CA, 2001), vol. 19, pp. 121–165.
13. B. A. Block, *J. Morphol.* **190**, 169–189 (1986).
14. F. G. Carey, *Science* **216**, 1327–1329 (1982).
15. R. W. Brill, *Comp. Biochem. Physiol.* **113**, 3–15 (1996).
16. H. A. Shiels, A. Di Maio, S. Thompson, B. A. Block, *Proc. Biol. Sci.* **278**, 18–27 (2011).
17. P. C. Castilho, A. M. Landeira-Fernandez, J. Morrissette, B. A. Block, *Comp. Biochem. Physiol.* **148**, 124–132 (2007).
18. E. D. Stevens, in *Encyclopedia of Fish Physiology: From Genome to Environment*, A. P. Farrell, E. D. Stevens, J. J. Cech, J. G. Richards, Eds. (Academic Press, San Diego, CA, 2011), vol. 2, pp. 1119–1131.
19. R. H. Rosenblatt, G. D. Johnson, *Copeia* **1976**, 367–370 (1976).
20. R. M. Runcie, H. Dewar, D. R. Hawn, L. R. Frank, K. A. Dickson, *J. Exp. Biol.* **212**, 461–470 (2009).
21. J. M. Blank *et al.*, *J. Exp. Biol.* **207**, 881–890 (2004).
22. K. C. Weng *et al.*, *Science* **310**, 104–106 (2005).
23. J. J. Polovina, D. Hawn, M. Abecassis, *Mar. Biol.* **153**, 257–267 (2008).
24. J. E. Olney, in *Species Identification Guide for Fisheries Purposes. Part 1 (Elopidae to Linophrynidae)*, K. E. Carpenter, V. H. Niem, Eds. (FAO, Rome, 1999), pp. 155–169.
25. J. R. Hyde, K. E. Underkoffler, M. A. Sundberg, *Mol. Ecol. Resour.* **14**, 1239–1247 (2014).
26. J. Childers, S. Snyder, S. Kohin, *Fish. Oceanogr.* **20**, 157–173 (2011).

NEURODEVELOPMENT

Live imaging of adult neural stem cell behavior in the intact and injured zebrafish brain

Joana S. Barbosa,[1,2] Rosario Sanchez-Gonzalez,[1] Rossella Di Giaimo,[1,3] Emily Violette Baumgart,[1] Fabian J. Theis,[4,5] Magdalena Götz,[1,6,7] Jovica Ninkovic[1,6]*

Adult neural stem cells are the source for restoring injured brain tissue. We used repetitive imaging to follow single stem cells in the intact and injured adult zebrafish telencephalon in vivo and found that neurons are generated by both direct conversions of stem cells into postmitotic neurons and via intermediate progenitors amplifying the neuronal output. We observed an imbalance of direct conversion consuming the stem cells and asymmetric and symmetric self-renewing divisions, leading to depletion of stem cells over time. After brain injury, neuronal progenitors are recruited to the injury site. These progenitors are generated by symmetric divisions that deplete the pool of stem cells, a mode of neurogenesis absent in the intact telencephalon. Our analysis revealed changes in the behavior of stem cells underlying generation of additional neurons during regeneration.

The maintenance of adult neural stem cells (aNSCs) is important for life-long organ homeostasis (*1*) and regeneration (*2–4*). There is presently a discrepancy between models describing the behavior of aNSCs in the mammalian brain, one proposing largely depletion of aNSCs (*5, 6*) and the other some degree of long-term self-renewal (*7*). In the adult zebrafish brain, aNSCs exist not only in a more widespread manner compared with those of mammals but also react to injury by regenerating neurons (*2, 3, 8–14*). Indeed, the cellular architecture is restored, which includes additional neurogenesis after stab wound injury in the adult zebrafish telencephalon (*2, 3, 11, 13, 14*). As aNSCs are positioned close to the surface in the zebrafish dorsal telencephalon (*12, 15*) (Fig. 1A), the behavior of aNSCs in the intact brain and during regeneration of the injured brain can be examined noninvasively by live in vivo imaging.

We established a protocol by which we could follow individual aNSCs over time [fig. S1A and supplementary materials (SM)]. We used the *brassy* zebrafish line, which has low pigment levels, crossed with the *Tg(gfap:GFP)mi2001* transgenic line (*16*), which labeled aNSCs (Fig. 1A). We sparsely labeled the glial fibrillary acidic protein promoter–driven green fluorescent protein (*gfap*:GFP)–positive aNSCs (see SM) by electroporation of plasmids encoding for red fluorescent proteins [tdTomato, mCherry, or red fluorescent protein (RFP)] (fig. S1 and SM). Most of the labeled cells with radial morphology were immunoreactive to GFAP (106 of 124 cells; 85%) (fig. S1, E and F) and did not differ with regard to their proliferation from the overall *gfap*:GFP–positive aNSCs (fig. S1, C and D). Individual tdTomato-labeled NSCs at the

dorsal brain surface were identified by their position relative to the stable *gfap*:GFP–positive cells (colored dots in Fig. 1C). These individual cells were then followed by imaging through the thinned skull for a period of 1 month (fig. S1A). As many reporter-positive cells neither moved nor divided, we used their distribution pattern in post-imaging immunostaining and microscopy to re-identify and confirm cell identity of imaged cells (figs. S2, S4, and S5).

In the intact brain, aNSCs rarely divide (*17, 18*). Indeed, 66 of 109 (61%) of the labeled aNSCs in the intact zebrafish telencephalon stayed quiescent without changing their identity throughout the imaging time (fig. S2), and only 1 of 109 cells followed by live imaging died. However, 14 aNSCs (13%, *n* = 109) divided during this time. We found that the aNSCs rarely divided symmetrically (1 cell of 109; 0.9%) (Fig. 1C; fig. S3, B and E; fig. S4; and movies S1 and S2), with one aNSC generating two aNSCs, both of which retained *gfap*:GFP expression and the characteristic thick radial process (fig. S4). In contrast, 13 of 14 dividing aNSCs (~93%) divided asymmetrically, generating one cell with aNSC identity (radial morphology and *gfap*:GFP expression) and one cell that lacked the radial morphology (Fig. 2; fig. S3, B and E; figs. S5 and S6; and movies S3 and S4). Of these progeny lacking radial morphology, 25% (two of eight cells) also lost *gfap*:GFP expression (GFP-negative progeny in fig. S3, B and D). Because GFP is very stable, the protein can persist even after the cell is no longer an aNSC (Fig. 1B), and some GFP-positive cells do not express aNSC markers (*15*). Although asymmetrically generated daughter cells differ in regard to inheritance of GFP, all of them lose the radial glia morphology, the defining criteria for the asymmetric divisions (93%, 13 of 14 dividing aNSCs). Some cells that had lost the radial process, however, were not immunoreactive for the neuronal marker HuC/D (figs. S3B and S5C), which implies that they may be intermediate progenitor cells.

To examine the behavior of Sox2-positive intermediate progenitors (fig. S7), we used Moloney murine leukemia virus–based retroviral vectors to stably transduce progenitor cells (*18*). We analyzed their clonal progeny that contained no glia

[1]Institute of Stem Cell Research, Helmholtz Center Munich, Munich, Germany. [2]Ph.D. Program in Biomedicine and Experimental Biology (BEB), Center for Neuroscience and Cell Biology, University of Coimbra, Coimbra, Portugal. [3]Department of Biology, University of Naples Federico II, Naples, Italy. [4]Institute of Computational Biology, Helmholtz Center Munich, Munich, Germany. [5]Institute for Mathematical Sciences, Technical University Munich, Garching, Germany. [6]Biomedical Center, University of Munich, Munich, Germany. [7]Munich Cluster for Systems Neurology "SyNergy," Ludwig Maximilian University of Munich, Munich, Germany.
*Corresponding author. E-mail: ninkovic@helmholtz-muenchen.de
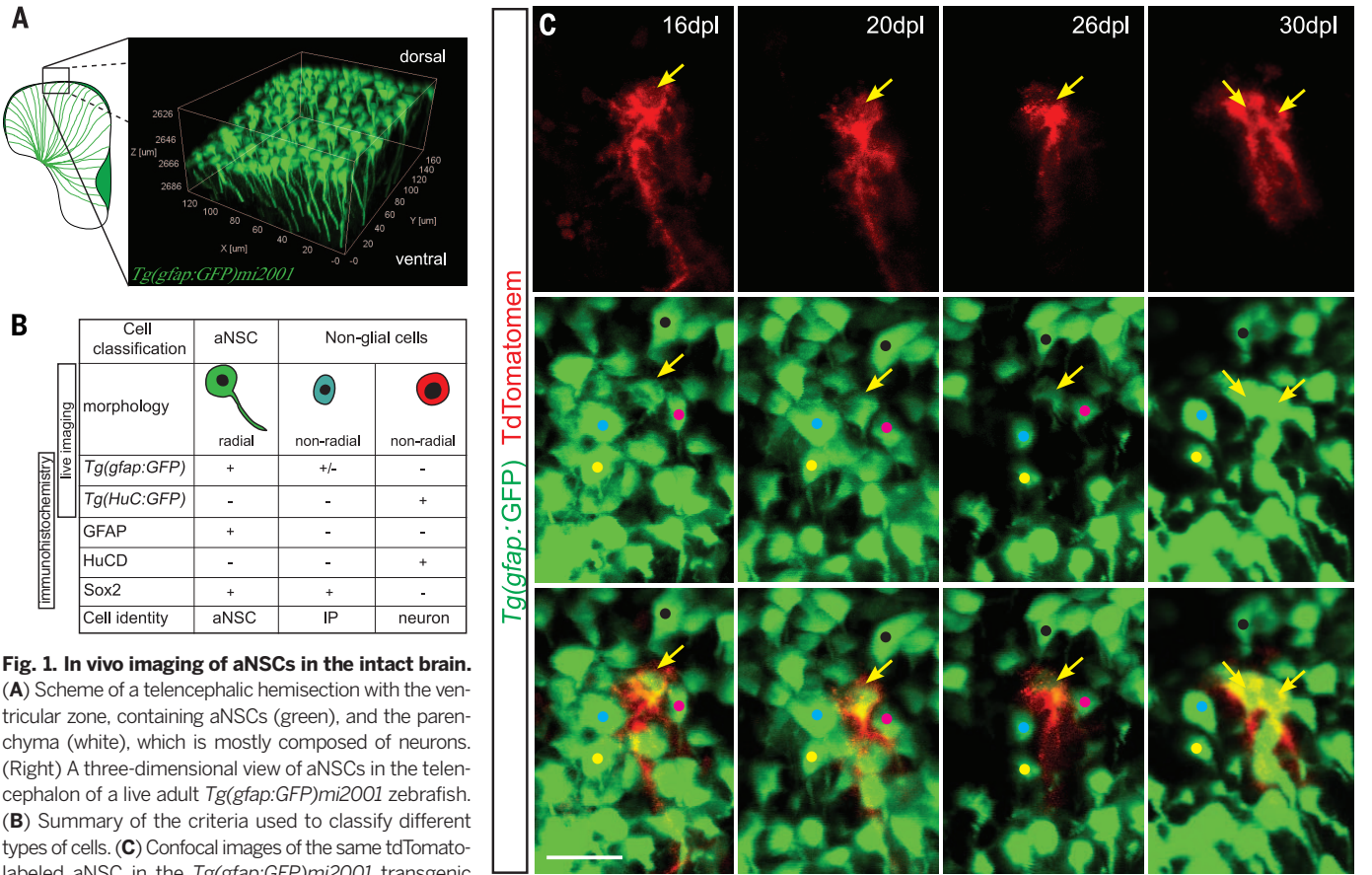
Fig. 1. In vivo imaging of aNSCs in the intact brain. (**A**) Scheme of a telencephalic hemisection with the ventricular zone, containing aNSCs (green), and the parenchyma (white), which is mostly composed of neurons. (Right) A three-dimensional view of aNSCs in the telencephalon of a live adult *Tg(gfap:GFP)mi2001* zebrafish. (**B**) Summary of the criteria used to classify different types of cells. (**C**) Confocal images of the same tdTomato-labeled aNSC in the *Tg(gfap:GFP)mi2001* transgenic line at different time points depicting its symmetric gliogenic (RG) division generating two aNSCs [30 days post labeling (dpl)]. (See also fig. S4 for all time points imaged.) Yellow arrows point to single cells. Scale bar, 20 μm. Abbreviation: IP, intermediate progenitors.

Fig. 2. Asymmetric division of an aNSC in the adult telencephalon. (**A**) Confocal images of the same tdTomato-labeled aNSC in the *Tg(gfap:GFP) mi2001* transgenic line at different time points depicting its asymmetric division producing one aNSC (yellow arrow) and one intermediate progenitor (8 dpl, blue arrow). (**B**) Orthogonal projections through the Z-stack. Scale bar, 20 μm.
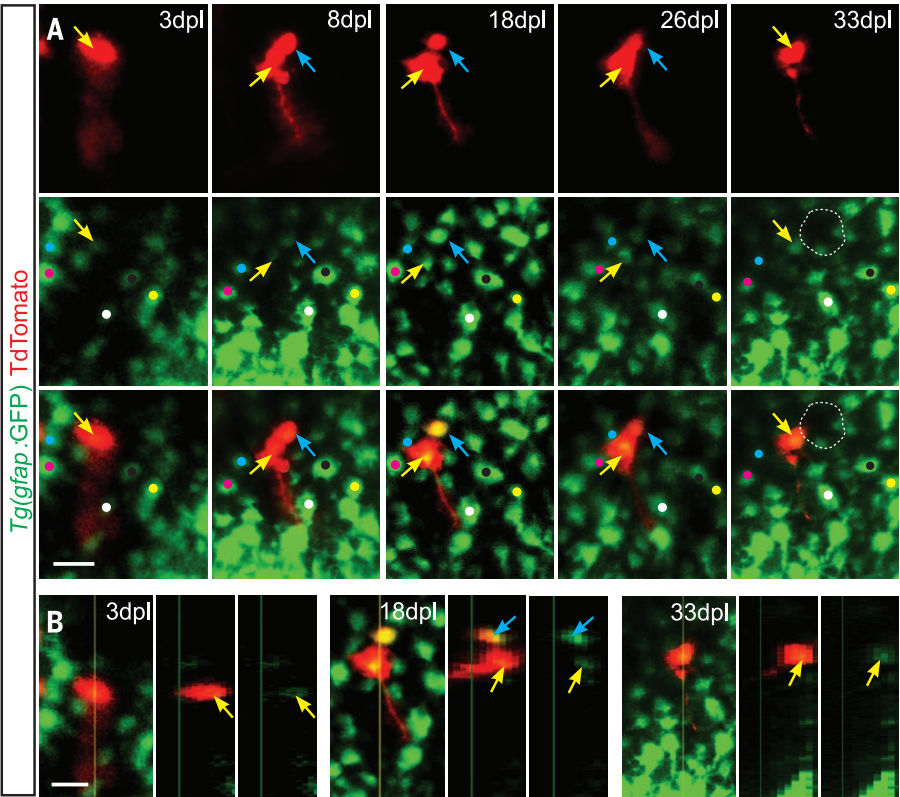
and therefore likely originated from the intermediate progenitors. The mean size of the clone was 3.9 cells, which indicated some degree of amplification in the lineages generated by intermediate progenitors (fig. S7). Among the amplifying clones (≥2 cells) 44% (four of nine clones) were HuC/D–positive cells only (fig. S7) (maximal clone size of pure neuronal clones was eight cells). We conclude that the number of neurons generated by a stem cell can be enlarged by intermediate progenitors.

Besides asymmetric division, we also found that 17% (19 of 109 cells) of the observed stem cells lost their aNSC hallmarks and up-regulated HuC/D (Fig. 3, A to D, and fig. S8), which is a representative neuronal marker (fig. S9, A and B) that is detected either by HuC/D immunostaining in postimaging analysis (Fig. 3, C and D) or GFP expression in the Tg(HuC:GFP) transgenic line in live imaging (fig. S9, C to E). These observations suggest that some aNSCs convert directly into neurons without division [for all the lineages that

show direct conversion, see (fig. S3, A and C)]. We cannot exclude that NSCs may have divided before our observation period. However, we found examples of aNSCs converting into neurons without division within more than 2 weeks of imaging time (fig. S3, A and C), which suggests that such a division must have occurred some time before [for an example of direct conversion at very early embryonic stages see (19)]. Taken together, during our observation period of several weeks, aNSCs generated neurons in a self-consuming mode (direct conversion) and a self-maintaining mode (asymmetric division) in the intact brain.

The stem cell pool is sustained by the mode of division in which 12% (13 of 109 cells) of aNSCs divide asymmetrically to generate another stem cell and a neuronal progenitor or neuron. The stem cell pool is only rarely added to by less than 1% (1 of 109 cells) of aNSCs undergoing symmetric divisions and depleted by self-consuming direct conversion [19 of 109 aNCSs (17%)]. As this behavior would predict a gradual net loss of NSCs, we determined the number of activated, proliferating cell nuclear antigen–positive aNSCs (Fig. 3E, fig. S10, and SM) at different ages using fluorescence-activated cell sorting (FACS) (Fig. 3E, fig. S10, and table S2). The number of aNSCs significantly decreased in 6 and 10 months compared with the number in 3-month-old fish (Fig. 3E and table S2), in agreement with the prediction based on the live imaging. Taken together, both live imaging and FACS analysis demonstrate the gradual net decrease of activated aNSC numbers (Fig. 3E and SM). This decrease parallels observations of decline in neurogenesis with age in zebrafish (20).

We then asked how the various modes of stem cell behavior may support the increased neurogenesis after stab wound injury in the telencephalic parenchyma (2, 3, 13). To follow aNSCs after injury, we labeled them by electroporation as described above, 4 to 8 days before the injury to allow the fluorescence protein to rise to levels sufficient for detection before the first imaging session. We imaged the aNSCs and their progeny using the same procedures as for the intact brain (fig. S1A). We found that proliferation of aNSCs increased twofold after injury [from 13% to 26% (8 of 31 aNSCs), P = 0.07] (Fig. 4B) in agreement with the increased number of proliferating aNSCs after injury previously observed at the population level (2, 3, 11). No single stem cell divided more than once in response to injury (fig. S3, B and D). Thus, the additional neurogenesis in response to injury is due to recruitment of quiescent aNSCs. Indeed, tracing aNSCs at the clonal level by using lipofection (fig. S11) fully supported the in vivo imaging data, as we detected a larger number of clones that underwent proliferation [two cell clones (fig. S11I)], but we did not observe an increase in the number of clones larger than two cells in response to injury. The recruited stem cells were not susceptible to cell death, as we observed fewer than 1% of cells with the morphological changes of dying cells in both intact and injured telencephalon (fig. S12A), and we found no increase in terminal deoxynucleotidyl transferase–mediated
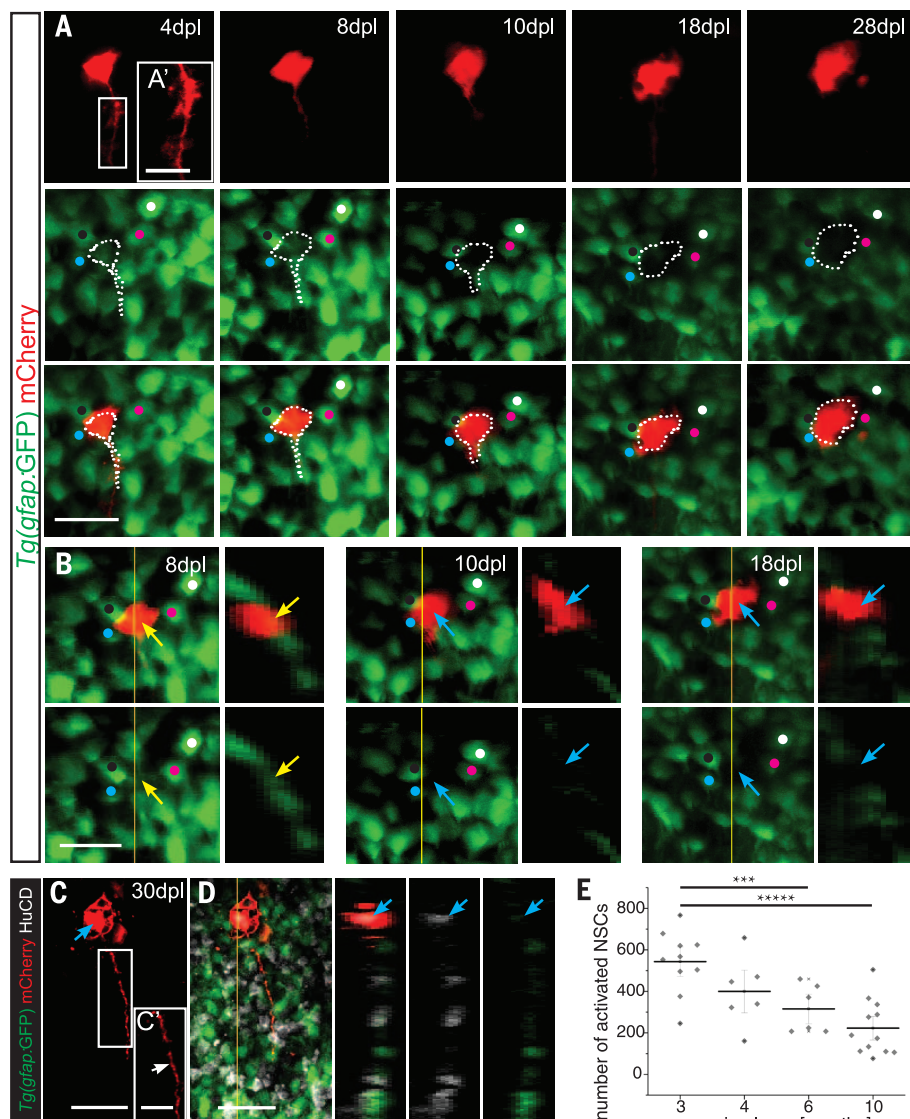
Fig. 3. aNSCs directly convert into neurons in the intact zebrafish telencephalon. (A and B) Confocal images with orthogonal projections (B) of the same mCherry-labeled aNSC in the Tg(gfap:GFP)mi2001 line at different time points, depicting the conversion of a gfap:GFP–positive aNSC with radial morphology [4 dpl, yellow arrow in (B)] to a gfap:GFP–negative cell without the radial morphology [28 dpl, blue arrow in (B)] (See also fig. S8 for all time points.) (C and D) Immunostainings at 30 dpl for GFP, mCherry, and HuC/D in whole-brain samples with orthogonal projections (D) confirming the neuronal (HuC/D⁺) identity of the imaged cell (blue arrows). Note the thicker, ramified typical RG process in (A') in contrast to the thinner neuronal process in (C'), only observed after staining. (E) The number of activated aNSCs determined by FACS in the dorsal telencephalon of animals at different ages. Dots represent single animals and lines the mean ± SEM for the single age. ***P < 0.005; *****P < 0.0001 (Mann-Whitney test). Scale bars: (A) to (D), 20 μm; (A') and (C'), 10 μm.

Fig. 4. Behavior of aNSCs after injury. (**A**) Confocal images of the same tdTomato-labeled aNSC (yellow arrow) in the *Tg(gfap:GFP)mi2001* transgenic line at different time points, depicting its symmetric division producing two non-RG cells [15 days post injury (dpi), blue arrows] (See also fig. S13 for all time points.) (**B**) The abundance of different aNSC behaviors in the control and injured telencephalon based on the live, single-cell in vivo imaging. *P < 0.05, ***P < 0.001 (one-sided Fisher's exact test). (**C**) The distance from the ventricular surface of electroporated cells generated from the aNSCs in the intact and injured brain. Red line marks the zone of adult constitutive neurogenesis. (**D**) The number of aNSCs 1.5 months after their labeling with the DNA base analog BrdU in the control and injured brain. Note the significant decline after injury. (C) and (D) *P < 0.05, **P < 0.01, ***P < 0.001 (Mann-Whitney test).
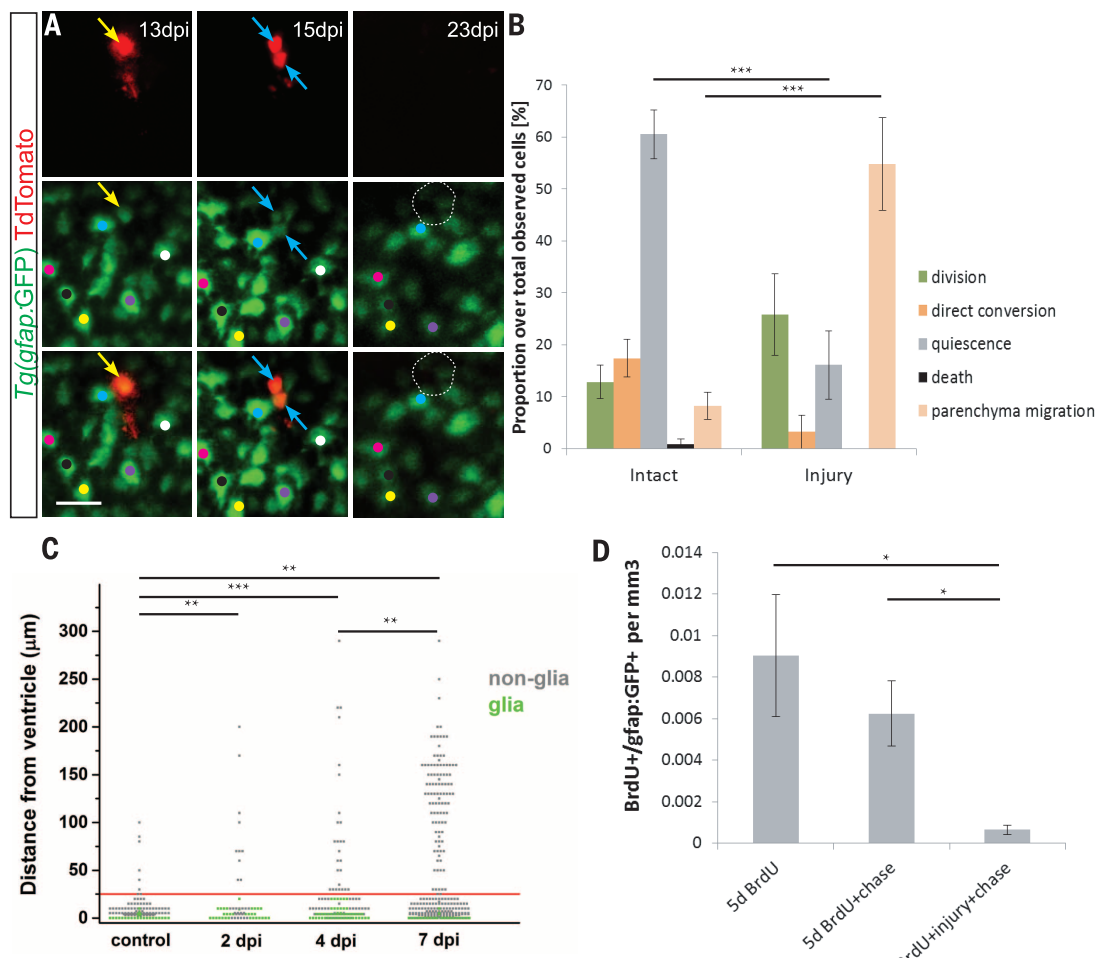
deoxyuridine triphosphate nick end labeling (TUNEL)–positive cells at the dorsal telencephalon surface either in aNSCs or their progeny after injury (fig. S12, C to I).

Next, we used live imaging to compare the mode of cell division after injury to the one observed in the healthy control brain. Asymmetric aNSC divisions remained the predominant mode of division even after injury [75% of all dividing aNSCs (6 of 8 divisions) compared with 93% (13 of 14 divisions) in the control brain] (fig. S3, D and E). In addition, we also observed symmetric divisions, but in contrast to the control brains, these were not maintaining aNSCs but generated two cells that lost the aNSC hallmarks [25% of all dividing aNSCs after injury (two of eight divisions)] (Fig. 4A and figs. S3E and S13). This mode of division, consuming NSCs for the generation of two intermediate progenitors—that then disappear from the aNSC layer (Fig. 4A) and migrate toward the injury (Fig. 4C)—appeared to be a special mode triggered by the injury, as we did not observe this type of division in the control brain (fig. S3E). The clonal analysis of aNSC progeny further corroborated this change in the cell division mode, as we could observe a twofold increase in the proportion of intermediate progenitor or neuronal clones containing two or more cells after injury (nonglial clones in fig. S14).

The increase in neuronal output via intermediate progenitors was coincident with the 55% (17 of 31 cells) of all labeled aNSCs migrating into the parenchyma that could no longer be followed by live imaging after injury (Fig. 4B and fig. S15A). With brains fixed and sectioned after electroporation (fig. S15, C to G), we observed a gradual increase in the number of labeled cells deep within the injured brain parenchyma (Fig. 4C). These were HuC/D-positive neurons (fig. S15, F and G). Likewise, when intermediate progenitors were labeled by retroviral vectors and brains were fixed and stained 14 days after injury, many of their derivatives had become HuC/D-positive neurons that migrated toward the injury site in the parenchyma (fig. S15, H to K). Increased consumption of aNSCs (migration to parenchyma, symmetric nongliogenic division, and direct conversion) in the injured brain compared with the control (Fig. 4B) suggests even faster depletion of aNSCs after injury. Indeed, we observed a significantly lower number of label-retaining aNSCs by immunostaining (see SM) in brains 6 weeks after injury compared with the controls (Fig. 4D and fig. S16). These data therefore suggest that changes in neurogenesis contribute to the response to injury: Fewer stem cells remain quiescent [16% (5 of 31 cells) NSCs in the injured brain versus 61% (66 of 109 cells) in the intact brain] (Fig. 4B), and

a pathway is added by which symmetric NSC division generates two intermediate progenitors that then give rise to a larger neuronal progeny (fig. S17).

Here, we show how aNSCs generate neurons in a manner that depletes the stem cell pool slowly with age, similar to the clonal aNSC behavior in the mouse subependymal zone, which leads to generating a discrete cohort of neurons and depleting itself (*6*). This depletion is further rapidly increased after injury in the zebrafish brain, as shown here by live imaging and immunostaining. Thus, the increase in neurogenesis after injury comes at the expense of depletion of aNSCs, perhaps drawing on quiescent NSCs. Therefore, the maintenance of aNSCs seems to be the key for long-term regeneration, and our data lay the basis for understanding the molecular pathways regulating NSC behavior involved in the regeneration process.

REFERENCES AND NOTES

1. I. Imayoshi *et al.*, *Nat. Neurosci.* **11**, 1153–1161 (2008).
2. E. V. Baumgart, J. S. Barbosa, L. Bally-Cuif, M. Götz, J. Ninkovic, *Glia* **60**, 343–357 (2012).
3. V. Kroehne, D. Freudenreich, S. Hans, J. Kaslin, M. Brand, *Development* **138**, 4831–4841 (2011).
4. L. Mchedlishvili *et al.*, *Proc. Natl. Acad. Sci. U.S.A.* **109**, E2258–E2266 (2012).
5. J. M. Encinas *et al.*, *Cell Stem Cell* **8**, 566–579 (2011).
6. F. Calzolari *et al.*, *Nat. Neurosci.* **18**, 490–492 (2015).

7. M. A. Bonaguidi et al., Cell **145**, 1142–1155 (2011).
8. M. M. Reimer et al., J. Neurosci. **28**, 8510–8516 (2008).
9. M. Carlén et al., Nat. Neurosci. **12**, 259–267 (2009).
10. K. Meletis et al., PLOS Biol. **6**, e182 (2008).
11. M. März, R. Schmidt, S. Rastegar, U. Strähle, Dev. Dyn. **240**, 2221–2231 (2011).
12. B. Adolf et al., Dev. Biol. **295**, 278–293 (2006).
13. B. Ayari, K. H. El Hachimi, C. Yanicostas, A. Landoulsi, N. Soussi-Yanicostas, J. Neurotrauma **27**, 959–972 (2010).
14. N. Kishimoto, K. Shimizu, K. Sawamoto, Dis. Model. Mech. **5**, 200–209 (2012).
15. M. März et al., Glia **58**, 870–888 (2010).
16. R. L. Bernardos, P. A. Raymond, Gene Expr. Patterns **6**, 1007–1013 (2006).
17. P. Chapouton et al., J. Neurosci. **30**, 7961–7974 (2010).
18. I. Rothenaigner et al., Development **138**, 1459–1469 (2011).
19. J. E. Bestman, J. Lee-Osbourne, H. T. Cline, J. Comp. Neurol. **520**, 401–433 (2012).
20. K. Edelmann et al., J. Comp. Neurol. **521**, 3099–3115 (2013).

ARCHAEOLOGY

The makers of the Protoaurignacian and implications for Neandertal extinction

S. Benazzi,[1,2]* V. Slon,[3] S. Talamo,[2] F. Negrino,[4] M. Peresani,[5] S. E. Bailey,[2,6] S. Sawyer,[3] D. Panetta,[7] G. Vicino,[8] E. Starnini,[9,10] M. A. Mannino,[2] P. A. Salvadori,[7] M. Meyer,[3] S. Pääbo,[3] J.-J. Hublin[2]

The Protoaurignacian culture is pivotal to the debate about the timing of the arrival of modern humans in western Europe and the demise of Neandertals. However, which group is responsible for this culture remains uncertain. We investigated dental remains associated with the Protoaurignacian. The lower deciduous incisor from Riparo Bombrini is modern human, based on its morphology. The upper deciduous incisor from Grotta di Fumane contains ancient mitochondrial DNA of a modern human type. These teeth are the oldest human remains in an Aurignacian-related archaeological context, confirming that by 41,000 calendar years before the present, modern humans bearing Protoaurignacian culture spread into southern Europe. Because the last Neandertals date to 41,030 to 39,260 calendar years before the present, we suggest that the Protoaurignacian triggered the demise of Neandertals in this area.

The timing and pattern of the biological and cultural shifts that occurred in Western Europe around 45,000 to 35,000 calendar years before the present (cal yr B.P.) fuel continuing debates among paleoanthropologists and prehistorians (1–3). During this period, Neandertals were replaced by anatomically modern humans (AMHs) (4), and a variety of "transitional" and early Upper Paleolithic cultures emerged. Among them, the Protoaurignacian is crucial to current interpretations regarding the timing of arrival of AMHs and their interaction with Neandertals (5–9).

The Protoaurignacian appeared around 42,000 cal yr B.P. (8, 10) in southwest and south-central Europe (fig. S1). In addition to the presence of personal ornaments, such as perforated shells and worked bones, the Protoaurignacian is characterized by a dominance of bladelets with typical retouched standardized implements such as Font-Yves points and Dufour bladelets produced from unipolar cores (5). This techno-complex has been tentatively linked to the Ahmarian industry of the Levant (6, 9). Because the Ahmarian has been attributed to modern humans (11), it has been suggested that the Protoaurignacian reflects a westward population movement of AMHs from the Near East (1, 7). However, because only three nondiagnostic human remains are associated with this culture, it is still uncertain who the makers of the Protoaurignacian were (9, 12). The fossil remains associated with the Protoaurignacian that are available for study consist of the undiagnostic skeletal fragments of a fetus retrieved from Le Piage rock shelter (France) (13), for which the stratigraphic integrity of the Châtelperronian/Aurignacian sequence has been questioned (5), and two deciduous incisors from two northern

[1]Department of Cultural Heritage, University of Bologna, Via degli Ariani 1, 48121 Ravenna, Italy. [2]Department of Human Evolution, Max Planck Institute for Evolutionary Anthropology, Deutscher Platz 6, 04103 Leipzig, Germany. [3]Department of Evolutionary Genetics, Max Planck Institute for Evolutionary Anthropology, Deutscher Platz 6, 04103 Leipzig, Germany. [4]Dipartimento di Antichità, Filosofia, Storia e Geografia, Università di Genova, Via Balbi 2, 16126 Genova, Italy. [5]Sezione di Scienze Preistoriche e Antropologiche, Dipartimento di Studi Umanistici, Corso Ercole I d'Este 32, Università di Ferrara, 44100 Ferrara, Italy. [6]Center for the Study of Human Origins, Department of Anthropology, New York University, 25 Waverly Place, New York, NY 10003, USA. [7]CNR Institute of Clinical Physiology, National Research Council, Via G. Moruzzi 1, 56124 Pisa, Italy. [8]Museo Archeologico del Finale, Chiostri di Santa Caterina, 17024 Finale Ligure Borgo, Italy. [9]Scuola di Scienze Umanistiche, Dipartimento di Studi Storici, Università di Torino, via S. Ottavio 20, 10124 Torino, Italy. [10]Museo Preistorico Nazionale dei Balzi Rossi, Via Balzi Rossi 9, 18039 Ventimiglia, Italy.
*Corresponding author. E-mail: stefano.benazzi@unibo.it

Fig. 1. Three-dimensional digital models of the Protoaurignacian human remains. The Bombrini tooth is a lower left lateral deciduous incisor (Ldi$_2$), whereas Fumane 2 is an upper right lateral deciduous incisor (Rdi^2). B, buccal; D, distal; L, lingual; M, mesial; O, occlusal. Scale bar, 1 cm.

Italian sites: Riparo Bombrini (western Ligurian Alps, Italy) and Grotta di Fumane (western Lessini Mountains, Italy). The lower left lateral deciduous incisor (Ldi2; Fig. 1) found in 1976 in Riparo Bombrini (14, 15) (figs. S2 to S5) and the upper right lateral deciduous incisor (Rdi2, Fig. 1) labeled Fumane 2, which was retrieved in 1992 from the Protoaurignacian deposit of Grotta di Fumane (15, 16) (figs. S6 and S7), have to date not been conclusively attributed to modern humans or Neandertals.

The crown diameters of deciduous incisors are undiagnostic for Neandertals and modern humans, as is also the case for other tooth classes (2). However, on the basis of the buccolingual crown diameter, the Bombrini specimen is close to the mean of Upper Paleolithic modern humans, whereas Fumane 2 is closer to the Neandertal mean (table S1). Other than that, the worn deciduous lower incisors do not provide any morphologically diagnostic information.

To establish the identity of the makers of the Protoaurignacian, we analyzed the three-dimensional enamel thickness components of the Bombrini Ldi2 using a digital approach (17), and we were able to investigate DNA from the Fumane 2 specimen (15).

The relative enamel thickness (RET) index has been recognized as an effective taxonomic discriminator between Neandertals and modern humans. Neandertal deciduous and permanent teeth are characterized by significantly thinner enamel relative to dentine volume (18).

To facilitate comparisons with the Bombrini specimen, which is affected by wear stage 4, the Neandertal and recent modern human (RMH) di2 samples were divided into subgroups based on their degree of wear (from wear stage 1/2 to wear stage 4) (15, 19) (Table 1 and table S2). The Neandertal di2 RET indices are lower than those of RMHs at similar wear stages, and no overlap in the range of variation is observed between the two groups. The RET index of Bombrini is higher than any values obtained for Neandertals (table S2), despite the missing portion of the enamel cap, and its computed standard (Z) score is close to the modern human mean in wear stage 4 (Table 1).

To test how much the loss of enamel on the mesial side of the Bombrini tooth affects the computed RET value, two RMH specimens were digitally worn and damaged to simulate the condition observed in Bombrini (15) (fig. S8). The results confirm that tooth wear, at least up to wear stage 4, decreases the RET index by about 10%, whereas the mesial loss of enamel affects the index by less than 1.6% (much less than the values considered acceptable for intra- and interobserver error) (2). Therefore, the RET value for the unworn Bombrini Ldi2 was certainly much higher (table S3), further supporting its attribution to modern humans.

DNA was extracted from the Fumane 2 tooth, which yielded few mitochondrial DNA (mtDNA) sequences (table S4). With respect to 63 "diagnostic" positions at which 10 Neandertal mitochondrial genomes differ from those of 311 present-day humans (20), these sequences were of modern human origin (table S5). To further explore this, we prepared a second DNA extract and two DNA

libraries from this specimen, which yielded a total of 335,628 unique mtDNA fragments (table S4).

The frequencies of cytosine (C) to thymine (T) substitutions at the ends of these fragments (34 to 37%, fig. S9), which reflect the deamination of cytosine residues typical of ancient DNA (21, 22), are consistent with results from other specimens of similar age (23–26). Among the fragments carrying terminal C-to-T substitutions, we estimated the residual present-day DNA contamination to be 3.8% (15).

Using these fragments, we reconstructed a mitochondrial genome of 157-fold coverage (fig. S10). This mtDNA sequence was aligned to the mtDNAs of 54 present-day humans, 10 ancient modern humans, 10 Neandertals, 2 Denisovans, a hominin from Sima de los Huesos (Spain), and a chimpanzee (*Pan troglodytes*). The Fumane 2 mitochondrial genome falls within the variation

of modern humans (Fig. 2) and basally in haplogroup R (table S6), as also observed for the ~45,000-year-old AMH specimen from Ust'-Ishim [in western Siberia (26)], a major group of related mtDNAs in Eurasia (27) into which most pre-agricultural mtDNAs in Europe fall (28).

As expected for an ancient specimen (23, 25), the Fumane 2 mtDNA has accumulated fewer nucleotide substitutions than present-day mtDNA (Fig. 2). Using 10 directly dated ancient modern humans (25, 26) as multiple calibration points, we estimated the age of the Fumane 2 terminal node to be 44,599 (95% highest posterior density: 19,755 to 72,070) yr B.P.

We thus conclude that the Fumane 2 individual carried a mitochondrial genome of a modern human type. This shows that this individual was a modern human or had at least some ancestors who were modern humans.

Table 1. 3D enamel thickness. Bombrini (Ldi2) is standardized to Z scores (for RET index) of the Neandertal and recent modern human (RMH) di2 sample in different wear stages. Standard deviations are indicated in parentheses. AET, average enamel thickness index; RET, relative enamel thickness index.

Taxon	Wear stage*	n	AET (mm)		RET (scale free)		Z scores for RET index
			Mean	Range	Mean	Range	
Bombrini	4		0.29		9.22		
Neandertals	1/2	3	0.29 (0.01)	0.28–0.30	7.88 (0.33)	7.54–8.20	4.06
Neandertals	3	2	0.26 (0.007)	0.26–0.27	6.95 (0.55)	6.56–7.34	4.13
RMH	2	3	0.35 (0.006)	0.35–0.36	11.41 (0.41)	10.97–11.77	−5.34
RMH	3	11	0.31 (0.04)	0.24–0.35	9.98 (1.17)	8.01–11.85	−0.65
RMH	4	4	0.26 (0.04)	0.22–0.32	8.67 (1.4)	6.98–10.40	0.39

*Based on (19).
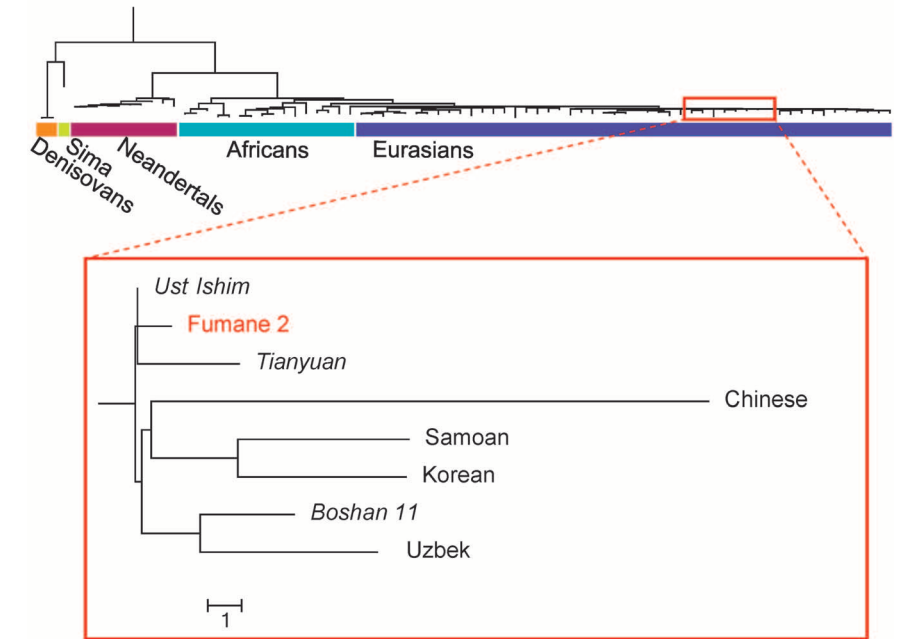
Fig. 2. Phylogenetic analysis of the Fumane 2 mtDNA genome, inferred using the neighbor-joining method. The Fumane 2 mitochondrial genome falls within the variation of modern humans and outside the variation of Neandertals, Denisovans, and a hominin from Sima de los Huesos. The insert shows the branches closest to Fumane 2. Other ancient modern humans are noted in italics. Branch lengths represent the evolutionary distance between individuals, reflected by the number of inferred substitutions per sequence.

Based on recent chronometric data for the Protoaurignacian deposit of Grotta di Fumane, the Fumane 2 specimen is dated to 41,110 to 38,500 cal yr B.P. (10), as recalibrated with IntCal13 (29). Among modern humans in western Europe, it is currently predated only by the contested Kent's Cavern maxilla (30, 31) and by the 45,000 to 43,000 cal yr B.P. AMH specimens from the Uluzzian levels of Grotta del Cavallo (2), about which a recent taxonomic reassessment is stimulating intense debate (32, 33).

Radiocarbon dates of the Protoaurignacian layers of Riparo Bombrini were obtained from faunal bones recovered during the G. Vicino excavation (five samples) and the more recent 2002–2005 excavations (three charcoal specimens and eight animal bones) (15) (tables S7 to S10). These dates confirm the integrity of the cemented deposit explored in 1976 by Vicino (which yielded the Ldi$_2$ tooth) but suggest that some stratigraphic disturbance affected a restricted area explored during the 2002–2005 excavations (15) (table S7 and

fig. S11). The ^{14}C dates of the Vicino 1976 excavation (table S7) were incorporated into a Bayesian model for the distribution of ages (34) (Fig. 3). The Protoaurignacian levels (level III to level II) are dated between 40,710 and 35,640 cal yr B.P. (68.2% probability), corresponding to a cold phase that marks the onset of Heinrich Stadial 4 (35).

The Bombrini Ldi$_2$ and potentially the Fumane 2 Rdi^2 thus represent the oldest AMH remains in an Aurignacian-related (i.e., Protoaurignacian or Early Aurignacian) archaeological context, confirming that by around 41,000 cal yr B.P. (68.2% probability), AMH populations bearing Protoaurignacian culture had spread into Europe along the Mediterranean coast. They are similar in age to, or slightly older than, the modern human remains from Peştera cu Oase (Romania, ~40,000 cal yr B.P.), which lack archaeological context; Kostenki 14, Layer III (Russia, ~38,000 cal yr B.P.), which is possibly Aurignacian; Kostenki 1, Layer III (~38,000 cal yr B.P.), which is associated with diagnostic Aurignacian artifacts; Kostenki 14, Layer IVb, and Kostenki 17, Layer II, which underlie the Campanian Ignimbrite tephra and are of comparable age to the Protoaurignacian in Italy, are tentatively assigned to AMHs, and also associated with an assemblage that includes bladelets; and La Quina-Aval and Brassempouy (France), which are Early Aurignacian and more recent than 40,000 cal yr B.P. [for a review, see (9)].

The Protoaurignacian dispersal overlaps in time with late Neandertal populations, as indicated by the 41,030 to 39,260 cal yr B.P. age of the last Mousterian sites (4) and the ~45,000 to 40,000 cal yr B.P. age of the Châtelperronian culture (3), which is currently attributed to Neandertals (36). The Protoaurignacian dispersal may therefore have been a cause (either directly or indirectly) of the extinction of the Neandertals, at least in northern Italy.
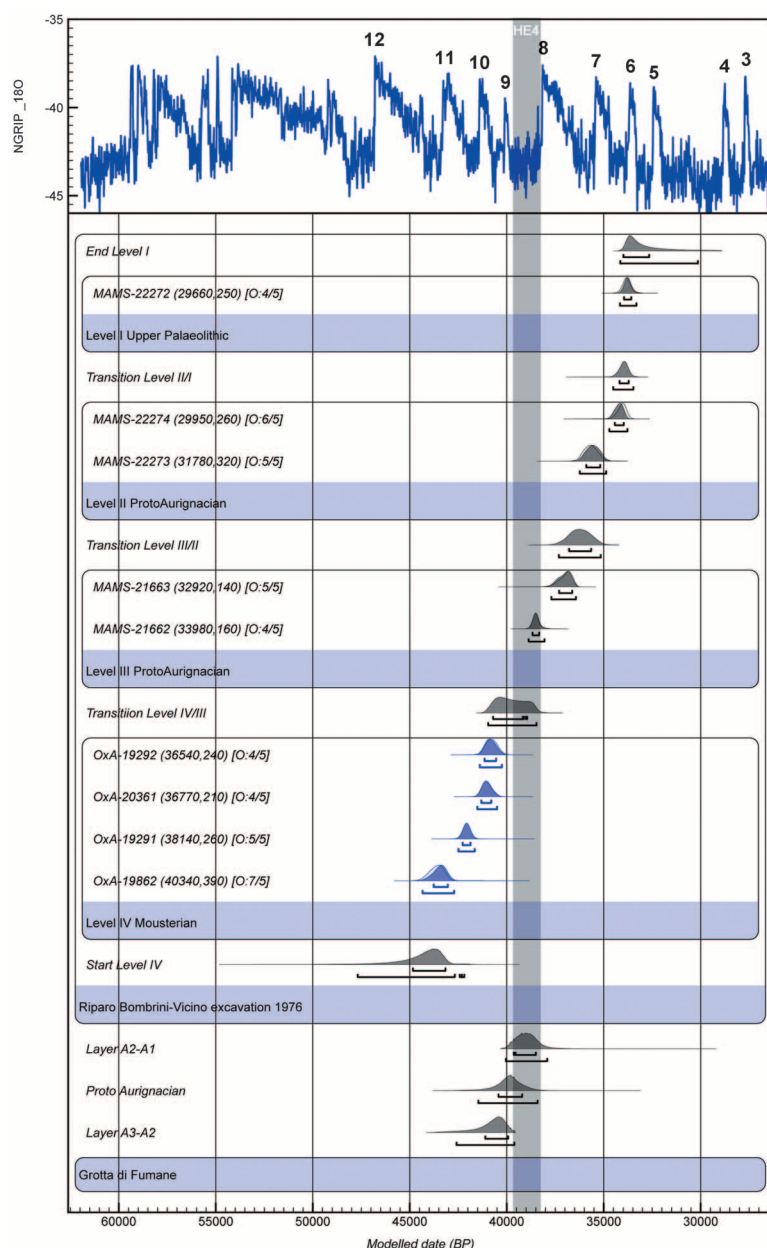
Fig. 3. Bayesian model of dates from the 1976 excavation by Vicino at Riparo Bombrini. Bombrini accelerator mass spectrometry results are compared with Grotta di Fumane boundaries created in (4). Bone samples treated with ultrafiltration are in gray; shell samples from the Mousterian level (4) are in blue. Radiocarbon dates were calibrated in IntCal13 (29) and Marine13 (29) for shell samples. The model and boundaries were calculated using OxCal 4.2 (34), including the performance of the General t-type Outlier Model (34). The results are linked with the North Greenland Ice Core Project δ^{18}O climate record (15). The gray-shaded bar denotes Heinrich event 4 (HE4) (35).

REFERENCES AND NOTES

1. J. F. Hoffecker, *Proc. Natl. Acad. Sci. U.S.A.* **106**, 16040–16045 (2009).
2. S. Benazzi *et al.*, *Nature* **479**, 525–528 (2011).
3. J.-J. Hublin *et al.*, *Proc. Natl. Acad. Sci. U.S.A.* **109**, 18743–18748 (2012).
4. T. Higham *et al.*, *Nature* **512**, 306–309 (2014).
5. J.-G. Bordes, in *The Chronology of the Aurignacian and of the Transitional Technocomplexes: Dating, Stratigraphies, Cultural Implications*, J. Zilhão, F. D'Errico, Eds. (Instituto Português de Arqueologia, Lisbon, Portugal, 2003), pp. 223–246.
6. O. Bar-Yosef, in *More than Meets the Eye: Studies on Upper Palaeolithic Diversity in the Near East*, A. N. Goring-Morris, A. Belfer-Cohen, Eds. (Oxbow Books, Oxford, 2003), pp. 265–273.
7. P. Mellars, *Nature* **439**, 931–935 (2006).
8. K. Douka, S. Grimaldi, G. Boschian, A. del Lucchese, T. F. Higham, *J. Hum. Evol.* **62**, 286–299 (2012).
9. J-J. Hublin, The modern human colonization of western Eurasia: When and where? *Quat. Sci. Rev.* (2014).
10. T. Higham *et al.*, *Quat. Sci. Rev.* **28**, 1257–1267 (2009).
11. C. A. Bergman, C. B. Stringer, *Paéorient* **15**, 99–111 (1989).
12. N. J. Conard, P. M. Grootes, F. H. Smith, *Nature* **430**, 198–201 (2004).
13. S. Beckouche, F. Poplin, in *Le Piage, Site Préhistorique du Lot*, F. Champagne, R. Espitalié, Eds. (Société Préhistorique Française, Paris, 1981), pp. 159–160.

14. V. Formicola, *Rev. Antropol.* **67**, 287–292 (1989).
15. Information on materials and methods and localities is available on *Science* Online.
16. G. Bartolomei *et al.*, *Preistoria Alpina* **28**, 131–179 (1992).
17. S. Benazzi *et al.*, *Am. J. Phys. Anthropol.* **153**, 305–313 (2014).
18. R. Macchiarelli *et al.*, *Nature* **444**, 748–751 (2006).
19. S. Molnar, *Am. J. Phys. Anthropol.* **34**, 175–189 (1971).
20. R. E. Green *et al.*, *Cell* **134**, 416–426 (2008).
21. A. W. Briggs *et al.*, *Proc. Natl. Acad. Sci. U.S.A.* **104**, 14616–14621 (2007).
22. S. Sawyer, J. Krause, K. Guschanski, V. Savolainen, S. Pääbo, *PLOS ONE* **7**, e34131 (2012).
23. J. Krause *et al.*, *Curr. Biol.* **20**, 231–236 (2010).
24. J. Krause *et al.*, *Nature* **464**, 894–897 (2010).
25. Q. Fu *et al.*, *Curr. Biol.* **23**, 553–559 (2013).
26. Q. Fu *et al.*, *Nature* **514**, 445–449 (2014).
27. P. Soares *et al.*, *Am. J. Hum. Genet.* **84**, 740–759 (2009).
28. I. Lazaridis *et al.*, *Nature* **513**, 409–413 (2014).
29. P. J. Reimer *et al.*, *Radiocarbon* **55**, 1869–1887 (2013).
30. T. Higham *et al.*, *Nature* **479**, 521–524 (2011).
31. M. White, P. Pettitt, *Eur. J. Archaeol.* **15**, 392–420 (2012).
32. W. E. Banks, F. d'Errico, J. Zilhão, *J. Hum. Evol.* **64**, 39–55 (2013).
33. A. Ronchitelli, S. Benazzi, P. Boscato, K. Douka, A. Moroni, *J. Hum. Evol.* **73**, 107–111 (2014).
34. C. Bronk Ramsey, S. Lee, *Radiocarbon* **55**, 720–730 (2013).
35. D. Fleitmann *et al.*, *Geophys. Res. Lett.* **36**, L19707 (2009).
36. S. E. Bailey, J.-J. Hublin, *J. Hum. Evol.* **50**, 485–508 (2006).

HUMAN BEHAVIOR

Sex equality can explain the unique social structure of hunter-gatherer bands

M. Dyble,* G. D. Salali, N. Chaudhary, A. Page, D. Smith, J. Thompson, L. Vinicius, R. Mace, A. B. Migliano

The social organization of mobile hunter-gatherers has several derived features, including low within-camp relatedness and fluid meta-groups. Although these features have been proposed to have provided the selective context for the evolution of human hypercooperation and cumulative culture, how such a distinctive social system may have emerged remains unclear. We present an agent-based model suggesting that, even if all individuals in a community seek to live with as many kin as possible, within-camp relatedness is reduced if men and women have equal influence in selecting camp members. Our model closely approximates observed patterns of co-residence among Agta and Mbendjele BaYaka hunter-gatherers. Our results suggest that pair-bonding and increased sex egalitarianism in human evolutionary history may have had a transformative effect on human social organization.

Contemporary mobile hunter-gatherers cooperate extensively with unrelated individuals across multiple social and economic domains. Many communities of mobile hunter-gatherers (hereafter hunter-gatherers) share food extensively within camp and hunt, gather, and fish cooperatively (*1*). Alloparenting is also commonplace (*2*, *3*). The importance of cooperative activities is reflected in many hunter-gatherer societies by a pervasive ethic of egalitarianism (*4*, *5*). Like a number of nonhuman primate species, humans live in multimale, multifemale groups (*6*). However, we maintain enduring pair bonds, resulting in what have been described as "multifamily" groups (*7*). In addition, and in contrast to the bounded and territorial groups of chimpanzees (*8*, *9*), bonobos (*10*), and gorillas (*11*), contemporary hunter-gatherers have fluid social networks where family units are relatively autonomous, with couples and their children moving often between bands (*12*), living with kin of either the husband or the wife. This residence pattern has been described as either "bilocal" or "multilocal" (*13*).

As well as being highly mobile, contemporary hunter-gatherer camps include a significant proportion of unrelated individuals (*14*) and are less closely related than groups of non-foraging small-scale societies (*15*). Given the inclusive fitness benefits of living with kin, why hunter-gatherers live with unrelated individuals is a puzzle, even more so if one considers that hunter-gatherers show a preference for living with siblings (*13*) and preferentially include kin in their campmate choices and social networks (*16*). Therefore, the mechanisms by which contemporary hunter-gatherers attempt to maximize co-residence and cooperation with kin, but nonetheless end up residing mostly with unrelated individuals, remain unclear.

Here, we offer a solution for this apparent paradox by demonstrating that, even where all individuals are actively assorting with kin, within-group relatedness is reduced if both sexes have influence over camp composition, as is the case among egalitarian, multilocal hunter-gatherers. We present a simulation of camp assortment where individuals attempt to reside with as many kin as possible under two conditions. In the egalitarian condition, men and women have equal influence on camp composition, whereas in the non-egalitarian condition, only one sex has influence. We compared the results with previously unpublished data from two hunter-gatherer groups, the Palanan Agta (*N* = 4055 dyads) and Mbendjele BaYaka (*5*) (*N* = 1863 dyads), as well as one farming population, the Paranan (*N* = 1049 dyads). We demonstrate that low within-camp relatedness emerges naturally from men and women seeking to maximize the presence of related kin. In contrast, in societies where decision-making on co-residence rests on one sex only, as in the case of patrilocal farmers, low relatedness does not emerge. Our model offers a mechanism that reconciles individual-level preferences for kin with reduced camp-level relatedness. Assuming that extant hunter-gatherers live in social structures resembling the ones existing in past hominins, our model explains how the shift from an ancestral hierarchical, female-dispersal system to a multilocal, egalitarian one would provide the selective context for expanded social networks, cumulative culture, and cooperation among unrelated individuals.

Among the Agta, we collected data from 191 adults across 11 camps, coding a total of 4055 dyadic relationships. Among the Mbendjele, we collected data from 103 adults across nine camps, totaling 1863 dyadic relationships. Mean experienced camp size was 18.09 adults (SD = 8.62) for the Mbendjele and 21.23 adults (SD = 8.61) for the Agta. Both populations were multilocal, with

University College London (UCL) Anthropology, 14 Taviton Street, London WC1H 0BW, UK.
*Corresponding author. E-mail: mark.dyble.12@ucl.ac.uk
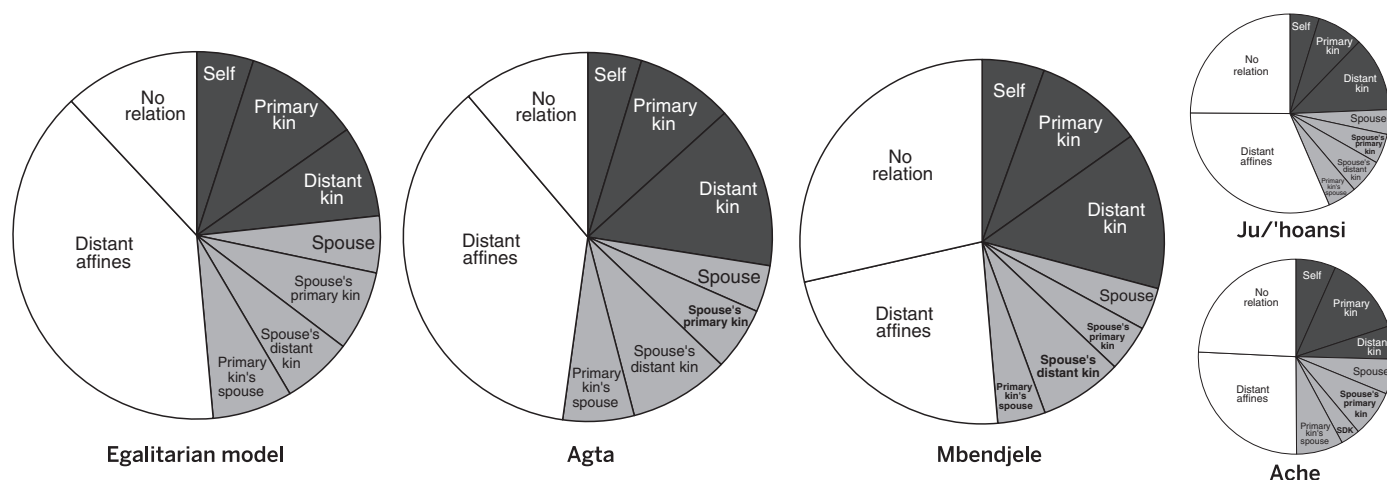
Fig. 1. Co-residence patterns across modeled and observed egalitarian populations. Chart area represents the proportion of all dyads across nine categories of relatedness for the egalitarian model (**left**), Agta (**middle left**), Mbendjele (**middle right**), Ache (**bottom right**), and Ju/'hoansi (**top right**). Ache and Ju/'hoansi data redrawn from Hill *et al.* (2011).
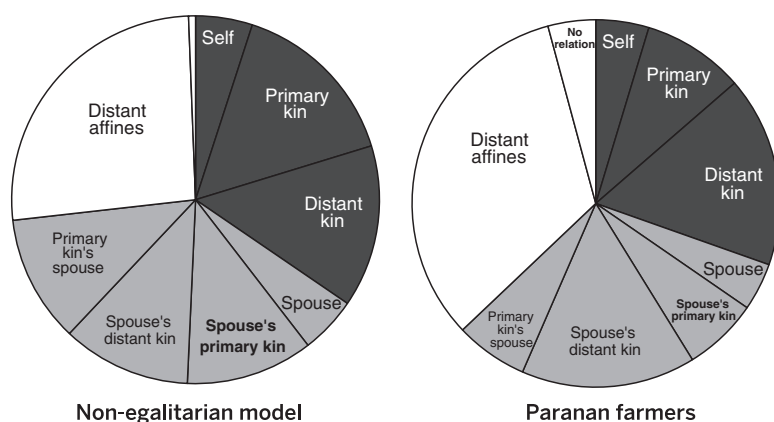
Fig. 2. Co-residence patterns across modeled and observed non-egalitarian populations. Chart area represents the proportion of all dyads across nine categories of relatedness for the non-egalitarian model (**left**) and Paranan (**right**).

husbands and wives living with similar numbers of consanguineal (genetic) kin (table S1 and fig. S1). In both groups, around 25% of dyads represented consanguineal kin, 25% were close affinal kin, and around 50% of dyads were distant affinal kin or unrelated individuals (Fig. 1 and table S2). These results are similar to those reported for the Ache and Ju/'hoansi by Hill and colleagues (*14*) (see Fig. 1).

In contrast to the unbiased residence patterns of the Agta and Mbendjele, Paranan farmers (*n* = 49 adults, 1049 dyads) demonstrate a significant male bias in residence, with men living with a larger number of primary kin (*n* = 23, mean = 2.65, SD = 2.29) than women (*n* = 26, mean = 1.27, SD = 2.05; *P* = 0.031). Despite having a comparable group size of 21.4 adults (SD = 9.30), the Paranan live with fewer unrelated individuals than the hunter-gatherers (4.2% versus 16.7%) (χ^2 = 108.93, *P* < 0.001) (Fig. 2).

Although it is possible that low within-camp relatedness could result from random dispersal, with households moving randomly between camps and living with related individuals only by chance, our results do not suggest that this is the case. Rather, the observed frequency of primary kin co-residence was significantly higher than would be expected if individuals assorted randomly across camps (Mbendjele, χ^2 = 451.62, *P* < 0.001; Agta, χ^2 = 982.00, *P* < 0.001). Thus, hunter-gatherer co-residence patterns are notable not only in their low-relatedness but because this low relatedness occurs despite the positive assortment of kin.

We developed a model to understand how hunter-gatherers come to co-reside with a large number of unrelated individuals at the group level, despite a preference toward living with kin at the individual level. We ran two versions of the model: one egalitarian, where both husband and wife have equal influence over where their household resides, and a non-egalitarian one, where only one sex has influence. Even at relatively small population sizes, these two conditions result in large differences in group composition. Across 100 simulations at a population size of 20, for example, there was a significantly larger

proportion of unrelated dyads in the modeled egalitarian camps (12.0% ± 8.4 SD) compared with the non-egalitarian, single-sex dispersal camps (0.6% ± 1.5) (χ^2 = 4372.36, *P* < 0.001; Figs. 1 and 2). Although it is known that group relatedness decreases with increased group size (*15*), modeled egalitarian camps show higher proportions of unrelated individuals irrespective of camp size (Fig. 3).

The modeled co-residence patterns also mirror our observed data. The proportion of unrelated dyads in the model at a comparable group size (*n* = 20 agents) (12.0% ± 8.4) was not significantly different from the observed proportion of unrelated co-residency among the Agta (11.2%, χ^2 = 1.98, *P* = 0.016). Although the Mbendjele had significantly larger numbers of unrelated individuals in the camps (28.6%) than predicted by the model (χ^2 = 440.76, *P* < 0.001), this was in the direction consistent with our hypothesis. The observed proportion of unrelated dyads among the Paranan (4.2%) was larger than the modeled proportion (0.6% ± 1.5, χ^2 = 183.41, *P* < 0.001), but it was lower than either of the observed hunter-gatherer populations (see above) and the egalitarian model (χ^2 = 58.65, *P* < 0.001).

Our results suggest that pair-bonding alone is not sufficient to explain the low levels of relatedness seen in hunter-gatherer groups. Rather, both pair-bonding and sex equality in residential decision-making act together to constrain the overall relatedness of groups, leading to the co-residence of individuals unrelated through either genetic or affinal ties.

It has been proposed elsewhere that the combination of pair-bonding, cooperation among unrelated males, and increased mobility derived from male alliances could account for the low relatedness of hunter-gatherer camps (*7*). We argue instead that low within-camp relatedness is a consequence of sex equality in hunter-gatherer couples, with husbands and wives having an equal influence over camp composition. Given sex equality, we have shown that unrelated individuals come to

co-reside even when they display a strong individual preference to live with kin, exemplified in hunter-gatherers by the frequent co-residence of brothers and sisters (14) and the higher frequency of related individuals in campmate and gift networks (16). Therefore, our simulations provide a mechanism for the emergence of low within-camp relatedness in hunter-gatherers by solving the apparent contradiction between individual-level preferences for living with kin and group-level co-residence with non-kin. Gender inequality reappeared in humans with the transition to agriculture and pastoralism (17). Once heritable resources, such as land and livestock, became important determinants of reproductive success, sex-biased inheritance and lineal systems started to arise, leading to wealth and sex inequalities (18). This predicted effect was demonstrated in our non-egalitarian model and data from Paranan agriculturalists. Our results also provide further evidence that multilocality, rather than patrilocality, is the norm among mobile hunter-gatherers.

Understanding hunter-gatherer sex egalitarianism and the shift from hierarchical male philopatry typical of chimpanzees and bonobos to a multilocal residence pattern is key to theories of human social evolution. A possible clue for the evolution of sex equality in the hominin lineage was the increase in the cost of human reproduction associated with larger brain sizes in early *Homo* (19). Higher offspring costs would require investment from both mothers and fathers (20), as seen among extant hunter-gatherers (3, 21). The need for biparental investment predicts increased sex equality (22), which is reflected in the high frequency of monogamy and the reproductive schedules of male hunter-gatherers, who typically stop reproducing early and exhibit long life spans after their last reproduction. This pattern contrasts with that of male farmers and pastoralists, whose reproductive spans extend well into late life (23). The recognition of affinal ties throughout our long life span has been argued to be an important step in human social evolution, and household residence may also be influenced by a tug of war between a husband and his affinal kin, who may want to live with their daughter or sister (7). The possibility of recruiting help from both maternal and paternal kin by moving camps might have been an important adaptation to meet reproductive costs in unpredictable environments—for example, by increasing the frequency of co-residence with grandmothers, who have an important provisioning role in many hunter-gatherer societies (24). Increased reproductive costs, cooperative breeding, and sex equality in residential decision-making can explain why hunter-gatherer parents live in groups containing multiple mated pairs, why hunter-gatherers recruit help both from related and unrelated individuals, and why hunter-gatherer camps exhibit low levels of relatedness.

Sex equality and the resulting low within-camp relatedness had many important consequences. Co-residence with unrelated individuals set the selective environment for the evolution of hyper-cooperation and prosociality (25). Sex equality suggests a scenario where cooperation among unrelated individuals can evolve in the absence of wealth accumulation, reproductive inequalities, and intergroup warfare (26). Couples freely moving between camps and sharing interests with kin and affines would be able to maintain cooperation without the need for more complex systems, such as cultural group selection and altruistic punishment (27).

Last, this social system may have allowed hunter-gatherers to extend their social networks, buffering environmental risk and promoting levels of information exchange required for cumulative culture (28–31).

REFERENCES AND NOTES

1. M. Gurven, *Behav. Brain Sci.* **27**, 543–583 (2004).
2. P. K. Ivey, *Curr. Anthropol.* **41**, 856–866 (2000).
3. C. L. Meehan, R. Quinlan, C. D. Malcom, *Am. J. Hum. Biol.* **25**, 42–57 (2013).
4. J. Woodburn, *Man* **17**, 431–451 (1982).
5. J. Lewis, in *Hunter-Gatherers of the Congo Basin: Cultures, Histories, and Biology of African Pygmies*, B. S. Hewlett, Ed. (Transaction, New Brunswick, NJ, 2014), pp. 219–244.
6. L. Rodseth, R. W. Wrangham, A. M. Harrigan, B. B. Smuts, *Curr. Anthropol.* **32**, 221–254 (1991).
7. B. Chapais, *Primeval Kinship: How Pair-Bonding Gave Birth to Human Society* (Harvard Univ. Press, Cambridge, MA, 2009).
8. M. L. Wilson, R. W. Wrangham, *Annu. Rev. Anthropol.* **32**, 363–392 (2003).
9. J. Mitani, D. Watts, *Behaviour* **138**, 299–327 (2001).
10. R. W. Wrangham, D. Peterson, *Demonic Males: Apes and the Origins of Human Violence* (Houghton Mifflin Harcourt, Boston, 1996).
11. P. Sicotte, *Am. J. Primatol.* **30**, 21–36 (1993).
12. R. Kelly, *J. Anthropol. Res.* **39**, 277–306 (1983).
13. F. Marlowe, *Curr. Anthropol.* **45**, 277–284 (2004).
14. K. R. Hill *et al.*, *Science* **331**, 1286–1289 (2011).
15. R. S. Walker, *Evol. Hum. Behav.* **35**, 384–388 (2014).
16. C. L. Apicella, F. W. Marlowe, J. H. Fowler, N. A. Christakis, *Nature* **481**, 497–501 (2012).
17. M. Martin, B. Voorhies, *Female of the Species* (Columbia Univ. Press, New York, 1975).
18. R. Mace, *Evol. Anthropol.* **22**, 251–258 (2013).
19. L. Aiello, P. Wheeler, *Curr. Anthropol.* **36**, 199–221 (1995).
20. H. Kaplan, K. Hill, J. Lancaster, A. M. Hurtado, *Evol. Anthropol.* **9**, 156–185 (2000).
21. K. Hill, A. M. Hurtado, *Proc. Biol. Sci.* **276**, 3863–3870 (2009).
22. H. S. Kaplan, J. B. Lancaster, in *Offspring: Human Fertility Behavior in Biodemographic Perspective*, K. W. Wachter, R. A. Bulatao, Eds. (National Academies Press, Washington, DC, 2003), pp. 170–223.
23. L. Vinicius, R. Mace, A. Migliano, *PLOS ONE* **9**, e112236 (2014).
24. K. Hawkes, J. F. O'Connell, N. G. Jones, H. Alvarez, E. L. Charnov, *Proc. Natl. Acad. Sci. U.S.A.* **95**, 1336–1339 (1998).
25. J. M. Burkart *et al.*, *Nat. Commun.* **5**, 4747 (2014).
26. D. P. Fry, P. Söderberg, *Science* **341**, 270–273 (2013).
27. H. M. Lewis, L. Vinicius, J. Strods, R. Mace, A. B. Migliano, *Nat. Commun.* **5**, 5789 (2014).
28. M. Kempe, A. Mesoudi, *Evol. Hum. Behav.* **35**, 285–290 (2014).
29. K. R. Hill, B. M. Wood, J. Baggio, A. M. Hurtado, R. T. Boyd, *PLOS ONE* **9**, e102806 (2014).
30. R. Lee, *The! Kung San* (Cambridge Univ. Press, Cambridge, 1979).
31. R. Tonkinson, *The Mardu Aborigines* (Holt, Rinehart, and Winston, New York, 1978).

Fig. 3. Modeling relatedness, equality, and group size. Results of the egalitarian model (**top**) and non-egalitarian model (**bottom**) at camp sizes between 10 and 80. From bottom to top, areas represent consanguineal (genetic) kin, affinal kin, distant affinal kin, and unrelated individuals. Exact proportions are given in tables S3 and S4.
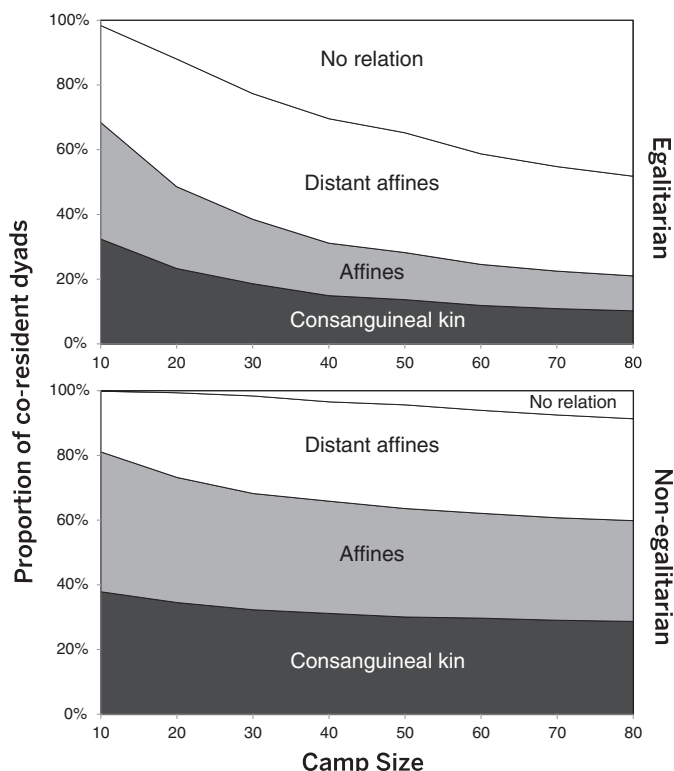
MITOSIS

Microtubule detyrosination guides chromosomes during mitosis

Marin Barisic,[1,2] Ricardo Silva e Sousa,[3]* Suvranta K. Tripathy,[3]* Maria M. Magiera,[4,5,6]*
Anatoly V. Zaytsev,[3,7,8] Ana L. Pereira,[1,2] Carsten Janke,[4,5,6]
Ekaterina L. Grishchuk,[3]†‡ Helder Maiato[1,2,9]†‡

Before chromosomes segregate into daughter cells, they align at the mitotic spindle equator, a process known as chromosome congression. Centromere-associated protein E (CENP-E)/Kinesin-7 is a microtubule plus-end–directed kinetochore motor required for congression of pole-proximal chromosomes. Because the plus-ends of many astral microtubules in the spindle point to the cell cortex, it remains unknown how CENP-E guides pole-proximal chromosomes specifically toward the equator. We found that congression of pole-proximal chromosomes depended on specific posttranslational detyrosination of spindle microtubules that point to the equator. In vitro reconstitution experiments demonstrated that CENP-E–dependent transport was strongly enhanced on detyrosinated microtubules. Blocking tubulin tyrosination in cells caused ubiquitous detyrosination of spindle microtubules, and CENP-E transported chromosomes away from spindle poles in random directions. Thus, CENP-E–driven chromosome congression is guided by microtubule detyrosination.

Chromosome congression is the process that leads to the formation of a metaphase plate at the equator of mitotic cells. During congression, peripheral chromosomes are first brought to the vicinity of spindle poles by the microtubule minus-end–directed kinetochore motor Dynein and are subsequently transported toward the equator by the plus-end–directed kinetochore motor centromere-associated protein E (CENP-E)/Kinesin-7 (1–3). Because different kinetochore motors are able to move chromosomes in opposite directions along anisotropic spindle microtubules, how chromosomes are guided toward the equator remains a critical longstanding question. This might involve spatial cues provided by intracellular gradients, such as the Ran guanosine triphosphate (GTP) gradient, which becomes established around aligned chromosomes (4). We tested this possibility by expressing the dominant-negative mutant RanT24N (5), which fails to bind GTP and inhibits RCC1-dependent RanGTP gradient formation from chromosomes, but found no major congression problems in human U2OS cells (fig. S1). Alternatively, the activity and/or affinity of kinetochore motors to microtubules might itself be regulated (for example, by phosphorylation) (6, 7). This model would account for the relative dominance of different kinetochore

[1]Chromosome Instability and Dynamics Laboratory, Instituto de Biologia Molecular e Celular, Universidade do Porto, Rua do Campo Alegre 823, 4150-180 Porto, Portugal. [2]Instituto de Investigação e Inovação em Saúde–i3S, Universidade do Porto, Portugal. [3]Department of Physiology, Perelman School of Medicine, University of Pennsylvania, Philadelphia, Pennsylvania, USA. [4]Institut Curie, 91405 Orsay, France. [5]Paris Sciences et Lettres (PSL) Research University, 75005 Paris, France. [6]Centre National de la Recherche Scientifique UMR 3348, 91405 Orsay, France. [7]Center for Theoretical Problems of Physicochemical Pharmacology, Russian Academy of Sciences (RAS), Moscow, Russia. [8]Federal Research and Clinical Centre of Pediatric Hematology, Oncology and Immunology, Moscow, Russia. [9]Cell Division Unit, Department of Experimental Biology, Faculdade de Medicina, Universidade do Porto, Alameda Professor Hernâni Monteiro, 4200-319 Porto, Portugal.
*These authors contributed equally to this work. †Corresponding author. E-mail: maiato@ibmc.up.pt (H.M.); gekate@mail.med.upenn.edu (E.L.G.) ‡These authors contributed equally to this work.

Fig. 1. Chromosome congression requires spatially regulated detyrosination of spindle microtubules. (**A**) Microtubule detyrosination was examined by means of immunoblotting with detyrosinated tubulin antibodies. Protein lysates of U2OS cells were obtained 24 hours after TTL–yellow fluorescent protein (YFP) transfection and 4 hours after adding parthenolide (20 μM). Glyceraldehyde-3-phosphate dehydrogenase (GAPDH) was used as loading control. (**B**) Deconvolved immunofluorescence images of U2OS cells stained for DNA [4′,6-diamidino-2-phenylindole (DAPI), magenta], α-tubulin, and detyrosinated tubulin (green). TTL-YFP signal was detected by means of direct fluorescence. Arrowheads highlight detyrosinated spindle microtubules in control cells. Detyrosination of spindle microtubules is undetectable after TTL-YFP overexpression or treatment with parthenolide. Scale bar, 10 μm.

motors in time and space, but it fails to explain the biased motion of pole-proximal chromosomes toward the equator. A third hypothesis predicts that kinetochore motors are sensitive to spatial cues encoded by the microtubule tracks they move on, which determine the direction of chromosome motion. These spatial cues may result from different stability within spindle microtubules (for example, astral versus kinetochore microtubules), or from their different organization (for example, individual versus bundled microtubules). However, recent work has shown that stable kinetochore microtubule bundles are dispensable for CENP-E–mediated chromosome congression (8), suggesting a different mechanism.

One possibility is that tubulin posttranslational modifications (PTMs) generate specific cues that guide CENP-E along specific spindle microtubules. This so-called "tubulin code" has been proposed to contribute to subcellular differentiation of microtubules (9, 10), and tubulin acetylation and detyrosination are specifically enriched on stable spindle microtubules that point to the equator (11–13). Tubulin acetylation and detyrosination regulate Kinesin-1–dependent transport in neurons (14–16), and recent in vitro reconstitution experiments have also demonstrated subtle but direct effects of tubulin PTMs on the motor activities of Kinesin-2, Kinesin-13, and Dynein (17).

To test whether tubulin detyrosination and acetylation are required for chromosome congression, we perturbed the function of enzymes responsible for specific catalytic steps (fig. S2, A and B). To modulate tubulin detyrosination in human U2OS cells, we overexpressed tubulin tyrosine ligase (TTL), which specifically converts soluble α-tubulin to its tyrosinated form (18). In parallel, we inhibited tubulin carboxypeptidase (TCP) with the cell-permeable drug parthenolide (19), thus preventing removal of the C-terminal tyrosine from polymerized α-tubulin (10). Both treatments specifically decreased tubulin detyrosination without affecting polyglutamylation (Fig. 1A and fig. S3) and reduced the detyrosination of spindle microtubules pointing to the equator (Fig. 1B and fig. S4A). These cells consistently showed misaligned pole-proximal chromosomes and delayed mitotic progression, phenocopying CENP-E inhibition (Fig. 1B, fig. S4B, movie S1). In contrast, perturbation of tubulin acetylation had no effect on chromosome congression (fig. S5, A to C). Thus, detyrosination of spindle microtubules pointing to the equator is required for congression of pole-proximal chromosomes.

Whereas CENP-E is mostly associated with kinetochores during early mitosis, we noticed that CENP-E–green fluorescent protein (GFP) expressed under control of its own promoter (20) specifically colocalized with the few detyrosinated microtubules (D-MTs) present in HeLa cells in G2 (fig. S6, A and B) (21). Moreover, inhibition of tubulin detyrosination with parthenolide led to CENP-E dissociation from these microtubules (figs. S4A and S7, A and B, and movie S2), suggesting that tubulin detyrosination promotes the interaction between CENP-E and microtubules in vivo. To
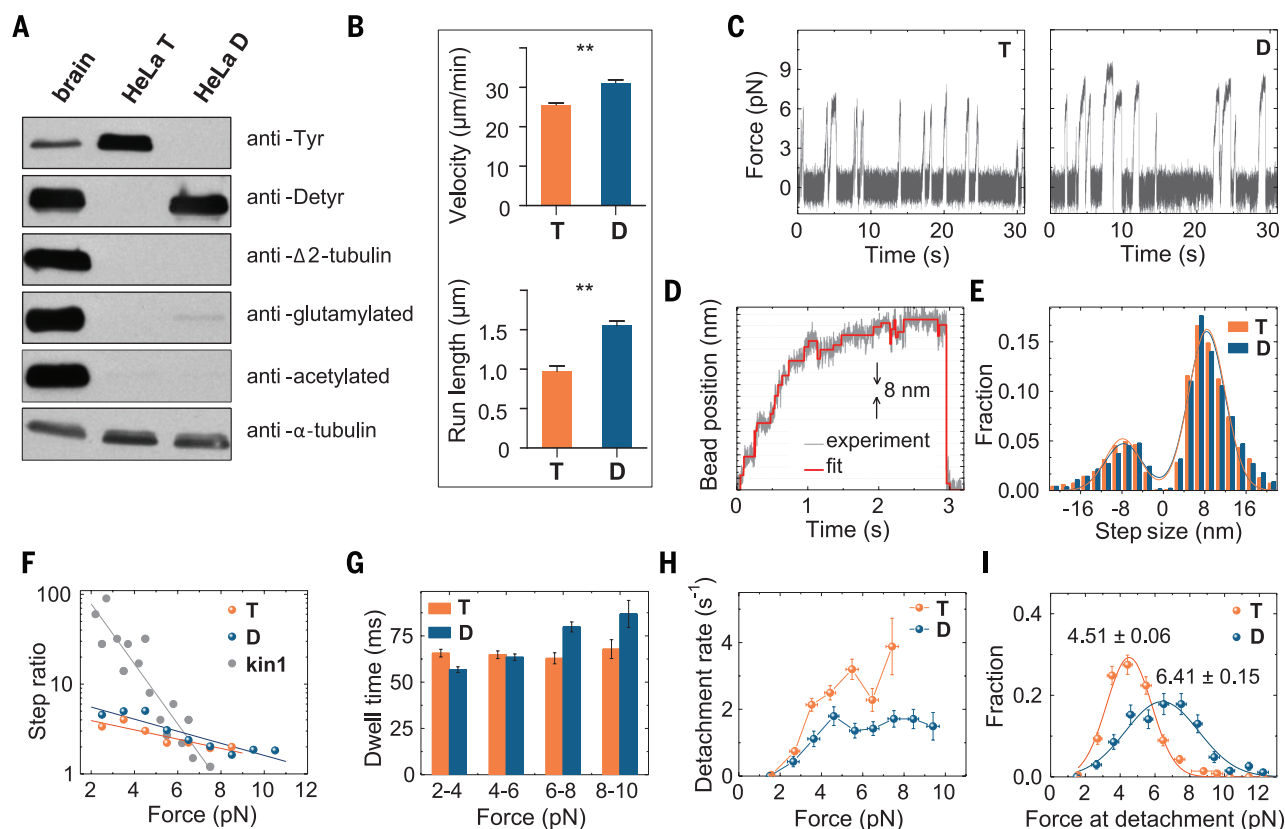
Fig. 2. CENP-E motility is enhanced on detyrosinated microtubules in vitro. (**A**) Immunoblot of purified tubulin from porcine brain or HeLa cells before (T) and after (D) detyrosination with carboxypeptidase A. Antibodies against tyrosinated, detyrosinated, Δ2, glutamylated (GT335), and acetylated tubulin were used to assess posttranslational modifications. Antibody to α-tubulin demonstrates similar amounts of tubulin in different lanes. (**B**) Mean velocity and characteristic run length of CENP-E for T-MTs (N = 3 independent experiments, n = 257 molecules) and D-MTs (N = 4 independent experiments, n = 401). Error bars are SEM; **$P ≤ 0.01$ based on unpaired t test with 95% confidence. (**C**) Typical traces of bead motions on T- and D-MTs, plotted as force versus time. (**D**) Example trace of CENP-E bead in a laser trap with step-size fit. (**E**) Step-size histograms were fit by the sum of two Gaussians (lines). Positive steps were away from the trap's center. Number of forward steps was 5146 and 3427, and number of backward steps was 1731 and 1114, for T- and D-MTs, respectively. (**F**) Ratio of forward to backward steps for CENP-E in comparison with Kinesin-1 [data from (25, 26)] with theoretical fittings for ratio >1. (**G**) Characteristic dwell times as a function of force within 2-pN bins. Total number of dwells for all forces was 6877 and 4541 for T- and D-MTs, respectively. (**H**) CENP-E detachment rate under load. Error bars for detachment rate were calculated by dividing the square root of the number of detachments by the total time within each bin. Error bars for force are SEM for measurements in each bin. (**I**) Histograms of detachment force with Gaussian fits. Numbers are the mean ± SEM, n = 491 detachments for T-MTs, and 269 for D-MTs. Vertical error bars are square roots of the number of detachments normalized by the total number of detachments.
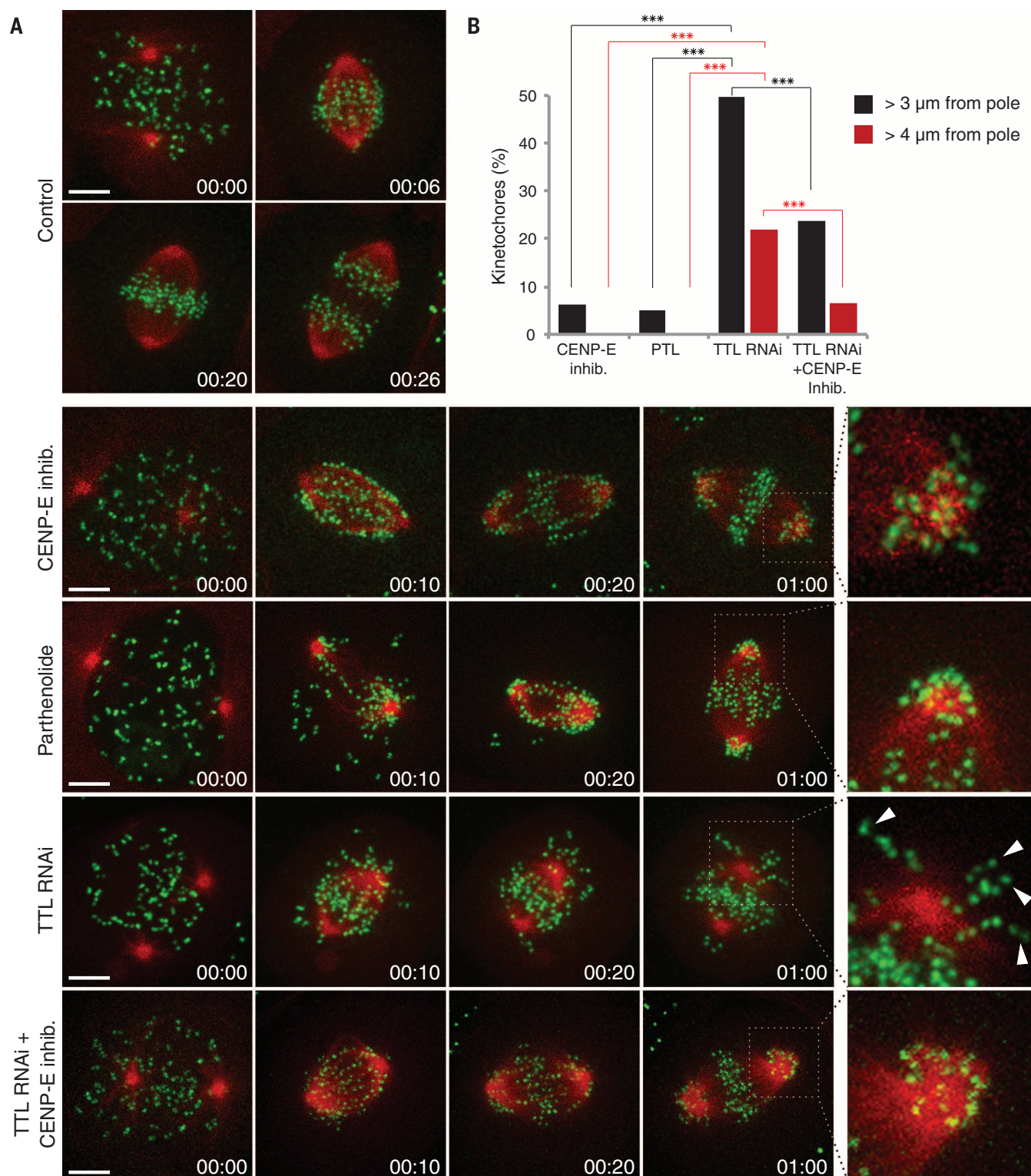
Fig. 3. Chromosomes cannot complete congression in TTL-depleted cells and are randomly transported away from the spindle pole by CENP-E. (**A**) Spinning-disk confocal imaging of live U2OS cells stably expressing CENP-A–GFP and mCherry-tubulin. Chromosome congression was impaired in 100% of cells treated either with CENP-E inhibitor (13 cells, three independent experiments) or parthenolide (nine cells, two independent experiments). Chromosome congression was impaired in 65% of cells depleted of TTL (23 cells, three independent experiments). Arrowheads highlight kinetochores transported away from the spindle pole toward the cell cortex. Enlarged insets highlight polar regions. Scale bar, 5 μm. Time is hours:min. (**B**) Quantification of the percentage of pole-proximal chromosomes that were transported away from spindle poles in the different conditions. *N* (CENP-E inh.) = 311 kinetochores from 10 cells, three independent experiments; *N* (parthenolide) = 388 kinetochores from 7 cells, two independent experiments; *N* (TTL RNAi) = 311 kinetochores from 18 cells, three independent experiments. *N* (TTL RNAi+CENP-E inh) = 720 kinetochores from 17 cells, three independent experiments. Asterisks indicate *z* test significance values; ***P < 0.001.

test whether this tubulin PTM affects CENP-E directly, we reconstituted CENP-E motility in vitro using purified components. Brain tubulin was not suitable for these experiments because it is highly detyrosinated and carries many other PTMs (Fig. 2A). We thus developed a method to purify tyrosinated tubulin from HeLa cells by using cycles of polymerization and depolymerization (22). A fraction of this tubulin was then treated with carboxypeptidase A to produce detyrosinated tubulin (Fig. 2A). These purified proteins were used to polymerize T- and D-MTs, and motility of recombinant CENP-E-GFP was examined by using total internal reflection fluorescence microscopy (fig. S8A and movie S3). CENP-E bound to and moved processively and unidirectionally on both types of microtubules, but it was slower on T-MTs as compared with D-MTs: 26.7 ± 0.4 versus 31.3 ± 0.7 µm/min, respectively (Fig. 2B and fig. S8B). Moreover, there was a ~60% decrease in the characteristic length of CENP-E runs on T-MTs compared with D-MTs (0.97 ± 0.07 versus 1.55 ±

0.06 µm), implying that CENP-E walks more processively on D-MTs assembled in vitro.

We next investigated the force produced by single CENP-E motors using a stationary optical trap (23). CENP-E motors carrying a C-terminal 6xHis-tag were linked to 0.54-µm streptavidin-coated polystyrene beads with biotinylated antibodies to 6X His tag. The beads were then positioned near the microtubule by using an infrared laser, and their motility was examined in a buffer with physiological levels of adenosine triphosphate. Bead-microtubule binding frequencies were similar for these two types of microtubules (0.45 and 0.41 s^{-1} for T- and D-MTs, respectively). As the bead moved away from the center of the trap because of CENP-E motor activity, it experienced greater trapping force and eventually detached and snapped back to the center of the trap (movie S4). These repeated motions led to the characteristic displacement spikes recorded with a quadrant photodetector (Fig. 2C). Whereas large forces generated by CENP-E were infrequent on

T-MTs, the force values on D-MTs extended into the 8 pN range (Fig. 2C and fig. S9C). Consistently, the average duration of the force spikes was shorter on T-MTs as compared with D-MTs (0.49 ± 0.02 versus 0.79 ± 0.05 s) (fig. S9D). Thus, CENP-E is unable to sustain large loads on T-MTs, which is in line with the persistence of pole-proximal chromosomes after inhibition of microtubule detyrosination in spindles (Fig. 1B).

To investigate the CENP-E stepping mechanism on different microtubule lattices, we analyzed high-resolution bead recordings (Fig. 2, D and E). On both types of microtubules, the average step size was ~8 nm (fig. S9E), which is as expected based on tubulin dimer spacing in the microtubule lattice (24). Backward steps were frequently observed, and with increasing trap load, the probability of a forward step decreased more gradually for CENP-E (Fig. 2F and fig. S9F) than for Kinesin-1 (25, 26). Although the forward stepping of CENP-E was slightly less frequent on T-MTs compared with D-MTs, the overall dependency
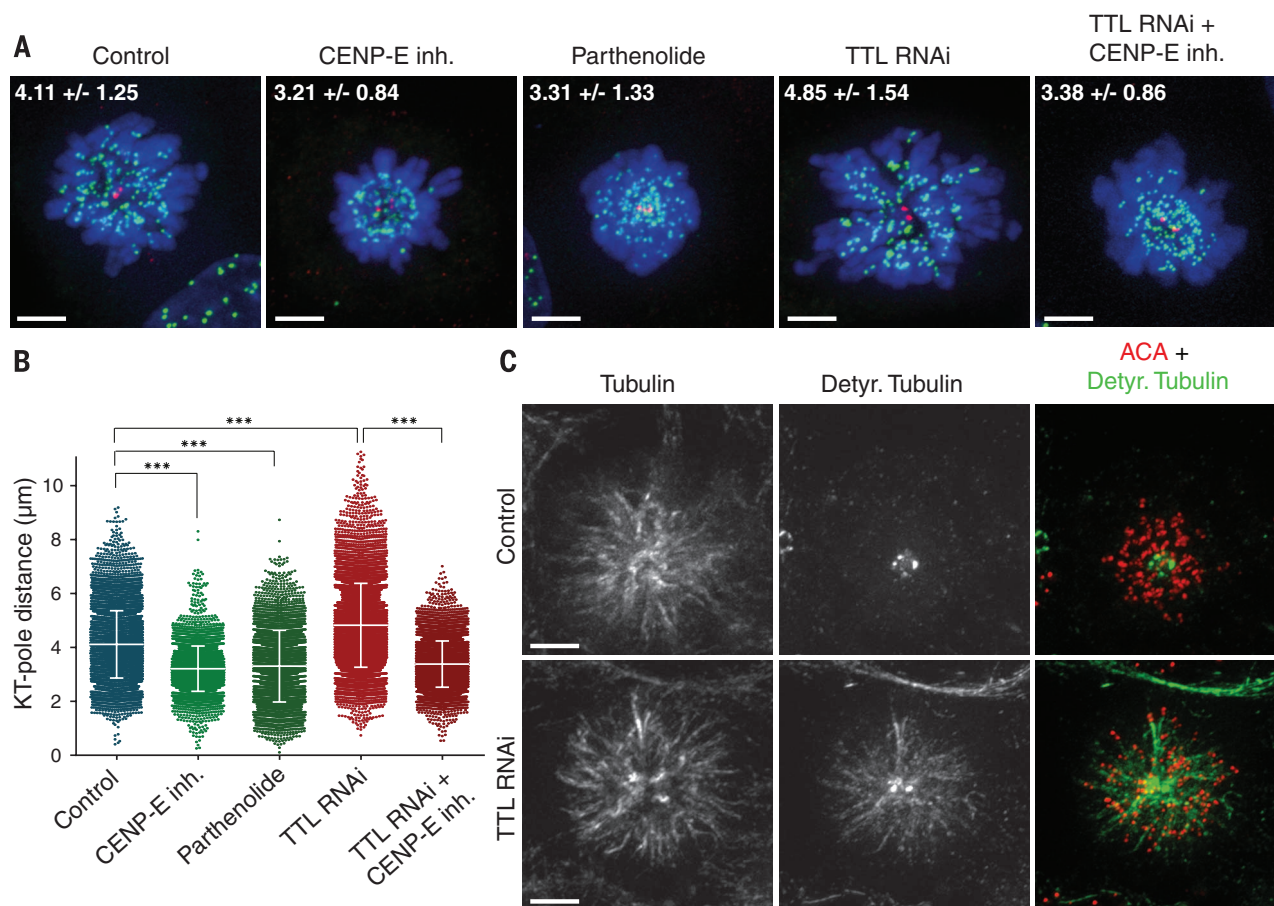
Fig. 4. CENP-E–dependent transport of pole-proximal chromosomes along ubiquitously detyrosinated spindle microtubules after TTL RNAi. (**A**) U2OS cells treated with the kinesin-5 inhibitor S-Trytil-L-Cysteine (STLC) and immunostained for DNA (DAPI, blue), kinetochores [anti-centromere antibodies (ACA), green] and centrioles (centrin = red). Maximum-intensity projection images of representative examples for each condition are shown. Numbers indicate mean kinetochore-to-pole distances ± SD of the pooled data from at least two independent experiments per condition. Scale bar, 5 µm. (**B**) Quantification of kinetochore (KT) to pole distances in STLC-treated cells under

different conditions; *n* (control) = 7185 kinetochores from 56 cells, three experiments; *n* (CENP-E inh) = 3877 kinetochores from 34 cells, two experiments; *n* (Parthenolide) = 3611 kinetochores from 30 cells, two experiments; *n* (TTL RNAi) = 8239 kinetochores from 61 cells, four experiments; *n* (TTL RNAi + CENP-E inh) = 5458 kinetochores from 45 cells, two experiments. Asterisks indicate Mann-Whitney *U* test significance values; ***$P < 0.001$. (**C**) Deconvolved immunofluorescence images of STLC-treated U2OS cells stained for α-tubulin, detyrosinated tubulin, and ACA. Detyrosination of spindle microtubules was highly increased after TTL RNAi. Scale bar, 5 µm.

of CENP-E stepping on the resisting force was similar on these two lattices. The average dwell time between the steps for the entire force range was also similar on T- and D-MTs (fig. S9G). We further observed a slightly shorter dwell time at low force on D-MTs, which is consistent with the faster velocity of CENP-E walking on this type of microtubules (Fig. 2G). CENP-E responded to larger loads by lengthening its dwells on D-MTs, but not on T-MTs. Under the load, CENP-E also detached less frequently from D-MTs (Fig. 2H). As a result, the peak force for CENP-E detachment was shifted to significantly higher values on D-MTs (Fig. 2I), indicating that the effect of tubulin detyrosination is exerted mostly on CENP-E detachment, rather than stepping. Thus, CENP-E can carry a significantly larger load on D-MTs in vitro.

Our data support a model in which CENP-E–dependent transport of pole-proximal chromosomes toward the spindle equator requires microtubule tracks that are detyrosinated. Therefore, increasing tubulin detyrosination should disrupt the biased motion of pole-proximal chromosomes toward the equator and cause their delivery to inappropriate cellular locations. To test this, we increased tubulin detyrosination by depleting TTL by means of RNA interference (RNAi) in U2OS cells (fig. S10A). TTL depletion caused ubiquitous detyrosination of spindle microtubules (including astral microtubules) during early mitosis (fig. S10B) (27). Of TTL-depleted cells, 65% delayed mitotic progression and failed to congress all the chromosomes (Fig. 3A and movie S5). In these cells, the pole-proximal chromosomes did not remain stuck at the spindle poles, as observed after CENP-E inhibition or after blocking tubulin detyrosination, but were transported in various directions, including toward the cell cortex (Fig. 3, A and B). This suggests that the spatial cues that normally guide CENP-E toward the equator were disrupted. CENP-E inhibition in live TTL-depleted cells significantly decreased the transport of chromosomes away from spindle poles (Fig. 3, A and B). This was confirmed in a large population of fixed cells by use of a quantitative monopolar spindle configuration assay (Fig. 4, A to C) (1), indicating that the random transport of chromosomes along ubiquitously detyrosinated spindle microtubules after TTL RNAi is mediated by CENP-E.

Taken together, our work establishes the specific molecular mechanism that guides CENP-E–dependent chromosome motion toward the cell equator. This mechanism is based on the ability of CENP-E to transport pole-proximal chromosomes preferentially on detyrosinated microtubule tracks, which are normally oriented toward the spindle equator (fig. S11). We propose that microtubule detyrosination works as a navigation system that guides kinetochore motors during cell division, ultimately contributing to faithful chromosome segregation.

REFERENCES AND NOTES

1. M. Barisic, P. Aguiar, S. Geley, H. Maiato, *Nat. Cell Biol.* **16**, 1249–1256 (2014).
2. T. M. Kapoor *et al.*, *Science* **311**, 388–391 (2006).
3. C. E. Walczak, S. Cai, A. Khodjakov, *Nat. Rev. Mol. Cell Biol.* **11**, 91–102 (2010).
4. P. Kalab, R. Heald, *J. Cell Sci.* **121**, 1577–1586 (2008).
5. T. Kiyomitsu, I. M. Cheeseman, *Nat. Cell Biol.* **14**, 311–317 (2012).
6. Y. Kim, A. J. Holland, W. Lan, D. W. Cleveland, *Cell* **142**, 444–455 (2010).
7. J. Whyte *et al.*, *J. Cell Biol.* **183**, 819–834 (2008).
8. S. Cai, C. B. O'Connell, A. Khodjakov, C. E. Walczak, *Nat. Cell Biol.* **11**, 832–838 (2009).
9. K. J. Verhey, J. Gaertig, *Cell Cycle* **6**, 2152–2160 (2007).
10. C. Janke, *J. Cell Biol.* **206**, 461–472 (2014).
11. G. G. Gundersen, J. C. Bulinski, *J. Cell Biol.* **102**, 1118–1126 (1986).
12. P. J. Wilson, A. Forer, *Cell Motil. Cytoskeleton* **14**, 237–250 (1989).
13. G. G. Gundersen, M. H. Kalnoski, J. C. Bulinski, *Cell* **38**, 779–789 (1984).
14. N. A. Reed *et al.*, *Curr. Biol.* **16**, 2166–2172 (2006).
15. Y. Konishi, M. Setou, *Nat. Neurosci.* **12**, 559–567 (2009).
16. J. W. Hammond *et al.*, *Mol. Biol. Cell* **21**, 572–583 (2010).
17. M. Sirajuddin, L. M. Rice, R. D. Vale, *Nat. Cell Biol.* **16**, 335–344 (2014).
18. K. Ersfeld *et al.*, *J. Cell Biol.* **120**, 725–732 (1993).
19. X. Fonrose *et al.*, *Cancer Res.* **67**, 3371–3378 (2007).
20. I. Poser *et al.*, *Nat. Methods* **5**, 409–415 (2008).
21. T. J. Yen, G. Li, B. T. Schaar, I. Szilak, D. W. Cleveland, *Nature* **359**, 536–539 (1992).
22. Materials and methods are available as supplementary materials on *Science* Online.
23. N. Gudimchuk *et al.*, *Nat. Cell Biol.* **15**, 1079–1088 (2013).
24. H. Yardimci, M. van Duffelen, Y. Mao, S. S. Rosenfeld, P. R. Selvin, *Proc. Natl. Acad. Sci. U.S.A.* **105**, 6016–6021 (2008).
25. N. J. Carter, R. A. Cross, *Nature* **435**, 308–312 (2005).
26. M. Nishiyama, H. Higuchi, T. Yanagida, *Nat. Cell Biol.* **4**, 790–797 (2002).
27. L. Peris *et al.*, *J. Cell Biol.* **174**, 839–849 (2006).

CANCER IMMUNOTHERAPY

A dendritic cell vaccine increases the breadth and diversity of melanoma neoantigen-specific T cells

Beatriz M. Carreno,[1]* Vincent Magrini,[2] Michelle Becker-Hapak,[1] Saghar Kaabinejadian,[3] Jasreet Hundal,[2] Allegra A. Petti,[2] Amy Ly,[2] Wen-Rong Lie,[4] William H. Hildebrand,[3] Elaine R. Mardis,[2] Gerald P. Linette[1]

T cell immunity directed against tumor-encoded amino acid substitutions occurs in some melanoma patients. This implicates missense mutations as a source of patient-specific neoantigens. However, a systematic evaluation of these putative neoantigens as targets of antitumor immunity is lacking. Moreover, it remains unknown whether vaccination can augment such responses. We found that a dendritic cell vaccine led to an increase in naturally occurring neoantigen-specific immunity and revealed previously undetected human leukocyte antigen (HLA) class I–restricted neoantigens in patients with advanced melanoma. The presentation of neoantigens by HLA-A*02:01 in human melanoma was confirmed by mass spectrometry. Vaccination promoted a diverse neoantigen-specific T cell receptor (TCR) repertoire in terms of both TCR-β usage and clonal composition. Our results demonstrate that vaccination directed at tumor-encoded amino acid substitutions broadens the antigenic breadth and clonal diversity of antitumor immunity.

M elanoma genomes harbor somatic mutations that are caused by exposure to mutagens such as ultraviolet light (1, 2). Tumor missense mutations, translated into amino acid substitutions (AASs), may provide a form of antigens that the immune system perceives as foreign, which in turn elicits tumor-specific T cell immunity (3–6). To examine the immunogenicity of tumor-encoded AASs, we obtained the consent of three patients with

stage III resected cutaneous melanoma (MEL21, MEL38, and MEL218) for genomic analysis of their surgically excised tumors. The three patients were then enrolled in a phase 1 clinical trial with autologous, functionally mature, interleukin-12p70 (IL-12p70)–producing dendritic cell vaccine (fig. S1) (7). All three patients had received prior treatment with ipilimumab (see supplementary materials). Exome sequencing was performed to identify somatic mutations in tumor samples (Fig. 1A). Multiple metachronous tumors were analyzed from patients MEL21 and MEL38 (tables S1 and S2). Tumor missense mutations, translated as AAS-encoding nonamer peptides, were filtered

[1]Department of Medicine, Division of Oncology, Washington University School of Medicine, St. Louis, MO, USA. [2]Genome Institute, Washington University School of Medicine, St. Louis, MO, USA. [3]Department of Microbiology and Immunology, University of Oklahoma Health Science Center, Oklahoma City, OK, USA. [4]EMD Millipore Corporation, Billerica, MA, USA.
*Corresponding author. E-mail: bcarreno@dom.wustl.edu

through in silico analysis to assess HLA-A*02:01 peptide-binding affinity (8), and expression of genes encoding predicted HLA-A*02:01 peptide candidates was determined by analysis of cDNA capture data (Fig. 1A) (9). Peptide candidates for experimental validation were selected according to the strategy described in fig. S2; HLA-A*02:01 binding was evaluated using the T2 assay (fig. S3) (10) and confirmed with the fluorescence polarization–based competitive peptide-binding assay of Buchli et al. (11). Seven AAS peptide candidates per patient were selected from validated HLA-A*02:01 binders (fig. S2 and table S4) for incorporation into a personalized vaccine formulation, along with the melanoma gp100-derived peptides G209-2M and G280-9V as positive controls for vaccination (7). The expression pattern of mutated genes encoding vaccine candidates is shown in Venn diagrams in Fig. 1A.

To examine the kinetics and magnitude of T cell immunity to AAS peptides upon vaccination, we collected peripheral blood mononuclear cells

(PBMCs) prior to vaccination and weekly thereafter. The CD8+ T cell response to each peptide was analyzed using a HLA-A*02:01/AAS-peptide dextramer assay after a single round of in vitro stimulation (fig. S4A) (7). Immune monitoring demonstrated that in each patient, T cell immunity to one AAS peptide could be detected in prevaccine PBMC samples after in vitro stimulation (MEL21, TMEM48 F169L; MEL38, SEC24A P469L; MEL218, EXOC8 Q656P) (Fig. 1B), although not directly from the blood (fig. S4B). Preexisting immunity to these three neoantigens was confirmed in ex vivo expanded, prevaccine-purified CD8+ T cells by means of dextramer assay (fig. S4B) and interferon (IFN)–γ production (12) (fig. S4C).

Vaccination augmented the T cell response to these neoantigens, with observed frequencies of 23% TMEM48 F169L+ CD8+ T cells, 64% SEC24A P469L+ CD8+ T cells, and 89% EXOC8 Q656P+ CD8+ T cells detected upon culture at the peak of response (Fig. 1B). Immune monitoring also

Fig. 1. Vaccine candidate identification and immune monitoring. (**A**) Distribution of somatic (exomic and missense) mutations identified in metachronous tumors of patients MEL21 and MEL38 (anatomical location and date of collection indicated) and tumor of patient MEL218. HLA-A*02:01-binding candidate peptides were identified in silico among AASs; expression of genes encoding mutated proteins was determined from cDNA capture data (tables S1 to S3). Venn diagrams show expression, among metachronous tumors, of mutated genes encoding vaccine neoantigens. The identities of the three immunogenic neoantigens identified in each patient are depicted; color coding identifies naturally occurring (red) and vaccine-induced (blue) neoantigens. (**B**) Immune monitoring of neoantigen-specific CD8+ T cell responses. Results are derived from PBMCs isolated before dendritic cell vaccination (prevaccine) and at peak (postvaccine). PBMCs were cultured in vitro in the presence of peptide and IL-2 for 10 days, followed by HLA-A*02:01/AAS-peptide dextramer assay. This immune monitoring strategy allows the reliable detection as well as the assessment of replicative potential of vaccine-induced T cell responses (fig. S4A). Color coding is same as in (A); numbers within dot plots represent percent neoantigen-specific T cells in lymph+/CD8+ gated cells.
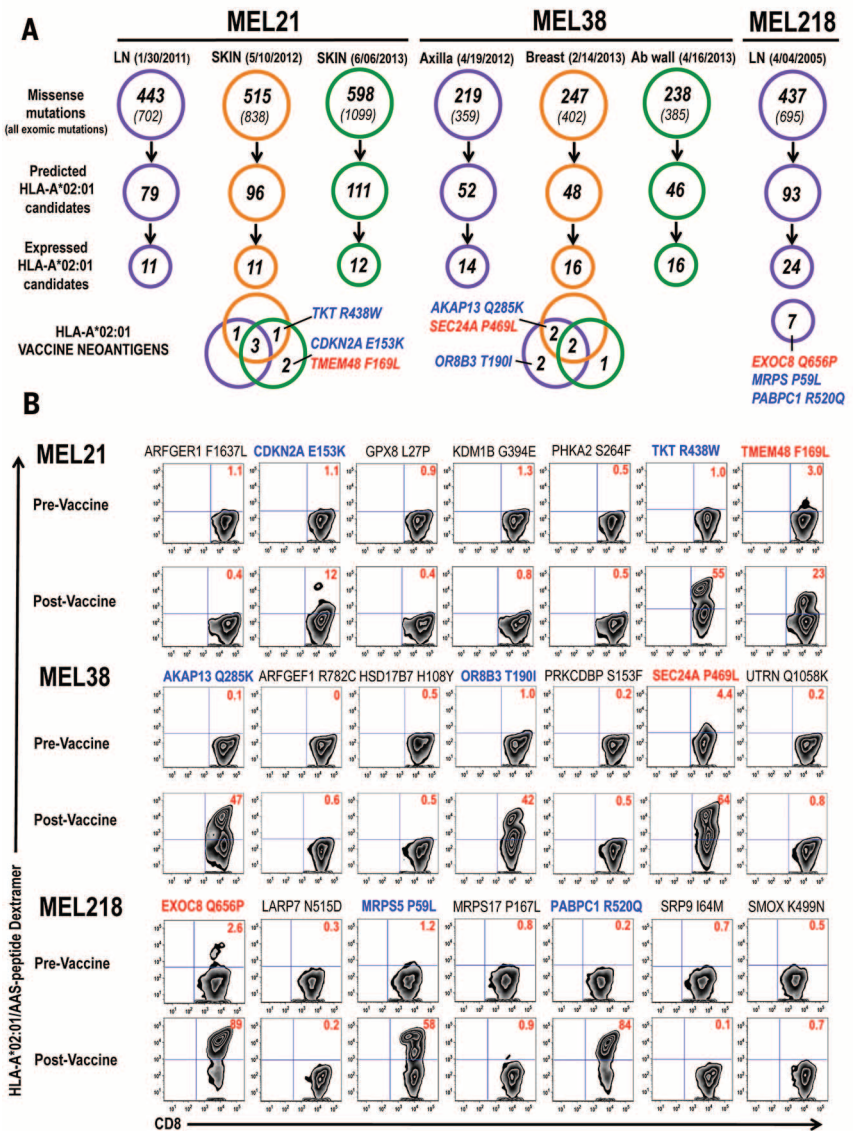
revealed vaccine-induced T cell immunity to two additional neoantigens per patient: TKT R438W and CDKN2A E153K (55% and 12%, respectively) in patient MEL21; AKAP13 Q285K and OR8B3 T190I (47% and 42%, respectively) in patient MEL38, and MRPS5 P59L and PABPC1 R520Q (58% and 84%, respectively) in patient MEL218 (Fig. 1B). Two of the three patients, MEL21 and MEL218, had preexisting immunity to G209-2M and G280-9V peptides, as determined by the presence of gp100-specific T cells in prevaccine PBMC samples and their ex vivo expansion upon antigen stimulation (fig. S5B). Upon vaccination, these T cell responses were enhanced in patients MEL21 and MEL218 and revealed in patient MEL38 (fig. S5). No T cell immunity to the remaining 12 AAS peptides was detected. Overall, robust neoantigen T cell immunity was detectable as early as week 2 and peaked at week 8 to 9 after the initial vaccine dose (fig. S4A). Neoantigen-specific CD8^{+} T cells were readily identified by dextramer assay directly in postvaccine PBMC samples (fig. S4B) and memory T cells were detected up to 4 months after the final vaccine dose.

Analysis of T cell reactivity among the three patients indicated no preferential skewing toward AAS at specific positions in the peptide sequence—that is, toward TCR contact residues or primary anchor residues (13). Rather, in each patient, T cell immunity appeared to focus on the three AAS candidates exhibiting the highest HLA-A*02:01 binding affinity, whereas the remaining medium- to high-affinity peptides were nonimmunogenic (table S4) (8, 11). Immunogenic AAS peptides (Fig. 1A) were not preferentially derived from genes with high allelic frequency or expression levels (tables S1 to S3).

To characterize the function of vaccine-induced neoantigen-specific T cells, we established short-term expanded CD8^{+} T cell lines and confirmed their antigen specificity by dextramer assay (fig. S4B) (7, 12). Neoantigen-specific T cells displayed significant levels of cytotoxic activity at AAS peptide concentrations of 1 to 10 nM, a finding that is consistent with high-avidity T cell recognition of antigen (Fig. 2A). OR8B3 T190I–specific T cells could not discriminate between AAS and wild-type peptide when presented on T2 cells, whereas all of the remaining T cell lines showed clear specificity for AAS peptide sequences (Fig. 2A). Next, we sought to characterize the cytokine production profile of these T cells, as a previous report suggests that IL-12p70–producing dendritic cells promote type 1 CD8^{+} T immunity, which in turn correlates with increased clinical benefit (7, 14). Upon antigen stimulation, most vaccine-induced neoantigen-specific T cells produced high amounts of IFN-γ relative to IL-4, IL-5, and IL-13—a pattern that is indicative of a type 1 phenotype (fig. S6). However, SEC24A P469L–specific T cells exhibited a type 2–skewed phenotype (high IL-4, IL-5, and IL-13 levels relative to IFN-γ), and TMEM48 F169L–specific T cells showed a mixed phenotype (high IL-13 levels, but not higher IL-4 or IL-5 levels, relative to IFN-γ) (fig. S6).

We next transfected DM6, a HLA-A*02:01[+] melanoma cell line (15), with tandem minigene constructs (TMCs) to evaluate neoantigen processing and presentation. Each minigene encoded an AAS, or the corresponding wild-type amino acid, embedded in 19 to 21 amino acids derived from the normal gene product (fig. S7A and table S5). TMCs also encoded the West Nile virus (WNV) SVG9 (16) and melanoma G280 (17) antigenic determinants as controls (figs. S5 and S7B). Seven of the nine immunogenic neoantigens—TMEM48 F169L, TKT R438W, CDKN2A E153K, SEC24A P469L, AKAP13 Q285K, EXOC8 Q656P, and PABPC1 R520Q—were processed and presented, as evidenced by cytotoxic activity (Fig. 2B) and IFN-γ production (fig. S7C) by corresponding neoantigen-specific T cells upon coculture with DM6 cells expressing AAS-encoding TMCs (AAS-TMCs). In contrast, neither cytotoxic activity (Fig. 2B) nor IFN-γ production (fig. S7C) was observed upon coculture of OR8B3 T190I– and MRPS5 P59L–specific T cells with DM6 cells expressing AAS-TMCs; this finding suggests that these neoantigens are not processed and presented from endogenously expressed protein. None of the neoantigen-specific T cells recognized wild type–encoding TMCs (Fig. 2B and fig. S7C).

On the basis of these findings and the immune monitoring results (Fig. 1B), the nine neoantigens identified in this study fall into three distinct antigenic determinant categories (18, 19). TMEM48 F169L, SEC24A P469L, and EXOC8 Q656P represent dominant antigens, as T cell immunity was detected prior to vaccination (naturally occurring) (Fig. 1B) and these neoantigens were processed and presented from endogenously expressed protein (Fig. 2B). TKT R438W, CDKN2A E153K, AKAP13 Q285K, and PABPC1 R520Q are characterized as subdominant antigens, as T cell immunity required peptide vaccination (Fig. 1B) and
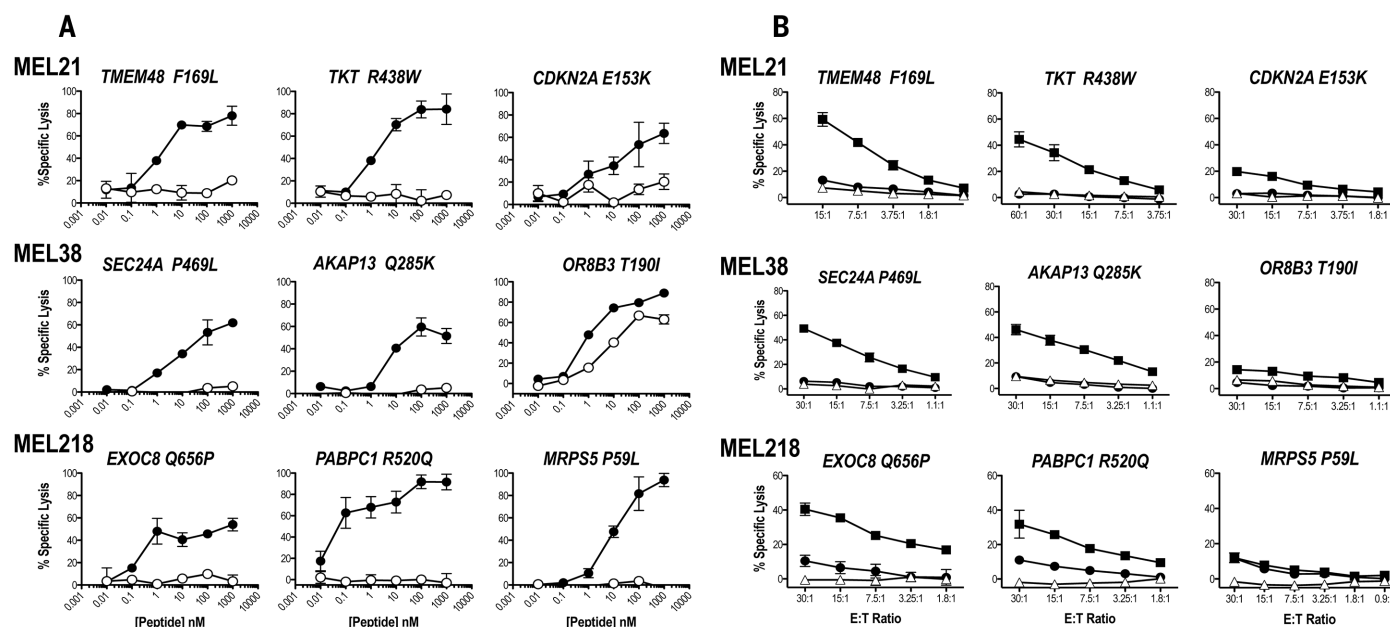
Fig. 2. Antigenic determinants recognized by vaccine-induced T cells. (**A**) Neoantigen-specific T cells recognition of AAS (solid circles) and wild-type (open circles) peptides was determined in a standard 4-hour ^{51}Cr release assay using peptide titrations on T2 (HLA-A*02:01) cells. Percent specific lysis of triplicates (mean ± SD) is shown for each peptide concentration; spontaneous lysis was <5%. Results are shown at E:T ratios of 10:1 for all T cell lines except TMEM48 F169L and CDKN2A E153K T cells (both at 60:1). A representative experiment of two independent evaluations is shown. (**B**) Neoantigen processing and presentation. Neoantigen-specific T cells were cocultured with DM6 cells expressing AAS-TMCs (solid rectangles) or wild type–encoding TMCs (solid circles) in a 4-hour ^{51}Cr release assay. Open triangles represent lysis obtained with parental DM6 cells. Percent specific lysis of triplicates (mean ± SD) is shown for each E:T ratio; spontaneous lysis was <5%. A representative experiment of two independent evaluations is shown.
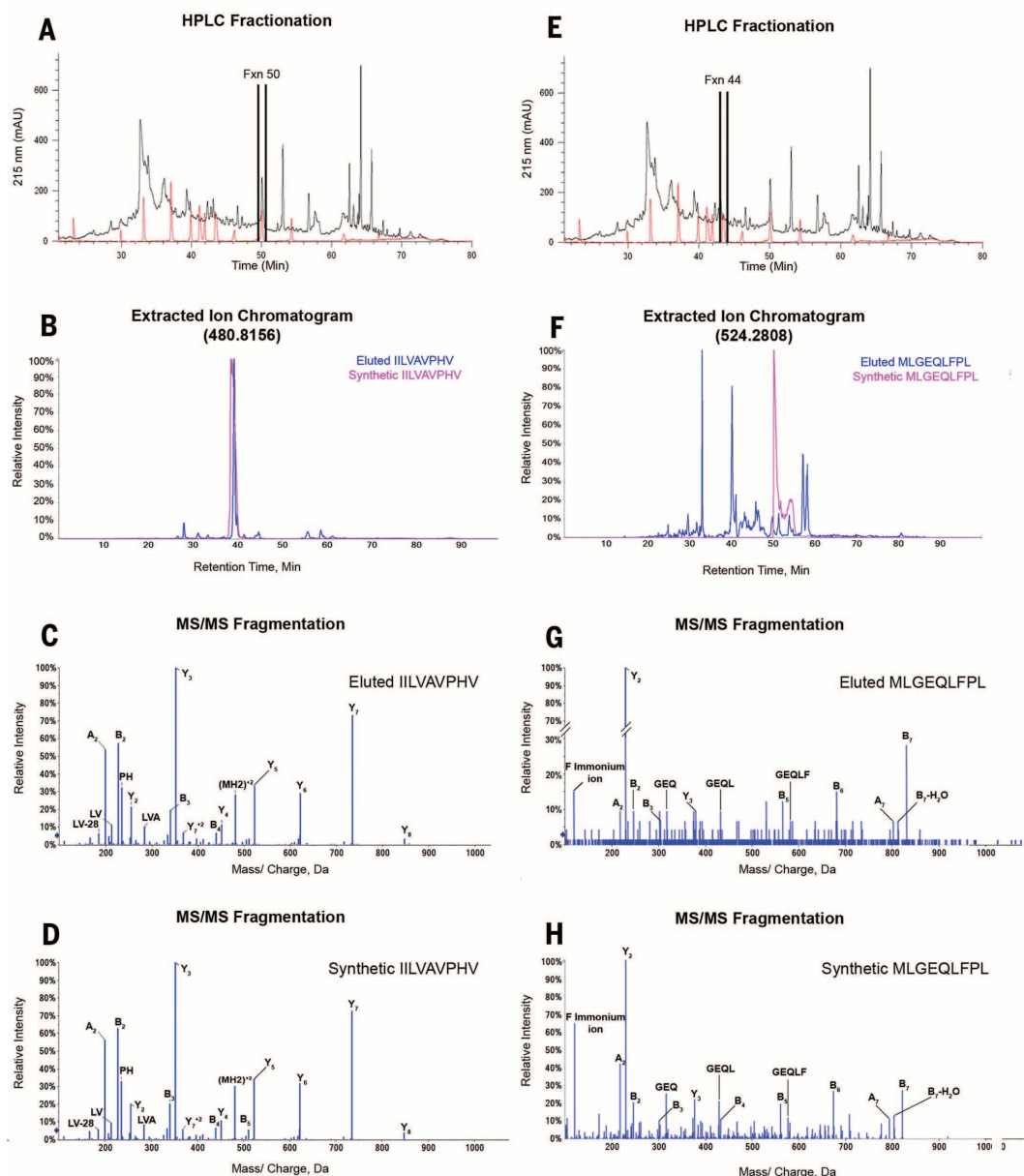
Fig. 3. Processing and presentation of tumor neoantigens. (**A**) RP-HPLC fractionation of HLA-A*02:01 peptides eluted from the AAS-TMC–expressing melanoma cell line (black trace) and the synthetic peptide mixture containing MEL218 neoantigen candidates (red trace), with fraction 50 indicated. (**B**) Extracted ion chromatogram of the parent ion with the theoretical mass/charge ratio (m/z) of 480.8156 (+2) in HPLC fraction 50 from the HLA-A*02:01 eluted peptides (blue) overlaid with the EXOC8 Q656P synthetic peptide (pink). (**C** and **D**) MS/MS fragmentation pattern of the EXOC8 Q656P ion eluted from HLA-A*02:01 identified as IILVAVPHV (C) and the corresponding synthetic peptide (D). (**E**) Same as in (A), with fraction 44 indicated. (**F**) Extracted ion chromatogram of the parent ion with the theoretical m/z of 524.2808 (+2) in HPLC fraction 44 from the HLA-A*02:01 eluted peptides (blue) overlaid with the PABPC1 R520Q synthetic peptide (pink). (**G** and **H**) MS/MS fragmentation pattern of the PABPC1 R520Q ion eluted from HLA-A*02:01 identified as MLGEQLFPL (G) and the corresponding synthetic peptide (H).

these neoantigens were processed and presented from endogenously expressed protein (Fig. 2B). Finally, OR8B3 T190I and MRPS5 P59L constitute cryptic antigens, because peptide vaccination elicited T cell immunity even though these neoantigens were not processed from endogenously expressed protein.

To validate neoantigen processing and presentation, we performed proteomic analysis on peptides eluted from soluble HLA-A*02:01 molecules isolated from melanoma cells expressing a TMC encoding AAS candidates from a tumor of patient MEL218 (*18*, *19*). Reverse-phase high-performance liquid chromatography (RP-HPLC) was used to reduce the complexity and determine the elution profile of the pool of soluble HLA-A*02:01–restricted peptides presented by melanoma cells, as well as the synthetic AAS peptide mixture (Fig. 3, A and E). The fractions corresponding to each synthetic peptide were subjected to nanoscale liquid chromatography–mass spectrometry (nano LC/MS). Extracted ion chromatograms revealed the presence of an eluted peptide with a retention time within 2 min of synthetic EXOC8 Q656P peptide in fraction 50 (Fig. 3B). MS/MS fragmentation pattern comparison of the eluted and synthetic peptides ensured EXOC8 Q656P sequence identity and confirmed HLA-A*02:01 presentation of this dominant neoantigen (Fig. 3, C and D). A similar analysis of fraction 44
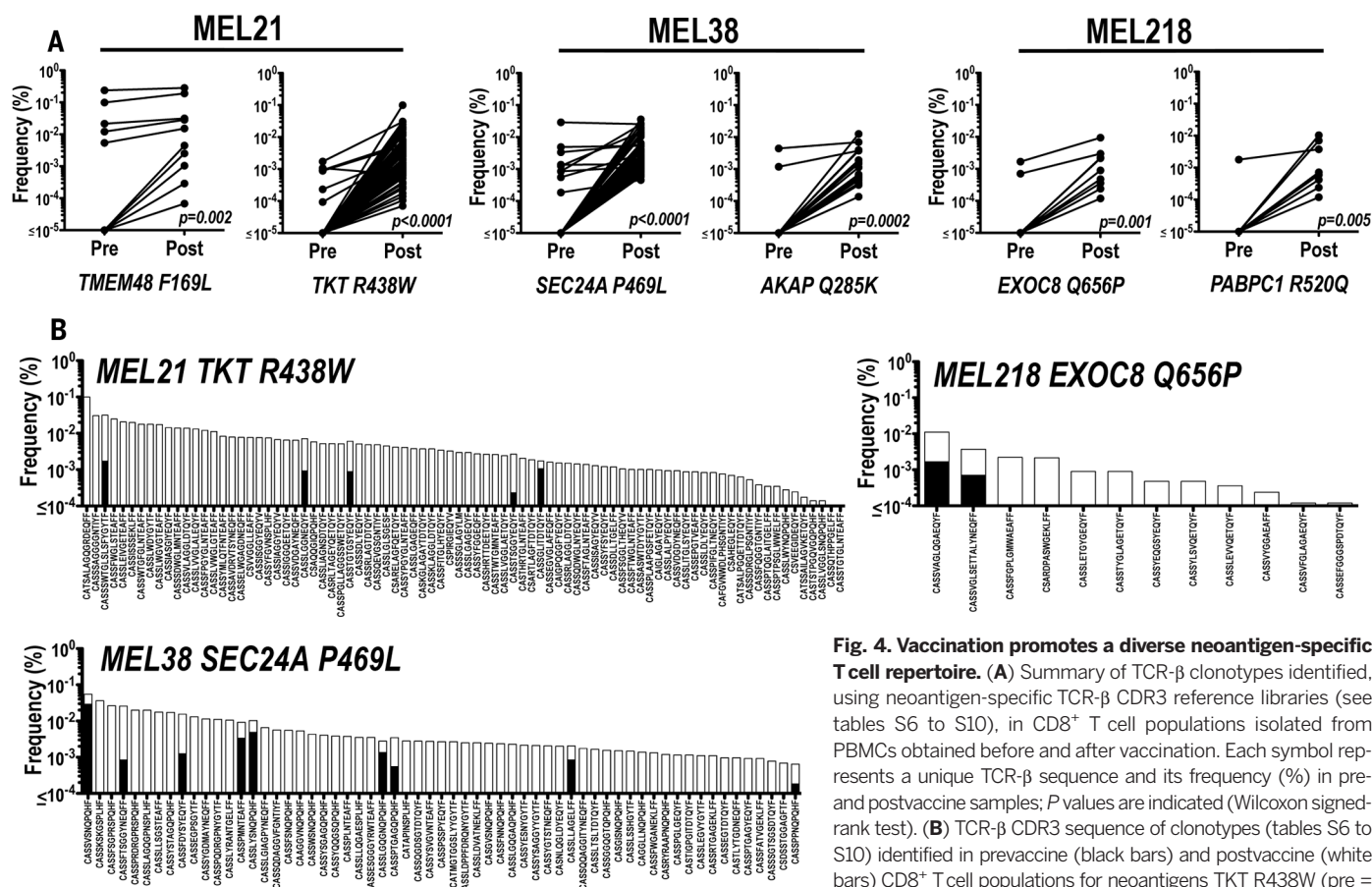
Fig. 4. Vaccination promotes a diverse neoantigen-specific T cell repertoire. (**A**) Summary of TCR-β clonotypes identified, using neoantigen-specific TCR-β CDR3 reference libraries (see tables S6 to S10), in CD8+ T cell populations isolated from PBMCs obtained before and after vaccination. Each symbol represents a unique TCR-β sequence and its frequency (%) in pre- and postvaccine samples; P values are indicated (Wilcoxon signed-rank test). (**B**) TCR-β CDR3 sequence of clonotypes (tables S6 to S10) identified in prevaccine (black bars) and postvaccine (white bars) CD8+ T cell populations for neoantigens TKT R438W (pre = 5, post = 84 clonotypes), SEC24A P469L (pre = 9, post = 61), and EXOC8 Q656P (pre = 2, post = 12). Frequency of each unique clonotype is reported as percentage of total read counts.

demonstrated the HLA-A*02:01 presentation of subdominant neoantigen PABPC1 R520Q (Fig. 3, E to H). Together, these results show that two of the seven neoantigens included in patient MEL218 vaccine, along with antigen controls WNV SVG9 and G280 (fig. S8), are processed and presented in the context of HLA-A*02:01 molecules.

Little is known about the composition and diversity of neoantigen-specific T cells (20, 21) or about the effect vaccination may have on these repertoires. To address this question, we generated reference T cell receptor–β (TCR-β) complementarity-determining region 3 (CDR3) sequence libraries (fig. S9 and tables S6 to S10) from short-term expanded sorted neoantigen-specific T cells (97 to 99% dextramer-positive; fig. S10) and used them to characterize neoantigen TCR-β clonotypes in purified CD8+ T cells isolated from pre- and postvaccine PBMC samples (22–24). In prevaccination CD8+ T cell populations, as few as 1 and as many as 10 unique TCR-β clonotypes per neoantigen were identified (Fig. 4A). Vaccination increased the frequency of most existing prevaccine TCR-β clonotypes and revealed previously undetected clonotypes for all six neoantigens (Fig. 4A). For both dominant and subdominant neoantigens, the TCR-β repertoire was increased significantly after vaccination (Fig. 4). For example, 84 clonotypes representing 19 TCR-β families were detected

for TKT R438W, 61 clonotypes representing 12 TCR-β families were detected for SEC24A P469L, and 12 clonotypes representing 8 TCR-β families were detected for EXOC8 Q656P (Fig. 4B). Thus, peptide vaccination with functionally mature dendritic cells may promote the expansion of a highly diverse neoantigen TCR repertoire.

Our results indicate that vaccination with high-affinity, patient-specific, tumor-derived mutant peptides augments T cell immunity directed at naturally occurring (dominant) neoantigens and expands the breadth of the antitumor immune response by revealing subdominant neoantigens (25). Vaccination against tumor neoantigens appears safe, as all three patients are alive and well with no autoimmune adverse events. Inclusion of subdominant neoantigens into any therapeutic strategy would be expected to exert pressure to reduce the selection of antigen loss variants, especially in the setting of clonal tumor evolution (26), which occurs with targeted agents such as BRAF inhibition in melanoma (27, 28). The revelation of a highly diverse TCR-β repertoire specific for dominant and subdominant neoantigens was surprising and points to a potentially rich pool of naïve tumor-specific T cells that remain ignorant unless activated by vaccination. The effect of prior ipilimumab exposure on the prevaccine T cell repertoire in the three patients reported is un-

known. However, recent data (29) indicate that administration of a CTLA-4 monoclonal antibody can influence TCR repertoire diversity in patients; this finding suggests a therapeutic strategy of testing checkpoint inhibitors, including ipilimumab, together with neoantigen vaccine formulations in order to further improve clinical outcomes. The paradigm described above could be applied to other malignancies presenting high mutational burdens, such as lung, bladder, and colorectal cancers (1). Other categories of genomic alterations such as deletions, insertions, and frameshift mutations may also generate potential neoantigens; mining these neoantigens may be particularly relevant in malignancies with low mutational burden, such as leukemias (30). Personalized immunotherapies targeting private somatic tumor alterations may become feasible in the near future.

REFERENCES AND NOTES

1. L. B. Alexandrov et al., Nature **500**, 415–421 (2013).
2. M. S. Lawrence et al., Nature **505**, 495–501 (2014).
3. T. Wölfel et al., Science **269**, 1281–1284 (1995).
4. P. G. Coulie et al., Proc. Natl. Acad. Sci. U.S.A. **92**, 7976–7980 (1995).
5. N. van Rooij et al., J. Clin. Oncol. **31**, e439–e442 (2013).
6. P. F. Robbins et al., Nat. Med. **19**, 747–752 (2013).
7. B. M. Carreno et al., J. Clin. Invest. **123**, 3383–3394 (2013).

8. M. Nielsen et al., Protein Sci. **12**, 1007–1017 (2003).
9. C. R. Cabanski et al., J. Mol. Diagn. **16**, 440–451 (2014).
10. J. Elvin, C. Potter, T. Elliott, V. Cerundolo, A. Townsend, J. Immunol. Methods **158**, 161–171 (1993).
11. R. Buchli et al., Biochemistry **44**, 12491–12507 (2005).
12. B. M. Carreno et al., J. Immunol. **188**, 5839–5849 (2012).
13. Y. Kim, A. Sette, B. Peters, J. Immunol. Methods **374**, 62–69 (2011).
14. W. H. Fridman, F. Pagès, C. Sautès-Fridman, J. Galon, Nat. Rev. Cancer **12**, 298–306 (2012).
15. T. L. Darrow, C. L. Slingluff Jr., H. F. Seigler, J. Immunol. **142**, 3329–3335 (1989).
16. C. P. McMurtrey et al., Proc. Natl. Acad. Sci. U.S.A. **105**, 2981–2986 (2008).
17. A. L. Cox et al., Science **264**, 716–719 (1994).
18. E. E. Sercarz et al., Annu. Rev. Immunol. **11**, 729–766 (1993).
19. E. Assarsson et al., J. Immunol. **178**, 7890–7901 (2007).
20. A. Gros et al., J. Clin. Invest. **124**, 2246–2259 (2014).
21. E. Tran et al., Science **344**, 641–645 (2014).
22. H. Robins et al., J. Immunol. Methods **375**, 14–19 (2012).
23. A. Lossius et al., Eur. J. Immunol. **44**, 3439–3452 (2014).
24. H. S. Robins et al., Sci. Transl. Med. **5**, 214ra169 (2013).
25. P. G. Coulie, B. J. Van den Eynde, P. van der Bruggen, T. Boon, Nat. Rev. Cancer **14**, 135–146 (2014).
26. M. Gerlinger et al., Annu. Rev. Genet. **48**, 215–236 (2014).
27. E. Shi et al., Cancer Discov. **4**, 80–93 (2014).
28. E. M. Van Allen et al., Cancer Discov. **4**, 94–109 (2014).
29. E. Cha et al., Sci. Transl. Med. **6**, 238ra70 (2014).
30. M. Rajasagi et al., Blood **124**, 453–462 (2014).

CENTROSOMES

Regulated assembly of a supramolecular centrosome scaffold in vitro

Jeffrey B. Woodruff,[1]* Oliver Wueseke,[1]* Valeria Viscardi,[2] Julia Mahamid,[3] Stacy D. Ochoa,[2] Jakob Bunkenborg,[4,5] Per O. Widlund,[1]† Andrei Pozniakovsky,[1] Esther Zanin,[2]‡ Shirin Bahmanyar,[2]§ Andrea Zinke,[1] Sun Hae Hong,[6] Marcus Decker,[1]‖ Wolfgang Baumeister,[3] Jens S. Andersen,[5] Karen Oegema,[2]¶ Anthony A. Hyman[1]¶

The centrosome organizes microtubule arrays within animal cells and comprises two centrioles surrounded by an amorphous protein mass called the pericentriolar material (PCM). Despite the importance of centrosomes as microtubule-organizing centers, the mechanism and regulation of PCM assembly are not well understood. In *Caenorhabditis elegans*, PCM assembly requires the coiled-coil protein SPD-5. We found that recombinant SPD-5 could polymerize to form micrometer-sized porous networks in vitro. Network assembly was accelerated by two conserved regulators that control PCM assembly in vivo, Polo-like kinase-1 and SPD-2/Cep192. Only the assembled SPD-5 networks, and not unassembled SPD-5 protein, functioned as a scaffold for other PCM proteins. Thus, PCM size and binding capacity emerge from the regulated polymerization of one coiled-coil protein to form a porous network.

Pericentriolar material (PCM), a matrix of proteins that regulates microtubule nucleation, anchoring, and dynamics (1, 2), assembles around centrioles to form centrosomes that contribute to cell division. The PCM scaffold is thought to form via the assembly of coiled-coil proteins [pericentrin and Cdk5RAP2/centrosomin in vertebrates and *Drosophila,* and SPD-5 in *Caenorhabditis elegans* (3–8)]. PCM expansion during mitotic entry requires SPD-2/Cep192 and is regulated by mitotic kinases, including the Polo family kinase Plk1 (9–13). However, the mechanism of PCM assembly remains unclear, partly due to the lack of an in vitro system.

In *C. elegans,* PCM assembly requires SPD-5, a protein with nine predicted coiled-coil domains (Fig. 1A) (7). Because coiled-coil domains often mediate homo-oligomerization (14), we hypothesized that SPD-5 self-association could underlie PCM assembly. To test this idea, we purified full-length, green fluorescent protein (GFP)–labeled SPD-5 (SPD-5::GFP) from baculovirus-infected insect cells (Fig. 1, A and B) (fig. S1A shows all proteins used in this study). Using total internal reflection microscopy to count GFP moieties in SPD-5::GFP particles by photobleaching revealed that SPD-5::GFP initially exists as monomers and dimers (Fig. 1C), consistent with in vivo data (15). To determine whether SPD-5 could form larger assemblies, we shifted SPD-5::GFP from ice to 23°C and observed samples with widefield fluorescence microscopy. After 120 min, 25 nM SPD-5::GFP assembled into dense structures spanning several micrometers that we term "networks" (Fig. 1D); similar assemblies were observed by phase contrast microscopy using untagged SPD-5 (fig. S1B). Network formation decreased with lower initial SPD-5::GFP concentrations (Fig. 1D). Temporal analysis using 25 nM SPD-5::GFP revealed single puncta that grew into extended meshworks (Fig. 1E); separate networks could also be observed coalescing during assembly (fig. S1C). SPD-5 networks readily dissolved after dilution or mechanical disruption, indicating that network formation is reversible (fig. S1D).

We calculated total SPD-5 network mass per sample by summing the integrated fluorescence intensity of all SPD-5::GFP networks (up to 200,000 per sample) in the imaged area (Fig. 1F). We also calculated the size distribution of the networks in each sample (fig. S1E). The kinetics of SPD-5::GFP network formation fit a sigmoidal curve typical of growing polymers, including a characteristic lag time and plateau (Fig. 1F). Thus, SPD-5 alone can polymerize in vitro in a concentration and time-dependent manner to form extended networks that reach sizes comparable to fully expanded PCM in vivo (11). Low-magnification cryo-electron microscopy of SPD-5 networks revealed dense, amorphous assemblies interspersed

[1]Max Planck Institute of Molecular Cell Biology and Genetics, Pfotenhauerstrasse 108, 01307 Dresden, Germany. [2]Department of Cellular and Molecular Medicine, Ludwig Institute for Cancer Research, University of California, San Diego, La Jolla, CA 92093, USA. [3]Department of Molecular Structural Biology, Max Planck Institute of Biochemistry, Martinsried 82152, Germany. [4]Department of Clinical Biochemistry, Copenhagen University Hospital, Hvidovre 2650, Denmark. [5]Department of Biochemistry and Molecular Biology, University of Southern Denmark, Odense, Denmark. [6]Department of Molecular and Cell Biology, University of California, Berkeley, Berkeley, CA 94720, USA.
*These authors contributed equally to this work. †Present address: Department of Chemistry and Molecular Biology, University of Gothenburg, Medicinaregatan 9 c, 40530 Gothenburg, Sweden ‡Present address: Department of Biology II, Cell and Developmental Biology, Ludwig-Maximilians-Universität München, Martinsried, Germany §Present address: Department of Molecular, Cell, and Developmental Biology, Yale University, 219 Prospect St., New Haven, CT 06520, USA ‖Present address: Department of Research Oncology, Genentech, 1 DNA Way South San Francisco, CA 94080, USA. ¶Corresponding author. E-mail: hyman@mpi-cbg.de (A.A.H.); koegema@ucsd.edu (K.O.)

with pores of various sizes (Fig. 2A); the assemblies lacked any distinct organization at higher magnification (Fig. 2B).

In vertebrate cells, Plk1 is required for the expansion and maintenance of the mitotic PCM (12, 13, 16–19). To determine whether *C. elegans* PLK-1 has a similar regulatory role, we constructed strains deleted for the endogenous *plk1 gene* that also expressed either wild-type PLK-1 (PLK-1^WT)

or an analog-sensitive PLK-1 mutant (PLK-1^AS) that can be inhibited by the drug 1NM-PP1 (20) (fig. S2A). Monitoring recruitment of the PCM marker GFP::γ-tubulin revealed that addition of 1NM-PP1 in S phase abolished mitotic GFP::γ-tubulin accumulation in embryos expressing PLK-1^AS but not PLK-1^WT (Fig. 3A). Addition of 1NM-PP1 to embryos arrested in mitosis also led to loss of GFP::γ-tubulin only in embryos expressing PLK-1^AS

(fig. S2B). Thus, PLK-1 activity is required for both assembly and maintenance of the mitotic PCM.

PLK-1 could control PCM assembly by phosphorylating SPD-5 to promote its polymerization. Consistent with this hypothesis, centrosomal SPD-5 accumulation was impaired in *plk-1(RNAi)* embryos (fig. S2C). Immunoprecipitation of SPD-5 from worm embryo extracts followed by mass spectrometry identified 19 phosphorylation sites
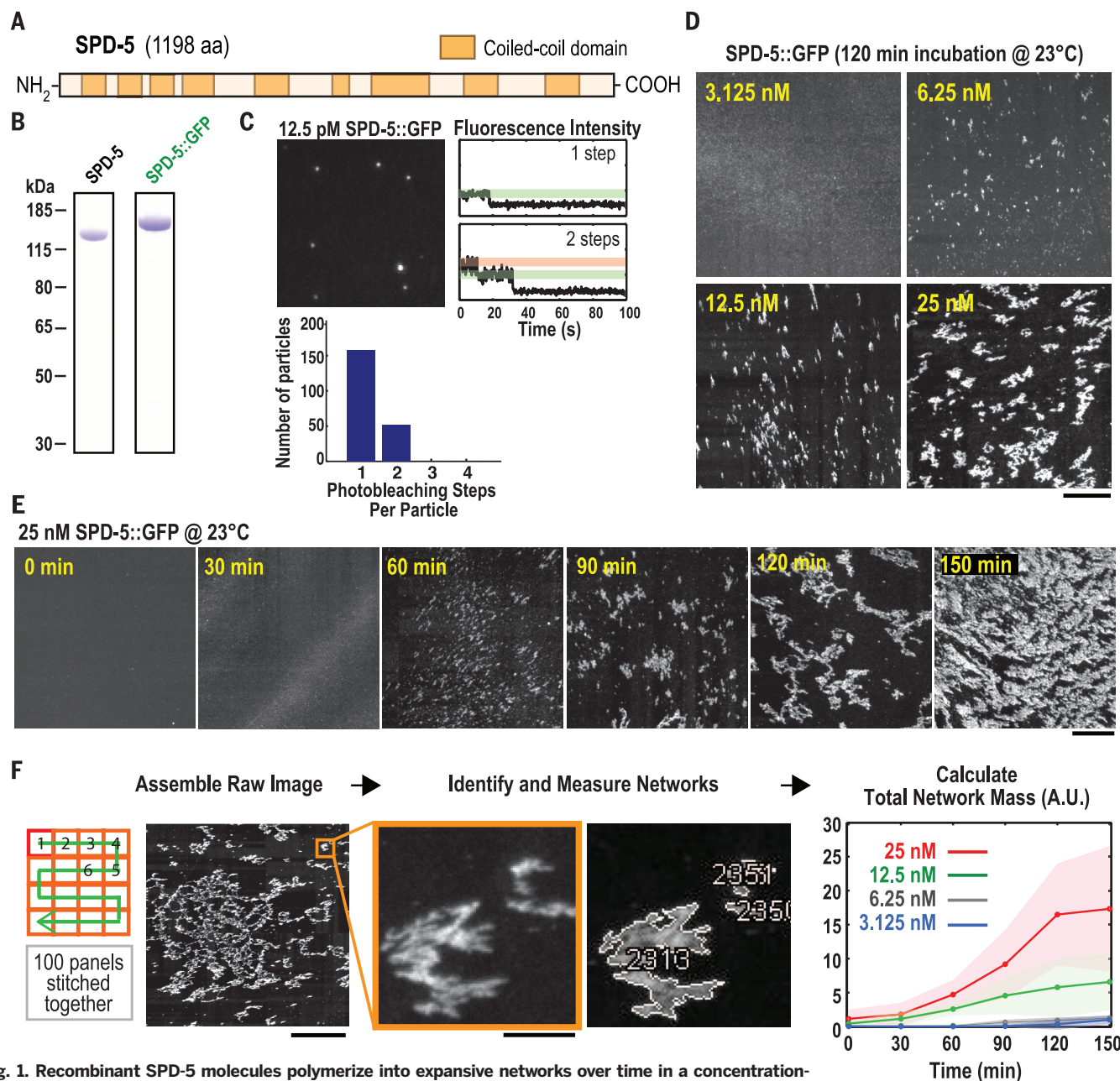
Fig. 1. Recombinant SPD-5 molecules polymerize into expansive networks over time in a concentration-dependent manner in vitro. (**A**) SPD-5 sequence with coiled-coil domains predicted by the MARCOIL algorithm (*31*) at 90% threshold. (**B**) Coomassie-stained gels depicting purified full-length SPD-5 and SPD-5::GFP. (**C**)12.5 pM SPD-5::GFP was squashed under a coverslip and imaged continuously by total internal reflection microscopy. The intensity of each fluorescent spot was measured over time, and photobleaching steps per spot were counted (*n* = 210). Representative photobleaching profiles are shown. Scale bar, 5 μm. (**D**) Visualization of different concentrations of SPD-5::GFP after 120 min. Scale bar, 25 μm. (**E**) 25 nM SPD-5::GFP was incubated at 23°C, then squashed under a coverslip at 30-min intervals. Scale bar, 25 μm. (**F**) Flowchart of automated SPD-5::GFP network quantification. For each sample, 100 images were collected and stitched together, a threshold was applied, and the networks were identified and measured. The graph plots the integrated intensity of all networks (total network mass) per sample at each time point [*n* = 4 to 10; mean with 95% confidence intervals (CIs)]. Scale bars, 25 μm (first panel), 2.5 μm (inset).
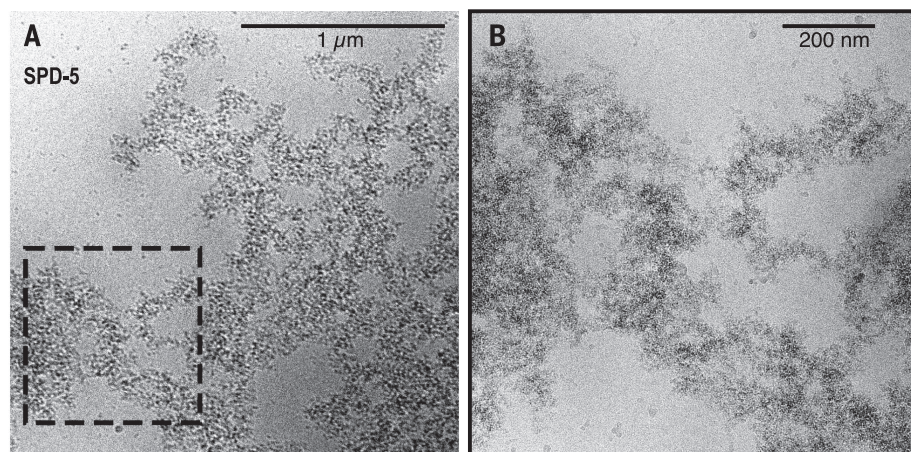
Fig. 2. High-resolution imaging of SPD-5 networks with cryo-electron microscopy. (**A**) Cryo-electron microscopy image of untagged SPD-5. (**B**) Higher magnification view.

(table S3). Among others, three central residues (S530, S627, and S658) were identified as likely to be PLK-1 target sites (Fig. 3B and table S2) (*21*). Residue S653 was also predicted to be a PLK-1 phosphorylation site, but we could not confirm its phosphorylation status. To investigate the importance of these residues, we generated RNA interference (RNAi)–resistant transgenes encoding GFP fusions with wild-type SPD-5 (GFP::SPD-5^WT) or with a mutant in which S530, S627, S653, and S658 were mutated to alanine (GFP::SPD-5^4A) (fig. S3A). Both transgenes were expressed at similar levels (fig. S3B). All subsequent experiments were performed after RNAi silencing of endogenous *spd-5* to ensure that the RNAi-resistant transgenes were the sole source of SPD-5 (fig. S3C).

In embryos expressing GFP::SPD-5^WT, centrioles entering the embryo during fertilization rapidly acquired a small shell of GFP::SPD-5^WT, and the PCM expanded as cells progressed into mitosis (Fig. 3C). In embryos expressing GFP::SPD-5^4A, centrioles acquired a small shell of GFP::SPD-5^4A,

Fig. 3. PLK-1 phosphorylation of SPD-5 drives PCM assembly in vivo and SPD-5 polymerization in vitro. (**A**) *plk-1*^WT (*n* = 9) and *plk-1*^AS (*n* = 13) embryos expressing the PCM marker GFP::γ-tubulin were visualized by fluorescence confocal microscopy (orange dashed line is embryo outline). 10 μM 1-NM-PP1 (PLK-1^AS inhibitor) was added to permeabilized embryos before mitotic entry (red arrow). Scale bars, 10 μm (**B**) Diagram of phospho-epitopes on SPD-5 and different mutant constructs. Canonical PLK-1 consensus motifs (*32, 33*) are indicated in red. The arrowheads indicate the phosphorylated residue in each motif. The complete set of phosphorylation sites identified by tandem mass spectrometry is included in table S3. (**C**) Centrosome size was visualized in embryos expressing RNAi-resistant GFP::SPD-5^WT or GFP::SPD-5^4A. Images are sum intensity projections from *z* stacks. Scale bar, 10 μm. See also fig. S3. (**D**) In vitro kinase assay. SPD-5^WT::GFP was incubated with buffer alone, PLK-1^WT, or a kinase-dead version of PLK-1 (PLK-1^KD). Phosphorylation at serine 530 was detected by Western blot using a phospho-specific antibody. (**E**) Kinetics of 6.25 nM SPD-5^WT::GFP network formation in vitro. Values represent mean with 95% CIs (*n* = 8 to 14). (**F**) Representative images of SPD-5::GFP networks from (E). Scale bar, 25 μm. (**G**) A phosphomimetic version of SPD-5 (SPD-5^4E::GFP) already formed networks at *t* = 0 min, bypassing the need for incubation at room temperature. Scale bar, 25 μm.

but the PCM failed to expand (Fig. 3C and fig. S3, D and E), similar to the *plk-1(RNAi)* phenotype (fig. S2C). γ-tubulin recruitment was also impaired, and centrosomes failed to separate (fig. S3, F and G). Consistent with an essential role in vivo, PLK-1 could also phosphorylate SPD-5 in vitro. An antibody raised against phosphorylated S530 recognized SPD-5 after incubation with PLK-1 and adenosine triphosphate (ATP), but not if S530 was mutated to alanine (SPD-5[1A]) or if a kinase-dead version of PLK-1 (PLK-1[KD]) was used (Fig. 3D). Additionally, a pan-phospho-specific antibody recognized previously dephosphorylated SPD-5 only after incubation with PLK-1 and ATP (fig. S5A). To investigate the relative importance of the four PLK-1 phosphorylation sites, we mutated S530, S627, S653, and S658 to alanine individually. Only the S658A mutant appreciably reduced PCM assembly (fig. S4). A double S653A S658A mutant reduced PCM assembly to an extent comparable to the 4A mutant (fig. S4). Thus, S658 is the most important site in this region, and phosphorylation of S653 can partially compensate when S658 cannot be phosphorylated. Phosphorylations on S530 and S627 are not essential but could also have redundant roles. Although these results suggest that phosphorylation of SPD-5 on these central sites controls mitotic PCM expansion, they do not exclude the possibility that a second PLK-1–based mechanism governs γ-tubulin maintenance.

Our results suggest that phosphorylation of SPD-5 by PLK-1 is required for PCM expansion in vivo. We therefore wanted to determine whether phosphorylation by PLK-1 would also promote SPD-5::GFP network formation in vitro. For all subsequent growth experiments, an initial concentration of 6.25 nM SPD-5::GFP was used. In the absence of PLK-1, SPD-5[WT]::GFP networks appeared after 90 min. Addition of 6.25 nM PLK-1 and 0.2 mM ATP enhanced network formation, such that SPD-5 networks appeared after 30 min (Fig. 3, E and F). This stimulation was abrogated when the 4A mutant (SPD-5[4A]::GFP) was used (Fig. 3, E and F). SPD-5[WT]::GFP and SPD-5[4A]::GFP polymerized similarly in the absence of PLK-1, indicating that, although insensitive to the effects of PLK-1, SPD-5[4A]::GFP is otherwise functional (fig. S5B). Although SPD-5[4A]::GFP formed networks at later time points in vitro, centrosomes did not expand in cells expressing the 4A mutant in vivo (Fig. 3C). This could be due to the short duration of the *C. elegans* embryo cell cycle. A SPD-5 mutant harboring four phosphomimetic mutations (SPD-5[4E]::GFP) (Fig. 3B) already formed networks at t = 0 min, suggesting that phosphorylation at these four residues is sufficient to catalyze SPD-5 polymerization (Fig. 3G). Thus, PLK-1 enhances SPD-5 polymerization through direct phosphorylation in vitro.

SPD-2/Cep192 has a conserved role in PCM assembly (9, 10, 22–25), yet its precise role remains unclear. We therefore addressed the role of *C. elegans* SPD-2 in PCM formation using our in vitro system. Addition of 12.5 nM purified full-length SPD-2 enhanced SPD-5::GFP network assem-

bly, such that networks were seen after 60 min (Fig. 4, A and B), indicating that SPD-2 by itself can promote SPD-5 polymerization. Simultaneous addition of 6.25 nM PLK-1 and 12.5 nM SPD-2 enhanced SPD-5::GFP network formation beyond what was observed by adding either PLK-1 or SPD-2 alone (Fig. 4A and fig. S6A). Thus, SPD-2 and PLK-1 cooperatively enhance SPD-5 polymerization in vitro, consistent with the essential roles for both proteins in PCM expansion in vivo.

In vivo, loss of SPD-5 abolishes recruitment of all known PCM proteins, suggesting that SPD-5 forms the structural framework of the PCM (7). To determine whether in vitro–assembled SPD-5 networks could serve as scaffolds for the recruitment of other PCM proteins, we observed SPD-5::TagRFP networks assembled in the presence of fluorescently labeled PLK-1 and SPD-2. PLK-1::GFP and GFP::SPD-2 were both recruited to SPD-5::TagRFP networks independently of each other (Fig. 4C). Purified γ-tubulin and four noncentrosomal proteins were not recruited to SPD-5::TagRFP networks (fig. S6, B and C), demonstrating that the association of PLK-1 and SPD-2 with SPD-5 networks is specific. Alexa405-labeled PLK-1 and GFP::SPD-2 were simultaneously recruited to the same networks (Fig. 4D). Thus, PLK-1 and SPD-2 can exist concomitantly on SPD-5 networks, and their localization is not interdependent.

Structured illumination microscopy revealed that non–network-associated SPD-5::TagRFP particles did not colocalize with either PLK-1::GFP
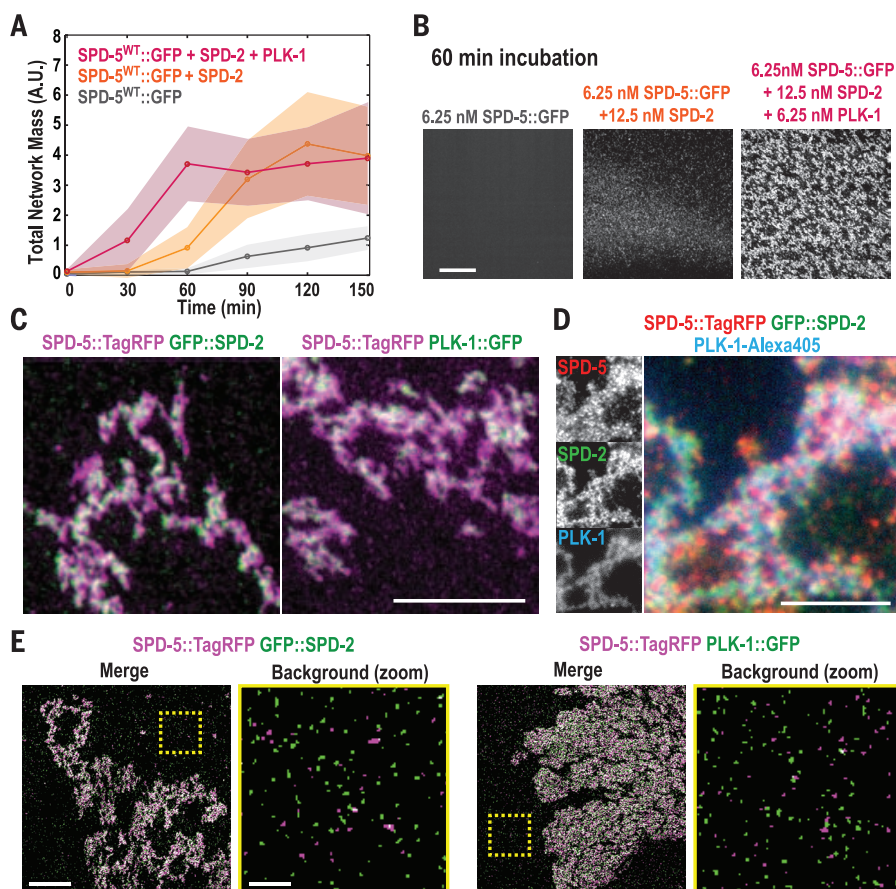
Fig. 4. SPD-2 and PLK-1 independently bind to SPD-5::GFP networks and cooperatively stimulate network formation in vitro. (**A**) Kinetics of 6.25 nM SPD-5::GFP network formation in the presence of 12.5 nM SPD-2 and/or 6.25 nM PLK-1. Values represent mean with 95% CIs (n = 8 to 14). (**B**) Representative images of SPD-5::GFP networks from (A) after 60 min. Scale bar, 25 μm. (**C**) Dual-color images of SPD-5::TagRFP networks assembled in the presence of GFP::SPD-2 or PLK-1::GFP. Scale bar, 5 μm. See also fig. S6. (**D**) Triple-color images of SPD-5::TagRFP networks assembled in the presence of GFP::SPD-2 and PLK-1-Alexa405. Scale bar, 5 μm. (**E**) Co-localization analysis using structured illumination microscopy. For each image pair, the right panel depicts a zoomed-in image of the non–network-assembled SPD-5::TagRFP particles selected from the area bounded by the yellow box. Scale bar, 5 μm (left panel), 1 μm (zoomed in, right panel).

or GFP::SPD-2 (Fig. 4E), suggesting that only the network-assembled form of SPD-5 can bind to PLK-1 and SPD-2. To further test this possibility, we determined the amount of SPD-2 or PLK-1 that coprecipitated with beads coated with nonassembled SPD-5. As expected, we did not detect enrichment in the amount of SPD-2 or PLK-1 pulled down by the SPD-5–coated beads as compared with the control beads (fig. S6D). Thus, SPD-5 networks, rather than unassembled SPD-5 molecules, serve as scaffolds for the recruitment of SPD-2 and PLK-1 in vitro. Indeed, a recent study shows that SPD-5, SPD-2, and PLK-1 do not interact before their incorporation into the PCM in living embryos (15). Yeast two-hybrid analysis has shown that a SPD-5 fragment can interact with SPD-2 (26). In light of our findings, it is possible that this interaction domain is blocked when SPD-5 is monomeric but becomes accessible when SPD-5 molecules assemble into a network.

In summary, we have developed an in vitro system for studying regulated PCM assembly. The coiled-coil protein SPD-5 can polymerize into interconnected, porous networks that specifically recruit downstream PCM proteins such as PLK-1, SPD-2, and ZYG-9 (chTOG homolog) (fig. S6, B and C). Thus, SPD-5 networks are likely to represent the structural framework of the PCM. PLK-1 kinase directly phosphorylates SPD-5 to promote its polymerization and mitotic PCM expansion, and SPD-2 makes an additional independent contribution to PCM assembly. Consistent with our findings for *C. elegans* SPD-5, PCM formation in *Drosophila* requires SPD-2 and Polo kinase phosphorylation at multiple sites on centrosomin (Cdk5RAP2) (27, 28). Like SPD-5, centrosomin is a large coiled-coil protein that recruits downstream PCM proteins (7, 27–30). Thus, SPD-2/Polo kinase-driven polymerization of a scaffolding component is a conserved mechanism for PCM assembly.

REFERENCES AND NOTES

1. E. A. Nigg, J. W. Raff, *Cell* **139**, 663–678 (2009).
2. J. B. Woodruff, O. Wueseke, A. A. Hyman, *Phil. Trans. R. Soc. B* **369**, 1–10 (2014).
3. J. B. Dictenberg et al., *J. Cell Biol.* **141**, 163–174 (1998).
4. W. C. Zimmerman, J. Sillibourne, J. Rosa, S. J. Doxsey, *Mol. Biol. Cell* **15**, 3642–3657 (2004).
5. J. J. Buchman et al., *Neuron* **66**, 386–402 (2010).
6. P. T. Conduit et al., *Curr. Biol.* **20**, 2178–2186 (2010).
7. D. R. Hamill, A. F. Severson, J. C. Carter, B. Bowerman, *Dev. Cell* **3**, 673–684 (2002).
8. M. Martinez-Campos, R. Basto, J. Baker, M. Kernan, J. W. Raff, *J. Cell Biol.* **165**, 673–683 (2004).
9. L. Pelletier et al., *Curr. Biol.* **14**, 863–873 (2004).
10. C. A. Kemp, K. R. Kopish, P. Zipperlen, J. Ahringer, K. F. O'Connell, *Dev. Cell* **6**, 511–523 (2004).
11. M. Decker et al., *Curr. Biol.* **21**, 1259–1267 (2011).
12. H. A. Lane, E. A. Nigg, *J. Cell Biol.* **135**, 1701–1713 (1996).
13. L. Haren, T. Stearns, J. Lüders, *PLOS ONE* **4**, e5976 (2009).
14. A. Lupas, J. M. Van Dyke, J. Stock, *Science* **252**, 1162–1164 (1991).
15. O. Wueseke et al., *Mol. Biol. Cell* **25**, 2984–2992 (2014).
16. I. Sumara et al., *Curr. Biol.* **14**, 1712–1722 (2004).
17. P. Lénárt et al., *Curr. Biol.* **17**, 304–315 (2007).
18. A. Santamaria et al., *Mol. Biol. Cell* **18**, 4024–4036 (2007).
19. K. Lee, K. Rhee, *J. Cell Biol.* **195**, 1093–1101 (2011).
20. A. C. Bishop et al., *Nature* **407**, 395–401 (2000).
21. Z. Liu et al., *Brief. Bioinform.* **14**, 344–360 (2013).
22. C. I. Dix, J. W. Raff, *Curr. Biol.* **17**, 1759–1764 (2007).
23. M. G. Giansanti, E. Bucciarelli, S. Bonaccorsi, M. Gatti, *Curr. Biol.* **18**, 303–309 (2008).
24. M. A. Gomez-Ferreria et al., *Curr. Biol.* **17**, 1960–1966 (2007).
25. F. Zhu et al., *Curr. Biol.* **18**, 136–141 (2008).
26. M. Boxem et al., *Cell* **134**, 534–545 (2008).
27. P. T. Conduit et al., *eLife* **3**, e03399 (2014).
28. P. T. Conduit et al., *Dev. Cell* **28**, 659–669 (2014).
29. T. L. Megraw, K. Li, L. R. Kao, T. C. Kaufman, *Development* **126**, 2829–2839 (1999).
30. E. P. Lucas, J. W. Raff, *J. Cell Biol.* **178**, 725–732 (2007).
31. M. Delorenzi, T. Speed, *Bioinformatics* **18**, 617–625 (2002).
32. A. Santamaria et al., *Mol. Cell. Proteomics* **10**, M110.004457 (2011).
33. K. Grosstessner-Hain et al., *Mol. Cell. Proteomics* **10**, M111.008540 (2011).

NONCODING RNA

piRNA-guided slicing specifies transcripts for Zucchini-dependent, phased piRNA biogenesis

Fabio Mohn,* Dominik Handler,* Julius Brennecke†

In animal gonads, PIWI-clade Argonaute proteins repress transposons sequence-specifically via bound Piwi-interacting RNAs (piRNAs). These are processed from single-stranded precursor RNAs by largely unknown mechanisms. Here we show that primary piRNA biogenesis is a 3′-directed and phased process that, in the *Drosophila* germ line, is initiated by secondary piRNA-guided transcript cleavage. Phasing results from consecutive endonucleolytic cleavages catalyzed by Zucchini, implying coupled formation of 3′ and 5′ ends of flanking piRNAs. Unexpectedly, Zucchini also participates in 3′ end formation of secondary piRNAs. Its function can, however, be bypassed by downstream piRNA-guided precursor cleavages coupled to exonucleolytic trimming. Our data uncover an evolutionarily conserved piRNA biogenesis mechanism in which Zucchini plays a central role in defining piRNA 5′ and 3′ ends.

The Piwi-interacting RNA (piRNA) pathway silences transposable elements (TEs) during animal gametogenesis. This pathway uses PIWI-clade Argonaute proteins bound to piRNAs that are ~23 to 30 nucleotides (nt) long; these piRNAs act as sequence-specific guides to specify targets via base-pair complementarity (1, 2). piRNAs are processed from single-stranded precursor transcripts via two biogenesis pathways, both of which are initiated by endonucleolytic definition of piRNA 5′ ends: 5′ ends of primary piRNAs (mostly loaded into *Drosophila* Piwi) are generated by Zucchini (3–8). They carry a 5′ uridine (1U) but otherwise appear to be derived randomly from their precursors (9–13). 5′ ends of secondary piRNAs [loaded into *Drosophila* Aubergine/Argonaute3 (Aub/AGO3)] are specified via piRNA-guided slicing. Here, reciprocal cleavages of complementary transcripts (ping-pong cycle) define piRNA pairs, whose 5′ ends display a 10-nt offset (14, 15). piRNA 3′ ends lack a nucleotide preference, and the molecular events underlying their formation are elusive. It is thought that after 5′ end definition, longer piRNA intermediates are loaded into PIWI proteins (16) and subsequently trimmed at their 3′ ends to mature piRNAs (17).

How are transcripts selected as piRNA biogenesis substrates? We noticed ectopic piRNA production from mRNAs in fly ovaries mutant for the Rhino-Deadlock-Cutoff complex (18–20). The corresponding piRNA profiles initiate abruptly (e.g., *row*) (Fig. 1, A and B), and some of these initiation sites are also apparent in wild-type (WT) ovaries [green fluorescent protein (GFP) control]. Consistent with suggestions that piRNA-guided transcript cleavage initiates 3′-directed piRNA biogenesis (21), we identified a target site in the *row* transcript with complementarity to a *1360* transposon piRNA (trigger-piRNA) (Fig. 1C). The 5′ end of this piRNA maps 10 nt away from the 5′ end of the most abundant *row* piRNA (responder-piRNA). Whereas the *1360* trigger-piRNA occupies

Institute of Molecular Biotechnology of the Austrian Academy of Sciences (IMBA), Dr. Bohrgasse 3, 1030 Vienna, Austria.
*These authors contributed equally to this work. †Corresponding author. E-mail: julius.brennecke@imba.oeaw.ac.at

Aub and AGO3 equally, the *row* responder-piRNA resides mostly in Aub (Fig. 1, B and C) (*22*). In contrast, *row* piRNAs originating downstream of the responder-piRNA (trail-piRNAs) occupy Piwi and, only to a small extent, Aub (Fig. 1B). We identified 570 mRNAs with similar characteristics. On average, responder-piRNAs predominantly populate Aub but are also present in AGO3 and Piwi (Fig. 1D). Trail-piRNAs instead are funneled into Piwi (~85%) and moderately into Aub (~15%) but not into AGO3. When considering all piRNAs mapping within 200 nt downstream of the trigger site, 70% of Aub/AGO3-bound piRNAs, but only 7% of Piwi-bound piRNAs, correspond to the responder-piRNA (Fig. 1D).

Only 8% of the 570 triggered transcripts harbor fully complementary target sites for Aub/AGO3-bound piRNAs at the responder position (fig. S1A). However, when allowing up to six mismatches, piRNA 5′ ends exhibit a high likelihood to align precisely 10 nt offset from responder-

piRNA 5′ ends (Fig. 1E). We could identify trigger-piRNAs in ~75% of the cases (fig. S1, B to G) (*22*). Based on this, slicing characteristics of Aub/AGO3 follow known features of Argonaute proteins (*23–25*). Trigger-piRNAs also conform to rules of heterotypic ping-pong (*14, 15*) (fig. S1E).

The 5′ ends of trail-piRNAs are immediately downstream of responder-piRNA 3′ ends (Fig. 1D), and trail-piRNAs in Piwi and Aub display pronounced phasing (Fig. 1F). The phase is ~27 nt, which is precisely one average piRNA length (23 to 30 nt) (Fig. 1F). Both phasing accuracy and piRNA levels decrease with increasing distance from the trigger site, which suggests that piRNA biogenesis occurs in a 3′-directed, processive fashion. To investigate whether slicing generally initiates directional and phased piRNA biogenesis, we analyzed TE-mapping piRNAs from WT ovaries. Piwi/Aub/AGO3-bound piRNAs mapping in the vicinity of abundant ping-pong piRNAs display patterns that are virtually identical to the ones described above

(fig. S2, A and B). Biogenesis of Piwi-bound piRNAs (by definition, primary piRNAs) is therefore largely a consequence of piRNA-guided target cleavage.

To investigate how tight piRNA 3′ end formation is coupled to 5′ end formation of the immediate downstream piRNA, we analyzed piRNA length and 3′ end patterns. On average, piRNAs exhibit a broad length distribution (Fig. 2, A to C) (*14*). We noticed that individual piRNAs sharing the same 5′ end often have distinct length profiles and 3′ ends (fig. S3A). We therefore grouped all piRNAs with unambiguous 5′ ends into length cohorts (Fig. 2, A to C, and fig. S3B) (*22*). Length profiles of AGO3-bound piRNAs are the least defined, whereas those bound to Piwi display the most accurate 3′ ends, irrespective of whether they are processed in the germ line or the soma (fig. S3, C to E). No obvious nucleotide bias within piRNAs correlates with their distinct length groups. However, uridine (U) residues are enriched immediately downstream of dominant piRNA 3′
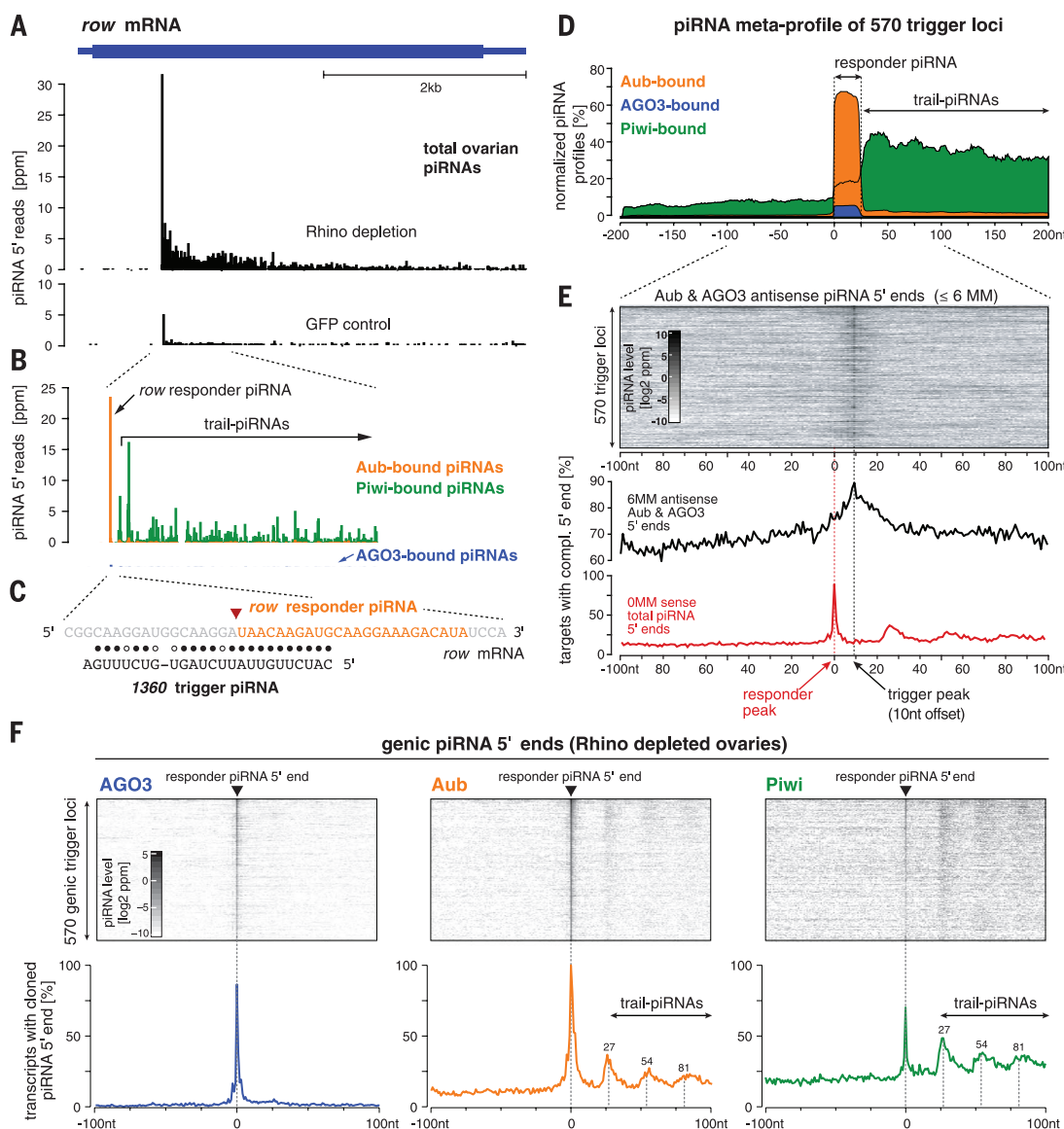
Fig. 1. Aub/AGO3-mediated slicing triggers phased piRNA biogenesis. (**A**) Normalized piRNA populations from Rhino-depleted ovaries or from control ovaries mapping to the *row* mRNA. ppm, parts per million. (**B**) As in (A), but piRNAs bound to Aub/AGO3/Piwi (*22*) are shown individually. (**C**) Alignment of the *1360* trigger-piRNA with the *row* mRNA. The inverted triangle denotes the slicer cleavage position. (**D**) Metaplots showing profiles of Aub/AGO3/Piwi-bound piRNAs (from Rhino-depleted ovaries) at genic trigger sites. Profiles represent the median of normalized values; responder peak: 100%. (**E**) Heat map indicating piRNA levels (Σ Aub/AGO3 5′ ends) mapping antisense (≤six mismatches) to 570 mRNAs with trigger events. Position 0 denotes the responder-piRNA 5′ end. The binary histograms show the percentage of transcripts with a cloned 5′ end of indicated piRNAs mapping in sense/antisense orientation at nucleotide resolution. (**F**) Heat maps indicating AGO3/Aub/Piwi-bound piRNA 5′ end levels from Rhino-depleted ovaries in a window centered on 570 genic responder-piRNAs. The corresponding binary histograms indicate the percentage of transcripts that exhibit a cloned piRNA 5′ end at a given position.

ends (Fig. 2, D and E, and fig. S3, F to J). Length cohorts with two dominant species display a downstream U bias for both prominent 3′ ends (e.g., cluster 7 in fig. S3H and cluster 6 in fig. S3J). The downstream U bias is strongest for Piwi-bound piRNAs and weakest for AGO3-bound piRNAs, where it is only evident for the most accurately defined length populations (Fig. 2E and fig. S3G). As Piwi/Aub-bound piRNAs display a 1U bias and primary piRNAs exhibit strong phasing, the pronounced downstream U bias implies that piRNA 3′ end formation simultaneously specifies the 5′ end of the downstream piRNA. When Piwi-bound piRNAs are aligned at their dominant 3′ ends, neighboring piRNA 5′ ends are highly enriched at the +1 position, irrespective of the tissue (fig. S4A).

To further investigate 3′ end formation, we focused on somatic Piwi-bound piRNAs. We selected the 5000 most abundant TE antisense piRNA 5′ ends, sorted them for their abundance, and displayed 5′ and 3′ ends of all piRNAs mapping in their immediate vicinity (Fig. 2F). The 3′ ends of neighboring piRNAs are enriched precisely 1 nt upstream of selected 5′ ends (position 0, dashed arrow in Fig. 2F). The 5′ ends of downstream piRNAs instead display a fuzzy enrichment around +27 nt (blue arrow head in Fig. 2F). However, re-sorting the heat map according to increasing length of the dominant piRNA species for each 5′ end at position 0 resolves the strong enrichment of 5′ ends precisely 1 nt downstream of the dominant 3′ ends (Fig. 2G and fig. S4B).

The obtained piRNA length cohorts (23 to 29 nt) (Fig. 2G and fig. S4B) display a strong downstream U bias (Fig. 2H). U residues are depleted upstream of 3′ ends of unusually long piRNA cohorts (27 to 29 nt), and an inverse trend is seen for the 23-nt

piRNA cohort. This suggests that 3′ ends of Piwi-bound piRNAs are defined by an endonuclease that cleaves immediately upstream of a U residue and 23 to 30 nt downstream of the piRNA 5′ end. Asymmetrically distributed U residues within the cleavage window force the generation of atypically long or short piRNAs.

To experimentally test the phased biogenesis of primary piRNAs, we generated transgenic flies expressing a piRNA biogenesis reporter harboring a piRNA target site (Fig. 3A). Without a target site, no piRNAs are produced (Fig. 3B). Insertion of a single complementary target site for an Aub/AGO3 piRNA represses GFP expression (fig. S5), triggers the generation of a ping-pong responder-piRNA, and forces the generation of 3′-directed, phased biogenesis of trail-piRNAs (Fig. 3C). Trail-piRNA levels and phasing accuracy decrease with increasing distance from the trigger site but are detectable for
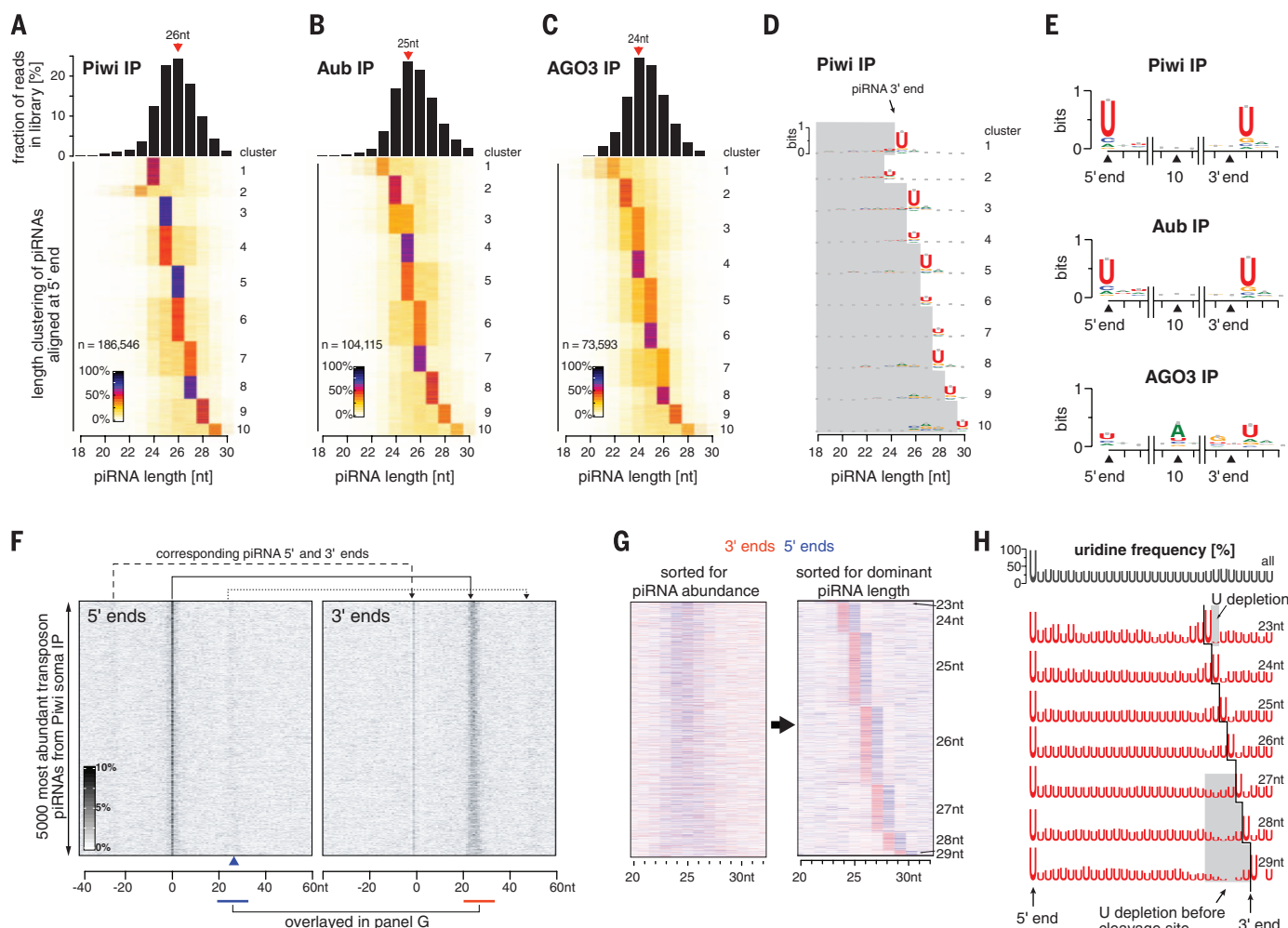
Fig. 2. Biogenesis of flanking primary piRNAs is coupled. (**A** to **C**) (Top) piRNA length histograms. IP, immunoprecipitation. (Bottom) Heat maps showing length groups for piRNAs in Piwi/Aub/AGO3. 5′ ends with similar length profiles were grouped using K-means clustering. n denotes the number of analyzed piRNAs. (**D**) Sequence logos indicating nucleotide biases for piRNA length clusters defined in (A). The gray shaded area denotes the piRNA body. For Aub/AGO3, see fig. S3. (**E**) Sequence logos indicating nucleotide biases for Piwi/Aub/AGO3-bound piRNAs at 5′ ends, position 10, and 3′ ends (only 3′ ends where ≥50% of piRNAs terminate were considered). (**F**) Heat maps displaying somatic Piwi-bound piRNA 5′ or 3′ ends in a window around the most abundant TE piRNAs. The sum of each line was scaled to 100% and sorted according to piRNA level at position 0. (**G**) Heat maps displaying 5′ or 3′ end counts of piRNAs mapping to positions 20 to 32 downstream of major piRNA 5′ ends [detail from (F)]. The left plot is sorted as in (F); the right plot is re-sorted for dominant piRNA length species (see also fig. S4B). (**H**) Sequence logos indicating uridine frequency along piRNA sequences of different length cohorts [defined in (G); black line indicates dominant piRNA 3′ ends].

several hundred nucleotides. To probe the effect of U residues on biogenesis patterns, we constructed a sensor with four Us in regular 26-nt intervals downstream of the trigger site. This increases levels and phasing accuracy of reporter-derived piRNAs (Fig. 3D). Spacing of single Us in decreasing intervals of 28 to 23 nt dictates piRNA 5′ ends but also defines piRNA 3′ ends precisely 1 nt upstream (Fig. 3E). These findings reinforce the notion that 3′ and 5′ ends of adjacent Piwi-bound piRNAs are formed via a single endonucleolytic cleavage upstream of a U residue.

The endonuclease Zucchini generates primary piRNA 5′ ends (3–8) and is therefore also the main candidate for their 3′ end formation. A direct test of this is precluded, as primary piRNAs depend on Zucchini. Thus, we asked whether Zucchini is involved in 3′ end formation of secondary piRNAs whose 5′ ends are formed via slicing. Many Aub/AGO3-bound secondary piRNAs are generated in Zucchini-depleted ovaries (26), and we used their 5′ ends as anchor points (fig. S6A). In WT ovaries, piRNAs mapping to these 5′ ends display the characteristic nucleotide bias at the first position (1U for Aub piRNAs) and the 10th position (10A for AGO3 piRNAs) (Fig. 4A). They also exhibit a downstream U bias. In Zucchini-depleted ovaries, the lengths of these piRNAs and therefore their 3′ ends are altered and the downstream U bias is lost, implicating Zucchini in 3′ end formation (Fig. 4A and fig. S6, B and C).

Thus, the downstream U bias is most likely a fingerprint of Zucchini, making it the central nuclease in piRNA biogenesis. The less severe effect on AGO3-bound piRNAs and their weaker downstream U bias suggest that many AGO3-bound piRNAs are Zucchini-independent or are resected at their 3′ ends in WT ovaries.

To experimentally test Zucchini's involvement in 3′ end formation of secondary piRNAs, we constructed a biogenesis reporter with a single target site for a Zucchini-independent piRNA. In WT ovaries, this reporter gives rise to a prominent ping-pong responder and to trail-piRNAs (Fig. 4B). As expected, loss of Zucchini ablates trail-piRNAs (Fig. 4C and fig. S2C). But although trigger-piRNA levels and reporter silencing were unaffected, levels of the responder-piRNA also dropped by a factor of >30 (Fig. 4C and fig. S6D). Zucchini is therefore centrally involved in 3′ end formation of ping-pong piRNAs. The piRNA target site in this reporter is from the F-element, one of the TEs that maintain high levels of secondary piRNAs in Zucchini-deficient ovaries (fig. S6E). How, then, are F-element piRNAs generated independently of Zucchini? The central difference between the F-element and the reporter is that the latter contains only a single Aub/AGO3 target site. We added a downstream target site for a second Zucchini-independent piRNA, which would generate a ~50-nt-long piRNA intermediate. This leads to recovery of the first but not the second

responder-piRNA in Zucchini-depleted ovaries (Fig. 4D and fig. S6F). Introducing a target site for a third Zucchini-independent piRNA leads to recovery of the first two responder-piRNAs (Fig. 4E and fig. S6G). A downstream slicer cleavage can therefore bypass Zucchini's role in piRNA 3′ end formation. This must be coupled to exonucleolytic trimming, consistent with the existence of an activity that resects intermediates to mature piRNAs (17).

To uncover an involvement of mouse Zucchini (MitoPLD) (8, 27) in piRNA 3′ end formation, we searched for a downstream U bias in published piRNA data sets. Although mouse piRNA populations group into well-defined length cohorts, they lack a downstream U bias (Fig. 4, F and G, and fig. S7A) (28). Similarly, piRNA 3′ ends and adjacent 5′ ends display no coupling signature (Fig. 4H), suggesting fundamental differences in piRNA 3′ end formation between flies and mice. However, Mili-bound primary piRNAs are extensively trimmed at their 3′ ends (28). Although mature Mili-bound piRNAs are ~24- to 28-nt-long, Mili associates with ~30- to 40-nt piRNA intermediates harboring mature 5′ ends in Tdrkh/Papi mutants (fig. S7, B and C). This suggests that Tdrkh recruits an exonuclease to PIWI proteins to facilitate piRNA precursor trimming (28, 29). Trimming might therefore occlude the downstream U bias defined by MitoPLD. Indeed, Mili-bound piRNA intermediates from
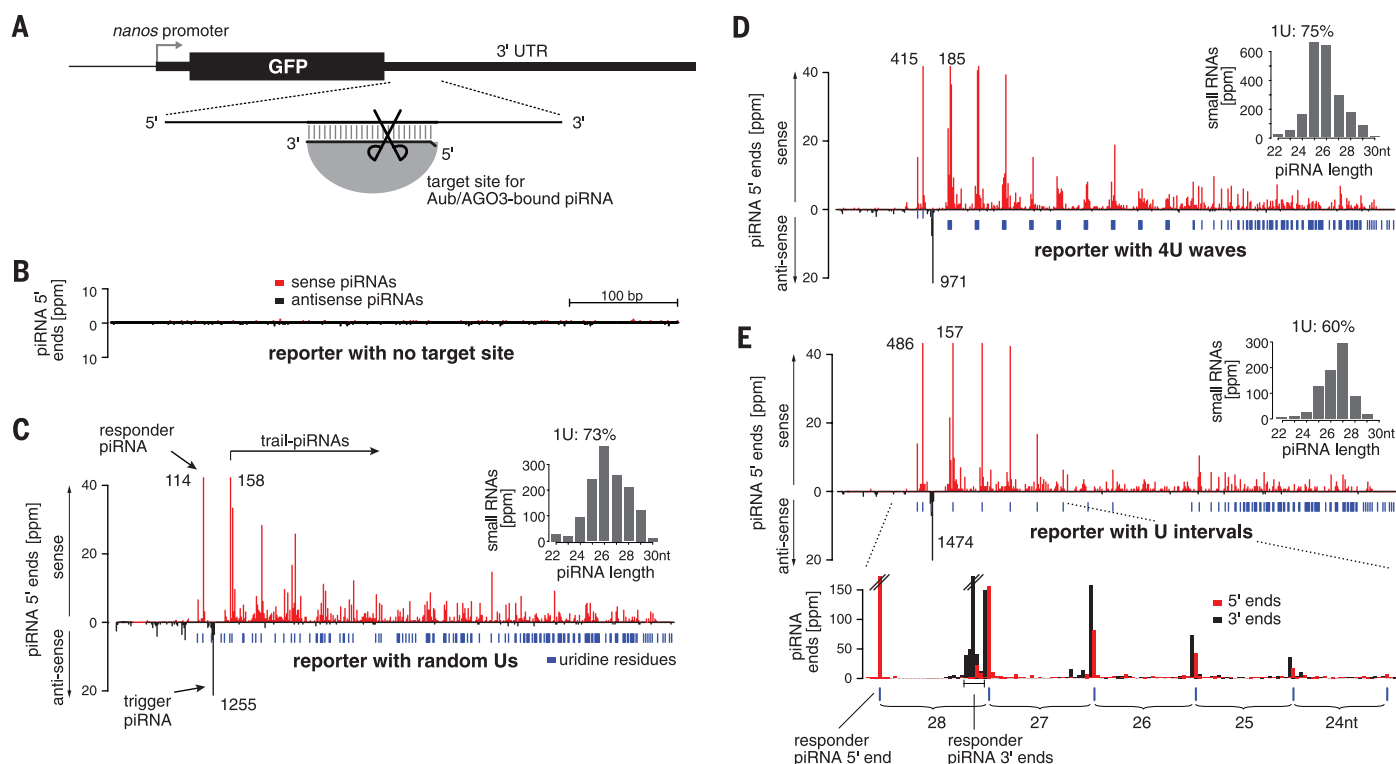
Fig. 3. Primary piRNA biogenesis is continuous and guided by uridine residues. (**A**) Cartoon of the piRNA biogenesis reporter with target site for an Aub/AGO3-bound piRNA. (**B** and **C**) Normalized small RNA 5′ end profiles from a reporter lacking a piRNA target site (B) or from a reporter with target site for an Aub/AGO3-bound piRNA. bp, base pairs. (C) Black denotes antisense reads, red indicates sense reads, and blue bars represent U residues. Numbers indicate normalized piRNA counts. Histograms indicate length profile and 1U bias of trail-piRNAs. (**D**) Similar to (C), but the reporter contains four U residues every 26 nt. (**E**) Similar to (C), but the reporter contains single U residues in the indicated intervals.
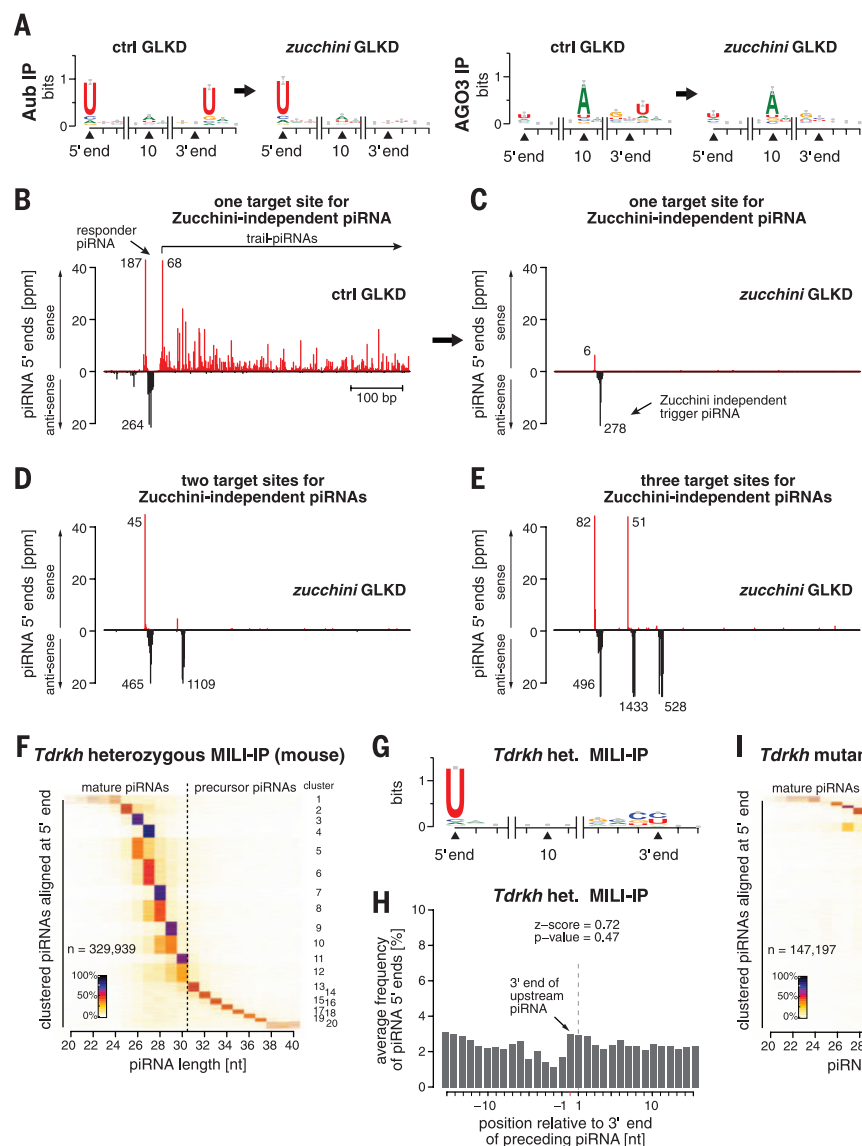
Fig. 4. Zucchini is involved in 3′ end formation of *Drosophila* and mouse piRNAs. (**A**) Sequence logos for nucleotides at 5′ ends, position 10, and 3′ ends of Aub- or AGO3-bound piRNAs in control or Zucchini-depleted ovaries. (**B**) Normalized WT small RNA 5′ end profile for a reporter (similar to Fig. 3D) with a single target site for a Zucchini-independent piRNA. (**C**) As in (B) but for piRNAs isolated from Zucchini-depleted ovaries. (**D** and **E**) As in (C), but the reporter contains target sites for two (D) or three (E) Zucchini-independent piRNAs. (**F**) Heat maps showing length cohorts of Mili-bound piRNAs from *Tdrkh* heterozygous mouse testes. (**G**) Sequence logos showing nucleotide composition around dominant piRNA 3′ ends for length cohorts defined in (G). For individual length clusters, see fig. S6. (**H**) Frequency of Mili-bound piRNA 5′ ends around aligned dominant piRNA 3′ ends from *Tdrkh* heterozygous testes. (**I** to **K**) As in (F) to (H) but from *Tdrkh* mutant testes.

Tdrkh mutants display a strong downstream U bias and exhibit strong coupling of 3′ ends with subsequent 5′ ends (Fig. 4, I to K, and fig. S7D). Hence, coupled biogenesis of neighboring piRNAs is conserved between *Drosophila* and mice.

Altogether, a model for piRNA biogenesis can be drawn (fig. S8). A critical first step is the specification of piRNA precursors, leading to the endonucleolytic definition of a piRNA 5′ end. In the fly germ line, the dominating process is piRNA-guided target slicing, which specifies the 5′ end of a responder-piRNA. 3′ end formation of this piRNA can occur via a second slicer cleavage event, which liberates a piRNA intermediate for exonucleolytic trimming. Alternatively, 3′ end formation is catalyzed by Zucchini, which cleaves the precursor upstream of a U residue. Zucchini-mediated 3′ end formation promotes phased and 3′-directed primary piRNA biogenesis. In flies, Zucchini cleavage products

seem directly compatible with Piwi binding. In mice, MitoPLD cleavage products are too long, making 3′ end trimming essential. Notably, how primary piRNA biogenesis initiates in *Drosophila* ovarian somatic cells or adult mouse testes remains elusive.

REFERENCES AND NOTES

1. C. D. Malone, G. J. Hannon, *Cell* **136**, 656–668 (2009).
2. M. C. Siomi, K. Sato, D. Pezic, A. A. Aravin, *Nat. Rev. Mol. Cell Biol.* **12**, 246–258 (2011).
3. A. Pane, K. Wehr, T. Schüpbach, *Dev. Cell* **12**, 851–862 (2007).
4. J. J. Ipsaro, A. D. Haase, S. R. Knott, L. Joshua-Tor, G. J. Hannon, *Nature* **491**, 279–283 (2012).
5. H. Nishimasu *et al.*, *Nature* **491**, 284–287 (2012).
6. K. Saito *et al.*, *Genes Dev.* **24**, 2493–2498 (2010).
7. D. Olivieri, M. M. Sykora, R. Sachidanandam, K. Mechtler, J. Brennecke, *EMBO J.* **29**, 3301–3317 (2010).
8. T. Watanabe *et al.*, *Dev. Cell* **20**, 364–375 (2011).
9. C. D. Malone *et al.*, *Cell* **137**, 522–535 (2009).
10. N. C. Lau *et al.*, *Genome Res.* **19**, 1776–1785 (2009).
11. A. Aravin *et al.*, *Nature* **442**, 203–207 (2006).
12. A. Girard, R. Sachidanandam, G. J. Hannon, M. A. Carmell, *Nature* **442**, 199–202 (2006).
13. X. Z. Li *et al.*, *Mol. Cell* **50**, 67–81 (2013).
14. J. Brennecke *et al.*, *Cell* **128**, 1089–1103 (2007).
15. L. S. Gunawardane *et al.*, *Science* **315**, 1587–1590 (2007).
16. A. Vourekas *et al.*, *Nat. Struct. Mol. Biol.* **19**, 773–781 (2012).
17. S. Kawaoka, N. Izumi, S. Katsuma, Y. Tomari, *Mol. Cell* **43**, 1015–1022 (2011).
18. C. Klattenhoff *et al.*, *Cell* **138**, 1137–1149 (2009).
19. Z. Zhang *et al.*, *Cell* **157**, 1353–1363 (2014).
20. F. Mohn, G. Sienski, D. Handler, J. Brennecke, *Cell* **157**, 1364–1379 (2014).
21. S. Shpiz, S. Ryazansky, I. Olovnikov, Y. Abramov, A. Kalmykova, *PLOS Genet.* **10**, e1004138 (2014).
22. See materials and methods and other supplementary materials on *Science* Online.
23. D. C. Swarts *et al.*, *Nat. Struct. Mol. Biol.* **21**, 743–753 (2014).
24. L. M. Wee, C. F. Flores-Jasso, W. E. Salomon, P. D. Zamore, *Cell* **151**, 1055–1067 (2012).
25. M. Reuter *et al.*, *Nature* **480**, 264–267 (2011).

26. D. Olivieri, K. A. Senti, S. Subramanian, R. Sachidanandam, J. Brennecke, *Mol. Cell* **47**, 954–969 (2012).
27. H. Huang *et al*., *Dev. Cell* **20**, 376–387 (2011).
28. J. P. Saxe, M. Chen, H. Zhao, H. Lin, *EMBO J.* **32**, 1869–1885 (2013).
29. S. Honda *et al*., *RNA* **19**, 1405–1418 (2013).

NONCODING RNA

piRNA-guided transposon cleavage initiates Zucchini-dependent, phased piRNA production

Bo W. Han,[1,2]* Wei Wang,[1,2,3]* Chengjian Li,[1,2] Zhiping Weng,[2,3]† Phillip D. Zamore[1,2]†

PIWI-interacting RNAs (piRNAs) protect the animal germ line by silencing transposons. Primary piRNAs, generated from transcripts of genomic transposon "junkyards" (piRNA clusters), are amplified by the "ping-pong" pathway, yielding secondary piRNAs. We report that secondary piRNAs, bound to the PIWI protein Ago3, can initiate primary piRNA production from cleaved transposon RNAs. The first ~26 nucleotides (nt) of each cleaved RNA becomes a secondary piRNA, but the subsequent ~26 nt become the first in a series of phased primary piRNAs that bind Piwi, allowing piRNAs to spread beyond the site of RNA cleavage. The ping-pong pathway increases only the abundance of piRNAs, whereas production of phased primary piRNAs from cleaved transposon RNAs adds sequence diversity to the piRNA pool, allowing adaptation to changes in transposon sequence.

In animals, PIWI proteins guided by single-stranded, 23- to 36-nucleotide (nt) small RNAs, PIWI-interacting RNAs (piRNAs), suppress germline transposon expression. In *Drosophila*, piRNAs bind the PIWI proteins Piwi, Aubergine (Aub), and Argonaute3 (Ago3) (*1*). Fly primary piRNAs derive from long transcripts from piRNA clusters—discrete genomic loci comprising transposon fragments (*2*). The endonuclease Zucchini (Zuc) is thought to cut cluster transcripts into fragments whose 5′ ends correspond to the 5′ ends of piRNAs, but whose length exceeds that of piRNAs; these piRNA precursors are loaded into Piwi and Aub and then trimmed from their 3′ ends, yielding mature primary piRNAs (*1, 3–5*). In the fly oocyte, maternally inherited and primary piRNAs made de novo initiate production of secondary piRNAs, which subsequently self-amplify via reciprocal cycles of Aub- and Ago3-catalyzed cleavage of transposon mRNAs and cluster transcripts, a process known as the ping-pong pathway (fig. S1) (*6, 7*). The ping-pong pathway increases piRNA abundance, but cannot create novel piRNA sequences. Yet, piRNA populations are highly diverse, with most individual species being of low abundance.

We used genetic mutants to separate primary, maternal, and secondary piRNAs. To assess the mutants' effects on the germ line, we examined piRNAs from the largest piRNA cluster, *42AB* (*6*). $aub^{HN2/QC42}$; $ago3^{t2/t3}$ double mutants lack the ping-pong pathway, so they contain only maternal and primary piRNAs (for *42AB*, Z_{10} = 0.6; Z-score ≥ 2.81 corresponds to P ≤ 0.005; Fig. 1A). In contrast, *zuc* mutants contain maternal and secondary, but not primary, piRNAs. Loss of Zuc decreased *42AB* piRNAs by a factor of 50 (fig. S2A), but the piRNAs remaining showed significant ping-pong amplification (*42AB* piRNAs, Z_{10} = 39; all piRNAs, Z_{10} = 42), consistent with a small pool of maternal piRNAs being amplified into secondary piRNAs.

The 5′ ends of piRNAs mapping to the same genomic strand and present in $aub^{HN2/QC42}$; $ago3^{t2/t3}$ but not $zuc^{HM27/Df}$ typically lay 25 to 28 nt apart, the same length as piRNAs themselves (fig. S2B). Thus, the maternal and primary piRNAs remaining in $aub^{HN2/QC42}$; $ago3^{t2/t3}$ double-mutant ovaries were phased, suggesting that a nuclease initiates production of piRNAs from one end of a piRNA precursor, moving 5′ to 3′ to clip off successive piRNAs.

The distance from the 3′ end of each piRNA to the 5′ end of the next downstream piRNA measures piRNA phasing (Fig. 1B). The most common 3′-to-5′ distance was 1 nt: A single cleavage event appears to produce the 3′ end of one piRNA and the 5′ end of the adjacent, downstream piRNA more often than expected by chance (Z_1 for w^I = 6.5). Production of phased piRNAs required Zuc but not ping-pong: The 1-nt peak was more prominent in $aub^{HN2/QC42}$; $ago3^{t2/t3}$ ovaries (Z_1 = 22) than in w^I, but was undetectable in $zuc^{HM27/Df}$ (Z_1 = 1.5).

piRNA phasing differed among the three *Drosophila* PIWI proteins (Fig. 1B). By 3′-to-5′ distance, Piwi-bound piRNAs displayed the most significant phasing (Z_1 = 21); Aub-bound piRNAs displayed reduced, but still significant, phasing (Z_1 = 4.0); Ago3-bound piRNAs were not phased (Z_1 = –1.3). Thus, Piwi- and Aub-, but not Ago3-bound, primary piRNAs are produced by a processive mechanism that requires Zuc.

piRNAs associated with Piwi and Aub, but not Ago3, typically begin with uridine (*6*). Phased piRNAs beginning with U could be produced by a processive nuclease complex measuring out ~26 nt, then cleaving at the nearest U. Alternatively, they could be made by the same nuclease measuring out ~26 nt, but cleaving at all nucleotides with similar efficiency; subsequent binding of Piwi and Aub would select for piRNAs starting with U. The first model predicts that the nucleotide immediately following the 3′ end of a piRNA—in genomic sequence but not mature piRNAs—is more likely to be U than expected by chance. The second model predicts that when one piRNA follows another in phase, the second piRNA is more likely to begin with U because of the preference of Aub and Piwi; the genomic nucleotide following a piRNA would not have any sequence bias, because selection for a 5′ U follows piRNA precursor cleavage. To distinguish between the models, we measured the composition of the nucleotide after the 3′ ends of piRNAs ("+1U percentage"). This nucleotide was typically uridine in both w^I and $aub^{HN2/QC42}$; $ago3^{t2/t3}$, but not in $zuc^{HM27/Df}$ (fig. S2D), indicating that phased piRNAs are likely produced by direct cleavage 5′ to U, before pre-piRNAs are loaded into PIWI proteins. Because purified Zuc shows no nucleotide preference (*4, 5*), we propose that other factors direct Zuc to cleave before U.

We analyzed piRNAs derived from *42AB* for 21 different mutant or germline RNAi strains. Phasing was detected in all strains except those with an impaired primary piRNA pathway (Fig. 1C) (*2, 8–13*). Compared to wild-type, phasing was more readily detected in mutants defective in ping-pong, likely because loss of secondary piRNAs reduced background signal. We also detected Zuc-dependent phasing for somatic piRNAs, which are always primary (fig. S2E). We conclude that phasing is an inherent feature of primary, but not secondary, piRNA production.

[1]RNA Therapeutics Institute, Howard Hughes Medical Institute, University of Massachusetts Medical School, 368 Plantation Street, Worcester, MA 01605, USA. [2]Department of Biochemistry and Molecular Pharmacology, University of Massachusetts Medical School, 368 Plantation Street, Worcester, MA 01605, USA. [3]Program in Bioinformatics and Integrative Biology, University of Massachusetts Medical School, 368 Plantation Street, Worcester, MA 01605, USA.
*These authors contributed equally to this work.
†Corresponding author. E-mail: zhiping.weng@umassmed.edu (Z.W.); phillip.zamore@umassmed.edu (P.D.Z.)

To determine whether the production of phased piRNAs depends on maternal piRNAs, we used a strain bearing a ~7 kilobase pair (kbp) transgene, $P\{GSV6\}$, inserted into $42AB$. $P\{GSV6\}$ carries both gfp and w^{+mC} and produces both sense and antisense piRNAs (fig. S3, A and B). Both transgene piRNA abundance and ping-pong were greater when $P\{GSV6\}42A18$ was inherited maternally (Fig. 2A and fig. S3A) (14–16), but primary piRNA phasing was unaltered by the parental

source of the transgene (Z_1 maternal = 13; Z_1 paternal = 13). As an additional test of the idea that phased piRNAs are primary, not maternal, we sequenced piRNAs from $vasa^{D5/PH165}$ ovaries that had inherited the $P\{GSV6\}$ transgene maternally or paternally (Fig. 2A); Vasa is required for ping-pong amplification. Regardless of which parent contributed the transgene, $P\{GSV6\}$-derived piRNAs displayed significant phasing (paternal, Z_1 = 12; maternal, Z_1 = 9.0; wild-

type, Z_1 = 13), consistent with the idea that phasing is a primary piRNA signature that requires neither maternal piRNAs nor ping-pong amplification.

Without Vasa, piRNA phasing (Z_1) and the percentage of uridine at the genomic nucleotide immediately after the 3′ ends of the piRNAs (+1U percentage) were unchanged, but the abundance of Piwi-bound piRNAs was less than one-tenth that of wild-type (Fig. 2B and fig. S3C).
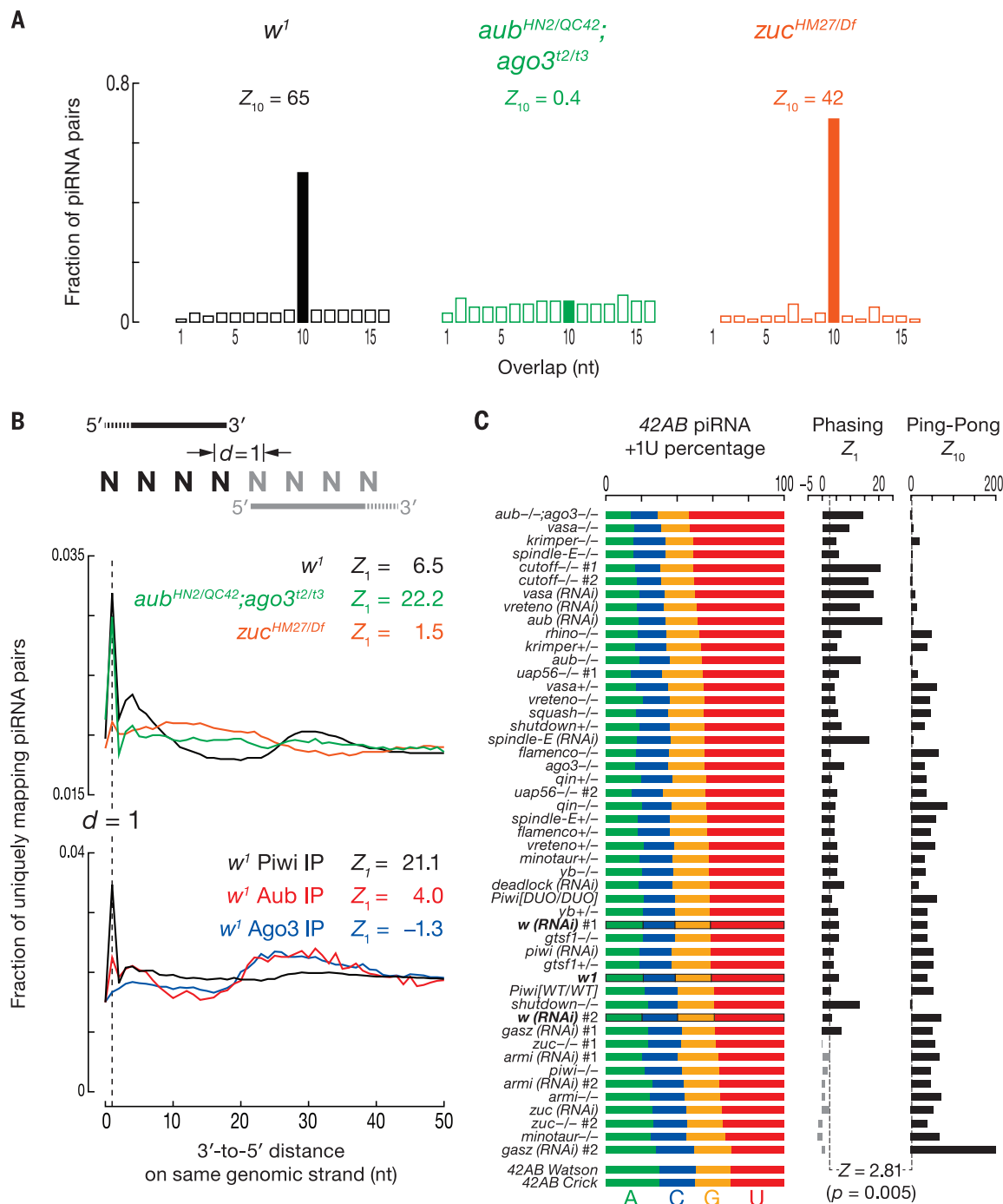
Fig. 1. Zuc-dependent phasing of primary piRNAs. (A) Ping-pong analysis of all piRNAs from w^1, $aub^{HN2/QC42}$; $ago3^{t2/t3}$, and $zuc^{HM27/Df}$. (B) Distance from the 3′ ends of upstream piRNAs to the 5′ ends of downstream piRNAs on the same genomic strand. (C) Nucleotide composition immediately after the 3′ ends of uniquely mapping $42AB$ piRNAs. Z_{10}: Ping-pong; Z_1: phasing.

Piwi is likely loaded only with primary piRNAs (fig. S3D) (16–18). Why then should Vasa, a central component of the secondary piRNA pathway, affect the abundance of Piwi-bound piRNAs? One explanation is that production of Piwi-loaded, phased primary piRNAs requires precursor cleavage directed by secondary piRNAs. To explore this idea, we sequenced the "degradome"— RNAs >200 nt and bearing 5'-monophosphates— to detect the RNAs cleaved by secondary piRNAs bound to Aub or Ago3. In w^1 control ovaries, we readily identified long transposon RNAs whose 5' ends were generated by Aub or Ago3 (fig. S4A) (19); such degradome reads were absent from $aub^{HN2/QC42}$; $ago3^{t2/t3}$ mutants ($Z_{10} = 0.8$). Moreover, degradome reads corresponding to Piwi-catalyzed cleavage were indistinguishable from background ($Z_{10} = 0.4$), consistent with Piwi silencing via transcriptional repression, rather than RNA cleavage (18). Thus, 3' cleavage products of Aub- or Ago3-catalyzed slicing are subsequently used to produce phased primary piRNAs.

We determined the fraction of piRNA 5' ends at each position ±150 nt from an Aub or Ago3 cleavage site (fig. S4B). In both w^1 and zuc mutant ovaries, piRNA 5' ends were more likely to map to the cleavage site than expected by chance (w^1, $Z_0 = 27$; $zuc^{HM27/Df}$, $Z_0 = 34$; fig. S4C). These piRNAs correspond to secondary piRNAs produced by the ping-pong cycle. We also detected phased piRNAs in w^1 as a peak ~26 nt after the Aub or Ago3 cleavage sites that corresponds to the 5' ends of primary piRNAs immediately following the 3' end of secondary piRNAs, and as a ~53-nt peak representing the 5' end of another primary piRNA immediately following the 3' end of the first primary piRNA. $zuc^{HM27/Df}$ ovaries lacked both peaks.

We separated degradome reads based on the likelihood ($P \leq 0.005$, χ^2 test) that they were produced by Aub versus Ago3 (fig. S4D) (19), then analyzed the distance between the 5' ends of Piwi-bound piRNAs and the sites of Aub- or Ago3-catalyzed cleavage. The 5' ends of Piwi-bound piRNAs coincided with the Zuc-dependent ~26- and ~53-nt peaks for both Aub- and Ago3-cleaved RNAs (Fig. 3). A small but significant fraction of Aub-, but not Ago3-bound piRNAs, also began ~26 and ~53 nt after the Ago3-cleaved sites.

Small RNA and degradome sequencing data from zuc mutant ovaries unambiguously identified sites cleaved by Aub or Ago3. These data show that, the 5' ends of Piwi-bound piRNAs in w^1 ovaries were typically ~26 and ~53 nt down-stream from where Aub or Ago3 cleaved (fig. S4E), a relationship not detected with degradome data from $aub^{HN2/QC42}$; $ago3^{t2/t3}$ ovaries, which lack secondary piRNAs (fig. S4F). Next, we measured the distance from the 5' ends of Aub- and Ago3-bound piRNAs to the 5' ends of Piwi-bound piRNAs on the same genomic strand (fig. S5A). Again, the 5' ends of Piwi-bound piRNAs were typically 26 nt downstream from the 5' ends of Ago3-piRNAs and 27 to 29 nt downstream of the 5' ends of Aub-piRNAs. Similarly, the 5' ends of Aub-bound piRNAs lay ~26 nt downstream from the 5' ends of Ago3-bound piRNAs. In contrast, the 5' ends of Ago3-bound piRNAs were no more likely to be ~26 nt downstream from the 5' ends of Aub-bound piRNAs than would be expected by chance. Thus, RNAs cut by Ago3 produce phased, Aub-bound piRNAs, but RNAs cut by Aub do not make phased, Ago3-bound piRNAs.

The distance between the 5' ends of Piwi-bound piRNAs and the 5' ends of Ago3- or Aub-bound piRNAs on the opposite genomic strand (i.e., ping-pong analysis) again suggests that the 3' cleavage product generated by Ago3 or Aub is initially processed into a secondary piRNA, and thereafter is used for the production of phased primary piRNAs loaded into Piwi (fig. S5B). Piwi

A

Maternal genotype	Paternal genotype	F1 genotype	Maternal piRNA	Primary piRNA	Secondary piRNA	Phasing Z_1	+1 U %	Ping-Pong Z_{10}
+/+	+/P{GSV6}42A18	+/P{GSV6}42A18	No	Yes	Yes	13	41%	3.5
P{GSV6}42A18/+	+/+	P{GSV6}42A18/+	Yes	Yes	Yes	13	47%	6.2
vasa/+	+/P{GSV6}42A18, vasa	vasa/P{GSV6}42A18, vasa	No	Yes	No	12	48%	0.8
P{GSV6}42A18, vasa/+	+/vasa	P{GSV6}42A18, vasa/vasa	Yes	Yes	No	9.0	48%	0.4

B
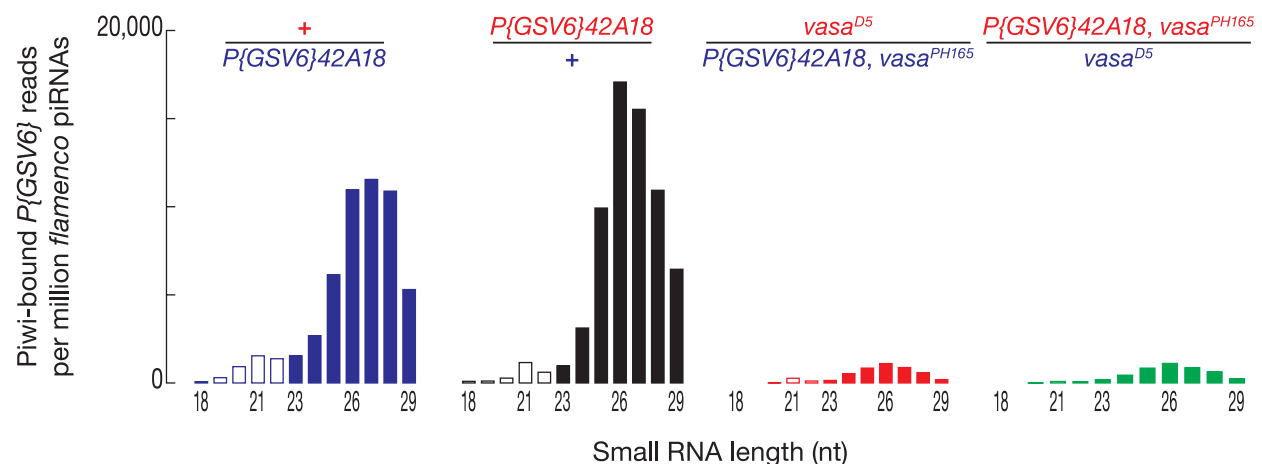
Fig. 2. Contribution of maternal and secondary piRNAs to phasing. (**A**) Ping-pong, phasing, and +1 U percentage were analyzed for P{GSV6}42A18-derived piRNAs inherited paternally or maternally, with or without Vasa. (**B**) Length distribution of Piwi-bound, uniquely mapping P{GSV6}42A18 piRNAs. Reads were normalized to flamenco-derived, uniquely mapping piRNAs.

does not directly participate in ping-pong, and the 5′ ends of Piwi-bound piRNAs did not map 10 nt from the 5′ ends of Aub- or Ago3-bound piRNAs. Instead, Piwi-bound piRNAs lay 15 to 19 nt after the 5′ ends of Aub- or Ago3-bound piRNAs. Such phased piRNAs have been detected previously, but were attributed to ping-pong amplification (20).

In the absence of Ago3 or Vasa, 42AB-derived, Piwi-bound piRNAs decreased to ~10% of the w^1 level (Fig. 4A). Loss of Aub had a more modest effect: 42AB-derived, Piwi-bound piRNAs were ~47% of the w^1 level. Thus, Ago3 initiates the production of most phased, Piwi-bound primary piRNAs. These data help explain why transposon silencing requires heterotypic Aub:Ago3 ping-

pong amplification (17): Homotypic Aub:Aub ping-pong cannot generate enough Piwi-bound, antisense, primary piRNAs.

Experiments in silkmoth cells and mice implicate the Tudor protein Papi in 3′ piRNA trimming (21, 22). To examine the role of 3′ trimming in the biogenesis of phased primary piRNAs, we sequenced small RNAs from papi mutant fly

Fig. 3. Phasing of Piwi-bound piRNAs after sites of Aub or Ago3 cleavage. Distance was measured from the 5′ ends of Piwi-, Ago3-, and Aub-bound piRNAs to sites of Aub or Ago3 cleavage on the same genomic strand.
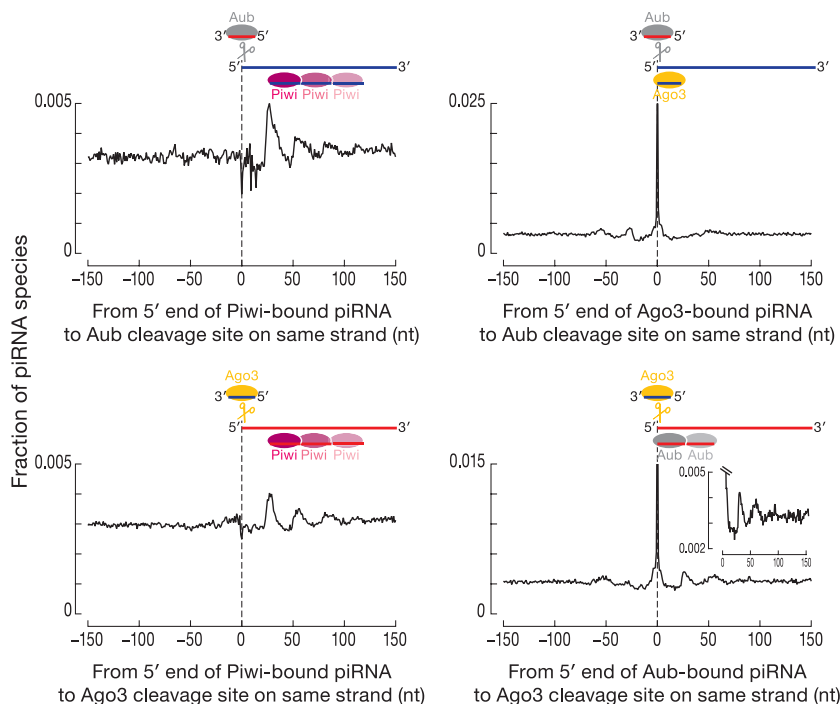
Fig. 4. Mouse piRNAs are phased. (A) Length distribution of Piwi-bound, uniquely mapping fly piRNAs derived from 42AB in w^1, $aub^{HN2/QC42}$, $ago3^{t2/t3}$, and $vasa^{D5/PH165}$. Reads were normalized to flamenco-derived, uniquely mapping piRNAs. (B) Distance from the 3′ ends of upstream piRNAs to the 5′ ends of downstream piRNAs on the same genomic strand for uniquely mapping piRNAs in $Tdrkh^{+/−}$ and $Tdrkh^{−/−}$ mouse testes at 11 dpp. (C) Genomic nucleotide composition 29 nt before and 1 nt after the 3′ ends of uniquely mapping mouse piRNAs.
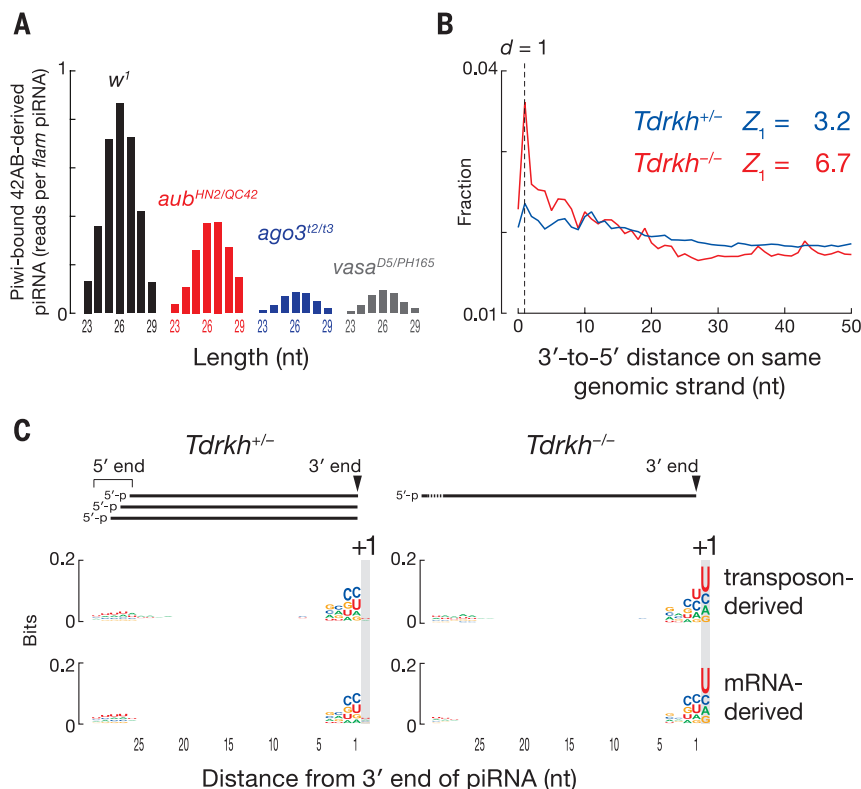
ovaries (fig. S6A). The median length of piRNAs from nearly all transposon families increased 0.35 nt ($P < 2.2 \times 10^{-16}$, Wilcoxon signed-rank test; fig. S6, B to D) and germline and somatic piRNA phasing became more pronounced (fig. S6, E and F). We propose that 3′ trimming of Piwi-bound piRNAs allows the use of uridines >26 nt after the 5′ end of a pre-piRNA as cleavage sites to make piRNAs.

In testes from wild-type mice, one piRNA 5′ end often lies 30 to 40 nt downstream from another (fig. S7, A to C), possibly because mouse pre-piRNAs are longer than those in flies and require the 3′ trimming of ~3 to 10 nt. Analysis of Papi ($Tdrkh^{-/-}$) mutant testes supports this view. $Tdrkh^{-/-}$ testes accumulate 31- to 37-nt RNAs instead of 26- to 30-nt piRNAs, and most of these longer species share their 5′ ends with mature piRNAs from $Tdrkh^{+/-}$ heterozygotes (22). At 11 days post partum (dpp), 3′-to-5′ distance analysis of piRNAs from $Tdrkh^{-/-}$ testes showed clear evidence for phasing (Fig. 4B). Mouse piRNAs typically begin with uridine, and the 3′ ends of the longer RNAs in $Tdrkh^{-/-}$ testes were generally followed by a uridine in genomic sequence (Fig. 4C). piRNA 5′-to-5′ distance analysis of $Tdrkh^{+/-}$ and $Tdrkh^{-/-}$ showed broad peaks at 35 to 43 nt—the same length as the pre-piRNAs detected in $Tdrkh^{-/-}$ (fig. S7D). We conclude that mammalian primary piRNAs are phased, but are more extensively trimmed than those in flies.

Our findings suggest a model for primary piRNA biogenesis (fig. S8) in which each RNA cleaved by Ago3 or Aub produces not only a secondary ping-pong piRNA, but also primary piRNAs from the sequences immediately 3′ to the secondary piRNA. Such a spreading mechanism calls to mind features of siRNA production in *Caenorhabditis elegans* and *Arabidopsis thaliana* (23–26), and primed CRISPR adaptation in *Escherichia coli* (27, 28). Although the detailed mechanisms differ, signal amplification with sequence diversification is clearly a recurrent theme for RNA-guided silencing in animals, plants, and bacteria.

REFERENCES AND NOTES

1. M. J. Luteijn, R. F. Ketting, *Nat. Rev. Genet.* **14**, 523–534 (2013).
2. C. D. Malone et al., *Cell* **137**, 522–535 (2009).
3. F. Voigt et al., *RNA* **18**, 2128–2134 (2012).
4. H. Nishimasu et al., *Nature* **491**, 284–287 (2012).
5. J. J. Ipsaro, A. D. Haase, S. R. Knott, L. Joshua-Tor, G. J. Hannon, *Nature* **491**, 279–283 (2012).
6. J. Brennecke et al., *Cell* **128**, 1089–1103 (2007).
7. L. S. Gunawardane et al., *Science* **315**, 1587–1590 (2007).
8. V. V. Vagin et al., *Science* **313**, 320–324 (2006).
9. A. Pane, K. Wehr, T. Schüpbach, *Dev. Cell* **12**, 851–862 (2007).
10. D. Olivieri, M. M. Sykora, R. Sachidanandam, K. Mechtler, J. Brennecke, *EMBO J.* **29**, 3301–3317 (2010).
11. V. V. Vagin et al., *RNA* **19**, 1064–1077 (2013).
12. B. Czech, J. B. Preall, J. McGinn, G. J. Hannon, *Mol. Cell* **50**, 749–761 (2013).
13. D. Handler et al., *Mol. Cell* **50**, 762–777 (2013).
14. J. Brennecke et al., *Science* **322**, 1387–1392 (2008).
15. A. de Vanssay et al., *Nature* **490**, 112–115 (2012).
16. A. Le Thomas et al., *Genes Dev.* **28**, 1667–1680 (2014).
17. Z. Zhang et al., *Mol. Cell* **44**, 572–584 (2011).
18. G. Sienski, D. Dönertas, J. Brennecke, *Cell* **151**, 964–980 (2012).
19. W. Wang et al., *Mol. Cell* **56**, 708–716 (2014).
20. N. C. Lau et al., *Genome Res.* **19**, 1776–1785 (2009).
21. S. Honda et al., *RNA* **19**, 1405–1418 (2013).
22. J. P. Saxe, M. Chen, H. Zhao, H. Lin, *EMBO J.* **32**, 1869–1885 (2013).
23. Z. Xie, E. Allen, A. Wilken, J. C. Carrington, *Proc. Natl. Acad. Sci. U.S.A.* **102**, 12984–12989 (2005).
24. M. Yoshikawa, A. Peragine, M. Y. Park, R. S. Poethig, *Genes Dev.* **19**, 2164–2175 (2005).
25. M. P. Bagijn et al., *Science* **337**, 574–578 (2012).
26. H. C. Lee et al., *Cell* **150**, 78–87 (2012).
27. D. C. Swarts, C. Mosterd, M. W. van Passel, S. J. Brouns, *PLOS ONE* **7**, e35888 (2012).
28. K. A. Datsenko et al., *Nat. Commun.* **3**, 945 (2012).

SUPPLEMENTARY MATERIALS

www.sciencemag.org/content/348/6236/817/suppl/DC1
Materials and Methods
Supplementary Text
Figs. S1 to S8
Table S1
References (29–39)

Grete Lundbeck European Brain Research Foundation

Call for Nominations for

THE BRAIN PRIZE

THE PRIZE OF € 1 MILLION WILL BE AWARDED IN COPENHAGEN JULY 2016

Nominations by 15 September 2015

Nominations will be reviewed by the Selection Committee:

HUDA AKIL, USA

ANDERS BJÖRKLUND, SWEDEN, VICE-CHAIRMAN

COLIN BLAKEMORE, UNITED KINGDOM, CHAIRMAN

JOSEPH COYLE, USA

TOM JESSELL, USA

RANGA R. KRISHNAN, SINGAPORE

PHILIP SCHELTENS, THE NETHERLANDS

IRENE TRACEY, UNITED KINGDOM

FOR THE NOMINATION FORM AND DETAILS OF THE NOMINATION PROCEDURE, PLEASE VISIT:

WWW.THEBRAINPRIZE.ORG

Prize Winners 2015

Winfried Denk, Max Planck Institute of Neurobiology, Germany, Arthur Konnerth, Technical University Munich, Germany,
Karel Svoboda, Janelia Research Campus, HHMI, USA, David W. Tank, Princeton University, USA

GRETE LUNDBECK
EUROPEAN
BRAIN RESEARCH
FOUNDATION

THE
BRAIN
PRIZE

The Brain Prize recognizes and rewards outstanding contributions to European neuroscience, from basic to clinical

Neural Transfection Reagent

The DNA-In Neuro is a new generation transfection reagent developed specifically for maximum nucleic acid delivery into neurons, typically achieving a twofold or greater improvement in efficiency over currently available competing reagents. Neurons are among the most difficult cell types to transfect. DNA-In Neuro Transfection Reagent offers researchers a cost-effective, robust and easy-to-use DNA delivery solution for transfecting freshly isolated and cryopreserved neurons. DNA-In Neuro Transfection Reagent reproducibly transfects neurons and neural stem cells at optimal efficiency with exceptionally low toxicity to support uncompromised post-transfection assays. Comprising a proprietary formulation of chemically defined compounds, DNA-In Neuro Transfection Reagent is completely free of animal-derived components. Designed for use with a quick and easy to follow, single-tube reagent protocol, DNA-In Neuro Transfection Reagent produces great results on the very first try.

AMS Biotechnology
For info: +44-(0)-1235-828200
www.amsbio.com

Xeno-Free and Serum-Free Medium

PRIME-XV T Cell Expansion XSFM is a xeno-free and serum-free medium optimized for the expansion of human T cells that reliably maintains potency and is the newest medium in the PRIME-XV cell therapy product line that supports immunotherapy. Immunotherapy has emerged as a viable approach for treating some forms of cancer. Using a process called adoptive cell transfer (ACT), T cells have been engineered to produce chimeric antigen receptors (CARs), a surface receptor that allows T cells to recognize tumor-specific proteins and subsequently kill the targeted tumor cells. This method has generated positive results in small clinical trials, indicating its potential as a treatment. To further support the research and development into ACT, efficient expansion of desired T cell subsets with proper potency is critical to ensure an adequate population of T cells with targeted specificity. To facilitate clinical applications and scale-up, PRIME-XV T Cell Expansion XSFM is available for custom formulation and packaging.

Irvine
For info: 800-577-6097
www.irvinesci.com/cell-therapy

96-Well Deep Well Plate

The new low-profile 96-well deep well plates achieve a storage volume of 1.1 mL/well in a height of just 27 mm enabling more plates to be stacked or stored in a given space. Manufactured from extractables-free polypropylene in an ISO 10,000 approved clean room environment, Porvair low-profile plates undergo extensive quality testing to ensure they are of the highest quality, certified free from DNase, RNase, and endotoxin contamination. Combining an affordable price with uncompromising high quality, Porvair low-profile 96-well deep well plates are precisely manufactured to comply with ANSI/SLAS dimensional standards ensuring complete compatibility with all automated sample handling systems, microplate readers, and washers. Complementing the low-profile plate, Porvair also offers a matching anti-evaporation cap mat, manufactured from thermoplastic elastomer, to ensure the long-term integrity of your stored samples.

Porvair Sciences
For info: +44-(0)-1978-666239
www.porvair-sciences.com

HPLC/UHPLC Columns

The Kinetex F5 is a robust pentafluorophenyl propyl (PFP) core-shell phase that overcomes reproducibility and performance limitations of existing PFP and F5 products on the market. The new Kinetex F5 phase delivers improved reproducibility compared to other PFP or F5 columns and can significantly reduce method development time with its dynamic and responsive chemical functionality. It is an ideal solution for high- and ultrahigh-performance liquid chromatography (HPLC/UHPLC) development work with its combination of polar and nonpolar interactions including hydrogen bonding, electrostatic, hydrophobic, aromatic, and steric/planar mechanisms. Additional versatility of this phase gives scientists the ability to use reversed phase, 2D-LC, HILIC, SFC, or even 100% aqueous separation modes. With its fluorinated groups and carbon ring structure, the Kinetex F5 is an excellent choice for both polar and nonpolar compound separations as well as challenging methods that include halogenated, conjugated, or isomeric compounds.

Phenomenex
For info: 310-212-0555
www.phenomenex.com

EMCCD Spectroscopy Camera

The new Synapse EM is a deep-cooled EMCCD Scientific camera for low-light and ultrafast spectroscopy experiments. The Synapse EM is available in front and back illuminated for optimal quantum efficiency. With a sensor format of 1,600 x 200 or 1,600 x 400 and a pixel size of 16 µm, the Synapse EM is the ideal candidate for high spectral resolution measurements. The camera comes with a standard dual readout mode that allows the users to switch automatically between EMCCD mode for low-light measurements and conventional CCD mode for standard spectroscopy. The SynapseEM comes with several sensor options including the QExtra technology. QExtra technology is available standard in the Synapse EM-BIQX and is an antireflective multilayer coating designed to greatly improve quantum efficiency of back-illuminated sensors over a broad spectral range, while suppressing undesirable etaloning effects. With a maximum frame rate above 1,600 spectra per second and outstanding linearity, the Synapse EM is the ideal EMCCD scientific camera for Raman, SERS/TERS, multitrack, transient, and single molecule spectroscopic applications.

Horiba
For info: 732-494-8660
www.synapseem.com

Join Keystone Symposia in Asia for our October Conferences on Nutrition and Diabetes

Human Nutrition, Health and Environment

October 14–18, 2015
China World Hotel | Beijing | China

Scientific Organizers: Martin Kussmann, Hannelore Daniel and Jacqueline Pontes Monteiro

Understanding interactions of nutrition and lifestyle with an individual's genetic makeup is vital for maintaining health and delaying disease onset. Toward that end, this meeting aims to: 1) Bring together researchers from traditionally separated disciplines: nutrition, (gen) omics, clinics, physiology, epidemiology, analytics, biomathematics; 2) Advance nutrition research as a quantitative, holistic and molecular science; 3) Review/challenge classical pre-clinical models and clinical study designs, incorporating improved translational in vitro and in vivo models, human intervention study designs, and innovative new tools/technologies for molecular phenotyping; and 4) Connect basic science to patient- and consumer-relevant outputs in terms of personalized dietary/nutritional counseling and monitoring/diagnostics.

Session Topics:
- The Interaction between Human Genome, Diet and Environment
- Translational Models for Human Nutrition and Health
- Human Nutritional and Lifestyle Interventions
- Capturing and Monitoring Human Individuality
- From Nutrigenomics to Systems Nutrition
- Nutrition 2.0 – Translation into Solutions for Human Health
- Global Nutrition and Sustainability

Global Health Travel Award Deadline (for investigators from developing countries): May 12, 2015;
Scholarship & Discounted Abstract Deadline: June 16, 2015; Abstract Deadline: July 14, 2015; Discounted Registration Deadline: August 13, 2015
For additional details, visit **www.keystonesymposia.org/15T1**.

Diabetes: New Insights into Molecular Mechanisms and Therapeutic Strategies

October 25–29, 2015
Westin Miyako Kyoto | Kyoto | Japan

Scientific Organizers: Takashi Kadowaki, Juleen R. Zierath, Nobuya Inagaki and Barbara B. Kahn

The prevalence of type 2 diabetes is rising to epidemic proportions worldwide. Type 2 diabetes is a complex disease caused by dysfunction of multiple organ systems, and disease susceptibility is profoundly influenced by both genetic and environmental factors. This meeting brings together leading professionals in the academic and pharmaceutical communities with various specialties in diabetes research to share new approaches and research paradigms. The meeting will present the latest discoveries in diabetes research, highlighting essential aspects of diabetes, as well as emerging themes that are likely to provide novel therapeutic approaches.

Session Topics:
- Islet Dysfunction in Diabetes
- Regenerative Medicine in Diabetes
- Gut Biology and Systemic Metabolism
- CNS Control of Metabolism
- Novel Insights into Adipocyte Biology
- Molecular Mechanisms Underlying Insulin Resistance
- Genetics and Epigenetics of Diabetes
- Diabetes and Healthy Lifespan

Scholarship & Discounted Abstract Deadline: June 25, 2015; Abstract Deadline: July 23, 2015; Discounted Registration Deadline: August 25, 2015
For additional details, visit **www.keystonesymposia.org/15T2**.

KEYSTONE SYMPOSIA™
on Molecular and Cellular Biology
Accelerating Life Science Discovery

Publish your brightest scientific masterpiece

Molecular Probes®

Exhibit the brightest cell images using Alexa Fluor® secondary antibodies

With over 30,000 citations, it's no secret Alexa Fluor® dye–labeled secondary antibodies are the leader in fluorescence. Consistently dependable and available in 20 different colors, their brilliant hues have helped scientists visualize their research for nearly two decades.

Find out more about Alexa Fluor® secondary antibodies at
lifetechnologies.com/alexafluor

life technologies

A **Thermo Fisher Scientific** Brand

LSU Health
NEW ORLEANS

School of Medicine
WILLIAM & SARAH JANE PELON ENDOWED CHAIR
DEPARTMENT OF MICROBIOLOGY, IMMUNOLOGY & PARASITOLOGY

LSU Health Sciences Center School of Medicine is initiating a search for a senior researcher to join the Department of Microbiology, Immunology and Parasitology. Candidates will be considered for appointment as Professor on the tenure track and should have a strong record of research accomplishment, lead an active, nationally funded research program, and have a commitment to developing collaborative translational research programs. This position is associated with the endowed William and Sarah Jane Pelon Chair, designed to enhance the scholarly productivity of the incumbent.

The ideal candidate will have a Ph.D. and/or M.D., demonstrated team-building ability, and a strong track record of developing translational research from basic scientific observations. Expertise in all areas of host/pathogen interaction will be considered, but special consideration will be given to those complementing existing core departmental strengths in HIV, HIV-related infections, and sexually transmitted diseases.

LSU Health Sciences Center School of Medicine offers a highly interactive and collegial environment, with a strong history of collaborative research programs and state-of-the-art infrastructure, including core laboratories in genomics, proteomics, bioinformatics, imaging, and flow cytometry. Excellent opportunities exist for interaction with clinical departments, and with research Centers of Excellence in Vaccine Development, Cancer, Alcohol and Drug Abuse, Cardiovascular Biology, and Neuroscience. Anticipated duties and responsibilities will include sustaining an exceptional research program, mentoring graduate students and postdoctoral fellows, and participation in departmental and school graduate and undergraduate teaching programs. The institution offers competitive start-up packages and salaries.

Qualified applicants with a substantial record of scientific achievement should send a single PDF document containing their curriculum vitae including details of publications, previous and current research funding, teaching experience, a statement of research plans, and the names of at least three referees to: **SOM-Recruits@lsuhsc.edu** with **Professor - MIP** in subject line.

LSUHSC is an Equal Opportunity Employer for females, minorities, individuals with disabilities and protected veterans.

中国科学院
病原微生物与免疫学重点实验室
CAS Key Laboratory of Pathogenic Microbiology and Immunology

CAS One-Hundred Talent Full-professor or Tenure-Track Associate Professor Positions in Virology and Immunology

CAS Key Laboratory of Pathogenic Microbiology and Immunology, Institute of Microbiology, Chinese Academy of Sciences invites applications for a number of faculty positions immediately available in research areas related to (1) Pathology of viral infection, particularly influenza virus and others causing severe diseases; (2) immune responses to infections, including immune regulation, development and activation; and (3) drug discovery for anti-infection and human monoclonal antibody isolation; (4) vaccine development for important pathogens; (5) Structure Virology, Structure Immunology. Candidates whose research focuses on interspecies transmission of pathogens or host cellular immunity are especially encouraged to apply.

CAS Key Laboratory strengths include a biosafety level 3 laboratory facility and the CAS Center for Influenza Virus Research and Early Warning. The successful candidate is expected to develop a strong extramurally funded research program. Candidates must have a Ph.D. or equivalent, and at least three years of postdoctoral research experience. Competitive salary and startup funds are available. Please submit a single PDF including a CV, summary of research program and future directions, and the names and contact information of at least three referees to: **Dr. George F. Gao, Director, CAS Key Laboratory of Pathogenic Microbiology and Immunology, Institute of Microbiology, Chinese Academy of Sciences via email: gaof@im.ac.cn.** The search will start immediately and will continue until the positions are filled.

63° north

KNOWLEDGE FOR A BETTER WORLD
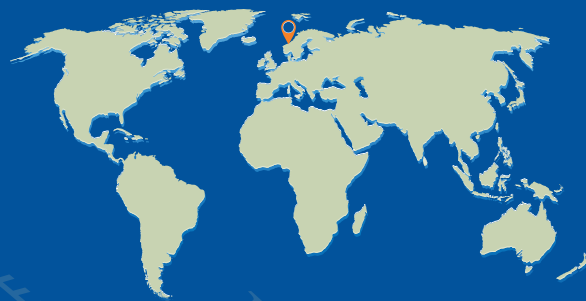
THE ONSAGER FELLOWSHIPS

12 tenure-track positions available at NTNU

The Norwegian University of Science and Technology (NTNU) is Norway's primary institution for educating the future's engineers and scientists. The university also has strong programmes in the social sciences, teacher education, the arts and humanities, medicine, architecture and fine art. NTNU's cross-disciplinary research delivers creative innovations that have far-reaching social and economic impact and that help contribute to a better world.

The Onsager Fellowship programme at NTNU is designed to attract the most talented scholars with an established reputation for high quality research and a commitment to learning and teaching at the university level.

APPLY FOR A TENURE-TRACK POSITION AS AN ASSOCIATE PROFESSOR IN:

- Linguistics
- Robotic vision
- Molecular biodiversity
- Medicine – bioinformatics
- Medicine – molecular biology
- Statistical machine learning
- Theoretical condensed matter physics
- Inorganic or hybrid functional materials

- Safety and reliability of complex systems
- Marine structures for the future – marine technology
- Zero emission refurbishment of the built environment
- Economics of natural resources and quantitative peace research

More info at: www.ntnu.edu/onsagerfellowship
Closing date: 25 May.

NTNU – Trondheim
Norwegian University of Science and Technology

TOP RESEARCH DEMANDS BRILLIANT MINDS
– WE'RE ALWAYS LOOKING FOR THE BEST
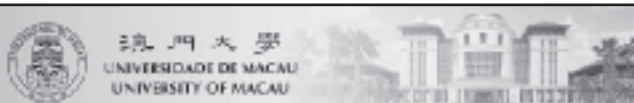
Academic Positions in the Institute of Chinese Medical Sciences

The University of Macau is a leading higher education institution in Macao, with English as its working language. In recent years, the University has made great progress in various areas, with increasing international recognition of its excellence in teaching, research and community service. The Times Higher Education World University Rankings 2014/2015 ranks the University among the world's top 300 universities. With the beautiful new campus (20 times larger than the old one) becoming fully operational, the launch of Asia's largest residential college system, the establishment of new faculties, and the increasing numbers of students and faculty members recruited from around the world, UM possesses great potential and provides exciting new possibilities for growth and development.

Established in 2002, the Institute of Chinese Medical Sciences (ICMS) is an academic unit of excellence in biomedical and pharmaceutical sciences in the region. It hosts the State Key Laboratory of Quality Research in Chinese Medicine – China's first and only state key laboratory in the field of Chinese medical sciences. Over the past decade, ICMS has secured outstanding funding support from both national and regional governments and built long-term strategic collaborations with top academic organizations around the world.

The Institute of Chinese Medical Sciences now invites applications at various academic ranks in the following areas: (1) innovative drug discovery, including Chinese medicine, biopharmaceutics, and chemical drugs; (2) functional food research and development; (3) pharmaceutical science and engineering; (4) quality testing; (5) food and drug safety.

Qualifications

Chair Professor / Professor: A PhD/MD degree; experience in a senior management position in academia; established reputation as a leader in relevant fields; demonstrable competence in fund-raising and industry collaboration
Associate Professor: A PhD/MD degree; a solid track record of research publications and funding support; strong commitment to excellent research and effective teaching
Assistant Professor: A PhD/MD degree; a solid track record of research publications, with teaching experience being desirable

The selected candidate is expected to assume duty within 2015.

Position and Remuneration

Remuneration and appointment rank offered will be competitive and commensurate with the successful applicants' academic qualification, current position and professional experience. The current local maximum income tax rate is 12% but is effectively around 5% - 7% after various discretionary exemptions.

Application Procedure

Application should include a cover letter indicating positions interested, a brief statement of research interest (required for independent professorship positions), and current curriculum vitae in English. Review of applications will commence in May 2015 and continue until the positions are filled. Applicants should visit **http://www.umac.mo/vacancy** for more details, and apply **ONLINE** at **Jobs@UM** (**https://isw.umac.mo/recruitment**) (**Ref. No.: ICMS/AR/09/2015**). Applicants may consider their applications not successful if they were not invited for an interview within 3 months of application.

Human Resources Office
University of Macau, Av. da Universidade, Taipa, Macau, China
Website: https://isw.umac.mo/recruitment;
Email: vacancy@umac.mo
Tel: +853 8822 8573; Fax: +853 8822 2412

The effective position and salary index are subject to the Personnel Statute of the University of Macau in force. The University of Macau reserves the right not to appoint a candidate. Applicants with less qualification and experience can be offered lower positions under special circumstances.

Personal data provided by applicants will be kept confidential and used for recruitment purpose only
** Under the equal condition of qualifications and experience, priority will be given to Macao permanent residents**

University of Macau - An ideal place to pursue your career
http://www.umac.mo

Director Position
Genomics Research Center
Academia Sinica, Taiwan

Academia Sinica, Taiwan, invites applications and nominations for the position of Director of the Genomics Research Center (GRC). The initial appointment is for a period of three years (renewable for a second term) starting July 12, 2016.

As the pre-eminent academic research institute in Taiwan, Academia Sinica is devoted to basic and applied research in mathematics and physical sciences, life sciences, and humanities and social sciences. GRC consists of 26 Principal Investigators, and 14 research specialists, focusing on four research themes: Chemical Biology, Medical Biology, Physical and Computational Genomics, and Biotechnology Incubation Center. GRC is well funded and equipped with modem research facilities staffed by experienced research specialists. It also maintains a high research standard with a high-quality publication record. For details about GRC, please see **http://www.genomics.sinica.edu.tw/index.php/en/about-grc**

Interested candidates should have a PhD or equivalent degree, with outstanding research accomplishments and demonstrated leadership ability. In addition to pursuing an internationally recognized research program at GRC, the successful candidate is also expected to provide intellectual leadership to GRC.

Applications and nominations, including a cover letter listing 3 to 5 names of references, and a complete curriculum vitae (prepared in English) with ten representative publications highlighted, should be sent to **Ms. Annie Lin, Genomics Research Center, Academia Sinica, 128 Academia Road, Section 2, Nankang, Taipei 115 Taiwan** or by Email to **annie@gate.sinica.edu.tw** . Screening of application/nominations will begin immediately, and will continue until the position is filled.

myIDP: A career plan customized for you, by you.

For your career in science, there's only one **Science**

my IDP
Science Careers

Recommended by leading professional societies and the NIH

Features in myIDP include:

- Exercises to help you examine your skills, interests, and values.

- A list of 20 scientific career paths with a prediction of which ones best fit your skills and interests.

- A tool for setting strategic goals for the coming year, with optional reminders to keep you on track.

- Articles and resources to guide you through the process.

- Options to save materials online and print them for further review and discussion.

- Ability to select which portion of your IDP you wish to share with advisors, mentors, or others.

- A certificate of completion for users that finish myIDP.

Visit the website and start planning today!
myIDP.sciencecareers.org

Science Careers In partnership with:

advancing the life sciences 1912-2012 **FASEB** Federation of American Societies for Experimental Biology

UCSF University of California San Francisco

MEDICAL COLLEGE OF WISCONSIN

BURROUGHS WELLCOME FUND

AWARDS

Terumo Life Science Foundation

We welcome your nominations for candidates for the
3rd Terumo Global Science Prize
–An academic award for biomaterials researchers–

■Purpose

In recent years, combined research in the fields of biomaterials and regenerative medicine is accelerating rapidly, and various efforts toward practical application are being made. The fusion of excellence in materials engineering, life science, and the related discipline of systems engineering is essential for this area. This Prize shall be awarded to outstanding researchers who have demonstrated unique, internationally renowned achievements in research, made significant contributions to the field of regenerative medicine particularly through novel biomaterials discovery, and continued to work in the frontline of research.

We hope that this Prize will be a great source of encouragement to researchers, resulting in the further evolution of research towards practical application and a brighter future for humankind.

■Details of the Prize

The Terumo Global Science Prize shall be awarded to one outstanding researcher. The awardee will receive a commemorative shield and a gift as the main prize, together with a supplementary monetary prize of 10 million yen.

■Award ceremony

The award ceremony as well as the commemorative lecture will be held in Tokyo sometime between July and August 2016. The recipient of the Terumo Global Science Prize is requested to be present at the ceremony and to give a speech.

■Application method

An application in the form of a recommendation shall be filed. (No self-recommendation accepted)

Please fill out the application form and submit it to the Secretariat along with all the required documents. The application can be made online or by post. Please refer to the official Web site for more details.

■Application Deadline

August 31(MON), 2015

By Post: Must be postmarked on or before the above date
Online: Must be sent at or before 5:00 PM(JST) on the above date

■The Awardee of the 2nd Terumo Global Science Prize

Dr. Sung Wan Kim
(Distinguished Professor, University of Utah)

NOW ACCEPTING APPLICATIONS
Official Web Site http://www.terumozaidan.or.jp/english

POSITIONS OPEN

By **Emily Nicholson**

Accounting for career breaks

Early in my scientific career, I pursued research while remaining blissfully unaware of the difficulty of securing a permanent academic position, especially for women and mothers. I drifted happily through a Ph.D. and two postdocs abroad, guided by interesting science, people, and places—and a nonscientist husband with ideas about where he wanted to live. It wasn't until I had been a postdoc for several years, with two children and a third on the way, that I recognized the need to adopt a sound strategic approach to securing a tenured faculty position, particularly given my career breaks.

For each of my three sons—born in 2009, 2011, and 2013—I took 8 months of maternity leave, and since then I've worked largely part time and continue to do so. Counted over calendar years, these breaks make my track record look ordinary. My early job applications—using a standard CV that mentioned my maternity leaves only in passing—reflected the apparent ordinariness of that track record: I didn't get so much as an interview. Then, with mentoring and advice from colleagues and friends, I reshaped my CV to account for the time I'd spent raising my family. I put my career breaks front and center, and I reported my productivity metrics to account for my time away from work. Numbers of publications, citation rates, and grant income are used widely to assess and compare researchers, so I wanted to make sure I was judged fairly.

The result: My first application after I made the adjustments yielded a tenured position in the city we had already settled in. Reframing my track record undoubtedly helped. Here's how I did it.

Get the data. First, I calculated how many years of full-time equivalent work I've done by tallying the time worked each month (e.g., 0% when on maternity leave, 60% when working part time, and 100% when working full time). Accounting for time off and part-time work, I've worked 5.6 full-time years during the 8.5 calendar years since I finished my Ph.D., the equivalent of 66% of full time. Since my first child was born 6 years ago, I have worked the equivalent of 3.3 full-time years, or 55% of full time. Next, I worked out how much I'd achieved each year in terms of publications, grants, student supervision, and so on.

Do the math. Rather than hoping the readers of my application would do the math on their own, I did it for them. I cor-
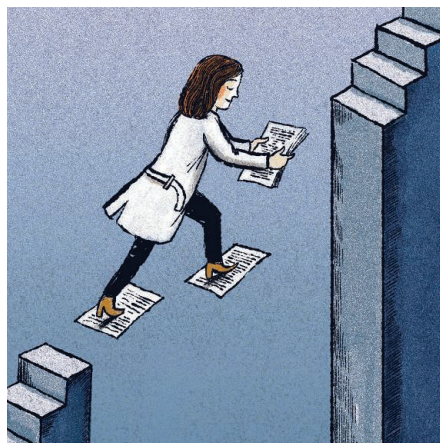
"I wanted to make sure I was judged fairly."

rected the number of publications I had each year to account for my maternity leaves. For example, in the 6 years since my first son was born I had 23 publications—equivalent to about 42 publications if I had been working full time. Similar corrections can be made to other common metrics: citations, grants, and so on.

Write about career interruptions up front and in a positive way. I present the data on career breaks, effective years worked, and achievements at the top of my CV, in cover letters for job applications, and in a prominent position on grant applications. Here's an example: "Since 2009, I have worked the equivalent of approximately 3.3 full-time years, 55% of full time. Yet it has been a highly productive period: 23 publications—including 12 as lead or last author—a research fellowship, and a major grant. On a pro-rata basis, that equates to about 42 publications in 6 years of full-time work."

I also like to emphasize—without complaining—that working part time while raising kids isn't easy. "This does not account for the effect reduced working hours and travel opportunities has on networking opportunities, which affect collaborations and citation rates. I have nonetheless established several fruitful national and international collaborations, and my research has scientific and practical impacts." I want readers to think, "If she managed this working part time, with breaks and sleep deprivation, imagine what she'll do once the kids are older!" ■

Emily Nicholson is a senior lecturer at the Centre for Integrative Ecology at Deakin University, Melbourne Burwood, in Australia. She is grateful to Mick McCarthy and Emma Johnston for their advice. For more on life and careers, visit sciencecareers.org. Send your story to SciCareerEditor@aaas.org.